

Azimuthal angular correlations of D mesons and charged particles with the ALICE detector at the LHC

Sandro Bjelogrić

A catalogue record is available from the Utrecht University Library.

ISBN: 978-90-393-6552-6

Copyright ©2016 by S.Bjelogrlić

All rights reserved. No part of this book may be reproduced, stored in a database or retrieval system, or published in any form or in any way, electronically, mechanically, by print, photoprint, microfilm or any other means without prior written permission of the author.

Typset using L^AT_EX

Printed by Ipskamp Drukkers, Enschede, The Netherlands

Azimuthal angular correlations of D mesons and charged particles with the ALICE detector at the LHC

Azimutale hoekcorrelaties tussen D mesonen en geladen deeltjes
met het ALICE experiment aan de LHC

(met een samenvatting in het Nederlands)

ter verkrijging van de graad van doctor aan de Universiteit
Utrecht op gezag van de rector magnificus, prof.dr. G.J. van der
Zwaan, ingevolge het besluit van het college voor promoties in
het openbaar te verdedigen op woensdag 4 mei 2016 des
ochtends te 10.30 uur

door

Sandro Bjelogrić

geboren op 10 oktober 1986 te Pula, Kroatië

Promotor: Prof. dr. R.J.M. Snellings

Copromotor: Dr. A. Mischke

Dit werk maakt deel uit van het onderzoekprogramma van de Stichting voor Fundamenteel Onderzoek der Materie (FOM), die deel uitmaakt van de Nederlandse Organisatie voor Wetenschappelijk Onderzoek (NWO).

This work is part of the research programme of the Foundation for Fundamental Research on Matter (FOM), which is part of the Netherlands Organisation for Scientific Research (NWO).

*Do not go where the path may lead,
go instead where there is no path
and leave a trail*
R.W.Emerson

Contents

1	Introduction	3
1.1	The standard model and QCD	3
1.2	QCD phase diagram	6
1.3	Heavy-ion collisions	8
1.4	Experimental signatures of the QGP	10
1.4.1	Azimuthal anisotropy	11
1.4.2	Parton energy loss	12
1.5	Cold nuclear matter effects: proton ion collisions	19
2	Heavy quarks in heavy-ion collisions	21
2.1	Heavy quark production	21
2.2	Heavy quarks in the QGP: energy loss	25
2.2.1	Energy loss models	27
2.3	Azimuthal correlations of heavy-flavour particles	32
3	The experimental setup	39
3.1	The Large Hadron Collider	39
3.2	The <i>ALICE</i> experiment	41
3.3	The central barrel detectors	43
3.3.1	The Inner Tracking System	43
3.3.2	The Time Projection Chamber (TPC)	44
3.3.3	The Time Of Flight Detector (TOF)	46
3.4	Tracking and vertexing	47
4	Analysis Strategy	49
4.1	Event selection	50
4.2	D ^{*+} reconstruction	50
4.2.1	Topological selections	50
4.2.2	Signal extraction	53
4.3	Background subtraction	56
4.3.1	Background from D ⁰ side-bands	56
4.3.2	Background from D ^{*+} side-bands	57
4.3.3	Subtraction of the background contribution	61
4.4	Associated track selection	63
4.5	Correction for detector inhomogeneities	63
4.6	Correction for D ^{*+} meson efficiencies	67
4.7	Correction for associated track efficiencies	68
4.8	Subtraction of correlations from D ^{*+} mesons coming from Beauty-hadron decays	69
4.9	Correction for secondary track contamination	72

CONTENTS

5	Monte Carlo analysis	75
5.1	Different contributions to the azimuthal angular correlations of hadrons and D mesons	75
5.2	Monte Carlo closure test	81
5.3	Event mixing normalisation	89
6	Systematic uncertainties	93
6.1	Azimuthal correlation distribution systematic uncertainties . . .	93
6.1.1	D ^{*+} meson yield extraction	95
6.1.2	Background subtraction	97
6.1.3	D meson efficiency correction	97
6.1.4	Tracking efficiency	100
6.1.5	Correction for contamination from secondary tracks . . .	103
6.1.6	Beauty feed-down correction	104
6.1.7	Total systematic uncertainty	106
7	Results	107
7.1	D ^{*+} -charged particle correlations	108
7.2	Average of D ⁰ , D ⁺ and D ^{*+}	108
7.3	Estimation of the baseline	115
7.4	Comparison to models	119
7.5	Comparison of azimuthal correlations in pp and p-Pb collisions .	120
7.6	Characterisation of the correlation distribution	123
7.6.1	Systematic uncertainties from the fitting procedure . . .	124
7.7	Near-side yield, width and baseline as function of the D meson and associated track p_T	125
8	Outlook	131
8.1	D ^{*+} -charged particle correlations in Pb-Pb collisions at $\sqrt{s_{NN}} = 2.76$ TeV	131
8.2	ALICE upgrades	132
8.3	Azimuthal correlations with EMCAL trigger	135
9	Conclusions	139

Outline

The study of fully reconstructed open heavy-flavour hadrons in collisions of heavy-ions was possible for the first time at the Large Hadron Collider, with the ALICE experiment. First results of the nuclear modification factor and the azimuthal anisotropy of open-charm mesons [1, 2] became available shortly after the first heavy-ion collision data was collected, presenting interesting and fascinating results.

This PhD thesis discusses the first results of the next step in the study of the physics of open-charm mesons, the azimuthal correlations of open-charm particles with charged particles. These results were obtained in pp and p-Pb collisions, providing the baseline for the measurements from collisions of heavy-ions. The latter are expected to be available in the near future, as the statistics collected from the first years of LHC operations is not enough to provide a reasonable precision.

The first two chapters provide an overview of Quantum Chromo Dynamics (QCD), the Quark Gluon Plasma (QGP) and the physics involving heavy-quarks in the context of heavy-ion collisions. The third chapter presents a description of the ALICE experiment and of the main sub-detectors, used for the purposes of the analysis presented here. Chapter 4 describes the analysis strategy, while chapter 5 discusses the studies on Monte Carlo simulations, performed to better understand the complex systems that are investigated. The systematic uncertainties are discussed widely in chapter 6. The 7th chapter presents the results of the azimuthal correlations between D mesons and charged particles in pp and p-Pb collisions and the comparison to theoretical models. A discussion on the future of this analysis is provided in chapter 8, before concluding the manuscript with a general summary in chapter 9.

The angular correlations of D mesons are performed with all the charged particles passing kinematic and track-quality selections. The majority of the associated particles are hadrons.

Henceforth, in this thesis, in the context of azimuthal correlations, the terms “charged particles”, “hadrons” and “associated particles” are used interchangeably, referring exclusively to charged particles, unless differently stated.

The results discussed in this thesis have been presented at international conferences [3] and will be published in the near future in the paper that is in preparation [4].

1

Introduction

The early years of the 20th century represented a breakthrough in the understanding of the microscopic world: the discovery of the electron by J.J. Thompson in 1897 and the first scattering experiments conducted by Rutherford in 1907 allowed us to get a clear understanding of the structure of atoms. However, the two fundamental forces known at the time (gravitational and electromagnetic interaction) were not enough to describe the observed structures. The introduction of the strong and weak interactions through studies of radioactive decays, completed the phenomenological picture of the nuclear physics at the time. At the same time, the first developments of the quantum theory showed the particle-wave nature of matter. This discovery allowed for a first interpretation of the electromagnetic waves in terms of particles (photons). The experimental observation of a wide “spectrum” of particles that were interacting electromagnetically, weakly and strongly, called for a quantum description of the interactions between them. The first attempts for the so-called “second quantisation” were carried out in the 1920’s, setting the foundations for the quantum field theory. This attempts culminated in the formulation of quantum electrodynamics (QED) in the early postwar period, giving a first successful quantum description of the electromagnetic interaction between charged particles. Similar efforts were carried out for the weak and strong interaction, leading to the formulation of the standard model of particle physics.

1.1 The standard model and QCD

The standard model represents the most complete theory of elementary particles and their interactions. It classifies all the known elementary particles and describes their strong, weak and electromagnetic interactions. It is based on a local gauge symmetry of the type $SU(3) \times SU(2) \times U(1)$. The non-abelian $SU(2) \times U(1)$ broken symmetry describes the electro-weak sector. The force is carried by the gauge bosons, the charged W^+ and W^- , and the neutral Z^0 and γ . $SU(2) \times U(1)$ is broken by the Higgs Mechanism [5], which is responsible for the masses of the elementary particles. The Higgs Mechanism requires the existence of a scalar field, represented by the Higgs Boson, which has been discovered in 2012 in pp collisions at the LHC by the *ATLAS* and *CMS*

CHAPTER 1. INTRODUCTION

collaborations [6, 7]. The strong interaction is mediated by massless bosons called gluons. The fermionic fields in the Standard Model are separated in two groups: the quarks, that experience all the three types interaction, as they carry the three charges considered in the standard model, and the leptons, which are classified in charged leptons (experience both the electromagnetic and weak interaction) and the neutrinos (that interact only weakly).

The classification of the elementary particles considered in the standard model is shown in figure 1.1.

Quantum Chromo Dynamics (QCD) is the theory that describes the strong interaction, and it is constructed in terms of the $SU(3)$ local gauge symmetry. The above mentioned gluons correspond to the 8 massless gauge field deriving from $SU(3)$ local gauge symmetry. The colour is the locally conserved charge of the gauge symmetry. The QCD Lagrangian is obtained by imposing invariance under local transformations and is defined as follows:

$$\mathcal{L}_{\text{QCD}} = \bar{\psi}_i (i(\gamma^\mu D_\mu)_{ij} - m \delta_{ij}) \psi_j - \frac{1}{4} F_{\mu\nu}^a F_a^{\mu\nu} \quad (1.1)$$

where ψ represents the fermionic field associated to a quark, and $F_{\mu\nu}^a$

$$F_{\mu\nu}^a = \partial_\mu G_\nu^a - \partial_\nu G_\mu^a + g f^{abc} G_\mu^b G_\nu^c \quad (1.2)$$

represents the gluon field strength tensor where G_ν^a is the gluon field, f^{abc} are the structure constants of the $SU(3)$ group, and g is the coupling constant.

The third term in equation 1.2 originates from the non-abelian nature of

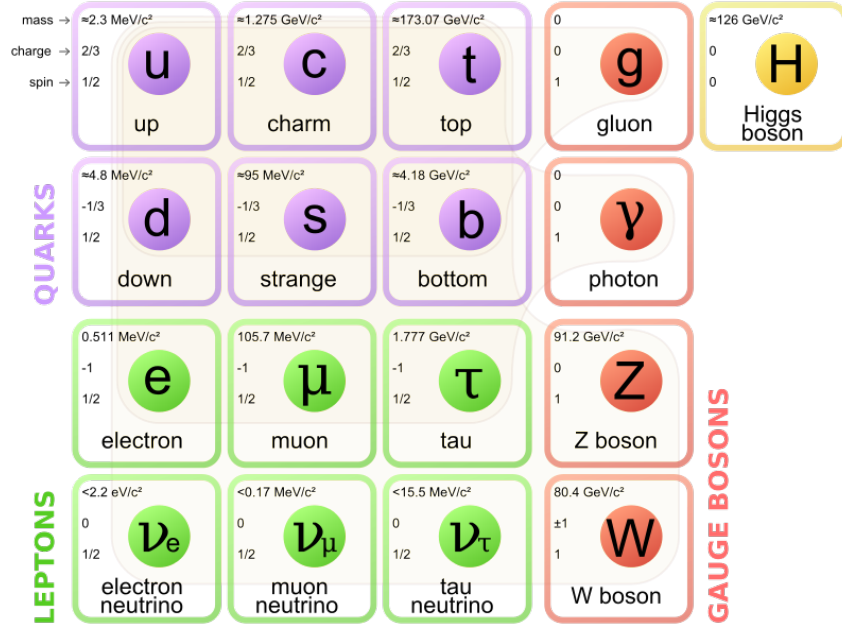


Figure 1.1: All the known elementary particles, predicted by the standard model and discovered experimentally.

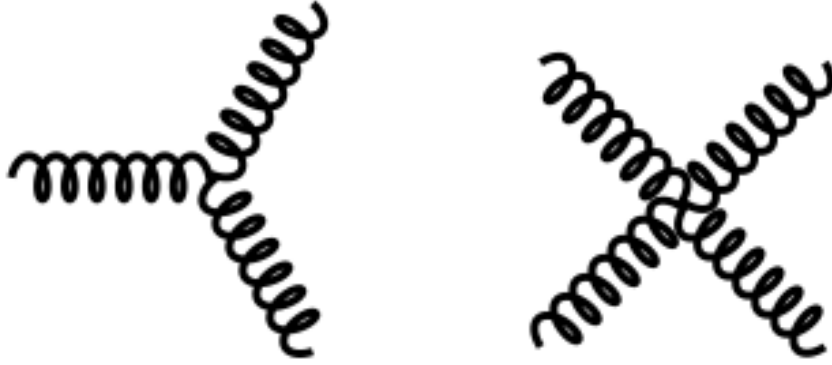


Figure 1.2: The non-abelian structure of $SU(3)$ allows for gluon self-interactions, which occur as three and four gluon vertices

$SU(3)$, and allows for self-interactions of the gluon fields. This means that the gluon field carries a colour charge itself. The product of the gluon field strength tensors (the last term of the QCD Lagrangian, equation 1.1 will contain three and four gluon interaction terms, which are shown as Feynman diagrams in figure 1.2.

In the (colour) charge renormalisation procedure, the presence of the gluon self-interactions leads to a dependency of the coupling constant α_s from the exchanged momentum in the interaction, Q . Equation 1.3 shows the dependency at the first order

$$\alpha_s(Q^2) = \frac{2\pi}{(11 - 2/3n_f) \ln(Q^2/\Lambda_{QCD}^2)} \quad (1.3)$$

where n_f represents the number of quark flavours, and Λ_{QCD} is a constant not predicted by the theory, which corresponds to the energy scale where the perturbatively-defined coupling would diverge. The dependency is shown graphically in Fig. 1.3. For large values of Q ($Q^2 \gg \Lambda^2$), α_s decreases asymptotically to zero. In this particular approximation (large transferred momentum, short distances), the quarks and gluons interact very weakly. This phenomenon is known as asymptotic freedom.

On the other hand, for small values of Q ($Q^2 \ll \Lambda^2$, corresponding to long distances), α_s increases. This “long distance limit” manifests itself in another peculiar property of QCD, known as confinement. Confinement can be understood in the picture of the “string model”: because of the gluon self-coupling, as a quark-antiquark pair separates, the gluon field forms a narrow tube (or string) of colour fields between them. As the distance increases, the energy of the tube increases, making energetically favourable the creation of a new quark-anti quark pair. Because of confinement, there are no coloured states in nature. Quarks are confined to exist in structured, colourless particles called hadrons.

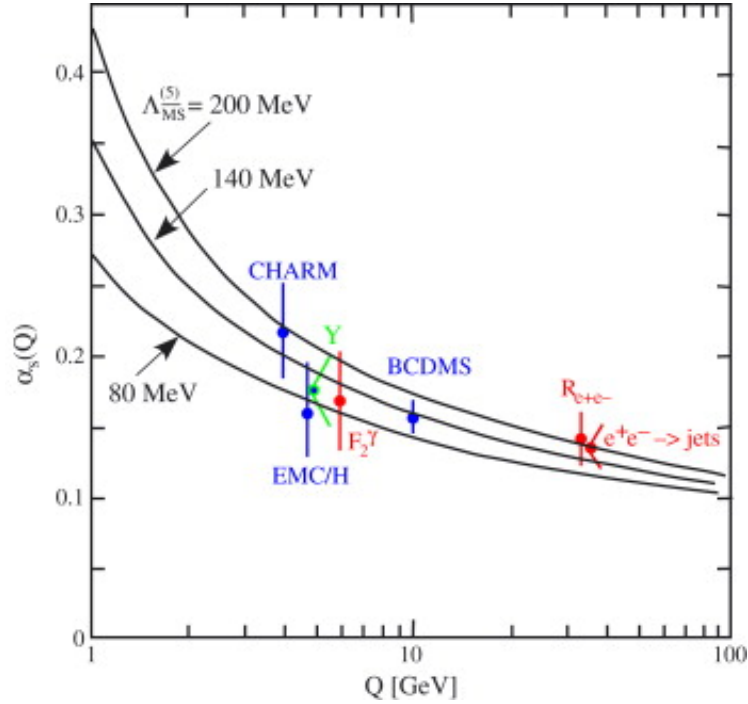


Figure 1.3: Dependence of the coupling constant, α_s , with Q , the momentum exchanged in the interaction [8].

According to current knowledge, hadrons exist in $q\bar{q}$ states (mesons) or in qqq ($\bar{q}\bar{q}\bar{q}$) states (baryons). Very recent result from the LHCb collaborations showed the existence of exotic particles composed of five quarks (called pentaquarks) [9].

1.2 QCD phase diagram

Under ordinary conditions, quarks and gluons are confined into hadrons by the strong interaction. Lattice QCD calculations [10] predict that by bringing the hadronic matter to extreme conditions (high temperature or densities), different thermodynamic states can be formed. The cartoon in figure 1.4 illustrates the key features of the hadronic matter as a function of the temperature T and the baryo-chemical potential, μ_B of the system. At low values of the temperature and baryo-chemical potential, quarks and gluons are bounded into hadrons, and this is the limit of the matter in ordinary conditions. With increasing temperature (at low values of μ_B), the hadronic matter gets deconfined: when the system exceeds its critical temperature, T_C , expected to be $T_C \sim 154$ MeV [11, 12], quarks and gluons keep interacting, but are not bound together anymore: they are deconfined in a plasma, the so-called Quark-Gluon Plasma (QGP). There is a net increase in the total number of degrees of freedom of the system, as now also the flavour, spin, colour and charge states of

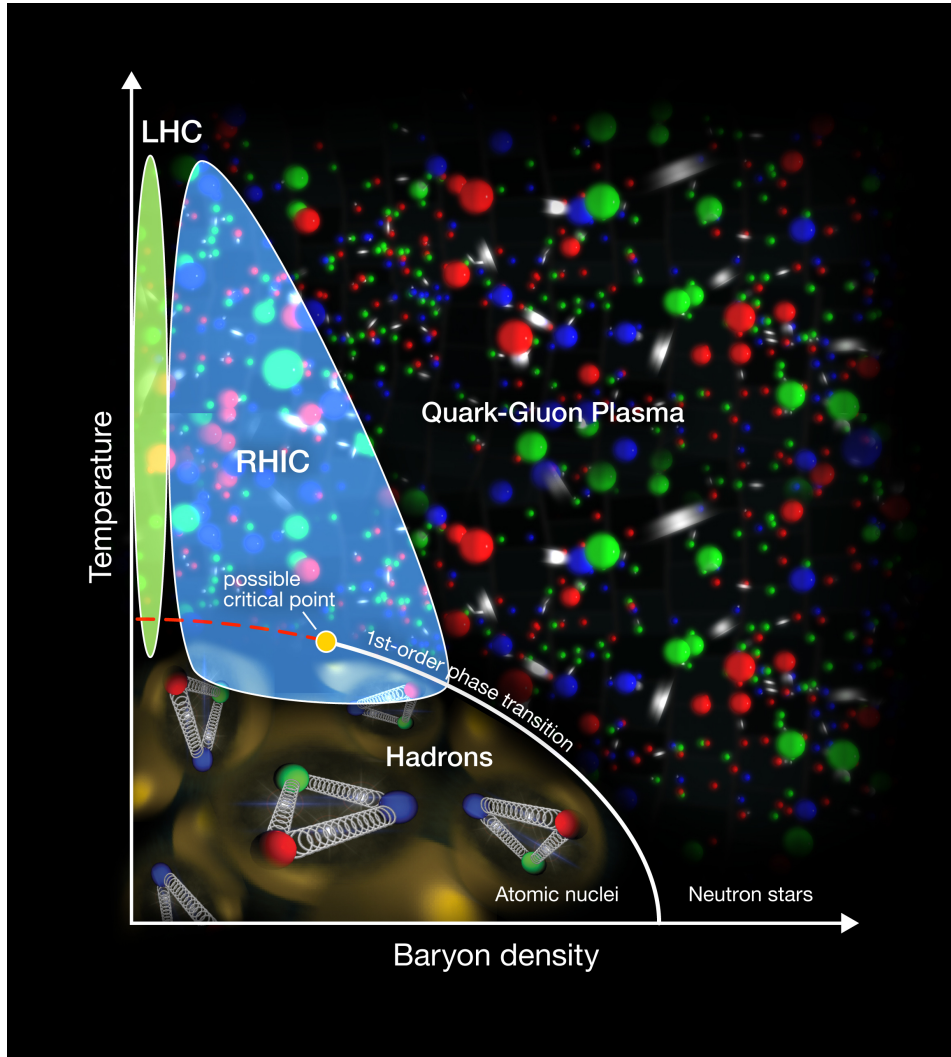


Figure 1.4: Schematic representation of the QCD phase diagram with respect to the temperature (vertical axis) and the baryon density (horizontal axis). At high temperatures, the phase transition to the QGP occurs. Image: Brookhaven National Laboratory

quarks and gluons become available.

Figure 1.5 shows the Lattice QCD calculation [13] of the energy density, ϵ (blue line) and of the pressure (red dashed line), both normalised to the temperature T to the fourth power. The energy density increases rapidly in the range $145 < T < 163$ MeV, which is the effect of the change in the effective degrees of freedom that happens during the phase transition. The early universe is believed to have existed in a state of Quark Gluon Plasma for about 10^{-6} seconds after the Big bang, until the temperature, decreasing because of the universe expansion, went below the critical temperature T_C . At this stage also the baryo-chemical potential was close to zero.

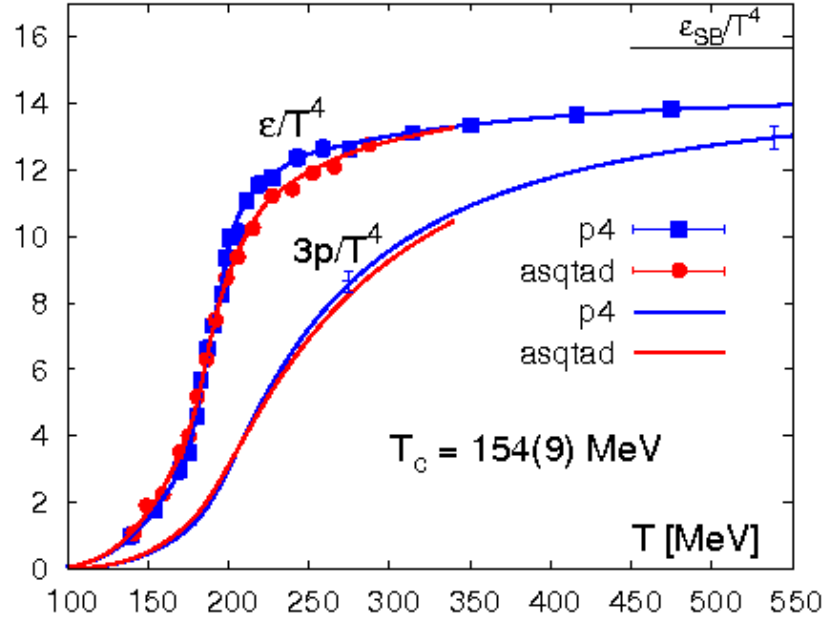


Figure 1.5: Lattice QCD prediction of the energy density and the pressure scaled by the temperature at the fourth power [13]. The steep change is due to the phase transition from hadronic matter to QGP and therefore an increase of number of the degrees of freedom of the system.

1.3 Heavy-ion collisions

The extreme conditions at which the QGP can be created are reachable nowadays in the laboratory by colliding heavy nuclei. The two main heavy-ion facilities currently used to study the QGP are the Relativistic Heavy Ion Collider (RHIC) in Brookhaven (BNL) and the Large Hadron Collider (LHC) at CERN.

At RHIC, different types of nuclei, such as gold, copper and uranium, are accelerated and collided at a centre of mass energy that ranges from 7.7 to 200 GeV per nucleon-nucleon pair. Two main experiments, PHENIX and STAR are used to detect the particles created in the heavy-ion collisions that carry the information of the strongly interacting matter.

On the other side of the Atlantic Ocean, at CERN, the LHC accelerates and collides lead nuclei at a centre of mass energy of 2.76 TeV per nucleon-nucleon pair (5.02 TeV starting from 2015), and the main experiments, ALICE, ATLAS, CMS and LHCb (as of 2015), detect the large amount of particles created in those collisions.

The collision of two heavy ions creates a strongly interacting system (often also called “fireball”), that evolves in a series of phases.

These phases are shown in figure 1.6 and are described below:

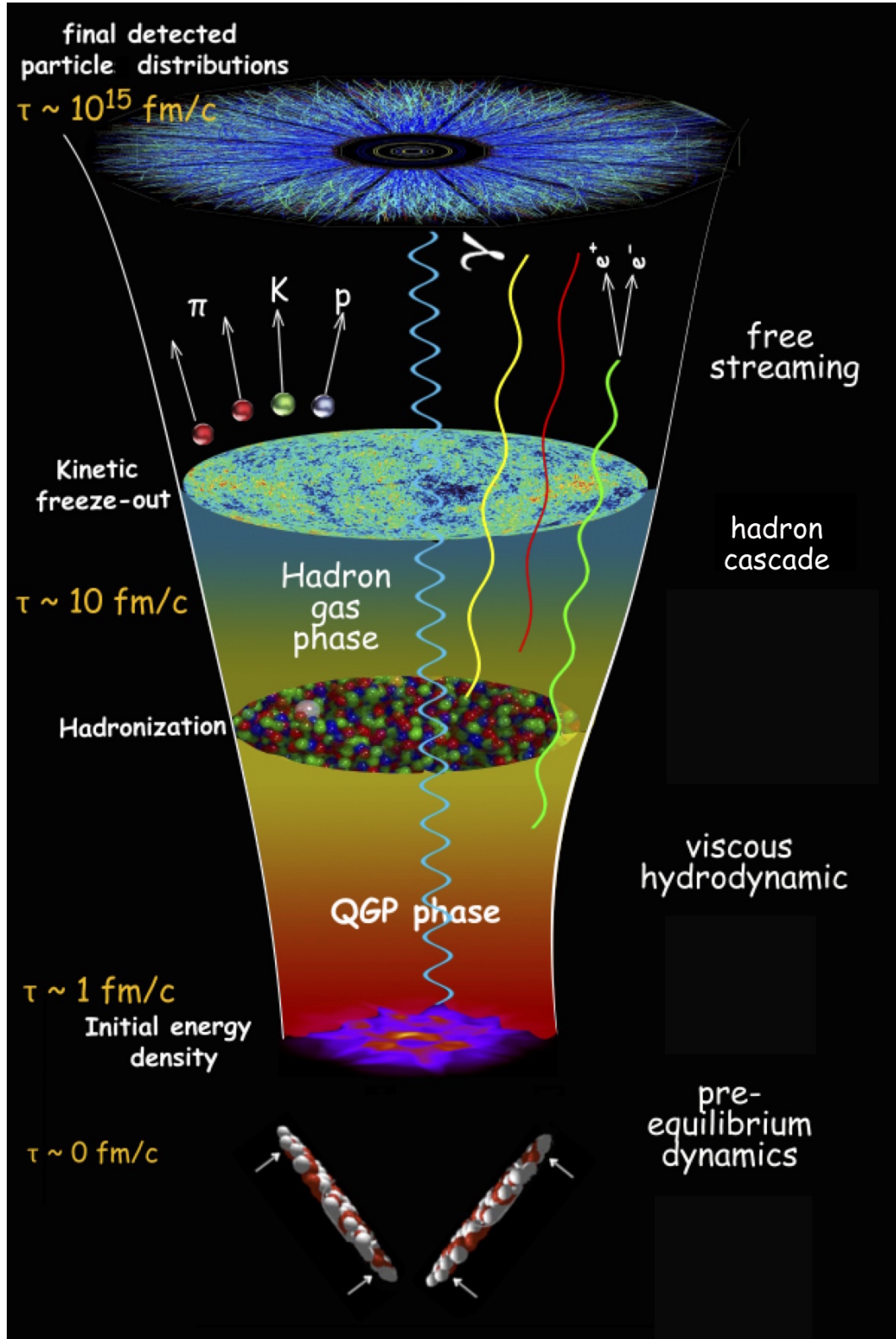


Figure 1.6: The evolution of a heavy-ion collision [14]. The time axis flows on the bottom to the top. The main phases of the evolution are shown (see text for more details).

1. **Pre-equilibrium phase:** is the phase that occurs just after the heavy-ion collisions. The partons, that are created from the hard scattering processes, begin to interact.
2. **QGP phase:** after a time period $\tau < 1 \text{ fm}/c$, the system reaches thermal equilibrium due to rescatterings among its constituents. In this phase, the mean free path of the interacting particles is small compared to the system size: this limit allows the system to be described in terms of hydrodynamics.
3. **Hadronisation:** the system expands and cools down. When the system temperature reaches the critical temperature T_C , a phase transition into the hadronic phase occurs. The transition from the deconfined plasma to hadrons results in a reduction of the effective degrees of freedom of the system.
4. **Chemical freeze-out:** after hadronisation, the hadrons undergo inelastic scatterings until the chemical freeze-out temperature, T_{Ch} , is reached. At this point, the hadronic species abundance are frozen (the only change in abundance that can still occur is due to decays of unstable particles).
5. **Thermal freeze-out:** after the chemical freeze-out occurs, the hadrons continue to undergo elastic scatterings. At the thermal freeze-out temperature, also the elastic scatterings cease and the hadrons leave the equilibrium stage. At this point, all the kinematical properties of the particles are defined.

The QGP cannot be studied directly because it exists for a very short time of the order of $t \approx 10 \text{ fm}/c$. The properties of the strongly interacting medium are studied after reconstructing the final state particles. The main experimental observables, relevant for the topics discussed in this thesis, are described in the next section.

1.4 Experimental signatures of the QGP

Heavy nuclei are not point-like, but they have a finite size. This means that not every collision will be head-on, but it can occur at different impact parameters. The impact parameter is the distance in the transverse plane between the centres of the two nuclei. With increasing impact parameter, not all the nucleons interact. This effect can be quantified in terms of centrality, a quantity that is measured in percentiles (a fraction of the total hadronic cross section): a head-on collision (i.e. with zero impact parameter) is said to be a central collision, and corresponds to low values of the centrality percentile. With increasing impact parameter, the centrality percentile increases and the collisions are said to be semi-central and peripheral. The centrality is determined experimentally

1.4. EXPERIMENTAL SIGNATURES OF THE QGP

via measurements of the total multiplicity or zero-degree energy [15].

Measurements of multiplicities, yields, transverse momenta and directions of the reconstructed particles are used to study the properties of the Quark Gluon Plasma.

This section presents the main observables relevant for this work, namely the azimuthal anisotropy, the nuclear modification factor and angular correlations.

1.4.1 Azimuthal anisotropy

The partons created in a heavy-ion collision interact chaotically among each other. These multiple rescatterings occurring between the medium constituents manifest themselves as flow. More interactions usually lead to a larger magnitude of the flow and bring the system closer to thermalization. Hence, the magnitude of the flow is sensitive to the level of thermalization of the system. The relativistic isotropic expansion of the medium causes the so-called radial flow, which can be studied by measuring the p_T -distribution of the final state hadrons.

On the other hand, if the system presents geometrical asymmetries, pressure gradients will be present that create the so-called anisotropic flow.

In particular, in a semi-central collision, that is schematically shown in figure 1.7, the fireball has an almond-like shape.

The different extension of the interacting system pushes the particles in a preferred direction. The reaction plane (RP), indicated in figure 1.7, is defined by the z -axis and the impact parameter of the two nuclei. It can be estimated experimentally by the event plane (EP), defined as the plane formed by the z -axis (the beam direction) and the preferred direction of the created particles. The anisotropy can be quantified by measuring the azimuthal direction of the particles relative to the reaction plane (RP), i.e.

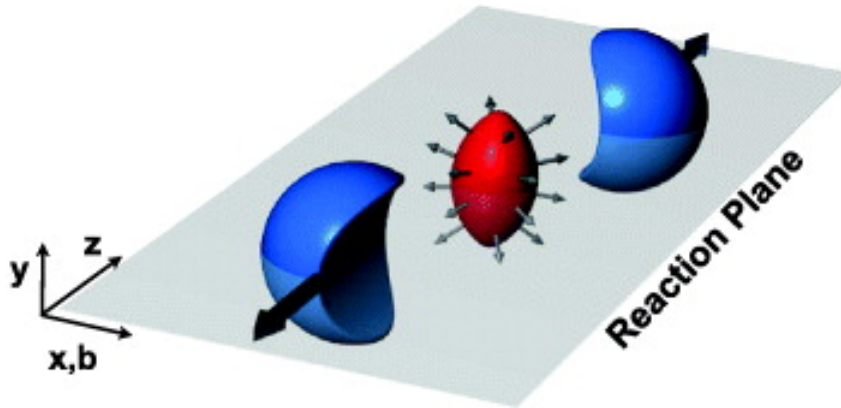


Figure 1.7: Cartoon showing a semi-central collision of two heavy nuclei. The spatial asymmetry of the almond-shaped fireball (red) creates different pressure gradients, therefore particles are pushed in a preferred direction (along the reaction plane).

$$\frac{d^3N}{d^3p} \propto \left(1 + 2 \sum_{n=1}^{+\infty} v_n \cos [n(\phi - \Phi_{RP})] \right) \quad (1.4)$$

where p is the momentum of the particle, ϕ is its direction, Φ_{RP} is the azimuthal direction of the reaction plane, and v_n are the coefficients that quantify a certain component of the anisotropic flow. In particular, the 2nd coefficient, the elliptic flow coefficient v_2 is sensitive to the asymmetries of the particle emissions inside and outside the reaction plane.

Figure 1.8(a) shows the v_2 of charged particles as function of p_T , measured by the ALICE collaboration [16], in Pb-Pb collisions at $\sqrt{s_{NN}} = 2.76$ TeV, in the centrality class 40-50%. The measurement is performed using different methods [17] (2-particle cumulants ($v_2\{2\}$) and 4-particle cumulants ($v_2\{4\}$)). The $v_2\{4\}$ is systematically lower than the $v_2\{2\}$ as it is less affected by non-flow contributions. Figure 1.8(b) shows the v_2 obtained with the 4-particle cumulants method in the centrality classes 10-20%, 20-30% and 30-40%. The ALICE results, measured at $\sqrt{s_{NN}} = 2.76$ TeV, are compared to the results from the STAR collaboration at $\sqrt{s_{NN}} = 200$ GeV. The p_T -dependence of $v_2\{4\}$ is in a remarkable agreement over more than one order of magnitude of $\sqrt{s_{NN}}$.

The elliptic flow is also sensitive to the shear viscosity (η/s). The v_2 is best described with values of the shear viscosity close to the limit of $\eta/s \sim 1/4\pi$ [16, 18, 19, 20], meaning that the QGP behaves as a perfect liquid.

1.4.2 Parton energy loss

One of the most relevant signatures of the presence of the Quark Gluon Plasma is the in-medium energy loss. High-momentum partons are generated in the initial hard-scattering processes. This effect is mainly due to two main sources:

- Energy loss due to the radiation of gluons from high- p_T partons, induced by the presence of the QGP, is called **radiative energy loss**. The radiative energy loss shows a different behaviour depending on the nature of the coupling due to the so-called colour coupling, which equals 4/3 for the quark-gluon coupling and 3 for the gluon-gluon coupling. The different colour factor has as effect a larger energy loss for gluons than for quarks. Additionally, the radiative energy loss depends on the path length of the parton L , and the average squared transverse momentum exchange per unit, known as the transport coefficient. In addition the gluon emission by quarks is subject to the dead-cone effect [21]. Due to the dead-cone effect, a gluon cannot be emitted with an angle smaller than the limit angle ϑ_0 . ϑ_0 depends on the parton mass, i.e. $\vartheta_0 \sim m/E$. Therefore, heavy-quarks are expected to lose less energy compared to lighter quarks, as the forward emission of gluons is suppressed.

1.4. EXPERIMENTAL SIGNATURES OF THE QGP

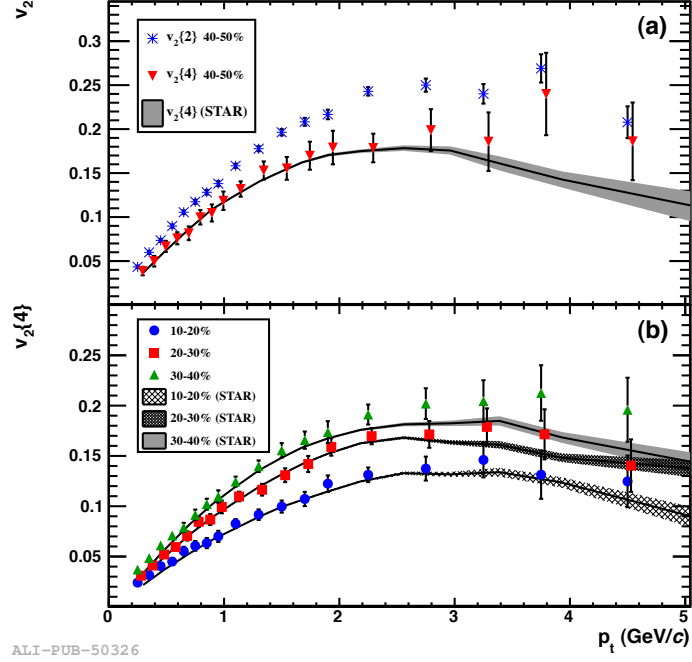


Figure 1.8: v_2 for semi-central collisions measured by ALICE[16]. The upper panel (a) shows the results with the 2- and 4-particle cumulant method in the centrality class 40-50% while the panel (b) shows the results with 4-particle cumulants in different centrality classes. The results are compared to measurements by the STAR collaboration at a lower collision energy.

- Energy loss from multiple scatterings with other partons present in the medium that is called **collisional energy loss**.

Both effects contribute to the energy loss of partons, however the dominance of one respect the other depends on the initial energy of the parton (E) as well as on the path length in the medium.

Deviation from binary scaling: the nuclear modification factor

The Glauber model [22] is a phenomenological model that provides a description of the nucleus-nucleus interaction based on the collision geometry, that plays a role as nuclei are extended objects. It is used to compute the number of binary collisions of the nucleons, $\langle N_{coll} \rangle$. Due to the overlap of the nuclear density functions, the p_T spectra of the hard scattering production in heavy-ion collisions is proportional to the p_T spectra in pp collisions. The factor of proportionality is $\langle N_{coll} \rangle$, which depends on the overlap of the two colliding nuclei. This property is called binary scaling.

The nuclear modification factor, R_{AA} , is the observable that derives naturally from the phenomenological aspects described above, and it is defined as

$$R_{AA} = \frac{1}{\langle N_{coll} \rangle} \frac{dN^{AA}/dp_T}{dN^{pp}/dp_T}, \quad (1.5)$$

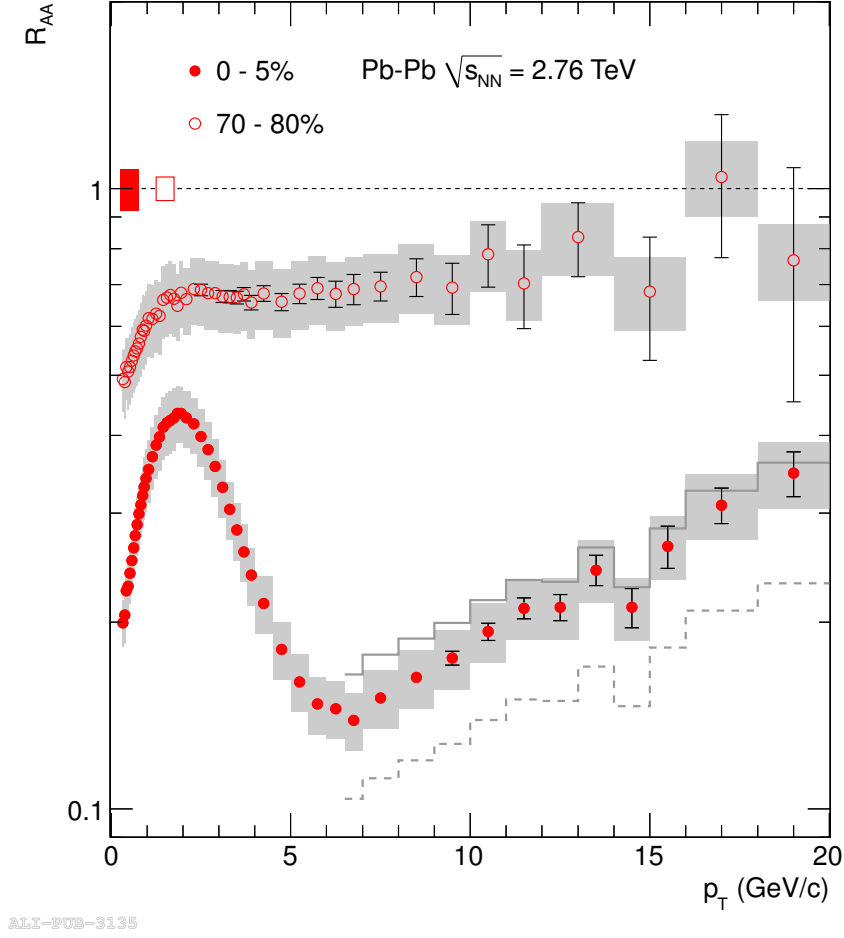


Figure 1.9: R_{AA} of charged particles measured by ALICE [23] in two different centrality classes (0-5% and 70-80%).

where dN^{AA}/dp_T and dN^{pp}/dp_T represent the measured p_T -spectra in heavy-ion and pp collisions, respectively. In absence of a strongly interacting medium, the p_T spectrum follows the binary scaling and the R_{AA} is, by definition, equal to unity.

If partons interact with the medium, they lose energy, and therefore the p_T spectrum gets modified beyond the binary scaling. This reflects in $R_{AA} \neq 1$. In particular, at higher values of p_T , the R_{AA} is expected to be smaller than one in case of energy loss by radiation of gluons or collision with the constituents of the medium.

Figure 1.9 shows the R_{AA} of charged particles measured by the ALICE collaboration [23], for central and peripheral collisions. In both cases $R_{AA} < 1$, which at high p_T is due to the energy loss of the partons created in Pb-Pb collisions at $\sqrt{s_{NN}} = 2.76$ TeV. From Fig. 1.9 it is also clear that the R_{AA} depends on the centrality of the collision, and is smaller for more central events. The strong suppression observed in the central collisions for higher p_T charged

1.4. EXPERIMENTAL SIGNATURES OF THE QGP

particles indicates a very strong parton energy loss in a very dense medium.

Jet quenching

The energy loss will manifest itself in quenched jets. Jets are defined as objects of collimated particles that are created because of a cascade of consecutive emission of partons, that started from a high energetic parton produced by the hard scattering process. Due to the confinement effect of QCD, these partons cannot exist separately, which will result in a cone of collimated particles travelling in the same direction. Partons are created in pairs, and given the size of the system, their creation can be approximated to happen in the same point. In pp collisions, this would lead, at first order, to the production of two back-to-back orientated jets with very similar total energy and momentum. In heavy-ion collisions, due to the presence of the medium, the two partons will not travel the same distance in the medium, meaning that one of them will lose more energy in the medium than the other. This effect is known as jet quenching.

The jet quenching is schematically shown in Fig. 1.10, where in the left panel the production of the two partons and the consequent hadronisation is shown when no medium is present (vacuum), while the right panel shows the same in presence of the medium. Jet quenching can be experimentally observed by studying the back-to-back production of jets in heavy-ion collisions. A momentum imbalance in di-jet events has been observed by the ATLAS and CMS collaborations [24, 25] at the LHC, where fully reconstructed jets can be

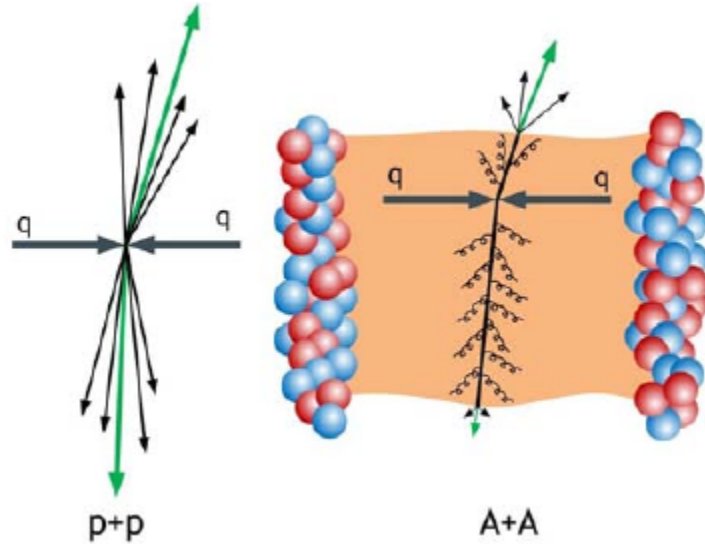


Figure 1.10: Cartoon illustrating the different jet production in pp collisions (left) and heavy-ion (right) collisions. In heavy-ion collision the back-to-back jets interact differently with the QGP, that leads to an asymmetry in the jet energies, on contrary to what happens in pp collisions.

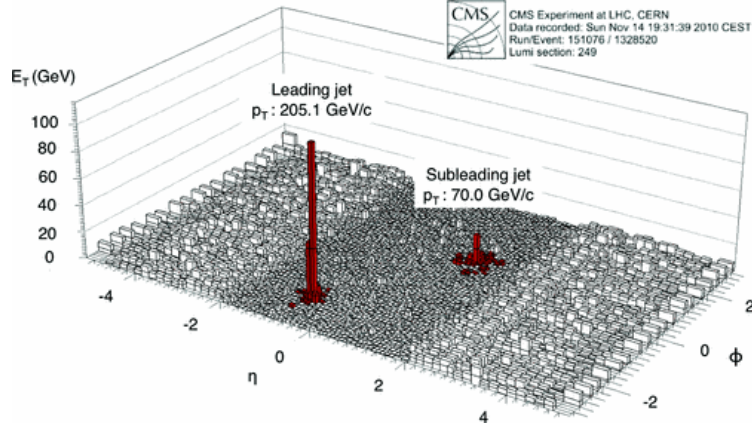


Figure 1.11: Transverse energy distribution in the η - ϕ plane of a di-jet event in heavy-ion collisions as measured by CMS[24]. The sub-leading jet is reconstructed with an energy that is much smaller than the leading jet. This is due to the jet quenching effect.

measured using the information from the hadronic calorimeters that provide an almost full 4π coverage. This effect indicates that the energy lost in the medium goes into low- p_T particles, far from the jet axis. Figure 1.11 shows an example of an imbalanced di-jet event, as observed by the CMS collaboration [24], where a relevant difference in transverse energy of the leading jet (the one with the highest transverse energy) and the subleading jet (the one with the lower energy in the opposite hemisphere) has been observed. This di-jet momentum imbalance can be quantified by the asymmetry ratio

$$A_J = \frac{p_{T,1} - p_{T,2}}{p_{T,1} + p_{T,2}} \quad (1.6)$$

that is shown in the upper row of Fig. 1.12 for different centrality classes. By construction, A_J peaks at zero if no imbalance is present (i.e. no jet quenching), while peaks at non zero values if an imbalance is present (i.e. the jets are quenched). The shift of A_J towards non zero values happens moving from peripheral to central events, as shown in the upper panel of Fig. 1.12, which reports the measurement of A_J by the ATLAS collaboration [25] compared to simulations from PYTHIA[26] + HIJING[27] (yellow histograms). The lower panel of 1.12 shows the azimuthal angular correlation between the leading and subleading jet.

Azimuthal angular correlations

Azimuthal angular correlations between charged particles are another observable to investigate jet quenching at lower p_T , a domain where jet reconstruction becomes difficult due to the background fluctuations, in particular in a high-multiplicity environment as the one produced in heavy-ion collisions.

1.4. EXPERIMENTAL SIGNATURES OF THE QGP

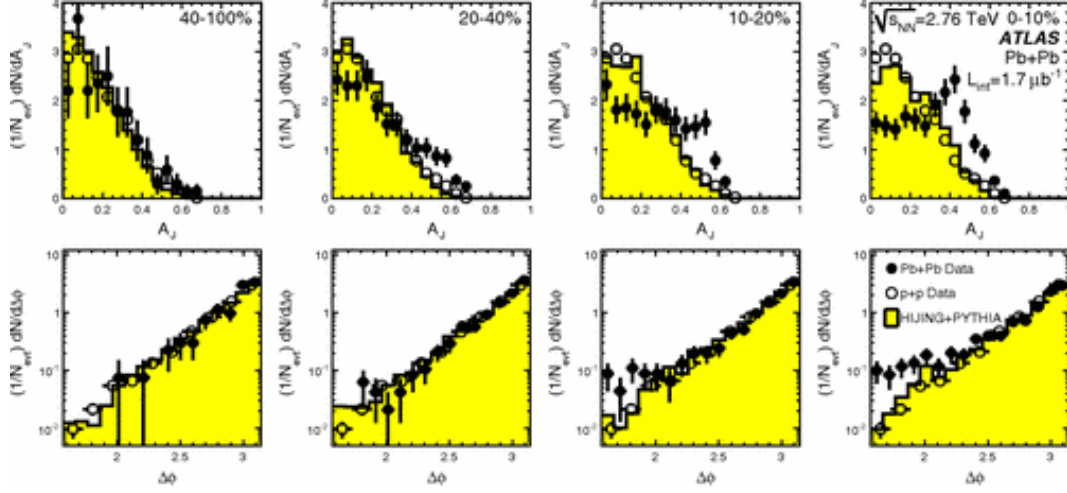


Figure 1.12: Upper panels: the asymmetry ratio A_J as function of the centrality (from left to right, from more peripheral to more central events) measured by ATLAS[25] and compared to PYTHIA+HIJING simulations. Lower panels: same as upper panels, but the variable presented is the $\Delta\varphi$ distribution of di-jets[25].

In this case, the reconstructed charged track with the highest p_T is defined as the trigger particle for the correlation, and is very likely to originate from the fragmentation of a high p_T parton produced in an initial hard scattering process. The difference in azimuthal angle, $\Delta\varphi$, with the other tracks present in the event is expected to show a peak around $\Delta\varphi = 0$ and a peak in the back-to back direction, $\Delta\varphi = \pi$. The peak at $\Delta\varphi = 0$ is called the near-side peak, and represents the tracks generated by the same jet as the highest p_T particle that is used as trigger particle. The second peak, centered at $\Delta\varphi = \pi$, is called the away-side peak, and is generated by the recoil parton. The effects of the medium on the jet production is visible when the azimuthal correlation distribution in heavy-ion collisions is compared to a distribution from a baseline measurement, namely from pp collisions. Figure 1.13 shows the di-hadron correlation measurement by the STAR collaboration [28], where the away-side peak from in most central Au+Au collisions is strongly suppressed compared to the one from pp collisions.

To quantify the modification of the associated particle yields a variable denoted I_{AA} is used. The I_{AA} is defined as

$$I_{AA} = \frac{Y_{AA}}{Y_{pp}} \quad (1.7)$$

where

$$Y = \frac{1}{N_{trig}} \int \frac{dN^{assoc}}{d\Delta\varphi} d\Delta\varphi \quad (1.8)$$

$\frac{1}{N_{trig}} \frac{dN^{assoc}}{d\Delta\varphi}$ is the azimuthal correlation distribution normalised to the number of trigger particles. Figure 1.14 shows the I_{AA} measurements by the ALICE

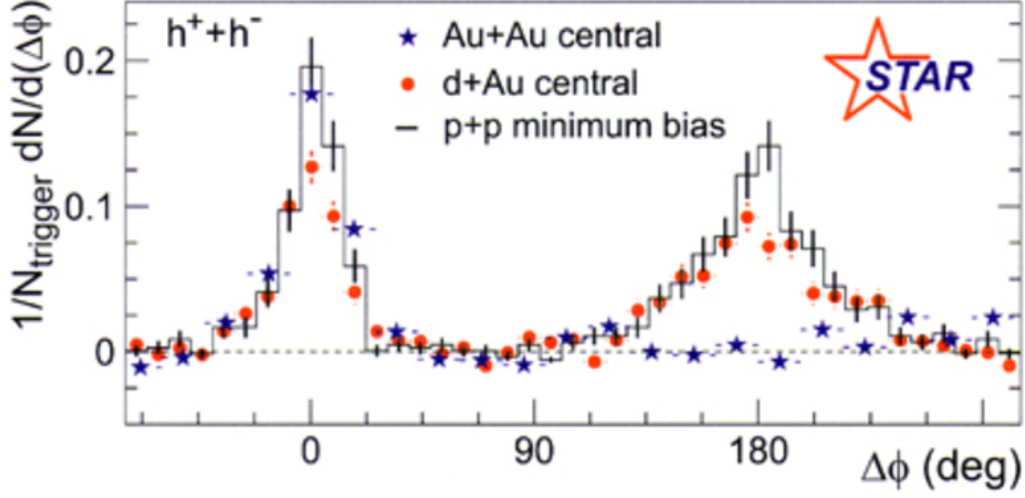


Figure 1.13: Di-hadron azimuthal correlations measured by STAR [28] in pp, d-Au and Au-Au collisions. In Au-Au collisions at $\sqrt{s_{NN}} = 200$ GeV, the strong suppression of the away-side peak is evidence of the jet quenching.

collaboration in Pb-Pb collisions at $\sqrt{s_{NN}} = 2.76$ TeV.

The right panel shows the I_{AA} for the away side. For central collision, the I_{AA} value is around 0.5, which means that a large suppression of the away-side yields has been measured (similar to the observation by STAR described above). On the near side, on the other hand, an enhancement of the order of 20% has been observed (left panel). The possible interpretation is given in the following subsection.

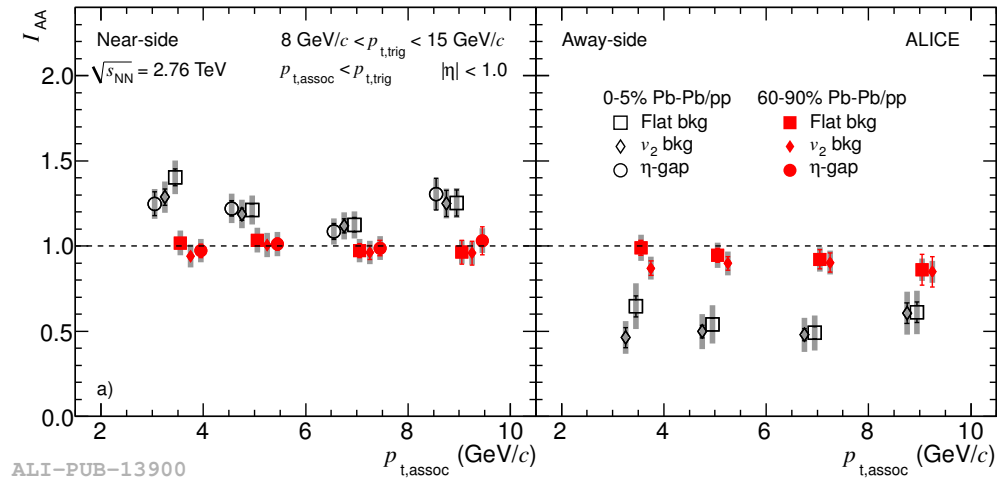


Figure 1.14: The I_{AA} for di-hadron correlations measured by ALICE in different centrality classes of Pb-Pb collisions at $\sqrt{s_{NN}} = 2.76$ TeV [29]. The left panel corresponds to the near side, while the right panel corresponds to the away side.

1.5. COLD NUCLEAR MATTER EFFECTS: PROTON ION COLLISIONS

The near side of azimuthal angular correlations

The near side of azimuthal angular correlations is of particular interest as it is sensitive to various effects [29]:

- **Change of fragmentation function:** modifications to the fragmentation function could induce a modification of the near side correlation. Namely, in Pb-Pb or p-Pb collisions a different fragmentation function would mean that the hadron (the trigger particle) carries a different fraction of the initial parton momentum compared to the one in the pp case. This would mean that a trigger particle with the same p_T would be produced by a parton with different initial p_T in the two collisional systems. In that case, also the production of associated particles differs, resulting in a different fragmentation function. In particular, a fragmentation function that softens with respect to pp, would manifest in $I_{AA} > 1$, while the I_{AA} would be smaller than one in the opposite case.
- **Possible change of the quark/gluon jet ratio in the final state:** jets can origin from quarks and gluons. Different coupling of gluons or quarks with the medium can lead to possible changes in the fraction of quark- and gluon- related jets in a given p_T range, leading to a possible modification of the azimuthal distribution on the near side.
- **Change due to modification of the parton- p_T spectrum:** an increase in the I_{AA} can be also explained in terms of modification of the parton- p_T distribution, even by keeping its fragmentation unmodified. Due to the rising slope of the R_{AA} at high p_T , the parton p_T distribution might be biased towards higher p_T , after energy loss. Therefore, for a given trigger p_T , the mean parton p_T would be larger in Pb-Pb, leading to an increase of the I_{AA} .

1.5 Cold nuclear matter effects: proton ion collisions

As discussed above, in heavy-ion collisions, the plasma of deconfined quarks and gluons is created. The difference in observables between heavy-ion collisions and the baseline measurements (pp collisions) is influenced not only by the plasma, but also by so called nuclear matter effects. Cold nuclear matter effects represent different phenomena that occur due to the interaction of the parton with the nuclear environment. It is not possible to disentangle the cold nuclear matter effects from the hot one (i.e. due to the presence of the medium). It is however possible to study the nuclear effect separately, by colliding protons and heavy-nuclei.

In collisions of protons and nuclei, the energy density is not expected to be high enough to generate the deconfined plasma. Therefore, it presents a unique

CHAPTER 1. INTRODUCTION

way to be sensible to cold nuclear matter effects only.

The k_T -broadening is one of the main cold nuclear matter effects. Before the hard scattering occurs, the partons of the nucleons can undergo multiple elastic scatterings. This elastic collisions transmit an initial transverse momentum k_T , which broadens the p_T spectra of particles produced in the hard scattering process. This would result in an enhancement of the nuclear modification factor, known as the Cronin effect[30].

The parton distribution functions (PDF) in the nuclear environment are affected by the presence of other partons. In particular, at low x (with x representing the fraction of the p_T of the parton over the p_T of the nucleon), a depletion of the PDF was observed experimentally. This effect is known as nuclear shadowing [31].

The low- x region of the PDFs is dominated by gluons. The gluon density increases with the momentum of the hadron until the system is completely saturated. This extreme condition of matter is known as Colour Glass Condensate (CGC) [32], which is extremely dense, but rather cold (compared to the Quark Gluon Plasma). One of the expected signatures of the CGC are long range correlations of particles [33]. However, similar structures could also originate from a collective behaviour of the system created in p-Pb collisions. The experimental observation of the long range correlations is reported in ref. [34, 35, 36].

Heavy quarks in heavy-ion collisions

Charm and beauty quarks (heavy quarks) represent a unique probe to study the properties of the Quark Gluon Plasma. This chapter presents a summary of the basic aspects of heavy quarks in heavy-ion collisions: their production mechanisms, their energy loss in the quark gluon plasma, the experimental results related to heavy quarks, and finally the theoretical description of the azimuthal correlations of heavy quarks.

2.1 Heavy quark production

Heavy quarks are produced in scattering processes with large momentum transfer ($Q^2 \gtrsim 4m_{b,c}^2$). In this range, the QCD coupling constant is smaller than unity, allowing for the use of perturbative QCD (pQCD). In this approach, the hard scattering amplitude is expanded in powers of α_s . The fact that $\alpha_s \ll 1$ grants the convergence of the expansion. The p_T -differential cross section for the production of heavy-flavour hadrons (H_Q) can be calculated directly from the partonic hard-scattering cross section that is convoluted with the parton distribution functions (PDFs) and the fragmentation function.

The parton distribution function, $f(x, \mu_F)$, describes the probability that the constituent of the nucleon that is interacting carries a fraction x of the total momentum of the nucleon.

On the other hand, the fragmentation function $D(z, \mu_F)$ describes the probability that a final-state quark, produced in the hard scattering, could create a hadron carrying a fraction z of the momentum of the quark.

This is known as the factorisation theorem of QCD, and can be summarised by the following equation

$$\frac{d\sigma^{pp \rightarrow H_Q}}{dp_T} = \sum_{i,j=q,\bar{q},g} \int dx_1 dx_2 f_i(x_1, \mu_F^2) f_j(x_2, \mu_F^2) \frac{d\hat{\sigma}^{ij \rightarrow Q\bar{Q}}}{d\hat{p}_T} D_Q^{H_Q}(z, \mu_F^2) \quad (2.1)$$

where $\frac{d\hat{\sigma}^{ij \rightarrow Q\bar{Q}}}{d\hat{p}_T}$ is the hard scattering differential cross-section for the production of heavy-quark pairs.

The leading order (LO) and next-to-leading order (NLO) processes for heavy-quark pair production are shown in the diagrams of figure 2.1. These produc-

CHAPTER 2. HEAVY QUARKS IN HEAVY-ION COLLISIONS

tion mechanisms can be classified in three different classes:

- **Pair production** is represented by the Feynman diagrams shown in 2.1(a) and 2.1(b), that are classified as a LO production mechanism. In these cases, the heavy-quark pair is produced back-to-back in order to conserve energy and momentum. The production mechanism shown in Figure 2.1(c) corresponds to a pair production process, but given the gluon emission by a final state heavy quark, it is classified as a NLO process. The emitted gluon does not modify the total cross section, but influences the kinematics.
- **Flavour excitation** classifies the processes in which a heavy quark from the parton distribution of one of the colliding nucleons is put on shell by scattering against a parton from the second other colliding nucleon. The process is illustrated in figure 2.1(d). As the quark is not a valence quark, it comes from a branching $g \rightarrow Q\bar{Q}$, therefore the process effectively results to be $gq \rightarrow Q\bar{Q}q$ or $gg \rightarrow Q\bar{Q}g$.
- **Gluon splitting** classifies the production mechanisms where a gluon splits to produce a $Q\bar{Q}$ pair. It can occur either in the initial (Fig 2.1(f)) or in the final state (Fig 2.1(e)).

Figure 2.2 shows the relative contribution of these processes to the total production cross section as obtained from pQCD calculations [37], neglecting non-perturbative contributions. The trends as function of the centre of mass energy, \sqrt{s} , have been computed for both the charm production (left panel) and beauty production (right panel). At low values of \sqrt{s} , the LO processes are dominant, namely the pair production mechanisms. With increasing energy, NLO processes become more relevant: at intermediate values of \sqrt{s} the flavour excitation mechanism is the dominant mechanism. The steeply increasing trend of the gluon splitting contribution with \sqrt{s} makes this process the dominant one at high centre of mass energies.

The energy scale at which the LHC operates gives access to the study of NLO processes in the heavy-flavour production. The azimuthal angular correlation ($\Delta\varphi$) of heavy-flavour hadron pairs allows to disentangle the LO from the NLO contributions. The trends are shown in figure 2.3. Due to the energy-momentum conservation, as already described above, the pair production process will show a strongly non-uniform distribution in $\Delta\varphi$, the angle between the two heavy-flavour hadrons, with a peaked structure at values $\Delta\varphi = \pi$, reflecting the back-to-back nature of this production mechanism. For the gluon splitting process, the $\Delta\varphi$ shows a near-side enhancement, that is due the relativistic boost of the gluon that produces the heavy-quark pair. On the other hand, the flavour excitation mechanism shows an enhancement on the away side, that is also due to the the energy-momentum conservation. The distribution is broader and lower compared to the pair-production mechanism, and this is due to the presence of the additional gluon in the the final state.

2.1. HEAVY QUARK PRODUCTION

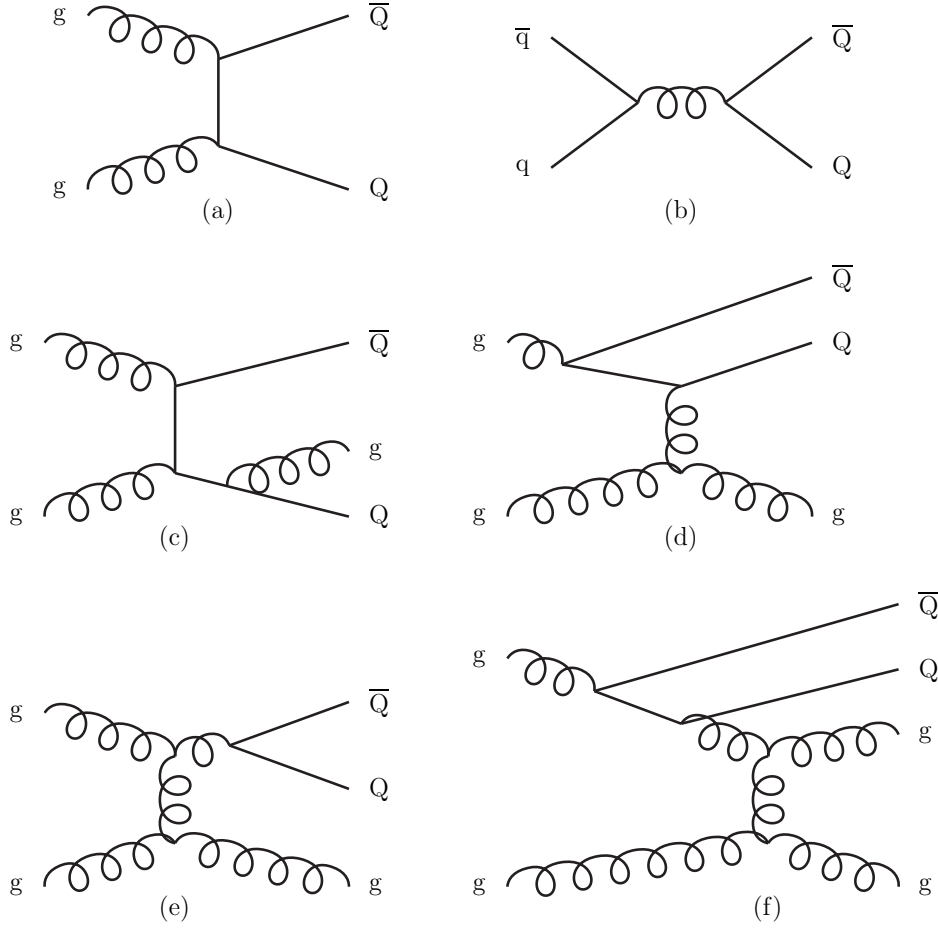


Figure 2.1: Diagrams representing the different processes for heavy quark production: a) and b) LO processes, gluon fusion and quark annihilation respectively; c) Pair production with gluon emission from one final state parton; d) Flavour excitation (NLO); e) Gluon splitting (NLO); f) Events classified as gluon splitting but entering into flavour excitation category.

The FONLL (fixed-order plus next-to-leading logarithms) framework [38] matches fixed next-to-leading order (NLO) QCD with all-order resummation to next-to-leading log (NLL) accuracy in the limit where the transverse momentum (p_T) of a heavy quark is much larger than its mass (m_Q). It allows for the calculation of the production cross section of heavy-flavour quarks (and hadrons), as function of the kinematical variables, typically p_T , η and y . The calculation of the heavy-flavour hadron cross section is done by convoluting numerically the perturbative cross section $d\sigma_Q^{FONLL}$ at the partonic level with a non-perturbative fragmentation function $D_{Q \rightarrow H_Q}^{NP}$. Additionally, a decay function $g_{H_Q \rightarrow l}^{weak}$ is added in the convolution in case it is necessary to consider a weak decay of the hadron into a lepton. Therefore, the total cross section with FONLL summarises in:

$$d\sigma_l^{FONLL} = d\sigma_Q^{FONLL} \otimes D_{Q \rightarrow H_Q}^{NP} \otimes g_{H_Q \rightarrow l}^{weak}. \quad (2.2)$$

CHAPTER 2. HEAVY QUARKS IN HEAVY-ION COLLISIONS

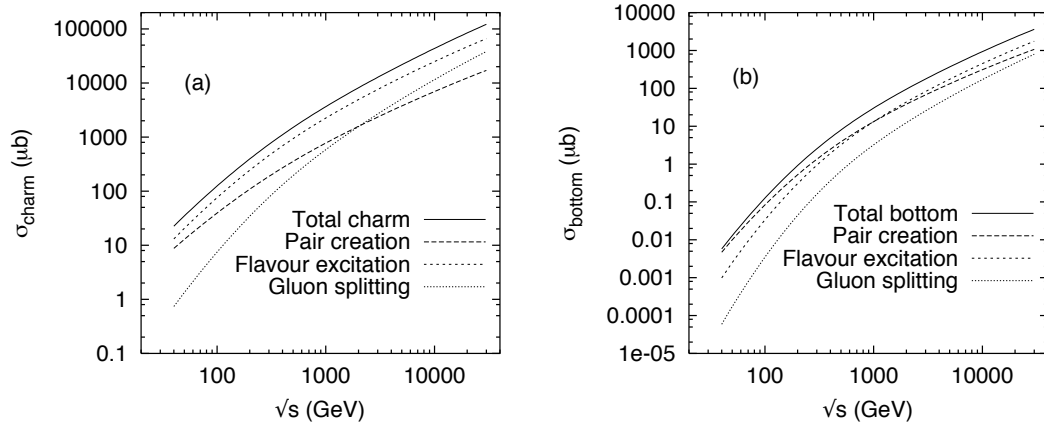


Figure 2.2: Contributions of flavour excitation, pair production and gluon splitting to the total charm and beauty production cross section (left and right respectively) in pp collisions, as a function of the center-of-mass energy \sqrt{s} [37].

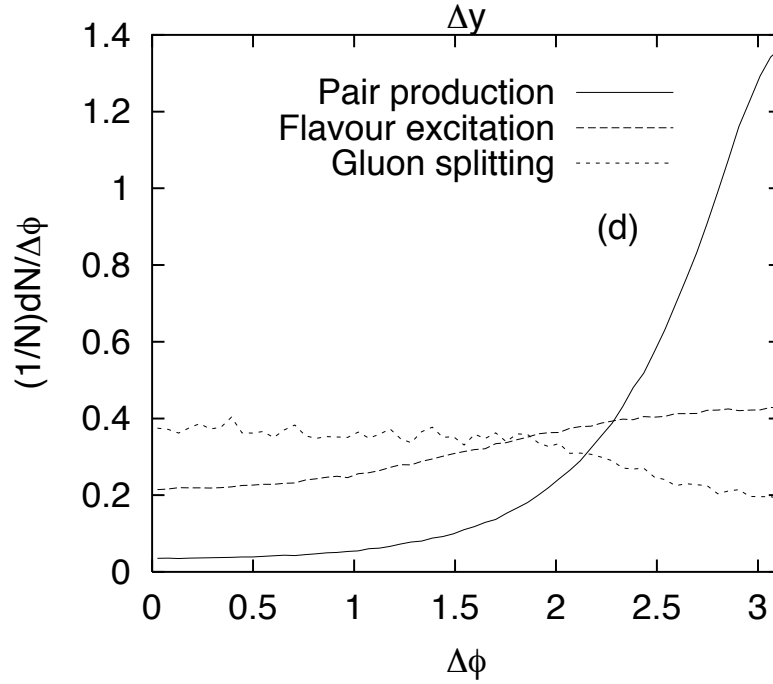


Figure 2.3: Angular correlations of heavy-flavour quark-antiquark pairs from different production mechanisms [37].

2.2. HEAVY QUARKS IN THE QGP: ENERGY LOSS

The fragmentation functions are determined from e^+e^- collisions data and a summary can be found in [39]. The central value of FONLL predictions is calculated by setting the factorisation and renormalisation scales of pQCD at the values of the transverse mass of the quark, $M_T = \sqrt{p_T^2 + m^2}$ and are varied respectively by a factor two (upwards and downwards) to estimate the uncertainty. The quark masses are fixed to $m_c = 1.5 \text{ GeV}/c^2$ and $m_b = 4.5 \text{ GeV}/c^2$ and a variation by $\sim 250 \text{ MeV}/c^2$ is used to estimate the uncertainty band. FONLL has been used to extensively predict the charm and beauty production at Tevatron [40, 41]. GM-VFNS (general-mass variable-flavour-number scheme) [42] represents another theoretical scheme to calculate the production cross sections. The m^2/p_T^2 -dependent terms are included in the hard scattering cross section, while the logarithmic terms of the type $\log p_T^2/m^2$ are absorbed in the heavy-quark PDFs of the colliding hadrons and in the fragmentation function. The fragmentation functions are extracted from measurements by OPAL [43], while CTEQ6.1M [44] is used as the default PDF. The theoretical uncertainties are computed following a very similar strategy as in FONLL. Figure 2.4 shows the differential production cross section of the prompt- D^{*+} meson as function of its p_T , measured by the ALICE collaboration [45] at $\sqrt{s} = 7 \text{ TeV}$. Prompt-D mesons are D mesons originating from the fragmentation of a charm quark. The feed-down contribution of D mesons originating from a beauty quark is subtracted based on FONLL calculations. The measurement is compared to the FONLL and GM-VFNS predictions, showing good agreement with the measured data within uncertainties. The same measurement has been performed for D^0 and D^+ mesons, leading to the same conclusion. Apart from being an excellent test of pQCD, the cross section measurement in pp collision is used as a reference measurement for the nuclear modification factor R_{AA} (equation 1.5) in heavy-ion collisions. More details are given in the next section.

2.2 Heavy quarks in the QGP: energy loss

In heavy-ion collision, charm and beauty quarks are produced as described in the previous section. The formation time of a parton is inversely proportional to its energy. In case of charm quarks with low momentum, it is of the order of $\tau_c \sim 0.1 \text{ fm}/c$, and even shorter for heavier quarks, like beauty. This time is shorter than the formation time of the QGP. This feature makes the heavy quarks unique probes to study the energy loss mechanism, given that they experience the full evolution of the medium and are subject to medium-induced effects.

As described in section 1.4.2, one of the variables used to quantify the energy loss is the R_{AA} . The R_{AA} of prompt D mesons (average of D^0, D^{*+}, D^+) has been measured by the ALICE collaboration [1, 46]. Figure 2.5 shows the R_{AA} of prompt D mesons measured in central collisions (0-20%, red markers), compared to the R_{AA} in semi-central collisions (40-80%, green markers) and

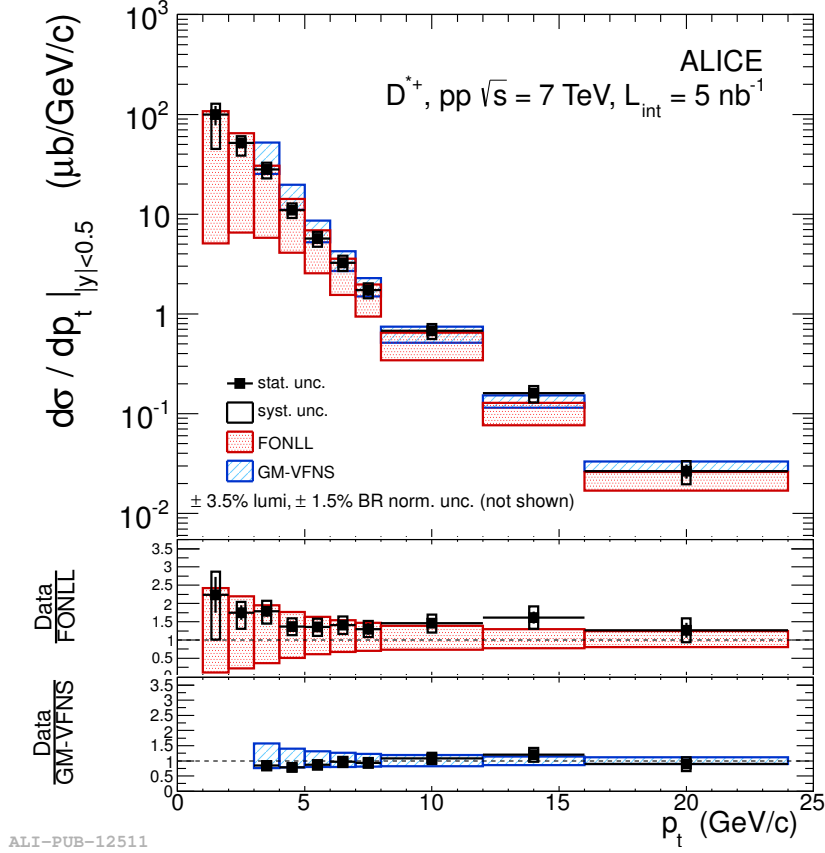


Figure 2.4: The differential production cross section of D^{*+} mesons as function of the transverse momentum, measured by the ALICE collaboration in pp collisions at $\sqrt{s} = 7$ TeV[45], compared to predictions by FONLL [38] and GM-VFNS calculations[42].

the R_{pA} , which quantifies the nuclear modification in p-Pb collisions. A large suppression ($R_{AA} < 0.25$) of the D-meson yield has been observed at high p_T in central collisions, while the suppression is smaller in semi-central collisions. From figure 2.5 it is possible to conclude (within the precision of the measurement) that the deviation from binary scaling observed in Pb-Pb collisions is due to final state effects.

Indeed, in p-Pb collisions, where no QGP creation is expected, the R_{pA} is compatible with 1 within the uncertainties, meaning that initial state effects cannot describe the large suppression observed in central heavy-ion collisions. Hence the heavy-quark energy loss is responsible for the observed behaviour. The interaction of heavy quarks with the plasma is treated in terms of radiative and collisional energy loss (as described in section 1.4.2). The ALICE collaboration measured also the elliptic flow coefficient v_2 of prompt D mesons [47]. A non-zero v_2 with a significance of 5.7σ has been measured in the p_T -range $2 < p_T(D) < 6$ GeV/c, suggesting that charm quarks take part in the

2.2. HEAVY QUARKS IN THE QGP: ENERGY LOSS

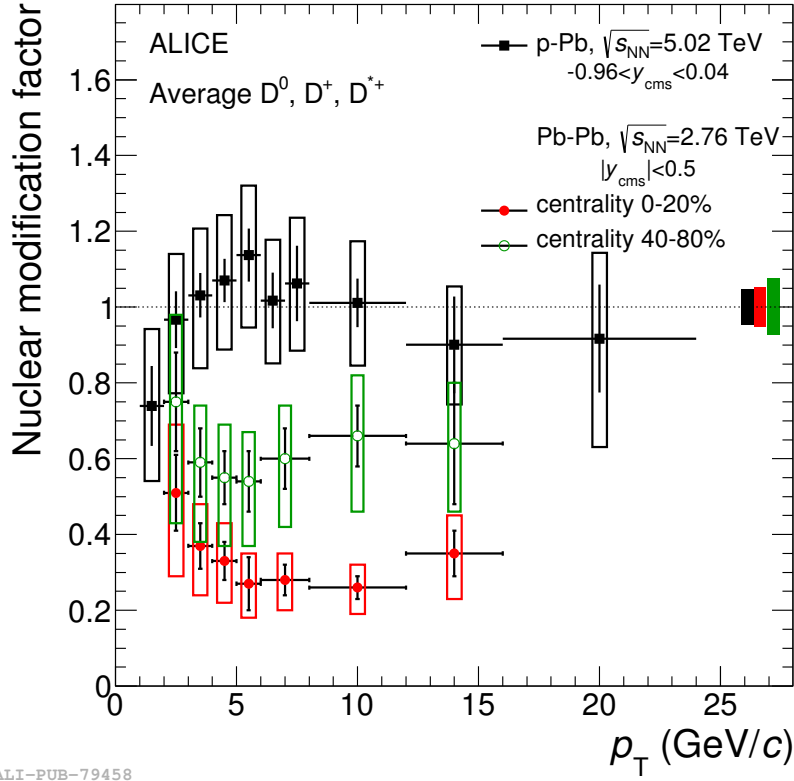


Figure 2.5: Measurement of the R_{AA} of D mesons as function of p_T in central and semi-central Pb-Pb collisions compared to the R_{pA} in p-Pb collisions measured by ALICE [46].

collective motion of the expanding medium.

2.2.1 Energy loss models

Different models are used to describe the interaction of the heavy quarks with the QGP. They use different combinations of energy loss mechanism, as well as different descriptions of the medium evolution and hadronisation mechanisms. A list with a brief description is provided here:

- **WHDG** [48] is a model that includes both radiative and collisional energy loss. The equations describing the energy loss are extracted using perturbative QCD in a 1D Bjorken expanding medium (i.e, without hydrodynamical expansion). The medium density is calculated using data at $\sqrt{s_{NN}} = 200$ GeV and is extrapolated to the LHC energies based on the multiplicity increase.
- **TAMU elastic** [49] is a heavy-flavour transport model based on the collisional energy loss mechanism only. The hydrodynamic evolution is

CHAPTER 2. HEAVY QUARKS IN HEAVY-ION COLLISIONS

included in the model and is constrained by light-flavour data. The model includes also the recombination of heavy quarks with light quarks, as well as the diffusion of heavy-flavour hadrons in the hadronic phase. The transport coefficient is calculated non-perturbatively, using the resonance formation mechanism to transfer the momentum from the heavy quark to the medium constituents.

- **POWLANG** [50] treats the heavy quark transport with the Langevin dynamics, which includes on collisional processes. The medium expansion is implemented using viscous hydrodynamics. The hadronisation is implemented via vacuum fragmentation function.
- **MC@sHQ+EPOS, Coll+Rad(LPM)** [51] is a pQCD model that includes both collisional and radiative energy loss mechanisms. For the radiative energy loss, the Landau-Pomeranchuk-Migdal [52] corrections are included. The medium expansion is modeled using the EPOS model [53].
- **BAMPS** [54] (*Boltzmann Approach to Multi Partons Scattering*) implements the partonic transport model based on the Boltzmann approach to multi-parton scattering. It includes the collisional energy loss mechanism, that is computed with running coupling constant. The missing radiative energy loss is taken into account by scaling the binary cross section. The scaling is tuned using RHIC data on heavy flavour decay electron measurements from RHIC.
- **UrQMD** [55] describes the medium evolution by combining hadronic transport and ideal hydrodynamics. The transport of heavy quarks is implemented using the Langevin approach, and is computed on a basis of a resonance model. The model includes hadronisation via quark coalescence and the parameters are tuned on RHIC data and are fixed for calculations at LHC energies.
- The model by **Cao, Qin and Bass** [56] is based on the Langevin approach, and includes also radiative energy loss as an additional force term. It models the medium evolution using a viscous hydrodynamic evolution, and includes also the recombination mechanisms in modelling the hadronisation.

Figure 2.6 shows the simultaneous comparison of the model predictions for the R_{AA} and the v_2 of D mesons with the experimental measurements by ALICE. A general observation [2] is that the models that include both charm quark in-medium energy loss and mechanisms that transfer to charm quarks the elliptic flow (interactions with the medium constituents and hadronisation by recombination) describe qualitatively the measured anisotropy. Models including both radiative and collisional energy loss describe the R_{AA}

2.2. HEAVY QUARKS IN THE QGP: ENERGY LOSS

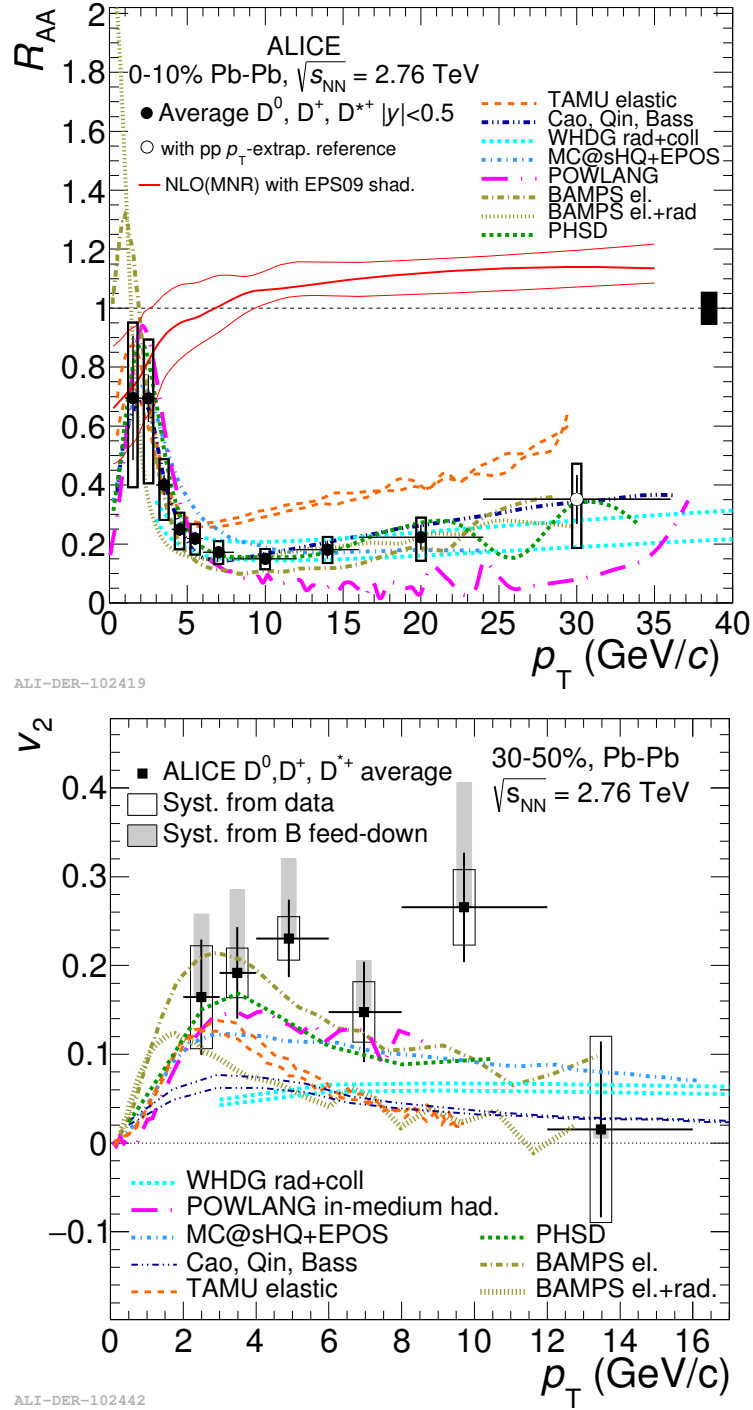


Figure 2.6: Upper panel: the R_{AA} of D mesons as function of p_T in 0-10% central collisions compared to the models described in the text. Lower panel: the v_2 coefficient of D mesons in the 30-50% centrality class compared to the same models.

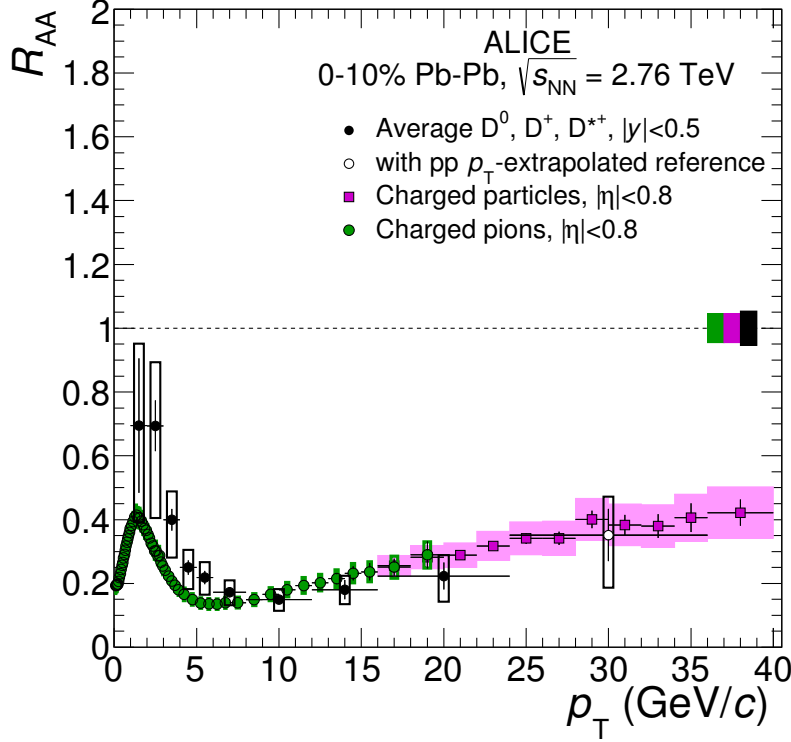


Figure 2.7: The R_{AA} of D mesons as function of p_T in 0-10% central collisions compared to the R_{AA} of pions and charged particles in the 0-10% centrality class.

within uncertainties. It is challenging for models to describe R_{AA} and v_2 simultaneously. The models that describe well the v_2 tend to underestimate the R_{AA} at higher p_T , as well as models that describe well the R_{AA} in the whole p_T range tend to underestimate the v_2 .

The energy loss is expected to depend on the color charge and the mass of the parton, i.e. the heavier the parton, the less energy it loses. In a very naive picture, this should result in a R_{AA} hierarchy, $R_{AA}(\text{light}) < R_{AA}(D) < R_{AA}(B)$. Figure 2.7 shows the comparison of the R_{AA} of prompt D mesons, charged pions and charged particles. For $p_T > 8$ GeV/c, the R_{AA} of D mesons and charged particles are compatible within uncertainties. At lower values of transverse momentum $p_T < 5$ GeV/c, the measured central value of the R_{AA} of D mesons is systematically higher than the one of charged particles and pions, however the uncertainties on the measurement do not allow for a strong conclusion. The interpretation of this result requires to consider the effect of the hadronisation process, that at higher p_T is dominated by the fragmentation. The heavy-flavour hadrons (D meson) originate from charm quarks and carry on average a large fraction of the parent quark momentum ($\langle z \rangle = 0.89$), while light hadrons are created both from gluon and light quark fragmentation (with a softer fragmentation function). Phenomenological calculations show

2.2. HEAVY QUARKS IN THE QGP: ENERGY LOSS

[57] that the inclusion of both the fragmentations of gluons and light quarks predict the R_{AA} of charged particles to be the same as the R_{AA} of D mesons. The mass ordering is more evident when comparing the R_{AA} of charm and beauty hadrons. Reconstruction of B mesons in heavy-ion collisions is still not available yet, however the CMS collaboration measured the R_{AA} of non-prompt J/ψ mesons [59].

The two panels of figure 2.8 show the R_{AA} of prompt D mesons as function of N_{part} (centrality) [58], for $8 < p_T(D) < 16$ GeV/c, and non-prompt J/ψ , $6.5 < p_T(J/\psi) < 30$ GeV/c.

The left panel shows the comparison with MC@sHQ+EPOS2 predictions [60] while the right panel show the prediction from the model of Djordjević *et al.* [61].

In central collisions, the R_{AA} of D mesons is lower than the one of non-prompt J/ψ , which indicates the mass ordering effect. Both the models shown in figure 2.8 show the prediction of the R_{AA} of the J/ψ originating from beauty using the energy loss of a beauty quark and assuming the energy loss of a charm quark. In the hypothesis of the charm energy loss, the R_{AA} assumes lower values, matching with the R_{AA} of D mesons in the case of MC@sHQ+EPOS2, and being slightly higher in the case of the model by Djordjević *et al.*

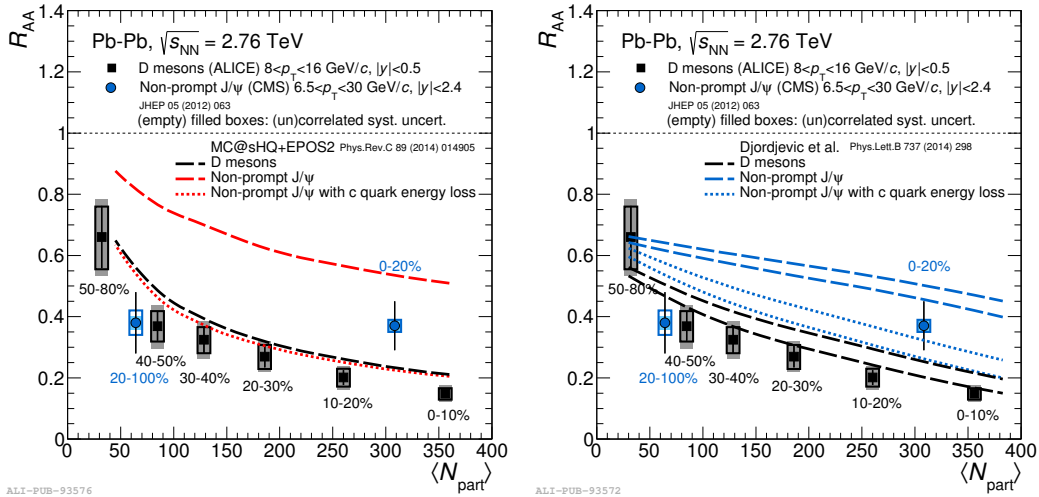


Figure 2.8: R_{AA} of D mesons for $8 < p_T(D) < 16$ GeV/c measured by ALICE [58] compared to the R_{AA} of non-prompt J/ψ mesons in $6.5 < p_T(J/\psi) < 30$ GeV/c measured by CMS [59] as function of N_{part} . The left panel shows the comparison to the predictions by MC@sHQ+EPOS2 [60], while the right panel the comparison to the model by Djordjević *et al.* [61].

2.3 Azimuthal correlations of heavy-flavour particles

Historically, the R_{AA} and the v_2 were the main observables to characterise the physics of heavy-flavour particles in the QGP. Azimuthal angular correlations of heavy-quarks represent a new observable to study the interactions of charm and beauty quarks with the medium constituents. Angular correlations have proven to be sensitive to different interaction mechanisms, as it will be shown in the summary of the theoretical work that will be presented later in this section.

A theoretical description of correlations of heavy-flavour particles in heavy-ion collisions became recently available in three different models, which are briefly discussed in the following paragraphs.

The role of the hadronisation

The **POWLANG** model [50] provides a description of angular correlations of heavy-flavour particles [62]. The model uses the POWHEG-BOX [63] package for the initialisation of the heavy-quark pair, while the evolution of the quarks in the viscous medium is described by the relativistic Langevin equation.

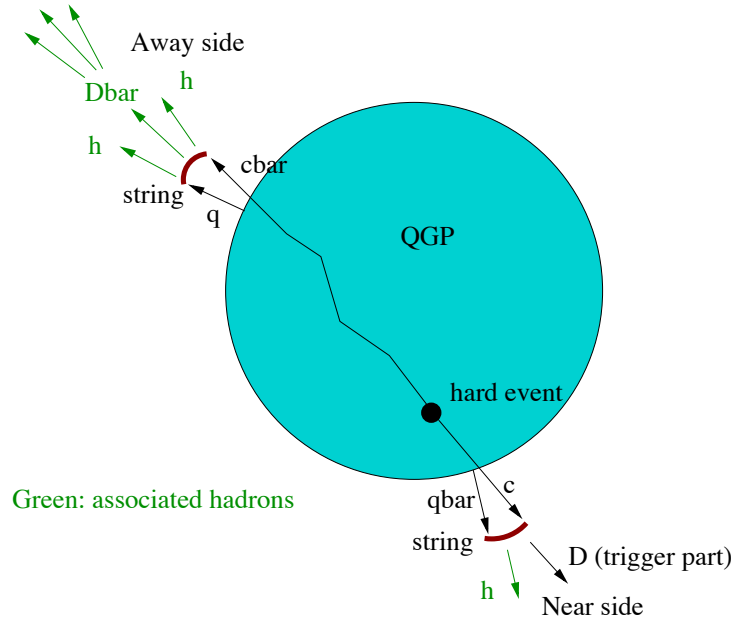


Figure 2.9: Cartoon representing the hadronisation model interfaced to the POWLANG transport code [62] at the end of the propagation of the heavy quarks in the plasma. It also illustrates how the information on the final particles from the string fragmentation can be used to study correlations of D mesons and charged particles.

2.3. AZIMUTHAL CORRELATIONS OF HEAVY-FLAVOUR PARTICLES

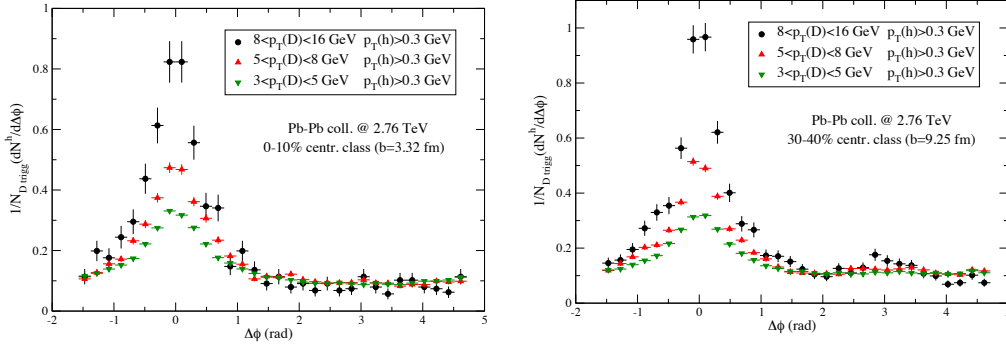


Figure 2.10: Prediction by POWLANG [62] of the azimuthal correlations of D mesons and charged particles in different ranges of p_T , for 0-10% central collisions in the left panel and for the 30-40% centrality class in the right panel.

A crucial point of the model is the hadronisation process, illustrated in the cartoon of figure 2.9: a heavy quark is coupled to a randomly picked light (anti)quark present in the fluid to form a string. The light quark is boosted using the four-velocity of the medium provided by hydrodynamics. Such a string is then passed to PYTHIA, and it simulates its fragmentation into hadrons and their decay if they are unstable.

This hadronisation mechanism allows for a better description of the role of the light quark in the D meson spectra and angular distribution at lower p_T . In addition it provides information about the full final state, making it possible to predict different observables, namely azimuthal correlations of $D\bar{D}$ pairs, as well as the correlation of D mesons and charged final state particles. The prediction for the azimuthal correlation of D mesons and hadrons in central collisions (0-10% centrality) is shown in figure 2.10. The strong suppression on the away-side peak can be attributed to the energy loss (if the associated particles are below the imposed cut on p_T) or either the angular decorrelation (broadening of the away-side peak).

The model predicts also the correlation distribution of $D\bar{D}$ pairs, shown in figure 2.11.

A clear double peak structure is present in the correlation distribution. The evident difference on the near and away-side when looking to $D\bar{D}$ and D-charged particle correlations can be attributed to different contributions: in D-charged particle correlations, the near-side peak receives contributions of fragments of the heavy quark Q , as well as from the \bar{Q} that is close in angle when it is originating from gluon-splitting. The decay products of the D mesons, that are not removed from the correlation, also contribute to the near-side enhancement. In the case of $D\bar{D}$ correlations, the only contribution on the near-side is the one obtained from the $c\bar{c}$ pair originating from gluon splitting. On the other hand, the away-side, the complete quenching of the away-side peak reflects partially the decorrelation effects, and in part is a visual effect due to the very enhanced near-side peak. Indeed, when looking at the magnitude of the away side peak

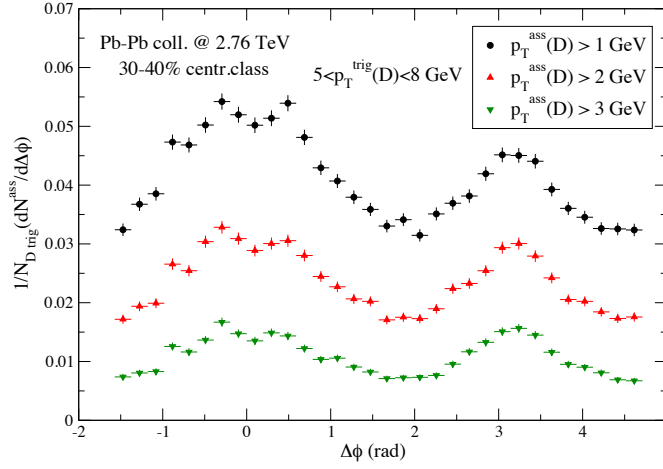


Figure 2.11: Prediction by POWLANG [62] of the azimuthal correlations of $D\bar{D}$ pairs in different ranges of p_T for the 30-40% centrality class.

in figures 2.10 and 2.11 for the 30-40% centrality case, they are similar.

Influence of the energy loss mechanisms on the azimuthal correlations of heavy quarks

In ref. [64], the effects of the different energy loss mechanisms on the azimuthal correlations of $c\bar{c}$ ($b\bar{b}$) quarks have been studied within the **MC@sHQ+EPOS**, **Coll+Rad(LPM)** framework. This model uses FONLL p_T -distribution and a flat y distribution to initialise the charm and beauty quark production. The medium is modelled using EPOS fluid dynamics [53]. The model studies independently the effects of the collisional energy loss and of the combination of the collisional and radiative energy loss on the azimuthal angular correlations of heavy quarks. When including the radiative energy loss mechanism, the model takes also into account the LPM effect [52]. In order to reproduce the available data, the scattering rates are rescaled by a global factor $K = 1.5$ for the pure collisional energy loss, while $K = 0.8$ for the collisional + radiative contribution. The model also studies the effect of the medium temperature, performing the calculations at two different values of the temperature, $T = 180$ MeV and $T = 400$ MeV.

The evolution of the azimuthal correlations is determined by how effectively the heavy quarks acquire momentum perpendicular to their original direction, p_{ini}^{\perp} . The scattering rate does not depend on the initial quark momentum, but shows an increasing trend with temperature, and in the purely collisional scenario it is larger than the collisional + radiative one. The average perpendicular momentum increases steeply for low values of p_{ini}^{\perp} and has an asymptotic behaviour towards higher values of p_{ini}^{\perp} . As a consequence of the higher scattering rates, also the average perpendicular momentum is larger for the case including the collisional energy loss and has an increasing trend with the

2.3. AZIMUTHAL CORRELATIONS OF HEAVY-FLAVOUR PARTICLES

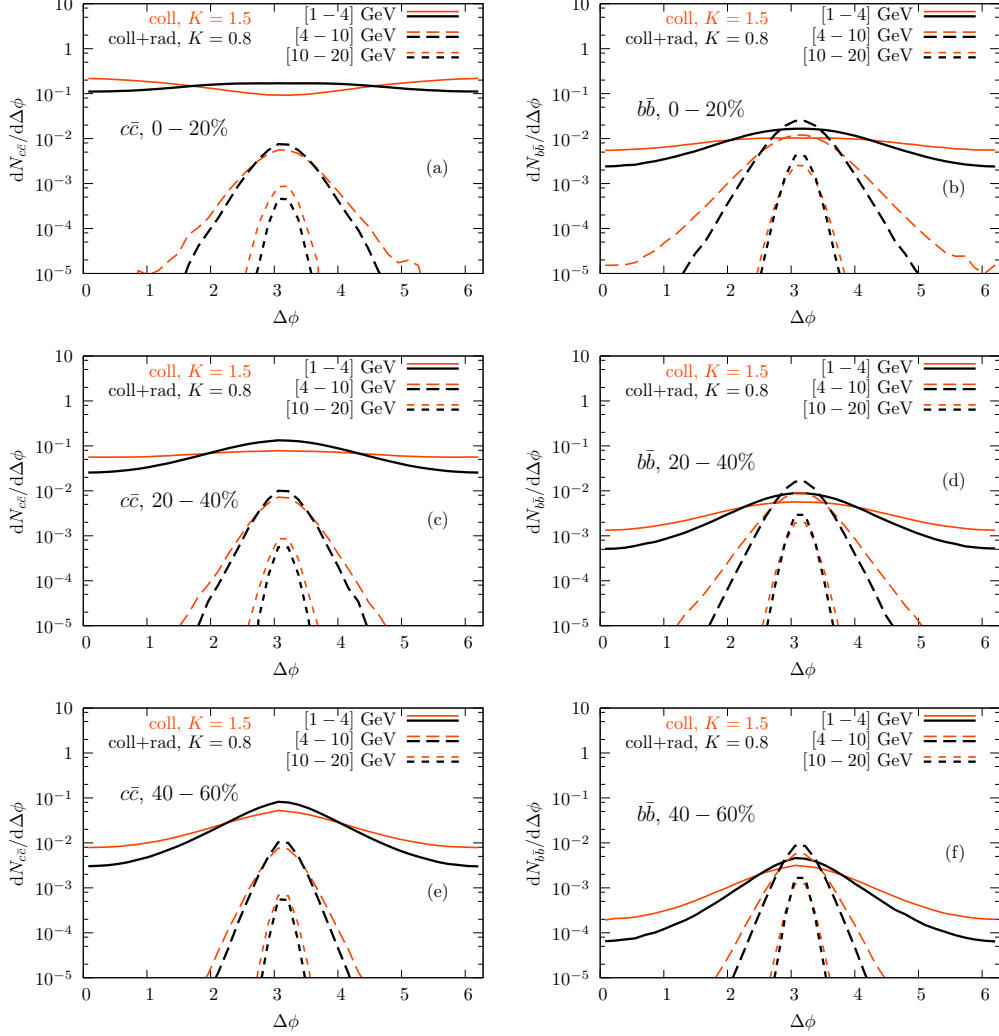


Figure 2.12: Left panel: azimuthal correlations of charm quark pairs in different centrality classes for different p_T intervals as predicted by the MC@sHQ+EPOS, Coll+Rad(LPM) model [64], for different energy loss mechanisms. Right panel: same as left but for beauty quark pairs.

temperature. These properties are reflected in the azimuthal distributions of heavy-quark pairs that are shown in figure 2.12.

The azimuthal distribution is obtained using a LO production process, requiring a back-to-back azimuthal initialisation, i.e. $\vec{p}_{T\bar{Q}} = -\vec{p}_{TQ}$. The results are shown in different centrality classes (the first row corresponds to the 0-20% centrality class, the middle row to the 20-40% centrality class while the lowest row to the 40-60% centrality class). Correlations of $c\bar{c}$ pairs are shown in the left column and $b\bar{b}$ pairs in the right column, for different p_T intervals are shown with different line styles. A general observation is that in all the centrality-flavour- p_T combinations, the starting delta-like distributions are broadened, the effect being larger for the purely collisional mechanism than when the com-

CHAPTER 2. HEAVY QUARKS IN HEAVY-ION COLLISIONS

bined collisional and radiative energy loss takes place. This follows as a direct consequence of the above mentioned larger average perpendicular momentum acquired by the heavy quark in the purely collisional energy loss scenario.

In the most central collisions (0-20% centrality class), the extension of the medium and its temperature are the largest, therefore the broadening is most effective.

In the lowest p_T bin, the initial back-to-back correlations are completely washed out. In this p_T range, in the purely collisional energy loss scenario, a near-side correlation peak appears. This is due to the radial flow that pushes the heavy-quark pair into the same direction. This effect is called “partonic wind effect” [65]. For increasing p_T , we see the away side peak is less and less broadened, and this can be interpreted as a combination of two effects: at higher p_T , the quark leaves the medium more rapidly, therefore there is less time for it to be affected by the medium.

The model by Cao *et al.* [66] uses the Langevin equation to describe the momentum exchange of heavy quarks in quasi-elastic scatterings, and includes a term that accounts for the radiative energy loss. The model is dependent on only one free parameter called the spatial diffusion coefficient, D that characterizes the interaction strength of the heavy quark with the medium. To predict the correlations of $c\bar{c}$ quarks, the model uses PYTHIA 8 [67] to simulate the initial production of the heavy-flavour quark pair, tuning the generator to reproduce the spectrum of charm hadrons from pp collisions at RHIC [68]. The model predicts correlations of $D\bar{D}$ pair in Au-Au collisions at a center of mass energy $\sqrt{s_{NN}} = 200$ GeV. The prediction for most central collisions (0-10% centrality), requiring that the D meson with higher p_T has to be with $p_T > 2$ GeV/ c is shown in figure 2.13. The model provides predictions for contributions of radiative, collisional and a combined radiative and collisional energy loss mechanism. The spatial diffusion coefficient D is tuned to reproduce the R_{AA} data of D mesons measured by ALICE, and the values are reported in the figure. In this p_T integrated scenario, qualitatively, the correlation distribution behaves in a similar fashion as in the prediction by the MC@sHQ+EPOS, Coll+Rad(LPM) model. In the case of purely collisional energy loss, the partonic wind effect pushes the $c\bar{c}$ pair in the same direction that manifest itself in a correlation at the near side, while the radiative energy loss tends to broaden the back-to-back away-side peak. In the more realistic scenario that includes both the contributions, the correlation distribution washes out. Figure 2.13 shows also the comparison of the effect of the collisional energy loss mechanism when the radial flow is present and is turned-off. In the later case, the near-side peak disappears.

2.3. AZIMUTHAL CORRELATIONS OF HEAVY-FLAVOUR PARTICLES

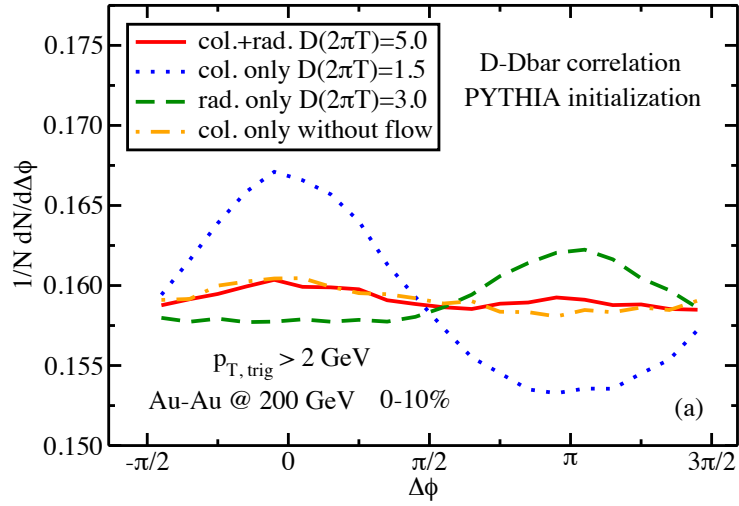


Figure 2.13: Azimuthal correlations of $D\bar{D}$ pairs as predicted by the theoretical model by Cao *et al.* [66] for heavy-ion collisions at $\sqrt{s_{NN}} = 200$ GeV, in the 0-10% centrality class, for different energy loss mechanisms.

3

The experimental setup

3.1 The Large Hadron Collider

The *Large Hadron Collider* (LHC) is the most powerful particle accelerator built at CERN, the European Center of Particle Physics, in the suburbs of Geneva, Switzerland. It consists of a 27-km-long ring of superconducting magnets that has been built in the underground tunnel beneath the French-Swiss border. The LHC is designed to accelerate beams of protons up to a nominal energy of $\sqrt{s}_{max} = 14$ TeV. In addition to protons, the LHC can also accelerate beams of lead nuclei, Pb^{82+} at a designed energy of $\sqrt{s_{NN}} = 5.5$ TeV per nucleon.

To keep the beams of such energies within the accelerator, the magnetic field provided by the LHC magnets has to be up to a value of 8.33 T. Such a magnetic field intensity is achievable only with superconducting magnets, that need to be cooled to a temperature of 1.9 K. Approximately 96 tons of liquid Helium are needed to reach the requested temperatures.

During the first two years of the LHC RUN-I (2010-2013), the LHC collided protons at a centre of mass energy of $\sqrt{s} = 7$ TeV. During the last month of data taking of these calendar years, the LHC collided lead nuclei at the centre of mass energy of $\sqrt{s_{NN}} = 2.76$ TeV per nucleon. The physics program of the LHC of 2012 consisted of pp collisions at a higher centre of mass energy, $\sqrt{s} = 8$ TeV.

The RUN-I successfully ended in the first months of 2013, when the LHC collided protons on lead nuclei, at a centre of mass energy of $\sqrt{s_{NN}} = 5.02$ TeV per nucleon.

The acceleration of protons and lead ions is done in a few steps using older accelerators that are used for pre-acceleration, before the beams are injected in the LHC ring where they reach the collision energy.

Protons are pre-accelerated in the LINAC up to an energy of 50 MeV. The acceleration process is continued in the Proton Synchrotron (PS), where they reach an energy of 26 GeV. At the last step they are injected in the 6.7 km long *Super Proton Synchrotron* (SPS), and the energy reaches 450 GeV. From the SPS they are injected in the LHC ring and accelerated up to the collision energy.

CHAPTER 3. THE EXPERIMENTAL SETUP

The lead ions are first accelerated by the linear accelerator LINAC 3, and the Low-Energy Ion Ring (LEIR) is used as an ion storage and cooler unit, before they get injected in the PS, SPS and LHC.

Four main experiments are constructed along the *LHC* accelerator.

ATLAS and *CMS* are general purpose particle detectors designed to study mainly the Higgs mechanism, standard model processes and new physics beyond the standard model in proton proton collisions.

The *LHCb* experiment is designed to study the CP violation in B-decays in pp interactions.

ALICE is a dedicated heavy-ion experiment, with the goal of studying the strongly-interacting matter created in collisions of heavy nuclei.

Figure 3.1 shows the accelerator complex of the LHC and the position of the four main experiments along the LHC ring.

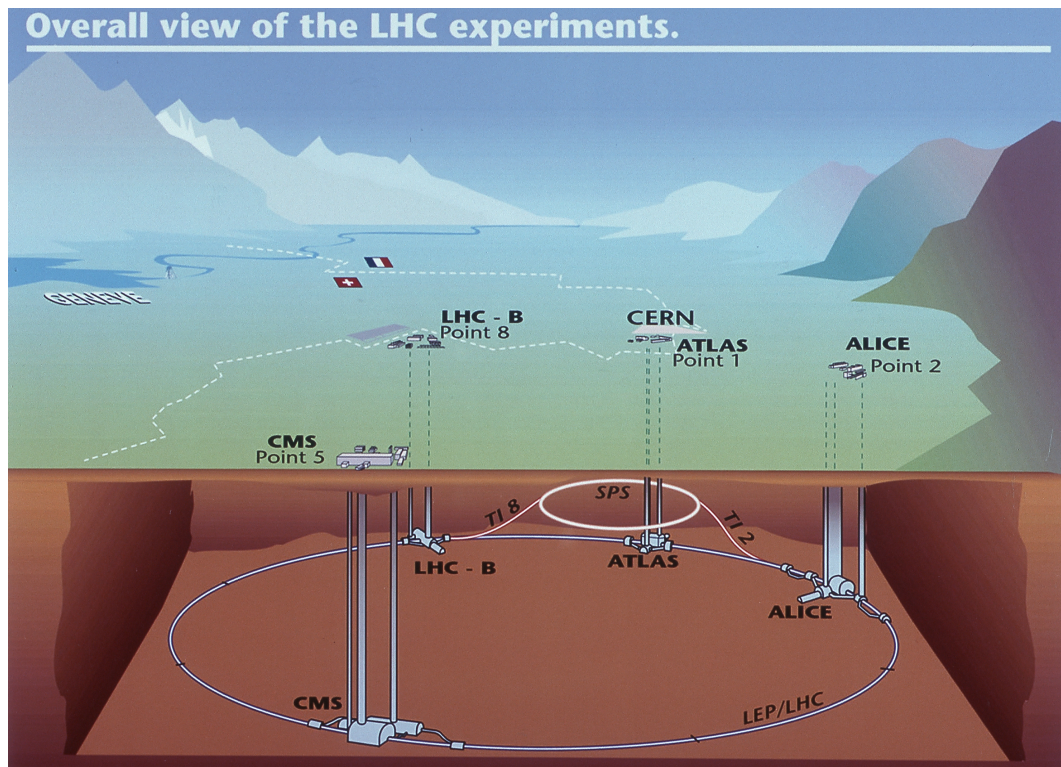


Figure 3.1: The Large Hadron Collider, extending over the franco-swiss border and the four main experiments (ALICE,ALTAS,CMS,LHCb).

3.2 The ALICE experiment

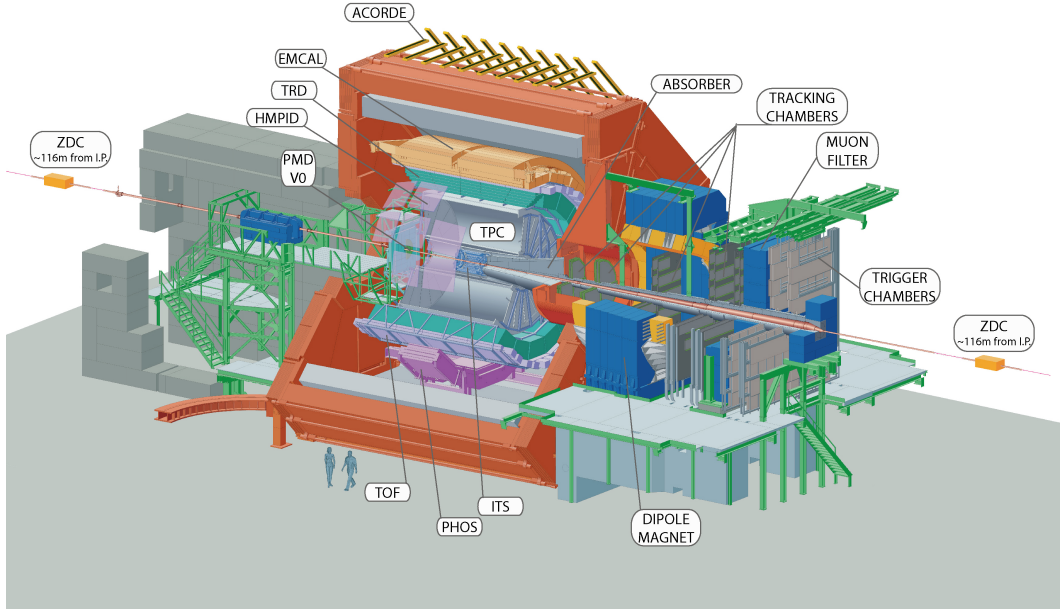


Figure 3.2: Layout of the ALICE detector. All the sub-detectors are indicated

ALICE is the only LHC experiment dedicated to the study of heavy-ion collisions. Designed to cope with a very dense multiplicity environment (up to 8000 tracks per unit of rapidity), the main goal of ALICE is to study the properties of the Quark-Gluon Plasma, that is expected to be produced in collisions of heavy nuclei. Besides heavy ions, ALICE provides a solid performance also in studying proton-proton and proton-nucleus collisions, which are used as references for comparison with heavy-ion studies.

ALICE is capable of reconstructing charged tracks in a very wide p_T range that spans over 3 order of magnitude, reaching a lower limit of $p_T \sim 0.1$ GeV/ c . The experiment is designed also to reconstruct short-lived particles, like open-charm mesons.

The central barrel is the main part of ALICE. It consists of sub-detectors covering the pseudo-rapidity range $-0.9 < \eta < 0.9$ (corresponding roughly to the polar angle interval $\pi/4 < \theta < 3\pi/4$ contained within the L3 magnet. Most of the sub detectors are dedicated to tracking, which is made possible by the solenoidal magnetic field provided by the L3 magnet ($B = 0.5$ T) that is parallel to the z-axis (the beam axis).

A muon spectrometer and other smaller detectors are placed outside the L3 magnet. They are mainly used for triggering and centrality determination. Additionally, two sets of hadronic calorimeters (ZDCs) are placed at a dis-

CHAPTER 3. THE EXPERIMENTAL SETUP

tance of 116 m from the interaction point. Their main scope is to measure the energy of the nucleons that do not take part in the collisions (the so-called spectators).

The central barrel consists of the following detectors:

- Inner Tracking System (ITS): The innermost detector of ALICE. It consists of 6 layers of silicon detectors and is used for track and vertex reconstruction.
- Time Projection Chamber (TPC): It is the main tracking detector, situated around the ITS. It is used also for particle identification through the measurement of the specific energy-loss of the charged particles.
- Time Of Flight detector (TOF): used for particle identification based on different flight times of particles with different masses.
- Transition Radiation Detector (TRD): Used for the identification of electrons, and it can also contribute to tracking.
- High Momentum Particle Identification Detector (HMPID) is a RICH (Ring Imaging CHerenkov) detector used for particle identification up to momenta of 5 GeV/ c .
- Electromagnetic Calorimeter (EMCal): Used for the identification of electrons or photons. It provides also triggering capabilities.
- Photon Spectrometer (PHOS) is a high-resolution electromagnetic calorimeter.

The HMPID, EMCal, and PHOS detector do not have limited coverage in η and φ in respect to the other central barrel detectors. The forward detectors are:

- T0 detector: used as reference to provide the start signal for the time-of-flight measurements and can also be used for triggering purposes. It provides a rough estimation of the interaction vertex
- Muon Spectrometer: consists of five tracking stations and two trigger stations, an absorber and a dipole magnet, covering a pseudo rapidity range $-2.4 < \eta < 4$.
- VZERO detector: used for triggering and centrality/multiplicity determination.
- Photon Multiplicity Detector (PMD): is a particle shower detector. It is used to measure the multiplicity and spatial distribution of photons.
- Forward Multiplicity Detector (FMD): provides an independent measurement of the orientation of the collisions in the vertical plane.

3.3. THE CENTRAL BARREL DETECTORS

- Zero-degree calorimeter (ZDC) is used to measure the energy of the spectators (i.e. nucleons that did not interact in the collisions).

The material budget of the central barrel detectors is kept very low through the usage of light materials in tiny layers, especially for the inner detectors. A remarkably low value of 13% X_0 is obtained from the primary vertex to the outer edge of the Time Projection Chamber. This helps to reduce the effects of Coulomb multiple scattering, which can spoil the low- p_T measurements.

3.3 The central barrel detectors

To perform the analysis discussed in this thesis, the detectors of the central barrel were used. The ITS and TPC were used to track the charged particles. Additionally, the excellent resolution on the determination of the primary and secondary vertices, provided by the ITS, is used for the reconstruction of D meson decay vertices. The particle identification, obtained combining the information on the specific ionisation energy loss provided by the TPC and the time of flight provided by the TOF detector is used to identify the daughters of the decaying D meson. In this section, the ITS, TPC and TOF sub-detectors are described in detail.

3.3.1 The Inner Tracking System

The Inner Tracking System is the detector closest to the collision point. It is composed of 3 pairs of cylindrical silicon detector subsystems, each pair constructed with a different technology, placed around the vacuum tube at a radial distance from the nominal beam axis position that varies from 3.9 to 43 cm.

The two closest detector layers are Silicon Pixel Detectors (SPD), that are designed to provide an excellent spatial resolution, needed to determine the positions of the primary and secondary vertices. The fast response of the pixel detectors can be used as first level (L0) trigger, mainly for the selection of minimum-bias events. Moreover, the extended pseudorapidity coverage of $|\eta| < 1.98$ allows for the use of the SPD for the measurement of the charged particle multiplicity.

The third and fourth layer are composed of silicon drift detectors (SDD), with the functioning principle based on the measurement of the drift time of the electron. The SDD provides full azimuthal coverage and a pseudorapidity coverage of $|\eta| < 0.9$. The SPD and SDD provide a good resolution in $r\phi$ and z to get sufficient two-track separation capabilities in high multiplicity environments that can grow up to 80 tracks per cm^2 .

The outermost part of the ITS is formed by two layers of Silicon Strip Detectors (SSD), having the same azimuthal and pseudo-rapidity coverage as the

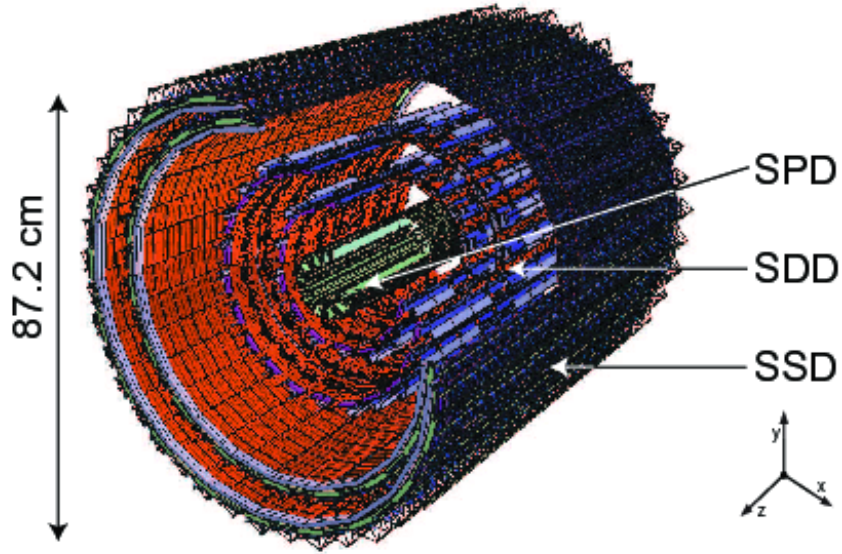


Figure 3.3: Schematic representation of the Inner Tracking System (ITS) with the indication of the different detector layers: from the innermost to the outermost they are the Silicon Pixel Detectors (SPD), Silicon Drift Detectors (SDD) and Silicon Strip Detectors (SSD).

SDD. The SSD has a poorer resolution along the z -axis compared to the innermost layers. The SSD plays a fundamental role in the matching of the tracks between the ITS and the TPC.

The SDD and SSD detectors provide also dE/dx measurements that can be used for PID. The layout of the ITS has been optimised to provide an excellent tracking performance and impact parameter resolution hence keeping the material budget of the layers as low as possible. Given that one of the main goals of ALICE is to measure tracks at low p_T , down to 100 MeV/ c , keeping the material budget low is of vital importance in order to reduce Coulomb multiple scattering, which would compromise the tracking resolution. The material budget of the ITS and its support structures is estimated to be 7.66 % X_0 for perpendicular tracks. Figure 3.3 shows the layout of the Inner tracking system, and the main characteristics are summarised in table 3.1. Figure (3.3) shows the layout and structure of the ITS detector, while the main properties of each layer are summarised in the table 3.1.

3.3.2 The Time Projection Chamber (TPC)

The Time Projection Chamber (TPC) is the main tracking device of ALICE. The TPC is able to track particles over three order of magnitudes, from 100 MeV/ c to 100 GeV/ c . The TPC is a cylinder filled with a gas mixture of $Ne - CO_2$ (90:10 proportion) that is placed around the beam axis, with the radial dimensions ranging from ~ 80 cm to ~ 250 cm. In the z direction, it is

3.3. THE CENTRAL BARREL DETECTORS

Layer	Type	r [cm]	$\pm z$ [cm]	$ \eta $	$\sigma_{r\varphi}$ [μm]	σ_z [μm]
1	SPD	4.0	14.1	1.98	12	100
2	SPD	7.2	14.1	1.4		
3	SDD	15.0	22.2	0.9	38	28
4	SDD	23.9	29.7	0.9		
5	SSD	38.5	43.2	0.9	20	830
6	SSD	43.6	48.9	0.9		

Table 3.1: The main characteristics of the ITS.

510 cm long. The TPC is divided longitudinally by a central membrane. The TPC layout is shown in figure 3.4.

Charged particles passing through the TPC ionise the gas mixture that fills the TPC. A uniform electric field of 400 V/cm directs the electrons from the ionisation point towards the end caps (away from the central membrane), where Multi Wire Proportional Chambers (MWPCs) collect the generated signals. In the azimuthal direction, the TPC is divided in 18 sectors, each providing a maximum of 159 points along the particle trajectory.

The z coordinate of the track is obtained by measuring the drift time of the electrons in the gas (typical drift velocity is $v_d \sim 2.7 \text{ cm}/\mu\text{s}$). Given the drift velocity and the distance between the central membrane and the endcaps, the maximum drift time is of $90 \mu\text{s}$. This limits the acquisition rate of the TPC to 11 kHz.

The analog nature of the signal collected by the MWPC readout allows to

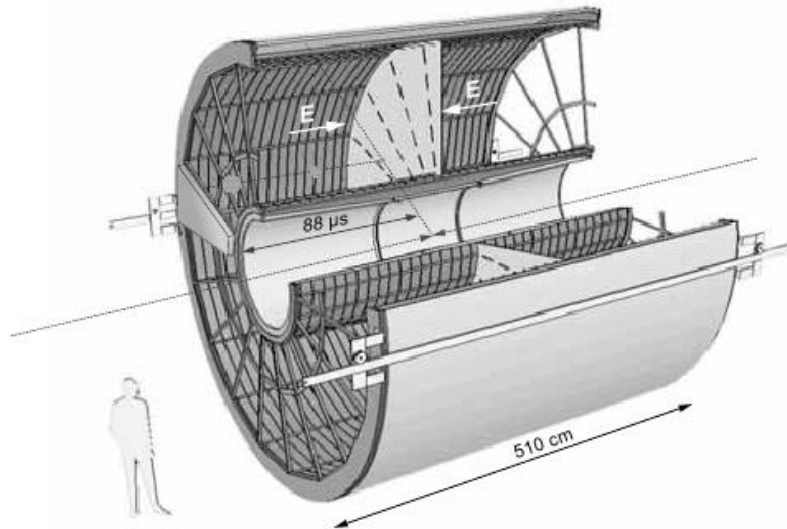


Figure 3.4: Schematic representation of the TPC. The gas-filled barrel is split into two parts with opposite electric field

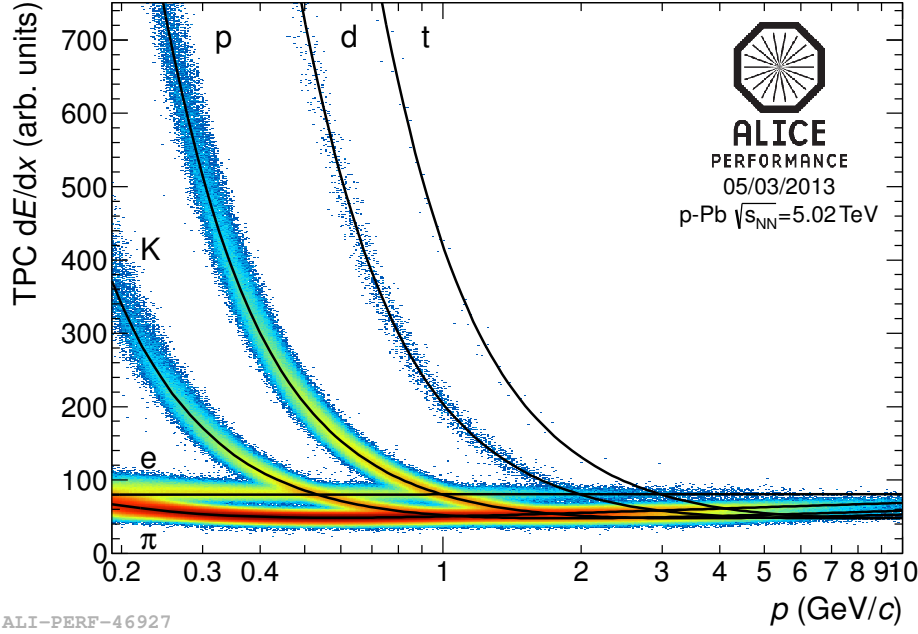


Figure 3.5: Specific ionisation energy loss measured with the ALICE TPC in p-Pb collisions as function of the momentum of the ionising particle. The black lines represent the Bethe-Bloch parametrizations for different particle species

measure the energy lost by the charged particle while travelling in the gas (dE/dx). The dE/dx measurements are used for particle identification at low and intermediate p_T , and can be extended at higher p_T by using statistical unfolding methods to measure the pion, kaon and proton yields at high p_T by exploiting the relativistic rise of the dE/dx Bethe-Bloch formula, i.e.:

$$-\frac{dE}{dx} = \frac{4\pi}{m_e c^2} \cdot \frac{nz^2}{\beta^2} \cdot \left(\frac{e^2}{4\pi\epsilon_0} \right)^2 \cdot \left[\ln \left(\frac{2m_e c^2 \beta^2}{I \cdot (1 - \beta^2)} \right) - \beta^2 \right]. \quad (3.1)$$

Figure 3.5 shows dE/dx as function of the charged track momentum, together with the expectation curves obtained from the parametrization of the Bethe-Bloch formula for different particles species in p-Pb collisions.

3.3.3 The Time Of Flight Detector (TOF)

The Time Of Flight Detector (TOF) is used for particle identification in the intermediate p_T region: up to $p_T \sim 2.5$ GeV/ c for the separation of kaons from pions and up to $p_T \sim 4$ GeV/ c for the separation of kaons from protons. The TOF provides full azimuthal coverage and a pseudo-rapidity coverage in the range $|\eta| < 0.9$. The TOF is segmented in 18 sectors in φ , each of them composed of 5 modules. Each module is composed of 15 to 19 multi-gap resistive gas filled chambers (MRPC), that provide a time measurement of the

3.4. TRACKING AND VERTEXING

detection of a charged track with a resolution of about 100 ps.

The PID strategy is based on the fact that, at a given momentum, particles with different masses travel at different velocities, which is reflected in different travel time from the interaction point to the TOF detector. The TOF measures the arrival time of particles in the TOF detector, while the start (interaction) time is provided by the T0 detectors.

Figure 3.6 shows the velocity of different particle species as function of the charged particle momentum, for Pb-Pb collisions.

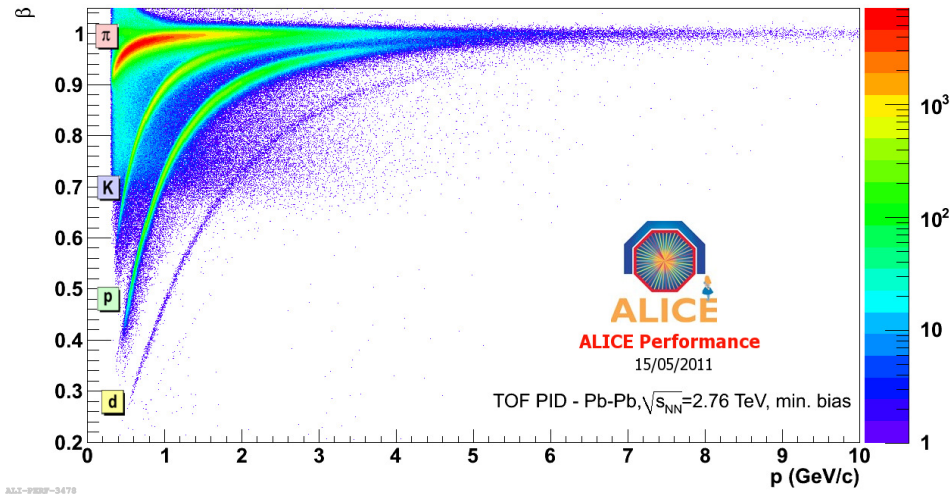


Figure 3.6: Measurement of velocity of different particle species as function of the charged particle momentum with the TOF detector for Pb-Pb collisions.

3.4 Tracking and vertexing

The trajectories of charged particles (tracks) are reconstructed using the information from the ITS and the TPC. The tracking is based on finding clusters in the detectors and using this information to reconstruct the trajectory of the charged particle. This is done by fitting the most likely path of the particle.

The determination of the primary vertex is done using the information from the pixel detectors, where the symmetry point of the distribution of the hits in pixels along the z-axis is used to get a first estimate of the position. The information of the tracklets is used. The tracklets are defined as pair of hits in the two layers of the SPD detector that lie in a small η and φ window. The pointing direction of the tracklets is then used to redetermine the position of the vertex along the x,y and z-axis.

Given the vicinity of the pixel detector to the interaction point, the particles are assumed to follow straight-line trajectories. The distribution of the intersections of the straight lines form a distribution whose centroid in the x and y direction determines the position of the primary vertex in the transverse plane.

CHAPTER 3. THE EXPERIMENTAL SETUP

Tracks are reconstructed using a *Kalman filter* algorithm [69]. The estimate of the parameters defining the track is updated when new data points are given in input to the algorithm. The algorithm starts with a first estimate (seed) of the track parameters based on the outer pads of the TPC and the interaction vertex position reconstructed with the SPD. At each following step, the track is propagated to the next detector layer and the cluster is searched within the expected space interval, determined by propagating the uncertainty of the parameters measured at the previous steps. Once the cluster is found, the track parameters are updated and the procedure is repeated.

The reconstruction starts from the outermost part of the TPC where the track density is the lowest. The procedure is repeated in the opposite direction (starting from the innermost clusters from the ITS towards the edges of the TPC), and previously associated clusters that now have a χ^2 that is too large are removed from the procedure. Once the second iteration is performed, the tracks are propagated to the outer detectors (TOF, EMCal and HMPID), and the track gets also the PID information.

At last, the Kalman filter is applied to fit again the track in the inward direction. This step is called “refit”, and it provides the the best determination of the track parameters in the vicinity of the interaction point.

4

Analysis Strategy

In this chapter, the procedure to obtain the fully corrected azimuthal angular distribution of D^{*+} mesons with charged particles is described. The following steps are applied in the analysis (each of them explained in detail in the coming sections).

1. D^{*+} mesons decaying into D^0 and π^+ with $D^0 \rightarrow K^-\pi^+$ are selected by computing the difference in invariant mass, $\Delta M = M(K\pi\pi) - M(K\pi)$, of K, π, π combinations obtained after topological selections were applied on the D^0 daughters. Three different p_T ranges ($3 < p_T(D^{*+}) < 5 \text{ GeV}/c$, $5 < p_T(D^{*+}) < 8 \text{ GeV}/c$, $8 < p_T(D^{*+}) < 16 \text{ GeV}/c$) are considered for the analysis in pp collisions, while for the analysis in p-Pb collisions only the two highest p_T intervals are considered.
2. Each time a D^{*+} candidate is identified, the difference in the azimuthal angle ($\Delta\varphi$) and pseudorapidity ($\Delta\eta$) between the candidate and all charged tracks in the event passing quality selections is calculated.
3. The same calculation is performed also by selecting the D^{*+} candidate from one event and associated charged tracks from different events. This is the so-called event-mixing correction, that is used to correct the correlation distributions for the bias arising from the limited detector acceptance in pseudorapidity, as well as for detector inhomogenities.
4. Each entry in the two-dimensional $\Delta\varphi - \Delta\eta$ distribution is weighted by the inverse of the product of the D^{*+} and associated track reconstruction and selection efficiency.
5. The remaining background candidates under the D^{*+} invariant mass peak are subtracted using the angular correlations of candidates in the D^{*+} invariant mass region. The side-band background distribution, corrected by event-mixing and efficiency, is rescaled by a proper scaling factor (estimated from the invariant D-meson mass distribution) in order to match the distribution from the correlations below the D meson invariant mass peak and is subtracted from the corrected inclusive distribution (the one obtained by selecting D^{*+} candidates in the peak region).

CHAPTER 4. ANALYSIS STRATEGY

6. The obtained distribution is then rescaled by the number of reconstructed D^{*+} mesons (trigger particles), that is calculated as the integral of the signal function of the ΔM distribution in the region of the D^{*+} peak.
7. The “per trigger” twodimensional distribution is then projected on the $(\Delta\varphi)$ axis before correcting it for the contamination arising from secondary associated charged tracks.
8. In order to obtain the prompt-charm distribution, the contribution of D^{*+} -charged particle correlations, when a D^{*+} comes from beauty-hadron decays, is subtracted.
9. Finally, the fully corrected D^{*+} -charged particle distribution is averaged with the fully corrected D^0 and D^+ -charged particle correlation distributions. In that way, the statistical and systematic errors are reduced.
10. The averaged azimuthal distribution is then fitted to double Gaussian distributions in order to study the correlation parameters describing the angular correlation distributions as function of the kinematical variables.

4.1 Event selection

The data sample used for the analysis contains about 3.14×10^8 pp minimum-bias (MB) events and 1.1×10^7 p-Pb minimum bias events collected during the 2010 pp data taking at $\sqrt{s} = 7$ TeV and the 2013 p-Pb data taking $\sqrt{s_{NN}} = 5.02$ TeV, respectively. The minimum-bias trigger was based on the SPD and VZERO detectors for pp collisions, by requiring at least one hit in either of the VZERO counters or in the SPD (with pseudorapidity coverage $|\eta| < 2$), in coincidence with the arrival of proton bunches from both directions. For p-Pb collisions, a VZEROAND trigger (coincidence in both VZERO detectors) has been used. Events with the z-coordinate of the primary vertex that has been reconstructed in the region $|Z_{vtx}| < 10$ cm have been selected for the analysis.

4.2 D^{*+} reconstruction

4.2.1 Topological selections

The D^{*+} meson is reconstructed via the hadronic decay channel [70]

$$D^{*+} \rightarrow D^0 + \pi^+ (BR = 67.7\%) \quad (4.1)$$

with

$$D^0 \rightarrow K^- + \pi^+ (BR = 3.89\%). \quad (4.2)$$

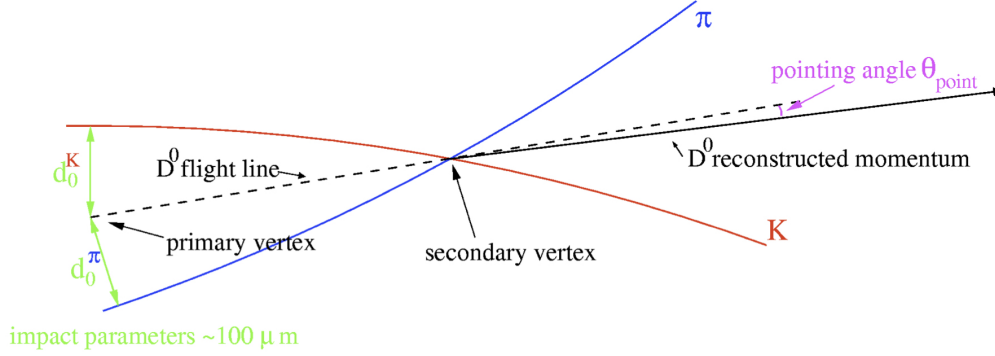


Figure 4.1: The decay topology for $D^0 \rightarrow K^- \pi^+$ [71].

Each D^0 candidate decaying as shown in equation (4.2) is reconstructed by combining pairs of opposite charge tracks that pass quality selection criteria, namely:

- at least 70 clusters (out of a maximum of 159) in the TPC;
- χ^2 per cluster of the momentum fit in the TPC smaller than 4;
- minimum of 2 hits in the ITS, out of which at least one in one of the first two layers (SPD);
- $|\eta| < 0.8$;
- $p_T > 0.4 \text{ GeV}/c$.

Because of the weak nature of the D^0 decay in equation 4.2, the D^0 has a mean proper decay length $c\tau$ of the order of a few hundreds of μm . This means that the D^0 decay vertex is displaced from the primary one (as shown in Figure 4.1) and this decay topology is exploited to apply further selections on the pairs of positively and negatively charged tracks that build the D^0 candidate.

The main cut variables are:

- The product of the impact parameters of the two tracks, $d_0^\pi \times d_0^K$;
- The cosine of the pointing angle, $\cos\theta_{point}$, which is defined as the cosine of the angle between the reconstructed momentum of the D^0 candidate and its flight-line, i.e. the line connecting the reconstructed primary and secondary vertex (Figure 4.1). For real D^0 candidates, the momentum of the reconstructed D^0 meson will point back to the production vertex. Therefore, $\cos\theta_{point}$ will be close to unity, while pairs of tracks not originating from real two-body decays will have a rather flat distribution in the range -1 to 1.

CHAPTER 4. ANALYSIS STRATEGY

All the cut variables are summarised below. The cut values applied in the p_T bin 4-5 GeV/ c are also reported.

- $M(K\pi)$ around the value of the daughter $D^0 < 0.032$ GeV/ c^2
- DCA (distance of closest approach between the tracks) < 0.07 cm
- $\cos(\theta^*) < 0.9$ (with θ^* being the angle between the Kaon and the D^0 flight line in the D^0 rest frame)
- $p_T(K) > 1$ GeV/ c
- $p_T(\pi) > 1$ GeV/ c
- $d_0(K) < 0.07$ cm
- $d_0(\pi) < 0.07$ cm
- $d_0 \times d_0 < 0.0001$ cm²
- $\cos\theta_{point} > 0.9$
- invariant mass half width of $D^{*+} < 0.3$ GeV/ c^2
- half width of $M(K\pi\pi) - M(K\pi) < 0.1$ GeV/ c^2
- $p_T^{min}(\pi_{soft}) > 0.05$ GeV/ c
- $p_T^{max}(\pi_{soft}) < 100$ GeV/ c
- θ , angle between the soft and decay plane of the $D^0 > 0.5$ rad

The cut values are optimised in order to maximise the statistical significance, defined as

$$Significance = \frac{S}{\sqrt{S+B}} \quad (4.3)$$

where S represents the signal and B represents the background. Given that the cut values are dependent on the p_T of the D^{*+} candidate, the signal and background values are determined for each p_T bin and are extracted from the fitted invariant mass distribution (the fitting procedure is described in the next subsection, 4.2.2). To further reduce the combinatorial background, particle identification through the measurement of the specific energy loss in TPC and of the Time of Flight with the TOF detector is applied on the daughters of the D^0 candidate. The obtained D^0 candidate is then associated to a charged track, originated at the primary vertex, in order to reconstruct a D^{*+} candidate, according to the decay shown in equation 4.1.

A fiducial acceptance cut is applied to the selected D^{*+} candidate selecting candidates that fall in the rapidity region $|y_D| < y_{fid}(p_T)$, with $y_{fid}(p_T)$ smoothly increasing from $y_{fid}(p_T) = 0.5$ at $p_T(D^{*+}) = 0$ to $y_{fid}(p_T) = 0.8$ at

$p_T(D^{*+}) = 5 \text{ GeV}/c$.

The invariant mass, defined as

$$M(daughter_i) = \sqrt{\sum_{i=1}^{N_{daugh}} E_i^2 - \sum_{i=1}^{N_{daugh}} \vec{p}_i^2} \quad (4.4)$$

is calculated, where E_i is the energy of the candidate daughter i , while \vec{p}_i is its reconstructed momentum of the same.

Given the D^{*+} decay chain (equations (4.1) and (4.2)), it is convenient to compute the difference in invariant mass defined as follows:

$$\Delta M = M(K^-\pi^+\pi^+) - M(K^-\pi^+). \quad (4.5)$$

The difference in invariant mass is expected to produce a narrow peak in the invariant mass spectrum centered at the value $\Delta M = 145 \text{ MeV}/c^2$. Given the way the variable is constructed, the resolution of the pion and kaon from D⁰ decay cancels out and the width of the invariant mass spectrum is driven by the resolution on the soft pion momentum.

4.2.2 Signal extraction

To extract the D meson yield, which will be later used for the normalisation of the correlation distribution, the invariant mass distribution is fitted with a fit function built as a sum of a Gaussian function to model the signal peak and a parametrisation of the background, i.e.

$$f_{fit}(\Delta M) = f_{sig}(\Delta M) + f_{bkg}(\Delta M) \quad (4.6)$$

with

$$f_{sig}(\Delta M) = Y_D \frac{1}{\sqrt{2\pi}\sigma} e^{-\frac{(\Delta M - \mu)^2}{2\sigma^2}} \quad (4.7)$$

and

$$f_{bkg}(\Delta M) = a\sqrt{\Delta M - m_\pi} e^{b(\Delta M - m_\pi)}. \quad (4.8)$$

The parameters a and b in the background parametrisation (4.8) are free parameters and are estimated in a first place by fitting only the invariant mass entries that are in the side-bands of the distribution. Once those parameters are obtained, they are fixed in the overall fit function (eq 4.6) and then the full invariant mass spectrum is fitted.

The parameter Y_D , the D meson yield, in equation 4.7 represents the raw yield. To build the correlation distribution, D meson candidates are selected in the invariant mass region $\Delta M = [\mu - 2\sigma, \mu + 2\sigma]$, where μ and σ are the mean and the width of the fitted invariant mass distribution. This selection of the range allows to reduce the background contribution by $\sim 30\%$, while the signal loss is of the order of $\sim 5\%$, resulting in a $\sim 50\%$ higher S/B ratio. The total number of D^{*+} triggers, used to normalise the correlation distribution,

CHAPTER 4. ANALYSIS STRATEGY

corresponds to $\sim 0.95Y_D$.

Figures 4.2 and 4.3 show the invariant mass distribution in fine p_T -bins (the fine bins are $1 \text{ GeV}/c^2$ wide for the p_T range $3 < p_T(D^{*+}) < 8 \text{ GeV}/c$, while in the range $8 < p_T(D^{*+}) < 16 \text{ GeV}/c$ they are split in $8 < p_T(D^{*+}) < 10 \text{ GeV}/c$, $10 < p_T(D^{*+}) < 12 \text{ GeV}/c$ and $12 < p_T(D^{*+}) < 16 \text{ GeV}/c$.

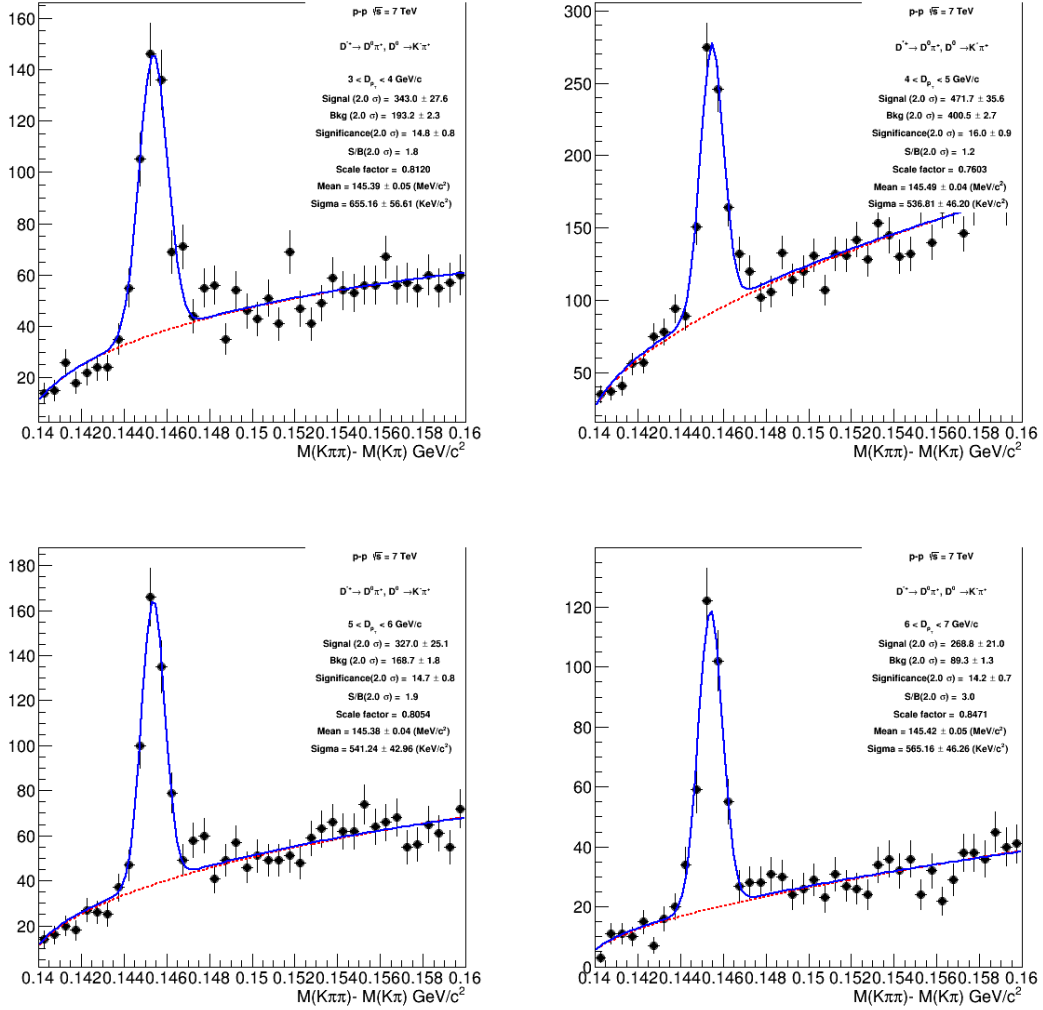


Figure 4.2: The (ΔM) distribution for the fine p_T -bins in pp collisions at $\sqrt{s} = 7 \text{ TeV}$. Upper left panel: $3 < p_T(D^{*+}) < 4 \text{ GeV}/c$. Upper right panel: $4 < p_T(D^{*+}) < 5 \text{ GeV}/c$. Lower left panel: $5 < p_T(D^{*+}) < 6 \text{ GeV}/c$. Lower right panel: $6 < p_T(D^{*+}) < 7 \text{ GeV}/c$

4.2. D^{*+} RECONSTRUCTION

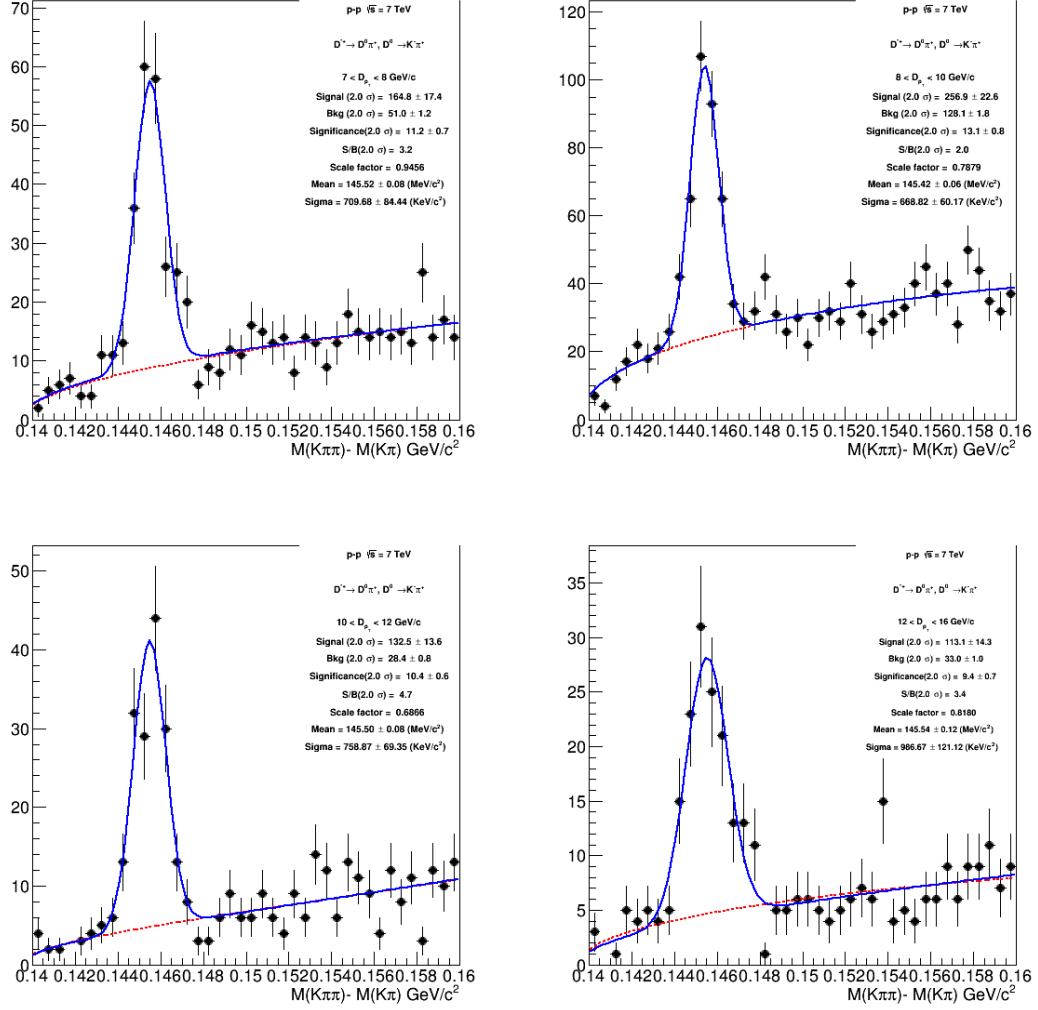


Figure 4.3: The (ΔM) distribution for the fine p_T -bins in pp collisions at $\sqrt{s} = 7$ TeV. Upper left panel: $7 < p_T(D^{*+}) < 8 \text{ GeV}/c$. Upper right panel: $8 < p_T(D^{*+}) < 10 \text{ GeV}/c$. Lower left panel: $10 < p_T(D^{*+}) < 12 \text{ GeV}/c$. Lower right panel: $12 < p_T(D^{*+}) < 16 \text{ GeV}/c$

4.3 Background subtraction

The correlations built from the inclusive candidates will inevitably have some residual background contribution. To estimate and remove this contribution and obtain the effective correlation of D^{*+} mesons and charged particles, the side-band method is used. The method consists essentially in selecting an invariant mass region that excludes the signal (4 to 8 σ at the left and right of the peak for example) and building the correlation distribution with the candidates whose invariant mass falls in this region. These candidates are originating from combinatorial background, therefore the obtained correlation distribution can be used as an estimate of the correlation distribution of the background under the D meson peak.

The D^{*+} decay chain (eq 4.1) allows for two independent approaches to the side-band subtraction, since two invariant mass distributions are build, one for daughter D^0 and one for the D^{*+} .

4.3.1 Background from D^0 side-bands

In this approach, D^0 candidates in the 4 to 8 σ region of the D^0 invariant mass (right plot in figure (4.4)) are selected and matched with soft pion candidates in order to reproduce a D^{*+} -like background candidate. The invariant mass obtained in such a way is expected to reproduce the combinatorial background shape.

The black points in figure (4.5) shows the ΔM distribution of $K\pi\pi$ combinations where the $K\pi$ invariant mass falls in the 3 σ region of the expected D^0 invariant mass. On the other hand, the red points represent the invariant ΔM obtained when selecting the $K\pi$ invariant mass in the left and right side-band region $4\sigma < |M(K\pi) - M_{D^0}| < 8\sigma$.

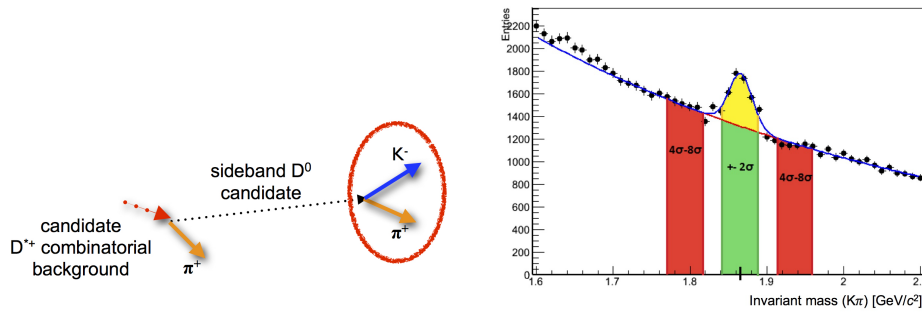


Figure 4.4: The cartoon in the left panel shows the reconstruction of a side-band candidate using the side-bands of the D^0 . A $K\pi$ pair, whose invariant mass falls in the side-band region (red region in the invariant mass plot on the right) is then associated with a soft pion candidate to reproduce a fake D^{*+} candidate, i.e. one from the combinatorial background.

4.3. BACKGROUND SUBTRACTION

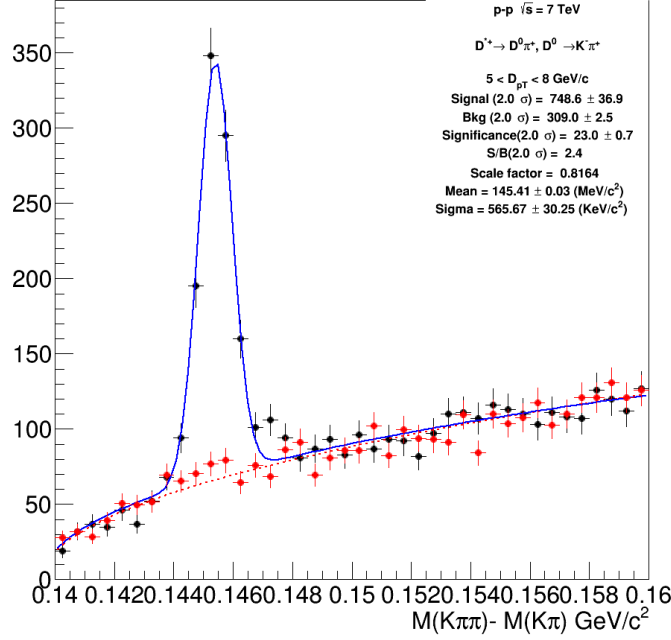


Figure 4.5: The black points represent the ΔM of D^{*+} candidates selected coming from good D^0 candidates, while the red points represent the D^{*+} candidates originating by selecting D^0 candidates from the side-band region.

The red distribution has been rescaled to match, on average, the values of the fit function of the background for the $\Delta M > 0.148 \text{ MeV}/c^2$ (red dashed line in figure (4.5)).

4.3.2 Background from D^{*+} side-bands

Another approach to estimate the correlation of background candidates is to use directly the correlation from the D^{*+} side-bands in the ΔM distribution. Given the fact that the background approaches zero at the π^+ mass value, due to the limited phase space, it is only possible to estimate the background contribution using the right side-band in the ΔM distribution. The range considered to estimate the background has been chosen to be $4\sigma < \Delta M - \Delta M_{D^{*+}} < 15\sigma$, which corresponds to the blue area in figure (4.6). The scaling factor (k_{sf}) is computed as the ratio of the integral of the background function (the red dashed line) under the peak (in the red region) and in the blue region, i.e.

$$k_{sf} = \frac{\int_{peak} f_{bkg}(\Delta M)}{\int_{sb} f_{bkg}(\Delta M)}. \quad (4.9)$$

As the displaced $K\pi$ pairs that fall in the 3σ region around the mass value of the D^0 are selected and then are matched with a soft pion candidate to

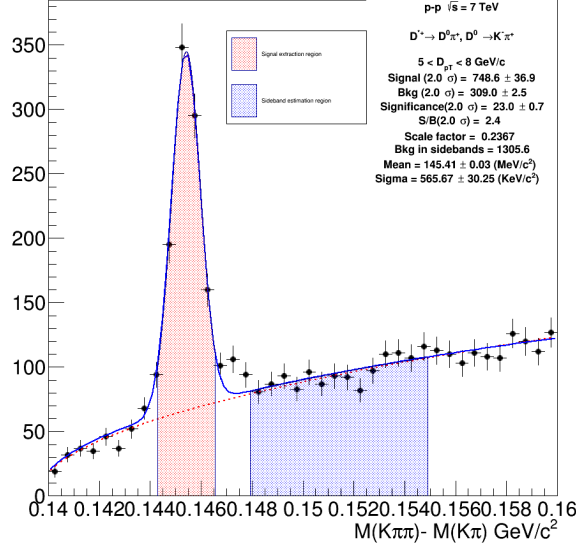


Figure 4.6: The ΔM distribution for the p_T -range $5 < p_T(D^{*+}) < 8 \text{ GeV}/c$. The blue area shows the ΔM used to define the sideband candidates, while the red area shows ΔM to define the D^{*+} candidates. The correlations are estimated by taking candidates from the blue region ($4\text{--}15 \sigma$ in the invariant mass distribution).

make a D^{*+} candidate, when considering the side-bands of this distribution there might be some residual contribution from true D^0 mesons. This means that, when subtracting the correlations from the side-band region, the estimated background distribution might contain some (D^0 -charged particle-like) azimuthal correlation.

To get an estimate of this contamination, the $K\pi$ invariant mass distributions obtained as reconstructed daughters candidates of D^{*+} candidates from the peak region as well as from the side-band region of ΔM are studied separately.

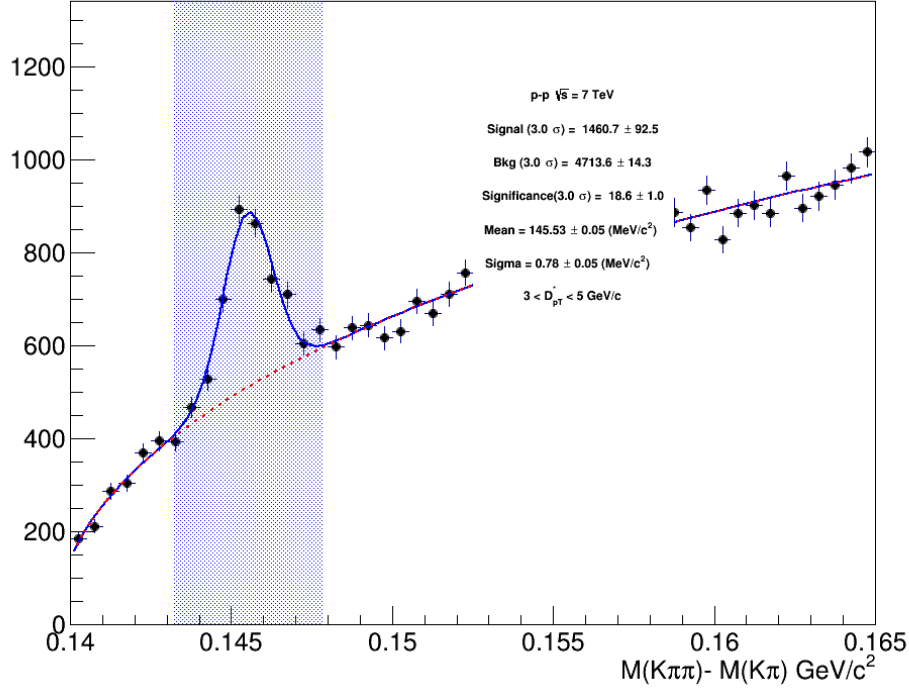
The plot in the lower panel of figure 4.7 shows the invariant mass distribution of the $(K\pi)$ pairs, reconstructed as a daughter of the D^{*+} candidate, i.e. the pairs whose ΔM , computed by matching the D^0 candidate with a soft pion candidate, falls in the signal region of the D^{*+} (blue region in the upper plot of figure 4.7).

In the lower panel of figure 4.8, the $K\pi$ invariant mass distribution is obtained from sideband candidates, i.e. those candidates that fall in the region $4\sigma < \Delta M - \Delta M_{D^{*+}} < 15\sigma$ (corresponding to the blue region in the upper panel of figure 4.8).

The signal-over-background ratio, S/B , in the case of $(K\pi)$ pairs from the peak region in the ΔM distribution is $S/B \approx 1$, while $S/B \approx 0.1$ when pairs are taken from the side-band region, confirming that most of the contribution

4.3. BACKGROUND SUBTRACTION

Study of invariant mass of the D^0 as function of D^+ daughter



Study of invariant mass of the D^0 as function of D^+ daughter

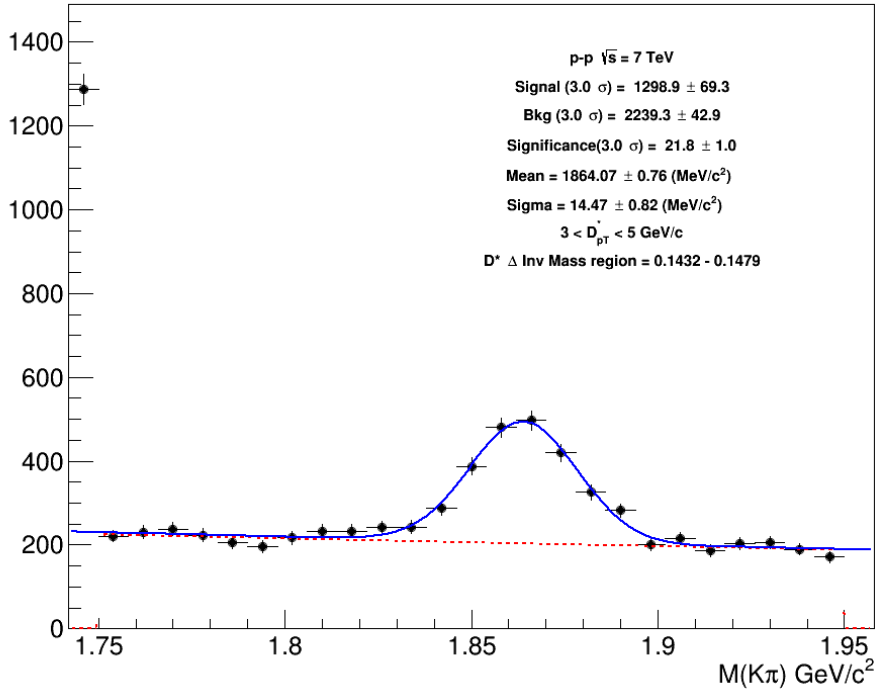


Figure 4.7: Upper panels: ΔM distribution. The blue region shows the ΔM region used to select the candidates to obtain the $M(K, \pi)$ distributions showed in the lower panels.

CHAPTER 4. ANALYSIS STRATEGY

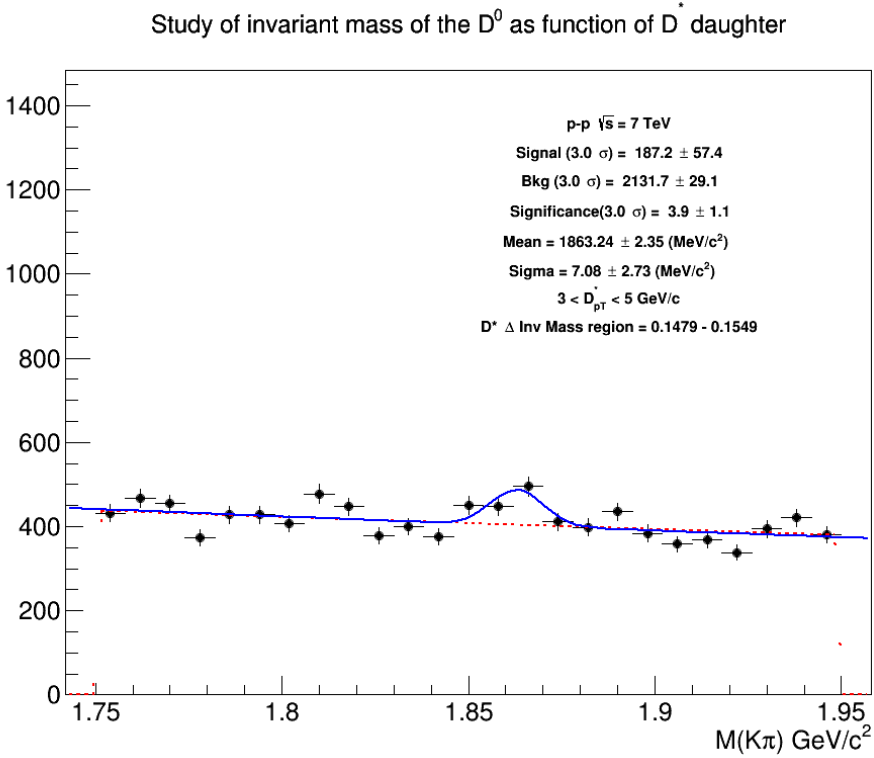
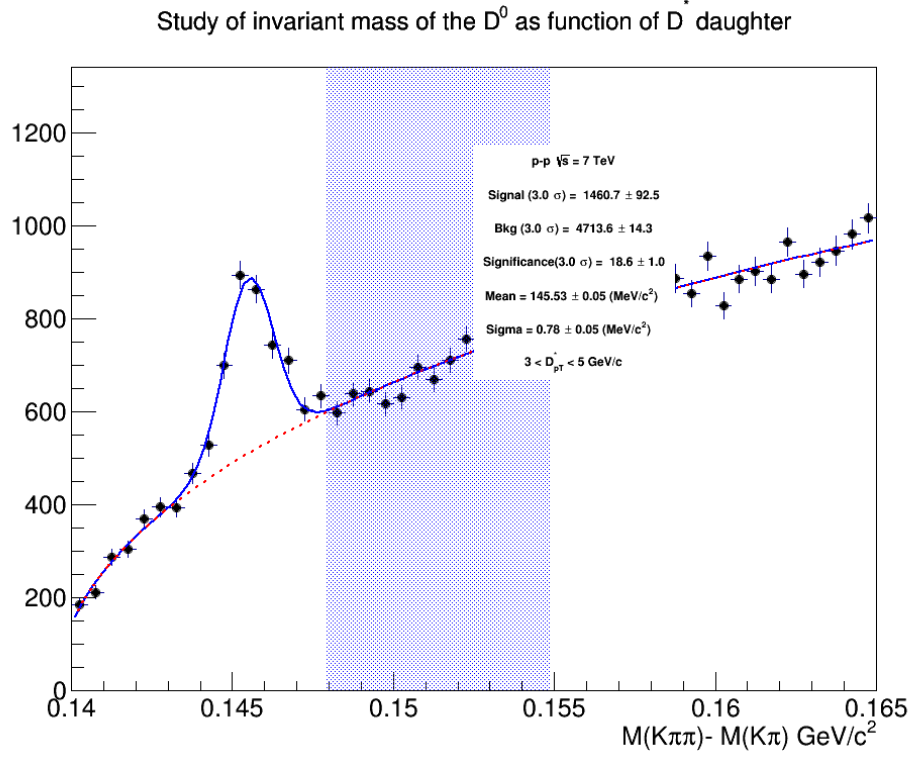


Figure 4.8: Upper panels: ΔM distribution. The blue region shows the ΔM region used to select the candidates to obtain the $M(K, \pi)$ distributions showed in the lower panels.

4.3. BACKGROUND SUBTRACTION

in this case is due to $K\pi$ combinatorial background.

The total yield of “real” D^0 triggers is a factor 10 smaller than the one from the signal region. An additional factor ~ 2.5 comes from the fact that the considered sideband region is of 11σ , while the one used for the signal region is 4σ wide. In addition to that, the correlations are rescaled by the scale factor (which for this particular case is ≈ 0.2).

This means that the final contribution to the estimated background azimuthal correlations due to real D^0 is $< 1\%$, which is negligible considered the estimated systematic uncertainty that is discussed later (see Chapter 6 on Systematic uncertainties).

4.3.3 Subtraction of the background contribution

The background subtraction is performed using the following equation

$$f_{D^{*+}}(\Delta\varphi) = f_{Incl}(\Delta\varphi) - k_{sf}f_{SB}(\Delta\varphi), \quad (4.10)$$

Figure (4.9) shows the $\Delta\varphi$ correlation distribution, corrected for the mixing event (described in the section 4.5), for the inclusive ($f_{Incl}(\Delta\varphi)$) D^{*+} sample (blue points), and the azimuthal correlation estimated from the side-bands, $f_{SB}(\Delta\varphi)$, (red points - this particular figure shows the case of the side-bands from the D^{*+}). As it can be seen from the figure, the $f_{SB}(\Delta\varphi)$ is strongly correlated at $\Delta\varphi = 0$, which suggests that most of the side-band candidates are actually contained with jets.

The left panel of figure (4.10) shows the comparison of the final, “per trigger”, azimuthal correlations of D^{*+} mesons and charged particles obtained with the two different background subtraction methods described in sections (4.3.1) and (4.3.2), while in the right panel the ratio of the correlation obtained with the side-bands of D^0 (section (4.3.1)) and the one obtained with the side-bands of D^{*+} (section (4.3.2)) is shown. Good compatibility of the two correlation distribution is shown, which is also confirmed by the ratio, that is fluctuating around 1 without showing any particular structure. As default method for the analysis, the correlations using the D^{*+} side-bands is used. This choice was done because of compatibility with other similar analysis (cf. D^0 and D^+ -charged particle azimuthal correlations [72, 73]), as well as the fact that the data set for the Pb-Pb analysis does not allow the use of the D^0 side-band method because all D^0 candidates exceeding the range of $\sim 4\sigma$ around the peak are cut off to reduce the number of the data sample, allowing to use the D^{*+} side-band method only.

CHAPTER 4. ANALYSIS STRATEGY

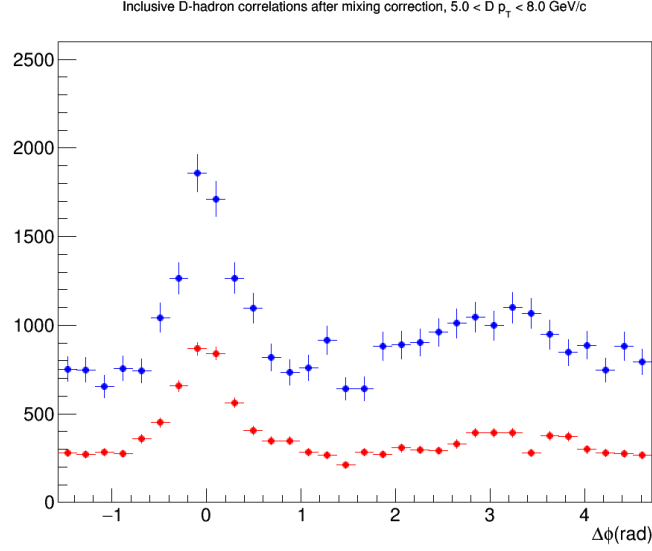


Figure 4.9: The $\Delta\varphi$ correlation distribution of inclusive D^{*+} candidates and charged tracks is shown in blue and the distribution of sideband candidates and charged tracks is shown in red. As most of the combinatorial background candidates are found within jets, a near-side correlation peak in the distribution with triggered by the side-band candidates is present.

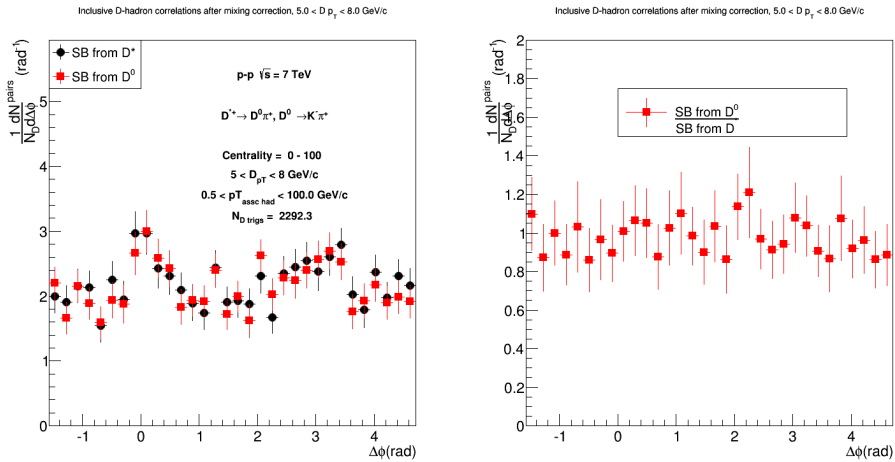


Figure 4.10: Left panel: comparison of the correlation distribution for $5 < p_T(D^{*+}) < 8$ GeV/c obtained using the two different sideband background methods. Right panel: ratio of the two distributions (red/black)

4.4 Associated track selection

The tracks selected to build the correlation distribution (associated tracks) are required to pass a set of quality criteria discussed in this section.

A maximum value of the χ^2/ndf on the track momentum fit in the TPC of 2 is required, which assures a good matching of the hits in the ITS and TPC. Each track is required to have a minimum of 70 clusters in the TPC (out of the possible 159), and a good refit of the track in the ITS and TPC is requested as well. For the analysis it is important to select mostly tracks originating from the primary vertex, and reject the so-called secondary tracks, i.e. tracks originating from decay products of long-lived strange particles and from interactions of primary particles with the detector (for example, electrons from photon conversions). This selection is performed by setting an upper bound on the distance of closest approach of the track to the reconstructed primary vertex. This cut value is set to 1 cm along the z-axis and 0.25 cm in the transverse, xy, plane. To grant enough resolution in the track impact parameter for the latter selection, a minimum of 3 hits in the ITS is required. A residual contamination of secondary tracks is still present and its treatment is discussed later in this chapter. No requirement on the presence of hits in one or both of the first two layers of the ITS (the SPD) has been required.

4.5 Correction for detector inhomogeneities

By calculating angular correlations of D^{*+} mesons and charged particles, it is possible to have some unphysical structures in the $\Delta\varphi$ distribution due to detector inhomogeneities. In addition, given the limited acceptance for the reconstruction of D^{*+} mesons and charged particles, a triangular-shaped correlation is expected to be present when computing the correlations in $\Delta\eta$. To correct for both these effects, the event-mixing technique is used. The event mixing basically consists of computing the $\Delta\varphi - \Delta\eta$ correlation distributions by taking D^{*+} or side-band candidates from one event and correlating them with charged tracks from a different event. The obtained distribution, since is not influenced by correlations coming from physical processes, would show structures in $\Delta\varphi$ that are due to dead zones of the detector, and is expected to reproduce the triangular $\Delta\eta$ shape due to the limited detector acceptance. The events are splitted in bins of multiplicity and position of the vertex along the z-axis, named pools, as follows

- Multiplicity bins: $(0 - 20)$, $(20 - 40)$, $(40 - +\infty)$ for pp collisions and $(0 - 40)$, $(40 - 65)$, $(65 - +\infty)$ for p-Pb collisions.
- Vertex z (cm) = $(-10, -2.5)$, $(-2.5, 2.5)$, $(2.5, 10)$

A minimum amount of 8 events in the pool is required to start performing the mixing correction. The calculation is basically done as follows: each time a

CHAPTER 4. ANALYSIS STRATEGY

D or side-band candidate is found in the event N, the $\Delta\phi - \Delta\eta$ correlation is computed with all the tracks stored in the event pool, if the pool is ready to perform the mixing (i.e. if the bin of the pool with the given multiplicity and z-vertex contains the minimum of 8 events). Once the event N is processed, it is saved in the event pool in the correspondent multiplicity/z-vertex bin and the calculation is repeated for the event N+1. In order to limit the memory consumption, the pool works on the FIFO (first in first out) principle, i.e. the first event that has been stored is cleaned from the pool when a new one is saved.

Once the correlation distribution for mixed events is obtained, it is used as weight to correct the distribution from the single event analysis. The correction is described by the following equation

$$\frac{dN^{corr}(\Delta\phi\Delta\eta)}{d\Delta\phi d\Delta\eta} = \frac{\frac{dN^{SE}(\Delta\phi\Delta\eta)}{d\Delta\phi d\Delta\eta}}{\frac{dN^{ME}(\Delta\phi\Delta\eta)}{d\Delta\phi d\Delta\eta}} \frac{dN^{ME}(0,0)}{d\Delta\phi d\Delta\eta}. \quad (4.11)$$

As it can be seen, the event mixing distribution is normalised to the value $\frac{dN^{ME}(0,0)}{d\Delta\phi d\Delta\eta}$. The basic assumption behind this correction is that, in first approximation, in this particular direction (i.e. $\Delta\phi, \Delta\eta = 0,0$), the trigger and associated particle experience the same detector condition and acceptance, therefore no correction is necessary (hence the correction to be 1). The event mixing correction is limited to the interval $|\Delta\eta| < 1$. Even though, given the acceptance of ALICE, this limit could be theoretically extended to a value of $|\Delta\eta| < 1.6$, because of the limited statistics in the single event correlation distribution, it was decided to limit it to the value of 1 to avoid the so-called wing effect, i.e. a rise at large $\Delta\eta$ of the correlation distribution due to the division of two relatively small numbers. Such wings could bias the near and away side peaks, as well as would bias drastically the estimation of the baseline due to uncorrelated background from the underlying event.

The correction procedure is illustrated in the figures 4.11, 4.12 and 4.13.

Figure 4.11 shows the correlation distribution of the inclusive D^{*+} sample for the single event analysis on the left and the side-band candidates on the right. The second row illustrates the same, but for the mixed-event analysis. Both the inclusive and side-band distributions are corrected using the equation 4.11, and the distributions shown in figure 4.12 are obtained (left for the inclusive case and right for the side-bands). The background subtraction is performed as described in section 4.3, and the final distribution (figure 4.13) is obtained.

4.5. CORRECTION FOR DETECTOR INHOMOGENITIES

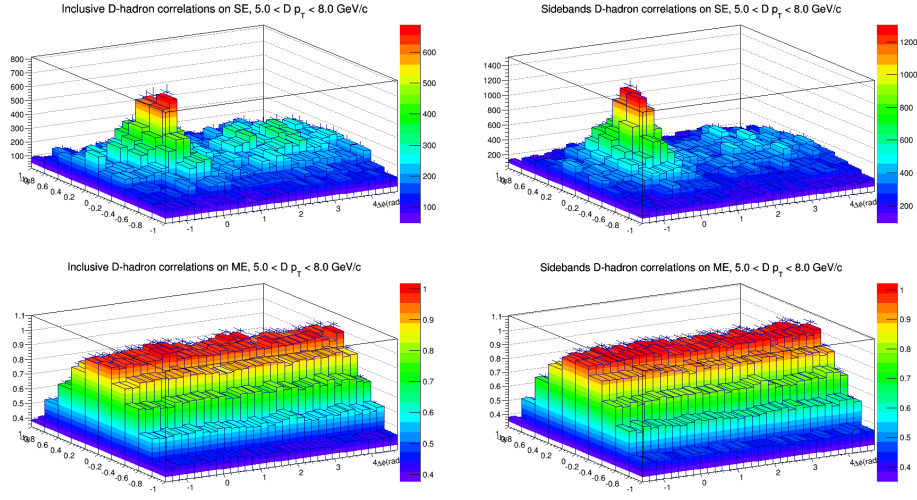


Figure 4.11: Correlation distribution for $5 < p_T(D^{*+}) < 8$ GeV/ c and $p_T^{assoc} > 0.3$ GeV/ c . Upper left panel: single event distribution for inclusive D⁺ candidates. Upper, right panel: single event distribution for sideband candidates. Lower left panel: mixed event distribution for inclusive D⁺ candidates. Lower right panel: mixed event distribution for sideband candidates.

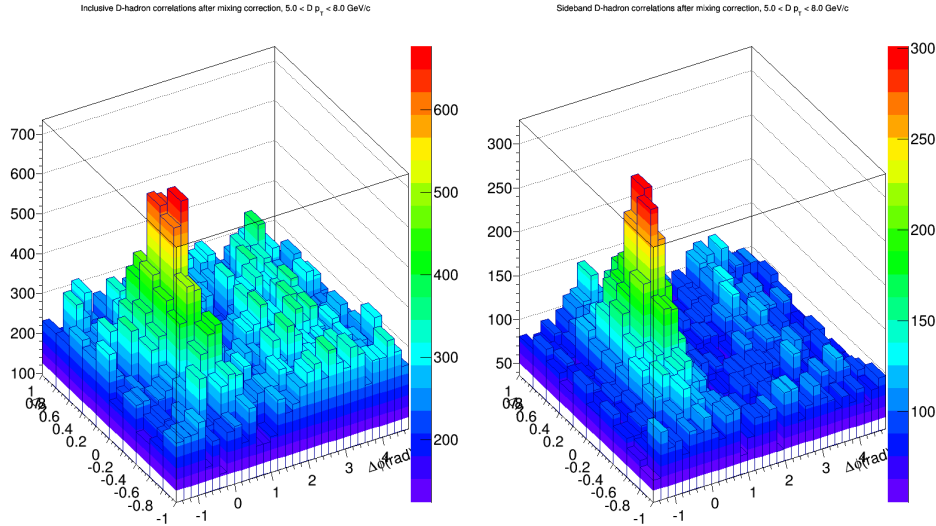


Figure 4.12: Correlation distribution for $5 < p_T(D^{*+}) < 8$ GeV/ c and $p_T^{assoc} > 0.3$ GeV/ c . Left panel: mixed-event-corrected distribution for inclusive D⁺ candidates. Right panel: mixed-event-corrected distribution for sideband candidates.

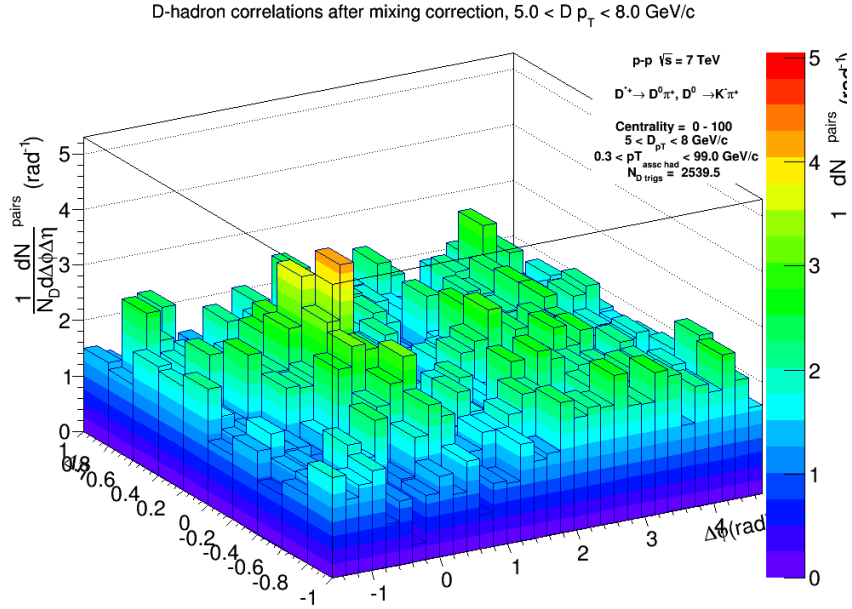


Figure 4.13: Correlation distribution for $5 < p_T(D^{*+}) < 8$ GeV/c and $p_T^{\text{assoc}} > 0.3$ GeV/c. Mixed-event corrected distribution for D^{*+} candidates after the side-band background subtraction.

4.6 Correction for D^{*+} meson efficiencies

The azimuthal correlation distribution is affected by the reconstruction and selection efficiency of D^{*+} mesons. Indeed, the correlations are estimated in wide p_T bins of the D^{*+} , where the efficiency increases steeply as function of the p_T of the D^{*+} . The correction for the D^{*+} meson efficiency is necessary to properly take into account the p_T -dependence of the correlation distribution within the given D^{*+} meson p_T interval. In fact, only the p_T dependence of the D^{*+} meson efficiency is relevant while the average value in the p_T range is simplified due to the normalisation of the correlation distribution to the number of trigger particles.

The efficiency is estimated using a PYTHIA + GEANT3 Monte Carlo sample for the pp case, while in p-Pb also HIJING is used to get a better description of the multiplicity distribution. Additionally, the obtained efficiency is corrected for the geometrical acceptance of the ALICE detectors. As an example, the $\epsilon \times acc$ for the prompt D^{*+} reconstruction in p-Pb collisions as function of the D^{*+} (p_T) and the multiplicity, quantified using the number of SPD tracklets, is shown in figure 4.14. The expected increase as function of both the variables is clearly visible.

The correction is applied during the analysis execution by weighting the two dimensional $\Delta\varphi, \Delta\eta$ correlation histogram with the inverse of the efficiency value for a given p_T and multiplicity bin, i.e. $1/\epsilon(p_T^{D^{*+}}, multiplicity)$, assuming that each reconstructed D^{*+} is a prompt D^{*+} (this assumption is further corrected as described in section 4.8).

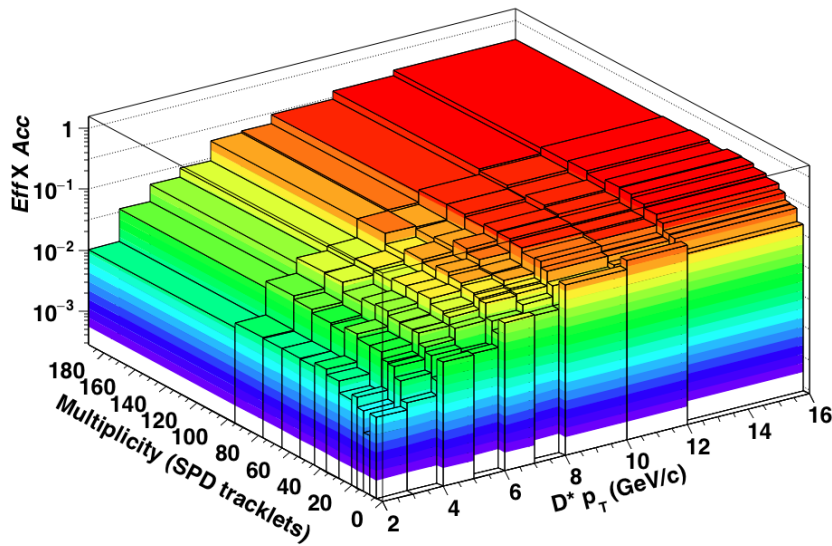


Figure 4.14: $\epsilon \times acc$ map of D^{*+} mesons in p-Pb collisions as function of the D^{*+} p_T and the event multiplicity.

CHAPTER 4. ANALYSIS STRATEGY

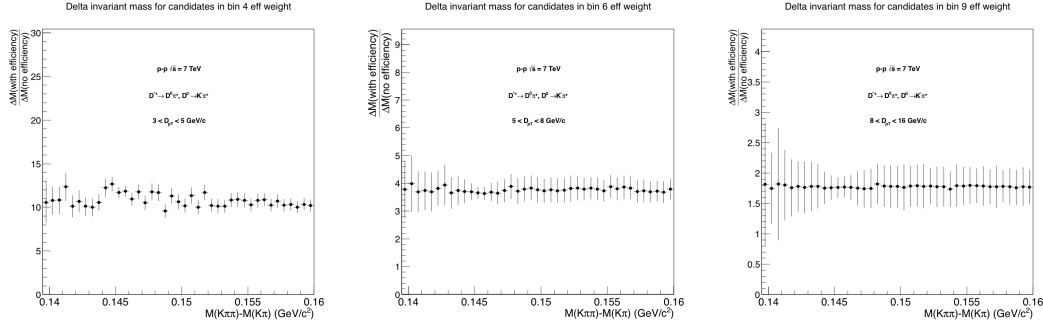


Figure 4.15: Ratio of the invariant masses with D-meson efficiency correction and without the correction. The upper panel is for $3 < p_T(D^{*+}) < 5$ GeV/c, the middle panel is for $5 < p_T(D^{*+}) < 8$ GeV/c The lower panel is for $8 < p_T(D^{*+}) < 16$ GeV/c.

Besides the correlation distribution, to properly account for the number of D^{*+} correlation triggers, also the invariant mass distribution is weighted by the same value. As the invariant mass in a wide p_T bin of the D^{*+} will be a weighted sum of more invariant mass distributions, the shape of the background might be distorted, biasing the background subtraction (as described in section 4.3). Figure (4.15) shows the ratio of the invariant mass distributions after weighting with the inverse of the efficiency and the corresponding raw distribution, for the three p_T bins considered in pp collisions. The ratio is flat within the errors in all the three p_T bins showing that there is no background distortion that might bias the background subtraction.

4.7 Correction for associated track efficiencies

A fraction of good associated particles in each event are not reconstructed or are rejected by the track quality selections. The amount of lost particles depends on the efficiency in the ITS and TPC. The correlation distribution needs to be corrected for this “loss”. The single track efficiency has been estimated using a similar strategy as the one discussed for the D^{*+} -efficiency correction. The efficiency maps are built by scaling the reconstructed spectra with the one generated using the PYTHIA event generator [26]. The efficiency map was determined as function of the charged track p_T , η and the position of the primary vertex along the beam axis. As it was done in the case of the D^{*+} correction, the single track efficiency is applied as weight during the execution of the analysis, i.e. the two dimensional $\Delta\varphi, \Delta\eta$ histogram is weighted by the inverse of the efficiency $\epsilon(p_T, \eta, z_{vtx})$. Figure 4.16 illustrates the efficiency dependence on the p_T of the charged track. The efficiency shows a steep raise in the range $0 < p_T^{track} < 2$ GeV/c, at 2 GeV/c there is a maximum and for $p_T^{track} > 2$ GeV/c it decreases slightly before reaching a *plateau*. To properly

4.8. SUBTRACTION OF CORRELATIONS FROM D^{*+} MESONS COMING FROM BEAUTY-HADRON DECAYS

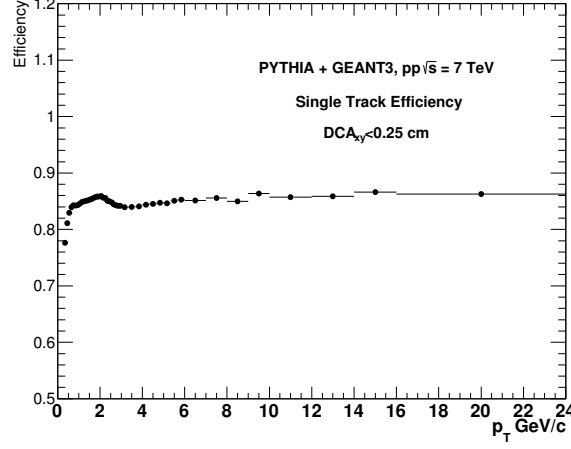


Figure 4.16: Single track efficiency as function of the track p_T for the standard track cuts.

take into account the rapidly changing shape, in the lowest p_T region a very fine binning of the spectra was used and was widen at higher p_T to reduce the fluctuations caused by the limited statistics.

4.8 Subtraction of correlations from D^{*+} mesons coming from Beauty-hadron decays

The selected sample of D^{*+} mesons will contain also contributions of those produced as decay products of beauty hadrons. With the current statistics it is not possible to measure the correlation of $(B \rightarrow D^{*+})$ and charged particles (called also feed-down contribution), so it was decided to subtract the beauty feed-down contribution using templates from Monte Carlo simulations. The procedure is done as follows: the feed-down azimuthal correlation distribution, estimated from the Monte Carlo sample, is rescaled by the fraction of D^{*+} mesons coming from beauty decays and then subtracted from the measured and corrected distribution, rescaled by the extracted D^{*+} yield. The latter is then rescaled by the fraction of prompt D^{*+} mesons, i.e. those that are coming from the fragmentation of charm quarks. The procedure is summarised as

$$\tilde{C}_{\text{prompt } D}(\Delta\phi) = \frac{1}{f_{\text{prompt}}} \left(\tilde{C}_{\text{inclusive}}(\Delta\phi) - (1 - f_{\text{prompt}}) \tilde{C}_{\text{feed-down}}^{\text{MC templ}}(\Delta\phi) \right). \quad (4.12)$$

The fraction of D^{*+} from charm, f_{prompt} is calculated using *FONLL* [38] predictions of p_T -differential cross-section for prompt and feeddown D^{*+} mesons,

CHAPTER 4. ANALYSIS STRATEGY

as well as the computed efficiencies and acceptance for the two cases

$$f_{\text{prompt}} = \left(1 + \frac{(Acc \times \epsilon)_{\text{feeddownD}^{*+}} \frac{d\sigma}{dp_T}^{\text{feeddownD}^{*+}}|_{|y|<0.5}}{(Acc \times \epsilon)_{\text{promptD}^{*+}} \frac{d\sigma}{dp_T}^{\text{promptD}^{*+}}|_{|y|<0.5}} \right). \quad (4.13)$$

The *FONLL*-cross sections are estimated at $\sqrt{s} = 7$ TeV.

In the case of the p-Pb analysis, an assumption on the nuclear modification of feeddown D^{*+} mesons has been done, and equation 4.13 is modified as follows

$$f_{\text{prompt}} = \left(1 + \frac{(Acc \times \epsilon)_{\text{feeddownD}^{*+}} \frac{d\sigma}{dp_T}^{\text{feeddownD}^{*+}}|_{|y|<0.5} \frac{R_{\text{pPb}}^{\text{feeddownD}^{*+}}}{R_{\text{pPb}}^{\text{promptD}^{*+}}}}{(Acc \times \epsilon)_{\text{promptD}^{*+}} \frac{d\sigma}{dp_T}^{\text{promptD}^{*+}}|_{|y|<0.5} \frac{R_{\text{pPb}}^{\text{promptD}^{*+}}}{R_{\text{pPb}}^{\text{promptD}^{*+}}}} \right) \quad (4.14)$$

where the ratio $\frac{R_{\text{pPb}}^{\text{feeddownD}^{*+}}}{R_{\text{pPb}}^{\text{promptD}^{*+}}}$ is varied in the range 0.9 – 1.3 and that variation is included in the evaluation of the systematic errors. In the p-Pb analysis, the f_{prompt} -calculation is done using the *FONLL* predictions at $\sqrt{s} = 5$ TeV, while the efficiencies are calculated from the p-Pb Monte-Carlo simulations. Figure (4.17) shows the f_{prompt} as function of the $D^{*+} p_T$ for pp (left panel) and for p-Pb (right panel). Figure (4.18) shows an example of the azimuthal correlations of feeddown D^{*+} mesons with charged hadrons obtained with three different *PYTHIA* tunes. Varying the parameters of the *PYTHIA* tunes affects mostly the process of parton fragmentation into hadrons, which might have an effect on the shape of the correlation distribution. The *PYTHIA*-Perugia 2011 [26] template is used as default value, while the other two are used to estimate the systematic uncertainties. As *PYTHIA* does not reproduce well the baseline of the uncorrelated background, before subtracting it from the measured correlation distribution, the baseline level is matched to the one in data. In the p-Pb analysis, an additional hypothesis on modulation of the

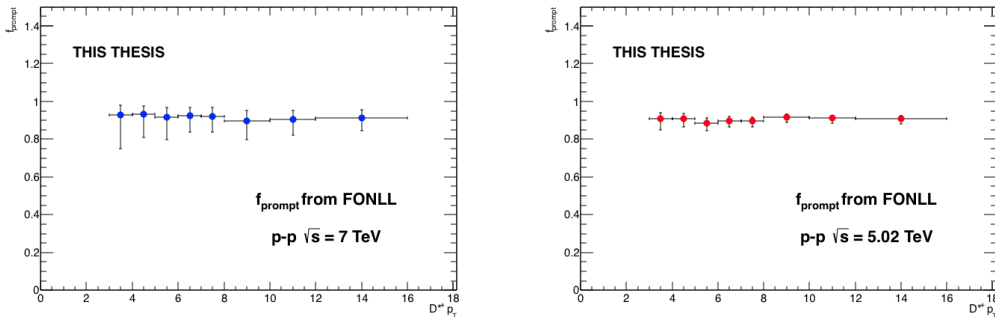


Figure 4.17: Calculated fraction of D^{*+} mesons originating from a charm quark: left panel is for pp collisions at $\sqrt{s} = 7$ TeV, while the right panel is for p-Pb collisions at $\sqrt{s_{NN}} = 5.02$ TeV.

4.8. SUBTRACTION OF CORRELATIONS FROM D^{*+} MESONS COMING FROM BEAUTY-HADRON DECAYS

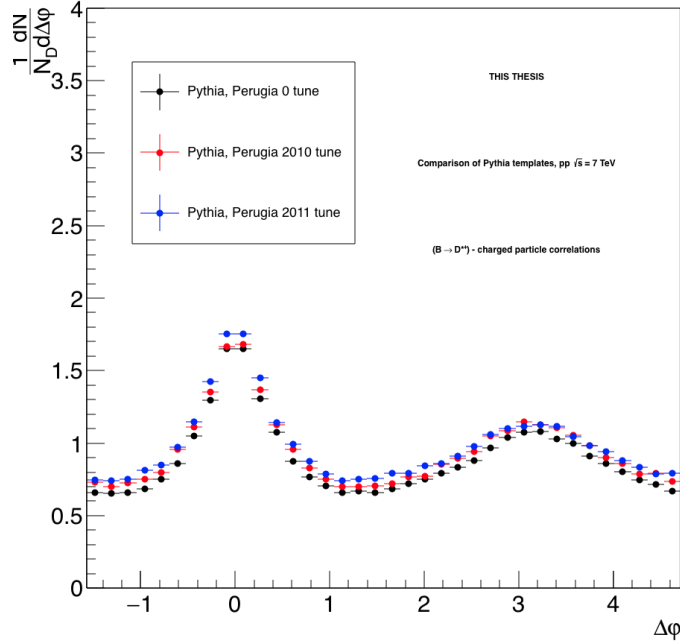


Figure 4.18: Monte Carlo templates using different tunes of PYTHIA for feed-down D^{*+} mesons.

baseline due to a v_2 of beauty hadrons is done, and it is added to the templates. This modulation enters in the evaluation of the systematic errors due to the B feed-down correction. The figure (4.19) shows the procedure for performing the modulation.

The baseline (green filled area) of the template is modulated with a v_2 -like contribution, (dashed line in magenta) defined as

$$f_{v_2}^{modulation} \propto (1 + 2v_2^D v_2^{had} \cos(\Delta\varphi)) \quad (4.15)$$

and this is added to the template (black line). The modulated template (red dashed line) is then inserted into the equation (4.12), and the feed-down subtraction is performed. The assumptions done on the values of the v_2 are as follows:

- $v_2^{(B \rightarrow D^{*+})} = 0.13$, representing an extreme upper bound for the v_2 of feed-down D mesons, given the expectation that $v_2(b) < v_2(c)$ and the measurement of the v_2 of prompt D mesons by ALICE [47]
- $v_2^{hadron} = 0.07$ for $0.3 < p_T^{had} < 1$ GeV/c and $v_2^{hadron} = 0.07$ for $p_T^{had} > 1$ GeV/c [34]

This contribution is also considered as source for the systematic uncertainty.

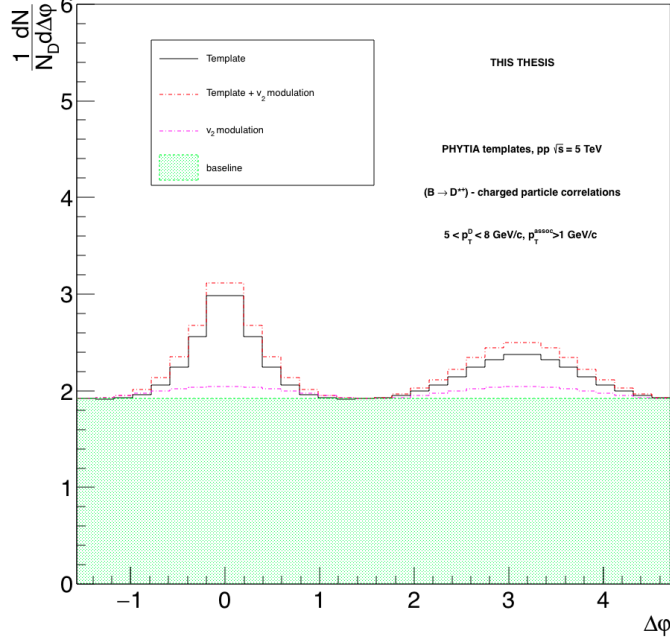


Figure 4.19: Example of a v_2 -like modulation of the PYTHIA templates .

4.9 Correction for secondary track contamination

As described in section 4.4, secondary tracks in the sample of associated tracks are removed via a cut on the distance of closest approach to the primary vertex in the transverse plane (DCA_{XY}). An upper cut on the charged track selection has been applied in order to remove secondary tracks. Secondary tracks are either decay products of long-lived strange hadrons or particles produced in interaction of particles with the detector (example electrons from photon conversion). The standard selection cut has been set to be at $DCA_{XY} < 0.25$ cm.

The left panel of figure (4.20) shows the distribution of primary (red line) and secondary (blue line) tracks as a function of the DCA_{XY} , which has been estimated from PYTHIA Monte Carlo simulations and the GEANT3 [74] particle transport package together with a detailed description of the geometry of the apparatus and of the detector response. The right panel of the figure shows the purity (the fraction of primary tracks) that is selected by the DCA_{xy} cut as function of the cut value. The purity is defined as:

$$purity = \frac{\int_0^{DCA_{XY}^{cut}} f_{prim}(DCA_{XY}) dDCA_{XY}}{\int_0^{DCA_{XY}^{cut}} f_{prim}(DCA_{XY}) + f_{sec}(DCA_{XY}) dDCA_{XY}} \quad (4.16)$$

where $f_{prim}(DCA_{XY})$ is the distribution of primary tracks as function of the DCA_{XY} (red distribution from the right panel of the same figure) and

4.9. CORRECTION FOR SECONDARY TRACK CONTAMINATION

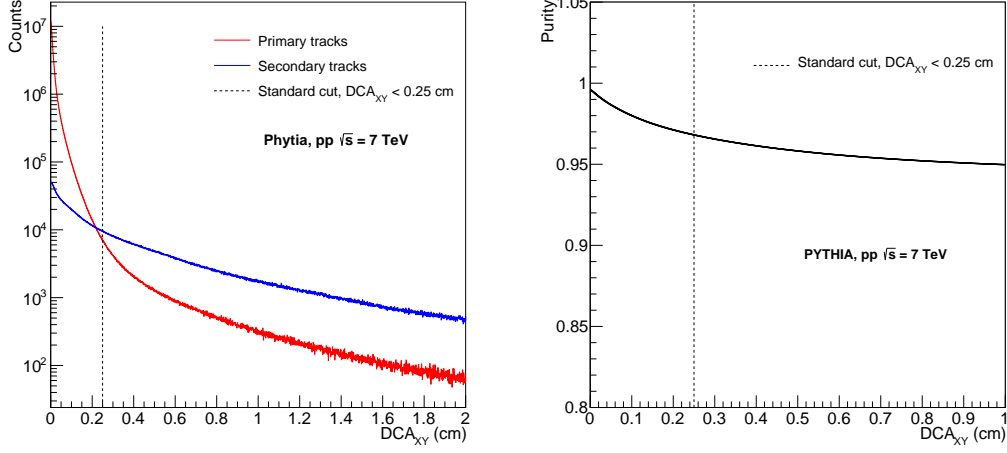


Figure 4.20: Left panel: distribution of primary tracks and secondary tracks as function of the DCA_{xy} . Right panel: Primary track purity distribution as function of the DCA_{xy} .

$f_{sec}(DCA_{XY})$ is the equivalent for secondary tracks (blue distribution from the right panel of the same figure). The estimated purity value for the default cut at $DCA_{XY} < 0.25$ cm is 0.97 for pp and 0.975 for p-Pb collisions. The correction is applied as a multiplicative factor on the corrected distribution, i.e.

$$C_{pc}(\Delta\phi) = purity \times \tilde{C}_{\text{prompt D}}(\Delta\phi) \quad (4.17)$$

where $\tilde{C}_{\text{prompt D}}(\Delta\phi)$ is the correlation distribution for prompt D^{*+} mesons defined by equations (4.13) and (4.14).

5

Monte Carlo analysis

This chapter presents the correlation analysis performed on the simulated Monte Carlo sample. For the case of pp collisions, the generation of events was done using the PYTHIA 6.4.21 event generator, with the Perugia0-tune [26]. The transport of particle through the ALICE detector (described in section 3.2) has been simulated using GEANT 3 [74]. In the analysis of the pp data sample, two different PYTHIA samples have been used:

- LHC10f6a: minimum bias PYTHIA Monte Carlo sample at the centre of mass energy $\sqrt{s} = 7$ TeV
- LHC10f7a: heavy-flavour enriched sample, at the centre of mass energy $\sqrt{s} = 7$ TeV : each event contains one $c\bar{c}$ or $b\bar{b}$, with D meson decays forced into the hadronic channels under study

For the p-Pb analysis

- LHC13d3: sample created using both PYTHIA and HIJING, used in the p-Pb collision mode,[27] at $\sqrt{s} = 5.02$ TeV. A pair of charm or beauty quarks is simulated with PYTHIA for each event, while HIJING is used to simulate the underlying event in a fraction of events corresponding to p-Pb interactions with $N_{coll} > 1$.

5.1 Different contributions to the azimuthal angular correlations of hadrons and D mesons

The analysis has first been performed at the generation level, i.e. without propagating the particles through the detector simulation by GEANT 3. D^{*+} mesons are identified by their Monte Carlo identity, while the associated tracks are selected as all the possible “trackable” final state particles, i.e. they are required to be electrons, pions, muons, kaons or protons. The D^{*+} is required to decay hadronically, according to the decay chain of equation 4.1. Both the D^{*+} and the charged particles are required to be within the ALICE acceptance ($|\eta| < 0.9$). The same request is applied on the daughters of the D^{*+} . The effect of the limited acceptance is corrected by using the mixing event correction (as described in section 4.5).

CHAPTER 5. MONTE CARLO ANALYSIS

The origin of the D^{*+} and the charged particles has also been studied. For the purpose of this analysis, it is interesting to separate the particles in those originating from a charm or beauty quark fragmentation. Particles not originating from a beauty or charm quark are tagged as “non heavy-flavour particles”. The flavour tagging is done as follows. For each D^{*+} and charged particle, the flavour of the mother (i.e. the particle that comes earlier in the production chain) is checked. If this happens to be a beauty quark, then the particle is tagged as a “beauty-origin”. If it happens to be a charm quark, then the particle is tagged as a “charm-origin”. This process is repeated until the heavy quark has been identified or no new mother is found. For the D^{*+} , if no charm or beauty quark is found, it is not considered for building the correlation distribution. In the case of charged tracks, if no heavy quark is found in the chain, the particle is tagged as a non heavy flavour particle.

The flavour-differential Monte Carlo analysis is done for the main contributors to the correlation distribution, i.e. the correlations are studied for the following cases:

- D^{*+} originating from a charm quark is correlated with tracks originating themselves from a charm quark (c-origin correlations);
- D^{*+} originating from a beauty quark is correlated with tracks originating themselves from a beauty quark (b-origin correlations);
- all the D^{*+} mesons are correlated with “non heavy flavour” particles (non HF-origin correlations).

Finally, also the inclusive D^{*+} mesons (from both charm and beauty origin) are correlated with the inclusive charged track sample (inclusive correlations). For compatibility with the analysis on data, only the azimuthal correlations within the range in pseudo rapidity $|\Delta\eta| < 1$ are considered.

Figure 5.1 shows the azimuthal correlations of D^{*+} mesons in the range $8 < p_T(D^{*+}) < 16$ GeV/ c and associated tracks in the range $p_T(hadron) > 0.3$ GeV/ c , obtained from the minimum bias Monte Carlo sample (LHC10f6a).

The red distribution in the figure represents the c-origin correlations, the green distribution the b-origin ones, the blue the non HF origin ones, while the black shows the inclusive origin correlation distribution.

The inclusive distribution shows the expected near and away side correlation peaks. Qualitatively speaking, the same trend is shown in the charm-origin case. For the beauty-origin case, the near-side correlation is visible, and is higher and narrower than that of the charm origin case, while on the away side there is no evident peak. However, no conclusion on the absence of the away-side peak can be drawn due to the limited number of D^{*+} mesons originating from beauty quarks in the minimum bias sample. The non-heavy-flavour origin case shows a rather flat distribution along $\Delta\varphi$, with an indication of an away side correlation peak. To better address the properties of the separated

5.1. DIFFERENT CONTRIBUTIONS TO THE AZIMUTHAL ANGULAR CORRELATIONS OF HADRONS AND D MESONS

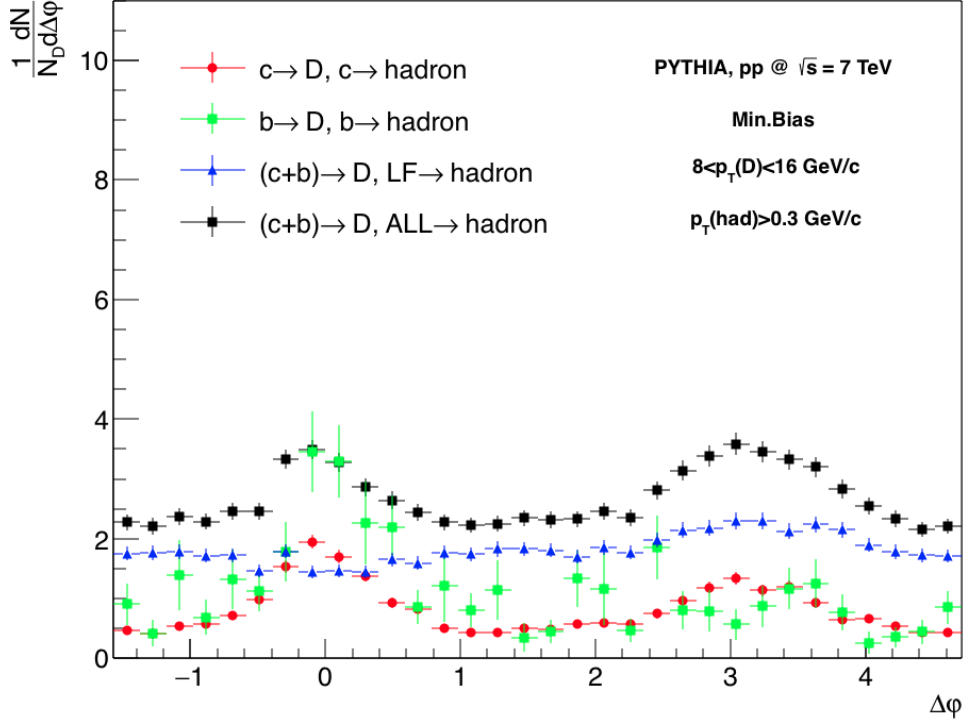


Figure 5.1: The azimuthal correlation distribution of D^{*+} mesons and charged particles studied differentially for different origins. The distribution is obtained from the minimum bias PYTHIA simulation at $\sqrt{s} = 7$ TeV, with $8 < p_T(D^{*+}) < 16$ GeV/c and $p_T(hadron) > 0.3$ GeV/c. The red distribution shows the correlations of a D^{*+} meson from a charm quark with charged tracks originating from a charm quark, the green distribution shows the correlations of a D^{*+} meson from a beauty quark with charged tracks originating from a beauty quark, the blue distribution depicts the correlations of a D^{*+} meson from a charm or beauty quark with charged tracks originating from a light quark or a gluon, while the black distribution illustrates the inclusive correlation of all D^{*+} mesons with all charged particles.

contributions, the same analysis has been performed on the heavy flavour enriched sample (LHC10f7a).

Figure 5.2 shows, as before, the azimuthal correlations of D^{*+} meson in the range $8 < p_T(D^{*+}) < 16$ GeV/c and associated tracks in the range $p_T(hadron) > 0.3$ GeV/c, obtained from the heavy flavour enriched sample, with the same colouring scheme for different origins as described above. From this figure, a clearer picture on the shape of the various contribution can be obtained. The correlations for the charm origin case are qualitatively the same, but less fluctuating because of the higher available statistics. For the beauty origin case, the correlations show a less fluctuating near-side peak with similar properties

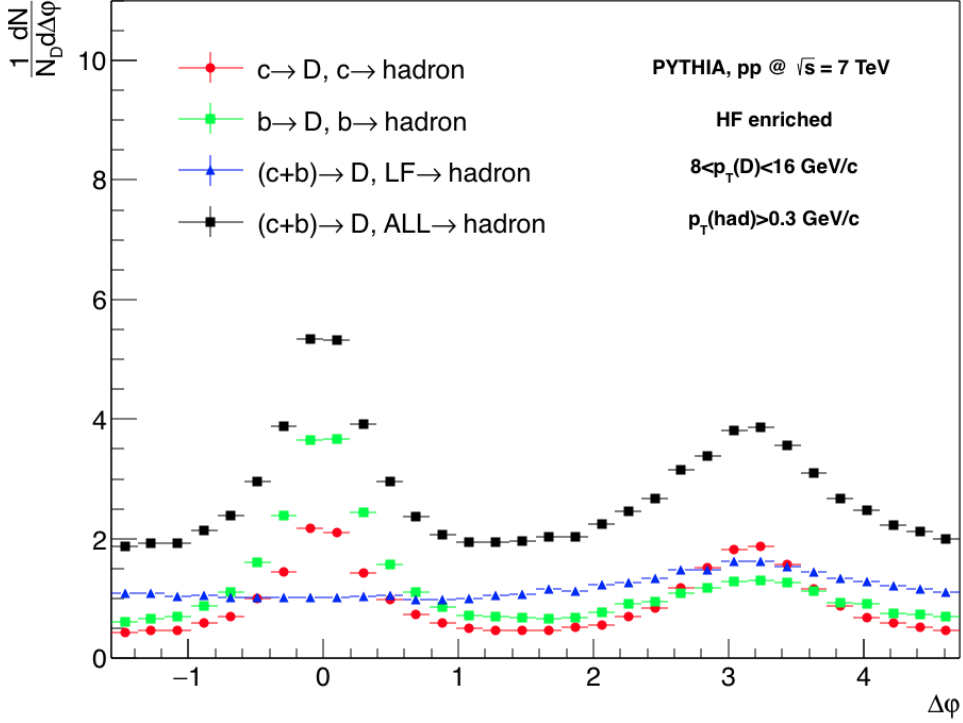


Figure 5.2: Same as Figure 5.1 but for different Monte Carlo sample. The distributions are obtained from the heavy flavour enriched PYTHIA simulation (LHC10f7a).

as the one from the figure 5.1. The beauty-origin case shows again a stronger correlation on the near side than the one from originating from charm. On the away side, the correlation peak is evident also for the beauty origin case. Compared to the charm case, it is lower and wider. For what concerns the non heavy flavour contribution, there is no contribution to the correlations on the near-side, while an away side correlation is present, although not as strong as the correlation for the two heavy flavour cases.

As described in the analysis procedure in chapter 4, the decay products of the D^{*+} are removed from the correlation. In a decay of a beauty meson, the final state can contain other charged particles together with the (feed-down) D^{*+} (charged leptons in a case of a semi-leptonic decay of the B meson, pions in the case of a hadronic decay...). These charged particles are not removed from the distribution shown in figure 5.2, and they contribute mostly to the near-side. A qualitative differential study of these contributions to the correlations of feed-down D^{*+} and charged particles is shown in figure 5.3: the left panel shows the correlation distributions of a D^{*+} with the heavy quark fragmentation products (i.e., excluding the decay products of any open-heavy flavour hadron), while the right panel shows the correlations with the decay products

5.1. DIFFERENT CONTRIBUTIONS TO THE AZIMUTHAL ANGULAR CORRELATIONS OF HADRONS AND D MESONS

of a B meson or the anti-D meson, excluding the other particles produces in the heavy quark fragmentation. In the latter case, it is immediately visible that on the near side the charm (D meson contribution) is flat at zero because of the daughter removal procedure, while the beauty case presents a very narrow and strong correlation due to the other particles produced in the B-meson decay together with the D^{*+} . When considering the fragments only, the charm contribution shows a stronger correlation than the beauty case. The different sources have been studied differentially as a function of the D^{*+} p_T , in the three p_T -bin considered for the analysis on data: in the four panels of figure 5.4, the black points represent the correlations of D^{*+} mesons with $3 < p_T(D^{*+}) < 5$ GeV/c, the red points represent the correlations of D^{*+} mesons with $5 < p_T(D^{*+}) < 8$ GeV/c, the blue points represent the correlations of D^{*+} mesons with $8 < p_T(D^{*+}) < 16$ GeV/c. All the plots in the figure are for associated tracks with $p_T(hadron) > 1$ GeV/c. The left upper panel shows the correlations for the charm origin case, the right upper panel shows the correlations for the beauty origin case, the left lower panel shows the correlations for the non heavy flavour origin case, the right lower panel shows the correlations for the inclusive case.

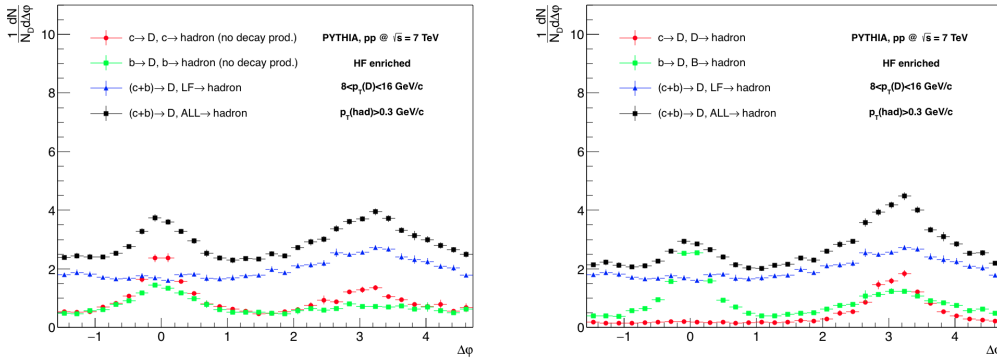


Figure 5.3: The azimuthal correlation distribution of D^{*+} mesons and charged particles studied differentially for different origins. The distribution is obtained from the charm enriched PYTHIA simulation at $\sqrt{s} = 7$ TeV, with $8 < p_T(D^{*+}) < 16$ GeV/c and $p_T(hadron) > 0.3$ GeV/c. Left panel: The red distribution shows the correlations of a D^{*+} meson from a charm quark with other particles produced in the fragmentation of the charm quark, the green distribution shows the correlations of a D^{*+} meson from a beauty quark with the products of the beauty quark, the blue distribution shows the correlations of a D^{*+} meson from a charm or beauty quark with charged tracks originating from a light quark or a gluon, while the black distribution shows the inclusive correlation of all D^{*+} mesons with all the fragments of different quarks. Right panel: similar to the left panel, but in this case the correlations for the charm origin (red distribution) and beauty origin (blue distribution) includes only the decay products of the charm/beauty a meson or baryon

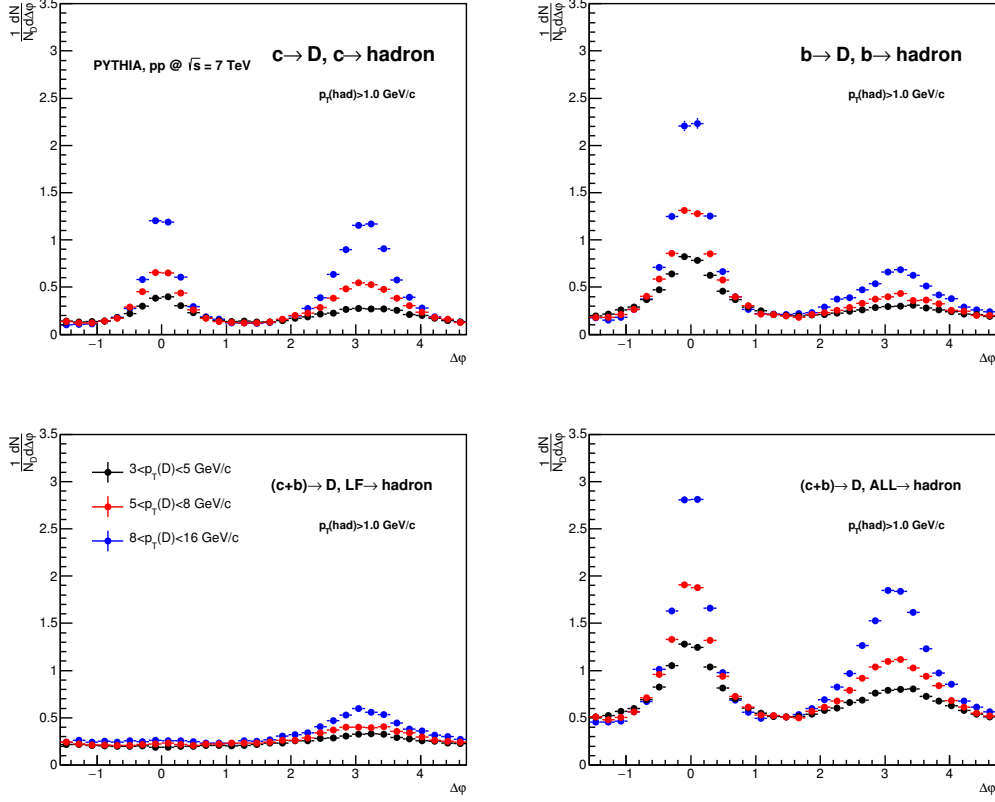


Figure 5.4: Dependence of the flavour-differential correlation distributions on the p_T of the D^{*+} mesons. The distributions are extracted from the LHC10f7a Monte Carlo sample of pp collisions at $\sqrt{s} = 7$ TeV. The upper left panel shows the correlations of D^{*+} mesons and associated tracks originating from a charm quark. The upper right panel shows the correlations of D^{*+} mesons and associated tracks originating from a beauty quark. The bottom left panel shows the correlations of D^{*+} mesons originating from a charm or beauty quark and associated tracks originating from light flavours. The bottom right panel shows the correlations of D^{*+} mesons originating from a charm or beauty quark and associated tracks originating from all possible flavours. The black distribution represents the range $3 < p_T(D^{*+}) < 5$ GeV/c, the red distribution represents the range $5 < p_T(D^{*+}) < 8$ GeV/c and the blue distribution represents the range $8 < p_T(D^{*+}) < 16$ GeV/c. For all the cases, the associated tracks are selected with $p_T(\text{hadron}) > 1$ GeV/c.

5.2. MONTE CARLO CLOSURE TEST

A strong p_T -dependence is observed on the near and away side correlations for the beauty and origin case, and it is also reflected in the inclusive distribution. The correlation strengthen with increasing p_T of the D meson. This is in agreement with the expected picture of a larger number of fragments with $p_T(hadron) > 1 \text{ GeV}/c$ with a higher p_T of the parton. The same is observed in the non heavy-flavour origin case, where the away-side peak shows the same dependence.

It is also important to notice that the minimum of the correlation (the pedestal), which can be estimated from the transverse region (i.e. around $\Delta\varphi \sim \pi$), shows no dependence on the trigger particle p_T , for any flavour differential origin case.

5.2 Monte Carlo closure test

In order to check the correction procedure discussed in chapter 4, the analysis was performed on the simulated Monte Carlo sample, including of the detector response (i.e. at reconstruction level). The obtained distributions are corrected for the D meson efficiency, associated track efficiency and event mixing, as described in chapter 4.

The distributions are produced as follows:

1. A D^{*+} meson is identified as a reconstructed object of a kaon and two pions. The Monte Carlo information of such an object is checked and is required to be a D^{*+} . Additionally, the kaon and one of the pions are required to be decay products of a D^0 , which is itself the decay product of the D^{*+} . This makes sure that the D^{*+} mesons, decaying according to the decay channel shown in equation 4.1 are selected. The number of triggers is estimated directly by counting them each time a “Monte Carlo-true” D^{*+} is found.
2. All the reconstructed charged tracks that pass the standard selections described in section 4.4 are correlated with the Monte Carlo reconstructed D^{*+} mesons.
3. The distribution is corrected for D^{*+} meson and single track reconstruction efficiency, as described in sections 4.6 and 4.7, respectively .
4. As the D^{*+} is identified by its Monte Carlo identity, there is no combinatorial background to subtract.
5. The obtained distribution is corrected for event mixing, as described in section 4.5.

The subtraction of the feed-down was not implemented in this checking procedure. Instead, the D^{*+} mesons and the charged tracks are separated by different origins as described in section 5.1. Once the flavour-differential reconstructed distributions are obtained, they are compared to the distributions

CHAPTER 5. MONTE CARLO ANALYSIS

obtained at the generated level shown in section 5.1. The check has been done both for the pp and p-Pb analysis, using the heavy-flavour enriched samples. For the pp analysis, the comparison of the reconstructed distribution to the Monte Carlo truth one is done for the three p_T intervals of the D^{*+} meson. For the associated tracks, three intervals are considered, i.e. $0.3 < p_T < 1$ GeV/ c , $p_T > 1$ GeV/ c , and the integrated range $p_T > 0.3$ GeV/ c . The figures 5.5, 5.6, 5.7 and 5.8 show all the nine considered p_T -range combinations of D^{*+} mesons and associated tracks, for the charm-origin case, beauty-origin case, non-heavy-flavour origin case and inclusive-origin case, respectively. Each column represents a different p_T of the D^{*+} (the left column shows the range $3 < p_T(D^{*+}) < 5$ GeV/ c , the middle column the range $5 < p_T(D^{*+}) < 8$ GeV/ c , while the right column shows the range $8 < p_T(D^{*+}) < 16$ GeV/ c).

The first row shows the fully integrated p_T -range for the associated hadrons, i.e. $p_T(hadron) > 0.3$ GeV/ c . The middle and the bottom rows show the correlations more differentially, namely the middle row shows the range $0.3 < p_T(hadron) < 1$ GeV/ c while the bottom one shows the range $p_T(hadron) > 1$ GeV/ c . In all plots, the blue distribution shows the generated Monte Carlo distribution (the same as described in section 5.1), while the red points represent the distribution obtained after the reconstruction, with all the corrections discussed above being implemented.

For all the four considered cases, and all the considered p_T cases, there is a very good agreement between the red and the blue distributions, meaning that the generated distributions are reproduced after applying the corrections discussed in chapter 4.

To quantify the compatibility of the two distributions, the ratio of the reconstructed over the generated distribution has been performed for all the considered cases. This is shown in the figure 5.9. The panels are distributed following the same scheme as in the case of the figures 5.5, 5.6, 5.7 and 5.8.

It is immediately evident that for all the cases, the points are fluctuating around unity. No evident structure is present in the ratios, showing that the shapes of the reconstructed and the generated correlation distributions are very well compatible.

Given the flatness of the ratio plots they have been fitted with a constant function, and the average ratios are reported in the table 5.1. All the values of the constants extracted from the fits fluctuate in a range 5 % around the unity. The ratios are, however, compatible with unity within 2σ , given the uncertainty.

The same check has been performed for the p-Pb data sample, where the Monte Carlo simulation has been done on the LHC13d3 data sample.

The check has been performed in the two considered p_T intervals of the D^{*+} , $5 < p_T(D^{*+}) < 8$ GeV/ c and $8 < p_T(D^{*+}) < 16$ GeV/ c ¹, while the associated tracks are selected in the same range as in the pp simulations. Figure 5.10

¹The case $3 < p_T(D^{*+}) < 5$ GeV/ c is not considered in this check as this p_T bin is not presented in this thesis in the p-Pb analysis, due to the lack of statistics

5.2. MONTE CARLO CLOSURE TEST

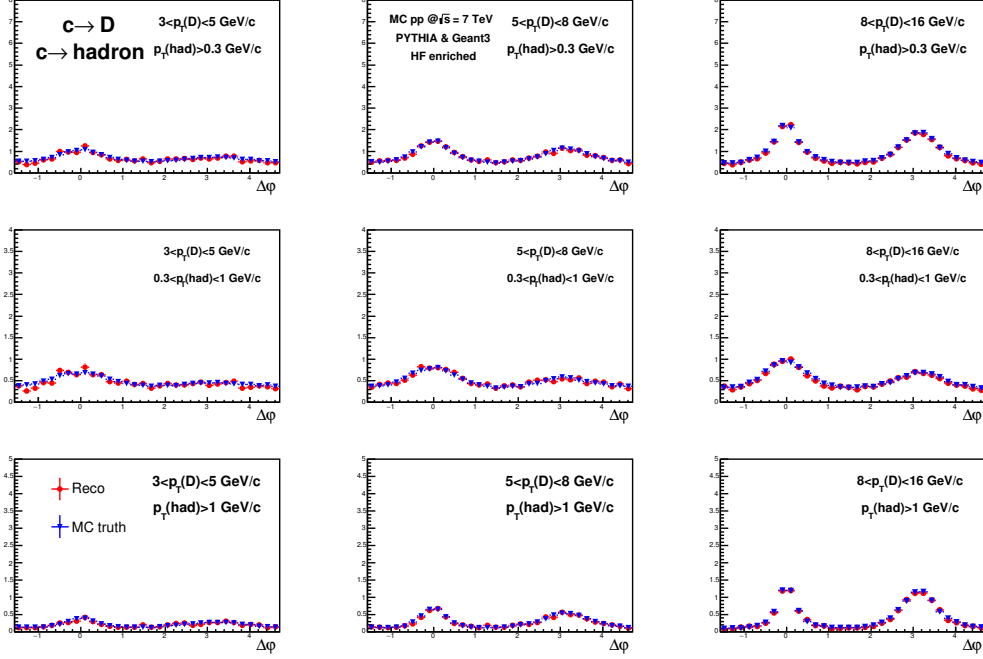


Figure 5.5: Compatibility of the reconstructed and corrected distributions (red points) with the distributions at generation level for D^{*+} mesons and associated tracks originating from a charm quark. The panels show different p_T combinations of D^{*+} and associated tracks. The simulation is done on the LHC10f7a, pp related, Monte Carlo sample at $\sqrt{s} = 7$ TeV. The left column shows the range $3 < p_T(D^{*+}) < 5$ GeV/c, the middle column the range $5 < p_T(D^{*+}) < 8$ GeV/c, while the right column shows the range $8 < p_T(D^{*+}) < 16$ GeV/c. The first row shows the fully integrated p_T -range for the associated hadrons, i.e. $p_T(hadron) > 0.3$ GeV/c. The middle row shows the range $0.3 < p_T(hadron) < 1$ GeV/c. The bottom row shows the range $p_T(hadron) > 1$ GeV/c.

illustrates the ratio of the corrected reconstructed distributions over the generated ones. For the ratios in the case of correlations with charged tracks with $p_T(hadron) > 1$ GeV/c, a near-side residual structure peaking up to 15 % for the beauty origin case (blue distribution in figure 5.10). Table 5.2 summarises the average values of the ratios. A discrepancy up to 8 % is present for the low p_T tracks ($0.3 < p_T(hadron) < 1$ GeV/c) for the non heavy flavour origin case (green distribution in figure 5.10), which then decreases to 6% in the inclusive origin case.

As the origin of the discrepancy has not yet been understood, it has been assigned as a contribution to the systematic uncertainties (described in chapter 6)

CHAPTER 5. MONTE CARLO ANALYSIS

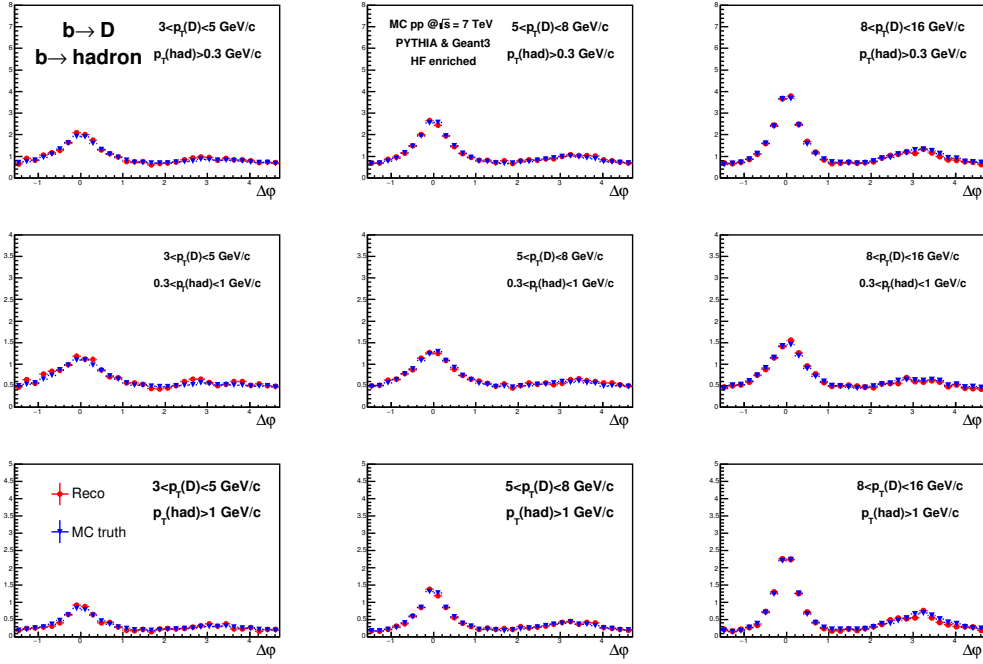


Figure 5.6: Same as Figure 5.5, but for D mesons and charged particles originating from a beauty quark.

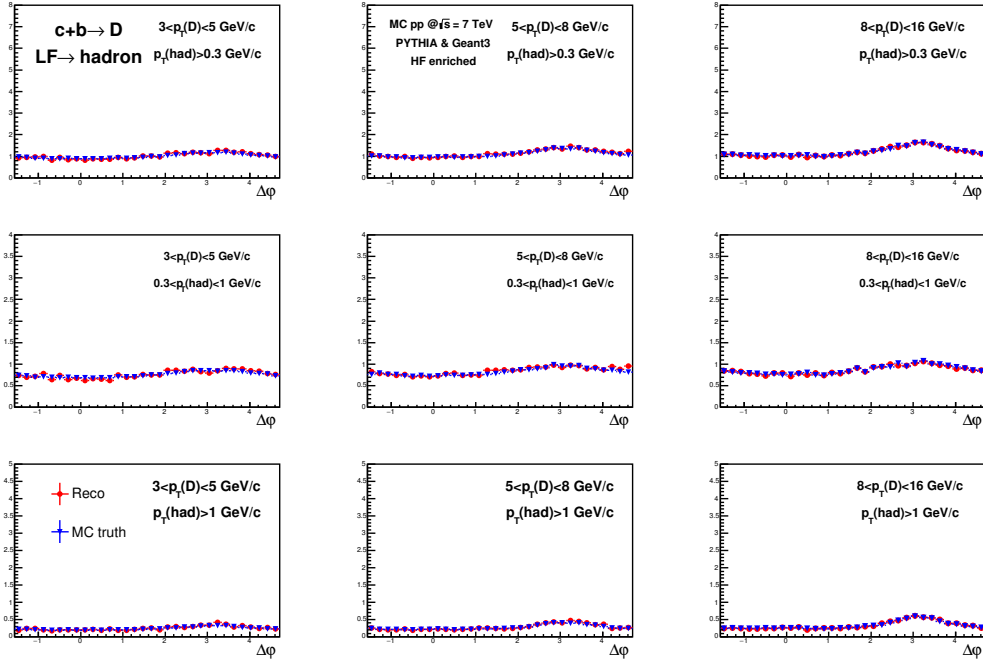


Figure 5.7: Same as Figure 5.5, but for D mesons originating from both charm and beauty quarks and charged particles not originating from a beauty quark (non heavy flavour origin).

5.2. MONTE CARLO CLOSURE TEST

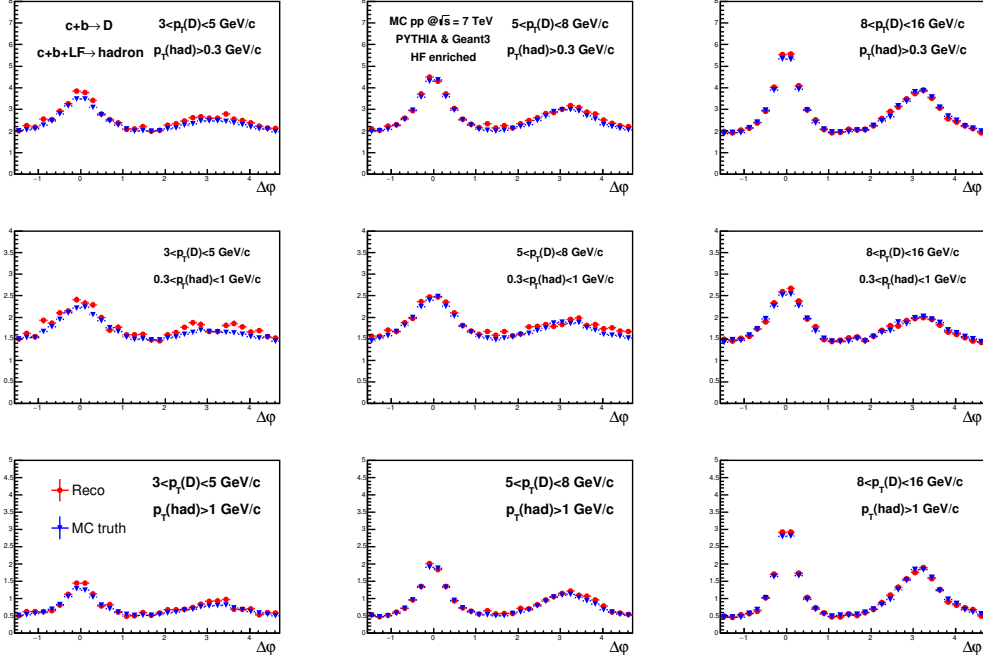


Figure 5.8: Same as Figure 5.5, but for D mesons originating from both charm and beauty quarks and no selection on the origin of the charged particles.

$p_T (D^{*+})$ range	3 – 5 GeV/c	5 – 8 GeV/c	8 – 16 GeV/c
p_T hadron 0.3-1 GeV/c	c-origin 0.96 ± 0.02	1.01 ± 0.02	0.97 ± 0.01
	b-origin 1.04 ± 0.02	1.02 ± 0.01	0.99 ± 0.01
	nonHf 1.01 ± 0.01	1.02 ± 0.01	1.00 ± 0.01
	Inclus 1.05 ± 0.01	1.04 ± 0.01	1.01 ± 0.01
p_T hadron >1 GeV/c	c-origin 0.98 ± 0.03	0.99 ± 0.02	0.98 ± 0.02
	b-origin 1.02 ± 0.02	1.02 ± 0.02	0.99 ± 0.01
	nonHf 1.04 ± 0.02	1.04 ± 0.02	1.02 ± 0.01
	Inclus 1.04 ± 0.01	1.05 ± 0.01	1.02 ± 0.01
p_T hadron >0.3 GeV/c	c-origin 0.97 ± 0.02	1.01 ± 0.02	0.98 ± 0.01
	b-origin 1.04 ± 0.02	1.02 ± 0.01	0.99 ± 0.01
	nonHf 1.02 ± 0.01	1.03 ± 0.01	1.00 ± 0.01
	Inclus 1.05 ± 0.01	1.04 ± 0.01	1.01 ± 0.01

Table 5.1: Average ratio of the corrected distributions at reconstruction level with the distributions at the generation level, for all the considered p_T -ranges and the different sources, for pp collisions at $\sqrt{s} = 7$ TeV.

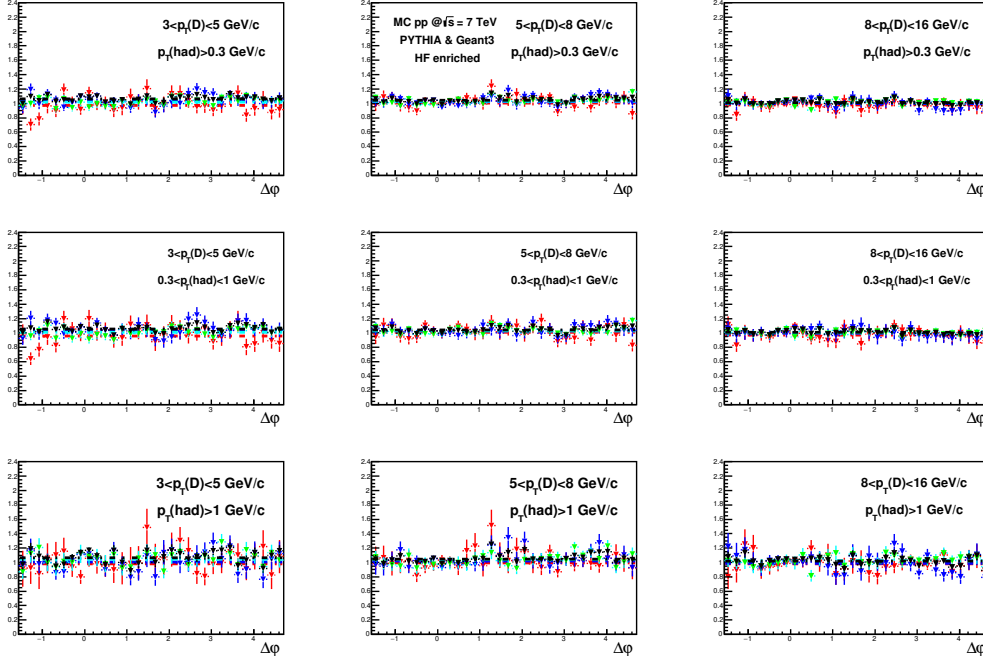


Figure 5.9: Ratio of the reconstructed and corrected distributions (red points) and to the distributions at generation level for D^{*+} mesons and associated tracks originating from a charm quark (red points), for D^{*+} mesons and associated tracks originating from a beauty quark (green points), for D^{*+} mesons originating from a charm or beauty quark and associated tracks originating from light flavours (blue points) and D^{*+} mesons originating from a charm or beauty quark and associated tracks originating from all possible flavours (black points). The simulated sample is the LHC10f7a for pp collisions at $\sqrt{s} = 7$ TeV. The panels show different p_T combinations of D^{*+} and associated tracks. The left column shows the range $3 < p_T(D^{*+}) < 5$ GeV/ c , the middle column the range $5 < p_T(D^{*+}) < 8$ GeV/ c , while the right column shows the range $8 < p_T(D^{*+}) < 16$ GeV/ c . The first row shows the fully integrated p_T -range for the associated hadrons, i.e. $p_T(\text{hadron}) > 0.3$ GeV/ c . The middle row shows the range $0.3 < p_T(\text{hadron}) < 1$ GeV/ c . The bottom row shows the range $p_T(\text{hadron}) > 1$ GeV/ c .

5.2. MONTE CARLO CLOSURE TEST

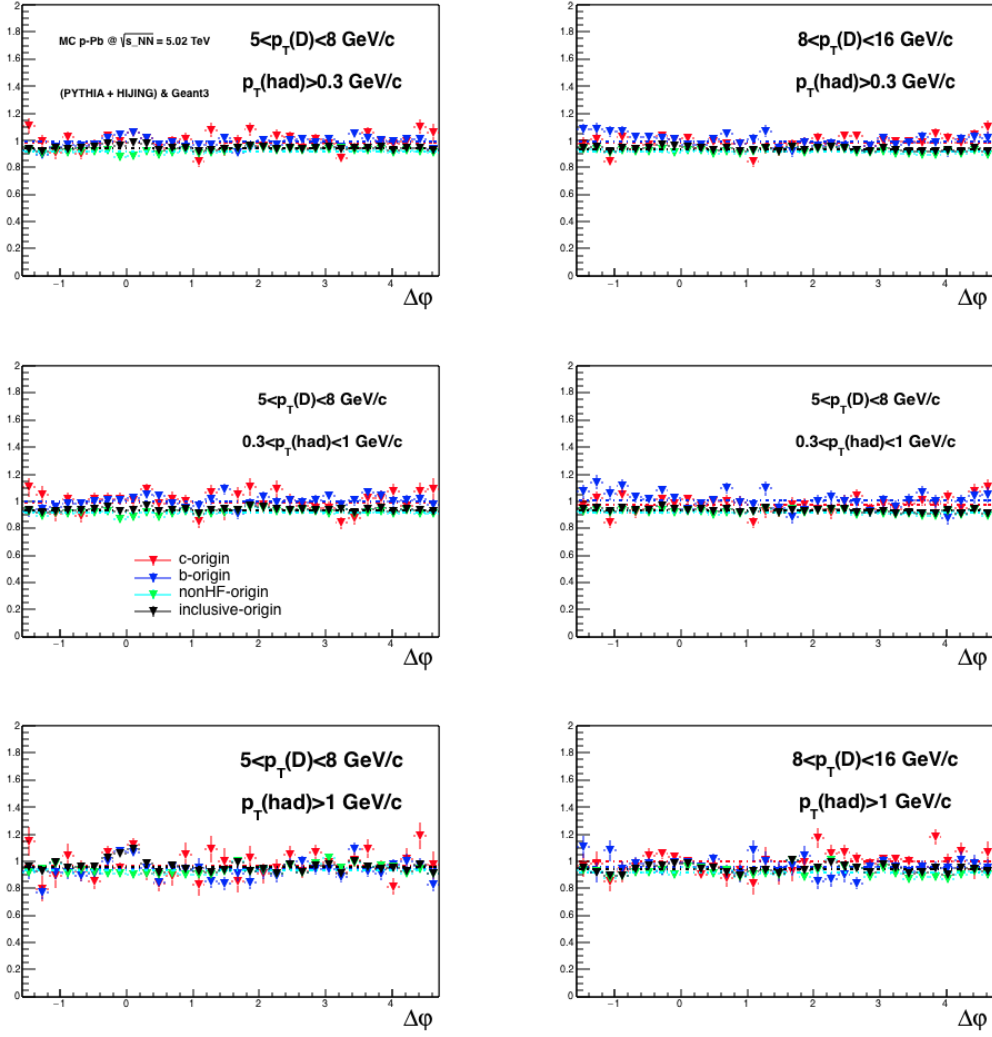


Figure 5.10: Same as 5.9, but for the different Monte Carlo sample used. The simulation is the LHC13d3 (p-Pb related) Monte Carlo sample at $\sqrt{s_{NN}} = 5.02$ TeV

$p_T(D^{*+})$ range	5 – 8 GeV/ c	8 – 16 GeV/ c
p_T hadron 0.3-1 GeV/ c	c-origin 0.99 ± 0.01	0.98 ± 0.01
	b-origin 1.00 ± 0.01	1.01 ± 0.01
	nonHf 0.92 ± 0.01	0.92 ± 0.01
	Incl 0.94 ± 0.01	0.93 ± 0.01
p_T hadron >1 GeV/ c	c-origin 0.99 ± 0.01	0.98 ± 0.02
	b-origin 1.02 ± 0.02	0.99 ± 0.01
	nonHf 1.04 ± 0.02	1.02 ± 0.01
	Incl 1.05 ± 0.01	1.02 ± 0.01
p_T hadron >0.3 GeV/ c	c-origin 0.97 ± 0.01	0.99 ± 0.01
	b-origin 0.95 ± 0.01	0.96 ± 0.01
	nonHf 0.93 ± 0.01	0.92 ± 0.01
	Incl 0.96 ± 0.01	0.94 ± 0.01

Table 5.2: Average ratio of the corrected distributions at reconstruction level with the distributions at the generation level, for all the considered p_T -ranges and the different sources, for p-Pb collisions at $\sqrt{s_{NN}} = 5.02$ TeV.

5.3 Event mixing normalisation

The limited geometrical acceptance of the ALICE detector along the beam axis affects the correlation distribution by introducing a triangular shape in the $\Delta\eta$ correlation. One of the main roles of the event-mixing correction (described in section 4.5) is to account for this effect. The distributions obtained using the event-mixing technique reproduce the triangular shape occurring due to the limited acceptance. The normalisation of the distribution is performed to the value of the bin $(\Delta\varphi, \Delta\eta) = (0, 0)$, as shown in equation 4.11.

The rationale behind this normalisation strategy originates from two-particle correlation measurements [29].

Namely, in hadron-hadron correlations, the associated particles that travel in the same direction of the trigger particle (i.e. when $(\Delta\varphi, \Delta\eta) = (0, 0)$) experience the same detector conditions and acceptance (this situation is schematically represented in the cartoon shown in left panel of figure 5.11). Therefore, in this case, the pair-efficiency equals 1, justifying the normalisation strategy. For the D-hadron azimuthal correlation measurements, the same normalisation strategy is used, although the same rationale cannot be applied. The right panel of figure 5.11 illustrates the problem. The D meson is a reconstructed object, where two or more decay particles are used to measure its direction. The associated track flying in the same direction as the D meson

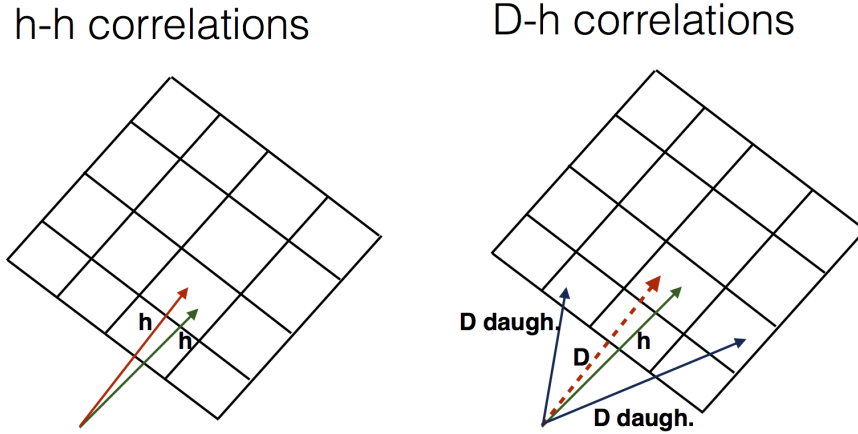


Figure 5.11: Cartoon illustrating the possible bias to the normalisation of the even-mixing distribution. A track that goes in the same direction as the trigger track in hadron-hadron correlations (left panel) experiences the same detector conditions and acceptance as the trigger particle. The same rationale does not work when D mesons are used as triggers, as they are reconstructed objects of two (three) tracks.

CHAPTER 5. MONTE CARLO ANALYSIS

(i.e. when $(\Delta\varphi, \Delta\eta) = (0, 0)$), might not experience the same detector conditions and acceptance as the D meson daughters, that are the particles that are directly reconstructed by the detector. In this case, the D meson-hadron pair-efficiency could also differ from unity in the bin $(\Delta\varphi, \Delta\eta) = (0, 0)$. However, due to the symmetry of the problem, the bin $(\Delta\varphi, \Delta\eta) = (0, 0)$ represents the point with the maximum-pair efficiency. For this analysis, the pair efficiency has been assumed to be equal to one, and the validity of this assumption has been tested using the Monte-Carlo simulations. For this purpose, the analysis has been repeated at the generated Monte-Carlo level after removing the acceptance requirements and not applying the event mixing correction. This distribution should be reproduced by the distributions with the acceptance cut that are corrected with the event-mixing technique. Figure 5.12 shows the distributions obtained at the generated level without acceptance cuts and without the application of the event mixing correction (black points) compared to the distribution at generated level with the acceptance cut and the mixing event correction (red points) and the same distribution obtained at reconstructed Monte-Carlo level (blue points).

The figure is split in three panels, the left one representing the p_T -bin $3 < p_T(D^{*+}) < 5$ GeV/ c , the middle one the p_T -bin $5 < p_T(D^{*+}) < 8$ GeV/ c and the right panel the bin $8 < p_T(D^{*+}) < 16$ GeV/ c . For all the three considered cases, the distributions are compatible within uncertainties. The compatibility gets better with increasing p_T of the D^{*+} . This can be explained as due to the stronger collimation of the D^{*+} meson daughter at higher transverse momenta.

5.3. EVENT MIXING NORMALISATION

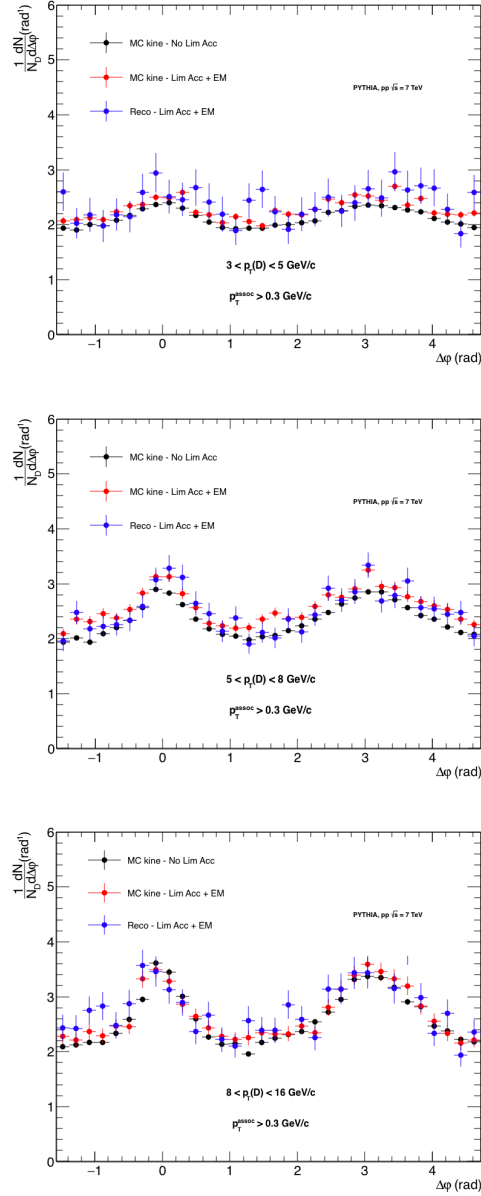


Figure 5.12: Compatibility of correlations at generated level without any acceptance selection (black markers), generated level with limited acceptance selection (red markers) and at reconstructed level with the applied corrections (blue markers), for $3 < p_T(D^{*+}) < 5 \text{ GeV}/c$ in the upper panel, $5 < p_T(D^{*+}) < 8 \text{ GeV}/c$ in the middle panel and $8 < p_T(D^{*+}) < 16 \text{ GeV}/c$ in the lower panel. The associated tracks are selected with $p_T^{assoc} > 0.3 \text{ GeV}/c$.

Systematic uncertainties

For the correlation analyses presented in this thesis, the systematic uncertainties have been estimated for the azimuthal correlation $\Delta\varphi$ distribution as well as for the correlation parameters extracted from the fits (correlation yields, widths and level of the baseline).

There are two main contributions to the systematic uncertainties in the azimuthal correlation $\Delta\varphi$:

- $\Delta\varphi$ -correlated systematic uncertainties: systematic uncertainties that are $\Delta\varphi$ -independent, i.e. the estimated value is the same for each measured point in $\Delta\varphi$. Those are all the systematic uncertainties related to the D^{*+} meson yield extraction, associated track selection and secondary track contamination.
- $\Delta\varphi$ -uncorrelated systematic uncertainties: systematic uncertainties that are $\Delta\varphi$ -dependent, i.e. the estimated value is computed for each measured point in $\Delta\varphi$. Those are the systematic uncertainties related to the beauty-feed down correction and the Monte Carlo closure test.

The $\Delta\varphi$ -correlated and $\Delta\varphi$ -uncorrelated uncertainties together with the definition of the baseline are used to estimate the uncertainties on the correlation strengths estimation (fitting procedure). These are discussed later in section 7.6.1.

6.1 Azimuthal correlation distribution systematic uncertainties

This section presents the evaluation of the systematic uncertainties for the azimuthal correlation distributions. They have been estimated separately for the pp and the p-Pb analyses.

Different contributions to the systematic uncertainties have been considered, namely the systematic uncertainties due to:

- the D^{*+} meson signal (yield) extraction
- the subtraction of the correlations from the combinatorial background

CHAPTER 6. SYSTEMATIC UNCERTAINTIES

- the D^{*+} meson efficiency correction (estimated via cut variation)
- the single track efficiency correction
- the purity correction
- the subtraction of correlations originating from a D^{*+} meson that is a decay product of a B hadron (feed-down)
- missing or non understood effect estimated from the Monte Carlo closure test

Table 6.1 summarises the estimated values of the systematic uncertainties for the azimuthal correlation distributions for different sources, for the pp and p-Pb analyses. In the next subsections, the evaluation of the systematics for

Source $p_T(D^{*+})$ (GeV/c)	3-5	pp 5-8	8-16	p-Pb 5-8	8-16
Yield extraction	$\pm 5\%$	$\pm 5\%$	$\pm 10\%$	$\pm 5\%$	$\pm 5\%$
Background subtraction	$\pm 10\%$	$\pm 10\%$	$\pm 10\%$	$\pm 5\%$	$\pm 10\%$
Cut variation	$\pm 10\%$	$\pm 10\%$	$\pm 10\%$	$\pm 5\%$	$\pm 10\%$
Tracking efficiency	$+10\%$ -5%	$+10\%$ -5%	$+10\%$ -5%	$\pm 4\%$	$\pm 4\%$
Track sample purity	$\pm 5\%$	$\pm 5\%$	$\pm 5\%$	$\pm 3\%$	$\pm 3\%$
Feed-down subtraction	$\Delta\varphi$ dependent			$\Delta\varphi$ dependent	
MC closure test	1%	1%	1%	-5%	-5%

Table 6.1: Summary of the different systematic uncertainties for the $\Delta\varphi$ distribution. See section 6.1.6 for values of the feed-down subtraction contribution.

every single source presented in table 6.1 will be discussed¹. Unless differently specified, in the following sections, all the presented plots relative to the pp analysis show a three panel structure representing the three different p_T -bins considered in the analysis (left $3 < p_T(D^{*+}) < 5$ GeV/c , middle $5 < p_T(D^{*+}) < 8$ GeV/c and right $8 < p_T(D^{*+}) < 16$ GeV/c). For the plots relative to the p-Pb analysis on the other hand, only two p_T -bins are shown (left $5 < p_T(D^{*+}) < 8$ GeV/c and right $8 < p_T(D^{*+}) < 16$ GeV/c).

¹but the Monte Carlo closure test, discussed in section 5.2

6.1. AZIMUTHAL CORRELATION DISTRIBUTION SYSTEMATIC UNCERTAINTIES

6.1.1 D^{*+} meson yield extraction

The first source of systematic uncertainty for the $\Delta\varphi$ distribution is the extraction of the D^{*+} yield from the invariant mass distribution. The yield enters in the correlation distribution as a normalisation factor as described in the section 4.2.2. Therefore, the systematic uncertainty due to the D meson yield extraction is expected to be completely correlated for the different points in the $\Delta\varphi$ distribution (statement valid only in first approximation²). To estimate the systematic uncertainty due to the signal extraction, the D^{*+} yields were calculated as follows

- using a different parametrisation of the background function;
- changing the width of the invariant mass distribution (i.e. by rebinning the invariant mass distribution);
- fitting the invariant mass distribution in a smaller range;
- counting the entries in the invariant mass region after the value of the background function has been subtracted.

No other modification to the procedure has been done.

Figure 6.1 shows the ratios of the correlation distributions obtained following the above-mentioned methods with the standard procedure for the yield extraction, for the pp analysis. It is done for the three considered p_T bins of the D^{*+} and for the integrated associated track p_T (i.e $p_T(hadron) > 0.3 \text{ GeV}/c$). As expected, no structure in $\Delta\varphi$ is present. The maximum discrepancy observed is of the order of 10% at the highest considered p_T -bin of the D^{*+} , while it is of the order of 5% for the lowest two p_T -bins. These values have been assigned as systematic uncertainty in the pp case. Figure 6.2 on the other hand shows the ratios of the correlation distributions obtained for the p-Pb analysis, following the same strategy as in the pp analysis. It is done for the two considered p_T -bins of the D^{*+} and for the integrated associated track p_T (i.e $p_T(hadron) > 0.3 \text{ GeV}/c$).

Also in this case, no structure in the $\Delta\varphi$ distribution is present. The maximum discrepancy shown is of the order of 5%, which has been taken as systematic uncertainty in the p-Pb case for all the two considered p_T -bins.

²In the yield extraction procedure, a different fit strategy might lead to the estimation of different widths of the correlation peak, therefore different invariant mass regions can be considered when computing the azimuthal correlations

CHAPTER 6. SYSTEMATIC UNCERTAINTIES

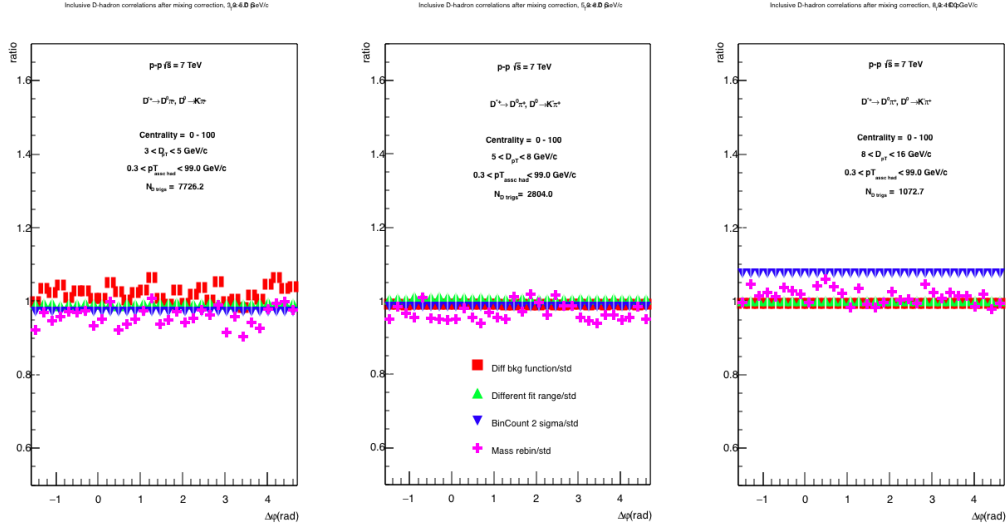


Figure 6.1: Ratio of the azimuthal correlation distribution with different D^{*+} yield extraction methods with respect to the standard strategy, for the pp analysis. The left panel shows the p_T range $3 < p_T(D^{*+}) < 5$ GeV/c, the middle panel the range $5 < p_T(D^{*+}) < 8$ GeV/c and the right panel the range $8 < p_T(D^{*+}) < 16$ GeV/c. The associated tracks are selected with $p_T(hadron) > 0.3$ GeV/c.

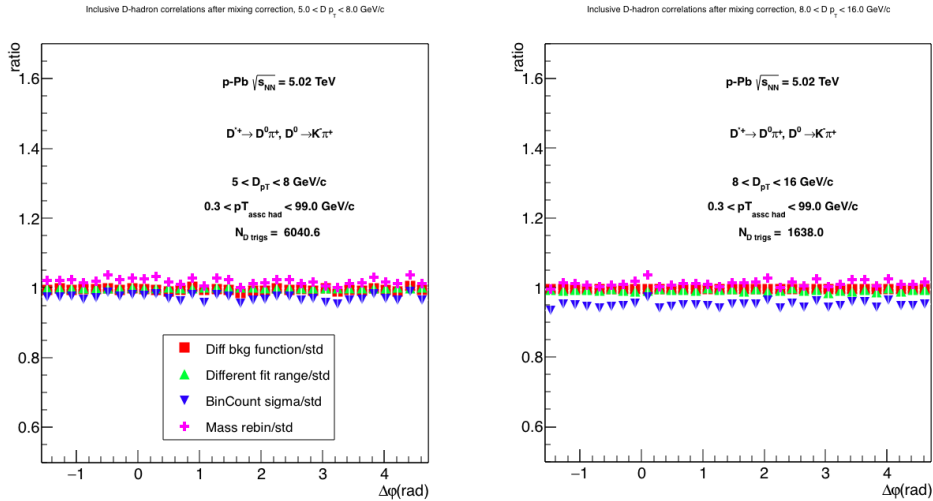


Figure 6.2: Same as figure 6.1, but for p-Pb collisions. The left panel shows the range $5 < p_T(D^{*+}) < 8$ GeV/c and the right panel the range $8 < p_T(D^{*+}) < 16$ GeV/c.

6.1.2 Background subtraction

The sideband background subtraction procedure has been repeated using a different range for the sideband estimation and has later been compared to the standard sideband estimation (right sideband in the $4-8\sigma$ region) to evaluate the systematic uncertainty. Although the azimuthal distribution of combinatorial background candidates with associated tracks is strongly correlated (as shown in figure 4.9) due to the jet topology, this contribution is also expected to be $\Delta\varphi$ -independent, as the structure of the background that is subtracted from the inclusive correlation distribution is expected to change only in total sum of entries and not in shape. The different correlation entries have been taken into account by the scale factor applied to the distribution of candidates from the sidebands, as described by equation 4.10). The background subtraction has been repeated selecting the sideband candidates in the following invariant mass regions

- $8-15\sigma$ at the right of the peak;
- $4-15\sigma$ at the right of the peak (the full available sideband region).

The quickly decreasing trend of the background distribution on the left-hand side of the invariant mass distribution of the D^{*+} does not allow a reliable estimation for the systematics using this sideband region.

No other modifications has been performed to the analysis procedure.

Figure 6.3 shows the ratios of the correlation distributions obtained following the above-mentioned methods with the standard procedure for the background subtraction, for the pp analysis. It is done for the three considered p_T bins of the D^{*+} and for the integrated associated track p_T , i.e $p_T(\text{hadron}) > 0.3$ GeV/ c .

As discussed before, no structure in $\Delta\varphi$ has been observed. The average shift of the points is estimated to be of the order of 10%, which has been taken as systematic uncertainty for this particular origin.

Figure 6.4 shows the same study done for the p-Pb analysis. No dependence in $\Delta\varphi$ is observed also in this case, as expected from the above discussion. A value of $\pm 5\%$ and $\pm 10\%$ has been assigned for the mid and high p_T , respectively.

6.1.3 D meson efficiency correction

A residual discrepancy between data and Monte-Carlo simulation might be present in the shapes of the variables used to perform the topological selection of the D^{*+} candidates. To estimate the systematic uncertainty due to this possible discrepancy, the analysis has been repeated changing the topological cuts on the D^{*+} reconstruction, loosening and tightening them with respect to the standard value. The reconstruction efficiency has been recomputed for each new cut combination and was applied to the analysis accordingly.

For each combination of cuts, a significant D meson peak was obtained, with

CHAPTER 6. SYSTEMATIC UNCERTAINTIES

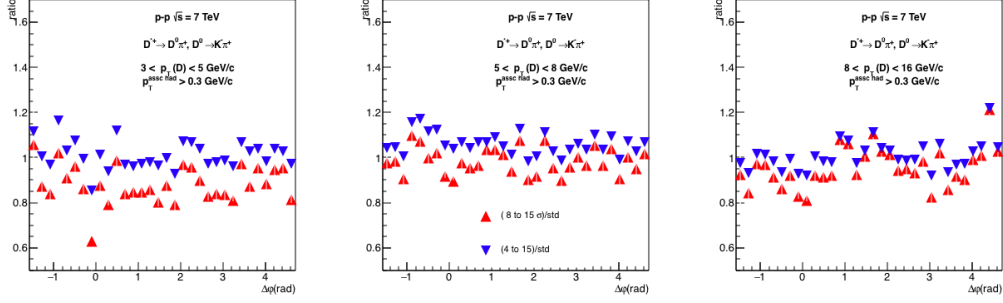


Figure 6.3: Ratio of the azimuthal correlation distribution obtained with different sideband estimation regions with respect to the standard $4\text{--}8\sigma$ range, in pp collisions. The left panel shows the p_T range $3 < p_T(D^{*+}) < 5 \text{ GeV}/c$, the middle panel the range $5 < p_T(D^{*+}) < 8 \text{ GeV}/c$ and the right panel the range $8 < p_T(D^{*+}) < 16 \text{ GeV}/c$. The associated tracks are selected with $p_T(\text{hadron}) > 0.3 \text{ GeV}/c$.

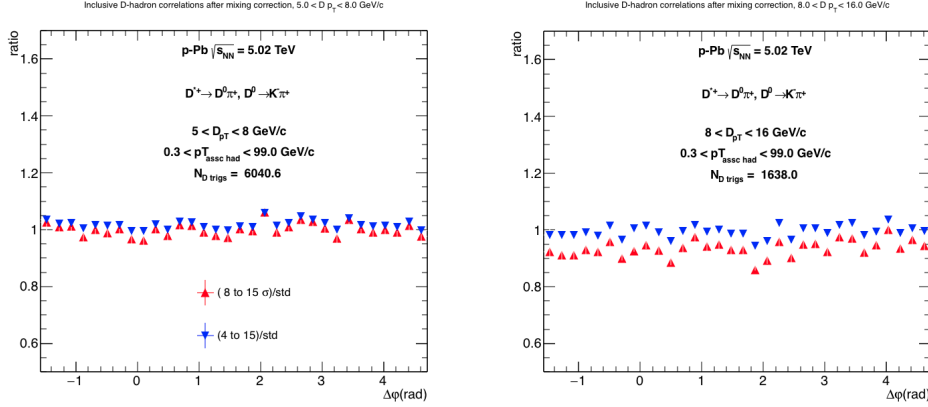


Figure 6.4: Same as figure 6.3, but for p-Pb collisions. The left panel shows the range $5 < p_T(D^{*+}) < 8 \text{ GeV}/c$ and the right panel the range $8 < p_T(D^{*+}) < 16 \text{ GeV}/c$.

raw yields varying by approximately of $\pm 20\%$ with respect to the standard cuts, while the combinatorial background changed up to a factor of two. This grants that the obtained correlation distributions are at least partially independent. The analysis has been repeated without any other further change.

Figures 6.5 and 6.6 show the ratio of $\Delta\varphi$ distributions obtained with a different D^{*+} topological selection with the $\Delta\varphi$ distribution obtained with the standard topological selection for the pp and p-Pb analysis, respectively. For both the cases the p_T^{hadron} has been selected to be $p_T > 0.3 \text{ GeV}/c$ in order to reduce the statistical fluctuations.

There is no evident structure in the ratios along $\Delta\varphi$, with the points fluctuating

6.1. AZIMUTHAL CORRELATION DISTRIBUTION SYSTEMATIC UNCERTAINTIES

on average within the range $\pm 10\%$, which has been assigned as systematic uncertainty for this source.

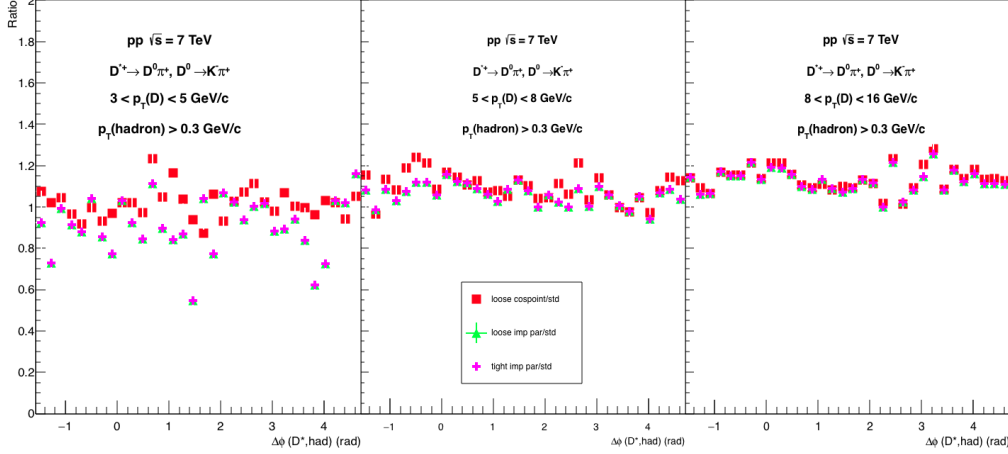


Figure 6.5: Ratio of the azimuthal correlation distribution obtained with different D meson topological selection cuts respect to the standard set, in pp collisions. The left panel shows the p_T range $3 < p_T(D^{*+}) < 5$ GeV/ c , the middle panel the range $5 < p_T(D^{*+}) < 8$ GeV/ c and the right panel the range $8 < p_T(D^{*+}) < 16$ GeV/ c . The associated tracks are selected with $p_T(hadron) > 0.3$ GeV/ c .

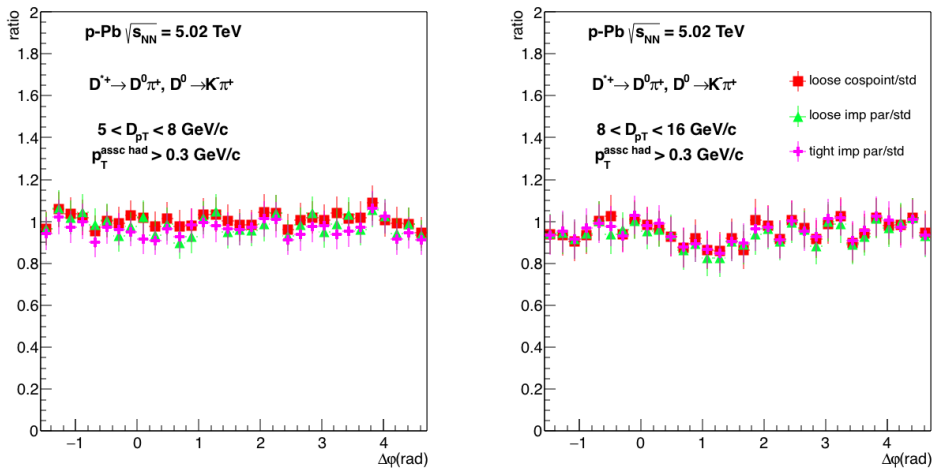


Figure 6.6: Same as figure 6.5, but for p-Pb collisions. The left panel shows the range $5 < p_T(D^{*+}) < 8$ GeV/ c and the right panel the range $8 < p_T(D^{*+}) < 16$ GeV/ c .

CHAPTER 6. SYSTEMATIC UNCERTAINTIES

6.1.4 Tracking efficiency

In a very similar way as for the D meson efficiency systematics (described in section 6.1.3), the systematic uncertainty for the associated track efficiency correction has been estimated by repeating the analysis after changing the selections on the associated tracks and recalculating the related single track efficiency maps. The used selections are reported in table 6.2.

The requirement of at least one hit in the pixel detector for the “TPC+ITS”

topological cut	default	TPC ONLY	TPC+ITS
Min ITS Clusters	3	0	3
Min TPC Clusters	70	70	70
ITS refit	No	No	Yes
TPC refit	Yes	Yes	Yes
Max DCA (z)	1cm	1cm	1cm
Max DCA (xy)	0.25cm	0.25cm	0.25cm
Hits SPD	No	No	> 1

Table 6.2: Three combinations of single tracks selections used for evaluating the systematic uncertainties.

cut option induces a non-flat ϕ distribution in pp, due to the inactivity of some pixel modules during the data-taking period. This induces modulations in the correlation distribution due to detector effects, which is accounted for by means of the event-mixing correction. Indeed, the mixed event distributions for this particular selection present a non-flat $\Delta\varphi$ trend together with the typical triangular shape along $\Delta\eta$. The ratios of the different azimuthal correlation distributions obtained with different selection cuts have been computed: Figure 6.7 illustrates them for the pp analysis. Different columns represent the different p_T -bins of the D^{*+} meson as described above. As this systematic uncertainty is related to the associated tracks, it has been studied for the integrated case, $p_T(\text{hadron}) > 0.3 \text{ GeV}/c$ (first row) and differentially, $0.3 < p_T(\text{hadron}) < 1 \text{ GeV}/c$ in the middle row $p_T(\text{hadron}) > 1 \text{ GeV}/c$ the low-ermost row.

Since no relevant structures along $\Delta\varphi$ appear, a flat ($\Delta\varphi$ -independent) asymmetrical systematic uncertainty of $^{+10\%}_{-5\%}$ in both all p_T bins has been estimated and assigned. Figure 6.8 shows the same study done for the p-Pb analysis, where the row and column disposition follow the same scheme as described for the pp case. In this case, the ratios are more stable, shifted by a maximum value of about 5%, which has been chosen as $\Delta\varphi$ and p_T independent systematic uncertainty in all the p_T bins

6.1. AZIMUTHAL CORRELATION DISTRIBUTION SYSTEMATIC UNCERTAINTIES

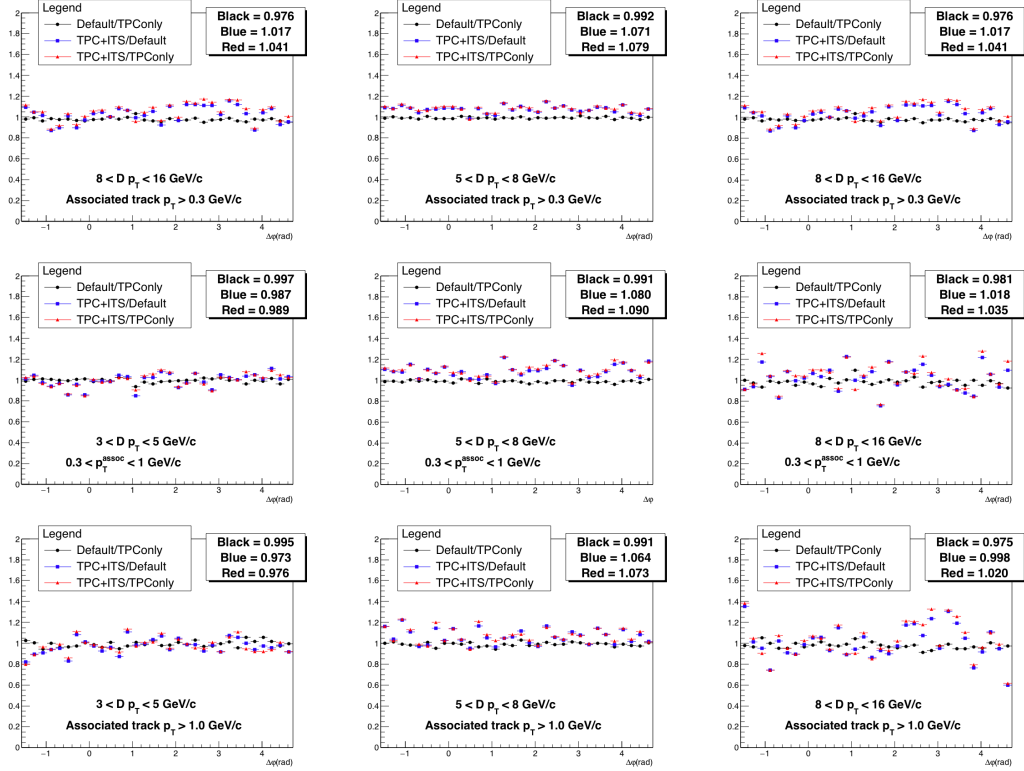


Figure 6.7: Ratio of the azimuthal correlation distribution in pp collisions obtained with different associated track selection cuts respect to the standard set. The left column shows the p_T range $3 < p_T(D^{*+}) < 5$ GeV/c, the middle column $5 < p_T(D^{*+}) < 8$ GeV/c and right column $8 < p_T(D^{*+}) < 16$ GeV/c. The upper row shows the range $p_T(hadron) > 0.3$ GeV/c, The middle row shows the range $0.3 < p_T(hadron) < 1$ GeV/c, the lower row the range $p_T(hadron) > 1$ GeV/c.

CHAPTER 6. SYSTEMATIC UNCERTAINTIES

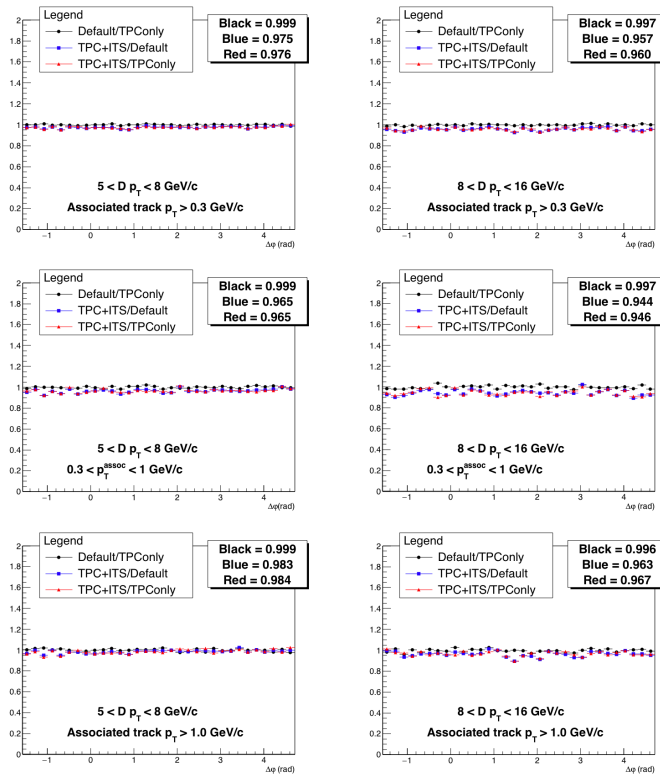


Figure 6.8: Same as figure 6.7, but for p-Pb collisions. The left column shows the $5 < p_T(D^{*+}) < 8 \text{ GeV/c}$ and right column $8 < p_T(D^{*+}) < 16 \text{ GeV/c}$.

6.1. AZIMUTHAL CORRELATION DISTRIBUTION SYSTEMATIC UNCERTAINTIES

6.1.5 Correction for contamination from secondary tracks

The purity correction, applied to the $\Delta\varphi$ distribution as described in section 4.9, should account for the residual contamination due to secondary tracks. To estimate the stability of the correction procedure, the analysis has been repeated after changing the DCA (distance of closest approach in the transverse plane) cut value and calculating the respective purity from the distribution shown in figure 4.20. The applied selections are as follows (in increasing order of secondary tracks contamination):

- $DCA_{XY} < 0.1$ cm
- $DCA_{XY} < 0.5$ cm
- $DCA_{XY} < 0.75$ cm
- $DCA_{XY} < 1.0$ cm

The obtained distributions are then compared to the standard one, $DCA_{XY} < 0.25$ cm. Figure 6.9 shows the ratios of the distributions obtained with the cuts listed above with respect to the standard one, for the pp analysis. The estimated uncertainty is 5%. Like figure 6.9, figure 6.10 shows the same ratios

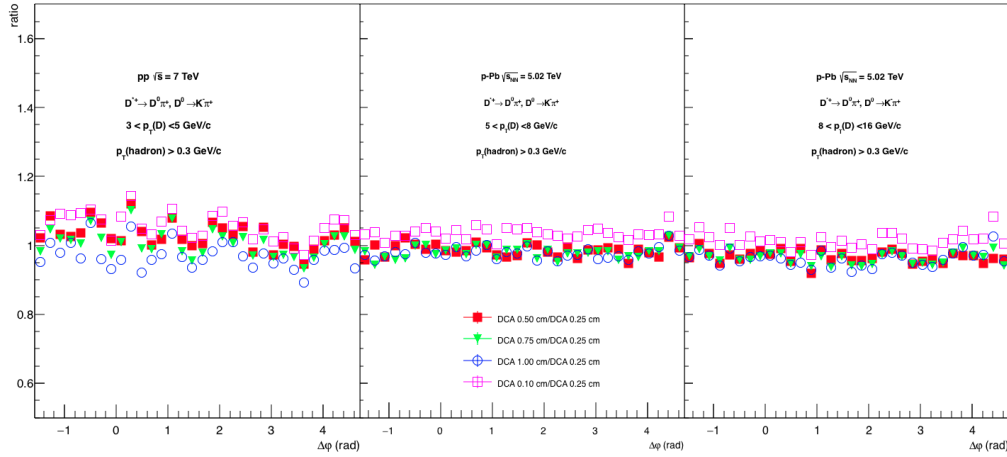


Figure 6.9: Ratio of the azimuthal correlation distribution obtained with different DCA_{XY} of associated track with respect to the standard range $DCA_{XY} < 0.25$ cm, in pp collisions. The left panel shows the p_T range $3 < p_T(D^{*+}) < 5$ GeV/c, the middle panel the range $5 < p_T(D^{*+}) < 8$ GeV/c and the right panel the range $8 < p_T(D^{*+}) < 16$ GeV/c. The associated tracks are selected with $p_T(hadron) > 0.3$ GeV/c.

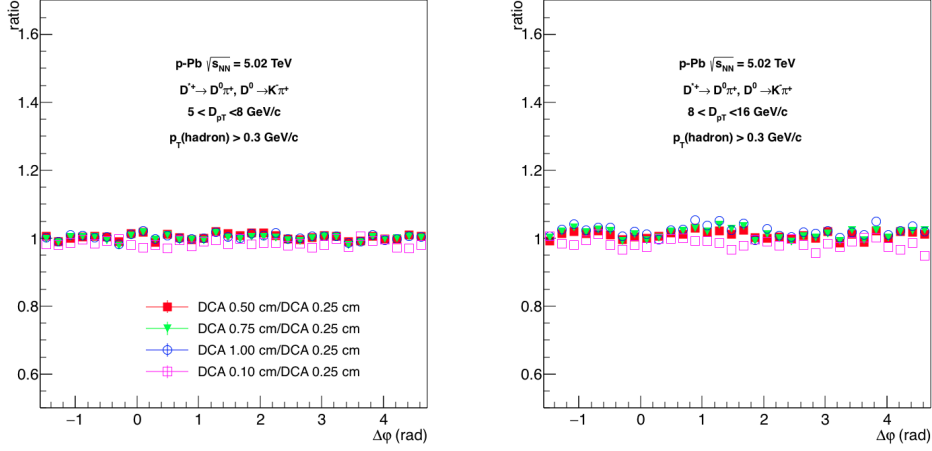


Figure 6.10: Same as figure 6.9, but for p-Pb collisions. The left panel shows the range $5 < p_T(D^{*+}) < 8$ GeV/ c and the right panel the range $8 < p_T(D^{*+}) < 16$ GeV/ c .

but for the p-Pb analysis. Due to the fact that the correction is itself independent of $\Delta\varphi$, the same is expected and observed for the systematic uncertainty. The estimated uncertainty is $\pm 3\%$.

6.1.6 Beauty feed-down correction

The systematic uncertainty due to the beauty feed-down correction has two (three for the p-Pb analysis) possible different sources

- f_{prompt} : the uncertainty on the calculation of the f_{prompt} , originating from the uncertainty on the quark masses and the QCD scales used in the FONLL calculations;
- Monte-Carlo template: the uncertainty on the Monte-Carlo template used for the azimuthal correlations of D mesons originating from the beauty hadron decays with charged tracks;
- v_2 -like modulation of the baseline (p-Pb only): possible modulation of the baseline correlation due to a possible non-zero v_2 of feed-down D mesons in p-Pb collisions.

The effect of the f_{prompt} uncertainty has been estimated using an upwards and downwards shift of the f_{prompt} central value within the estimated uncertainty, and recalculating the correction as described in equation 4.12. The effect of the second contribution (due to the Monte-Carlo template) has been estimated performing the feed-down subtraction using the Perugia-2010 and 2011 Monte-Carlo tunes, instead of the Perugia-0 tune [26]. In the p-Pb analysis, a very conservative assumption of a $v_2(B \rightarrow D) = 0.13$ has been made to

6.1. AZIMUTHAL CORRELATION DISTRIBUTION SYSTEMATIC UNCERTAINTIES

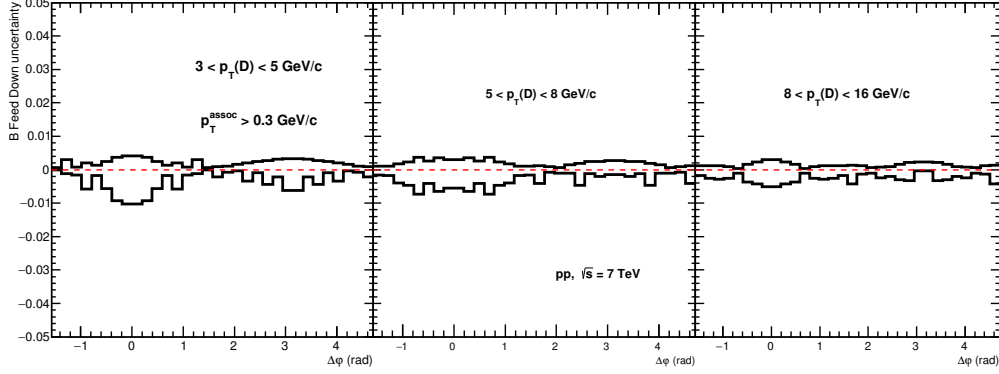


Figure 6.11: Total envelope of the B feed-down correction in pp collisions. The left panel shows the p_T range $3 < p_T(D^{*+}) < 5 \text{ GeV}/c$, the middle panel the range $5 < p_T(D^{*+}) < 8 \text{ GeV}/c$ and the right panel the range $8 < p_T(D^{*+}) < 16 \text{ GeV}/c$. The associated tracks are selected with $p_T(\text{hadron}) > 0.3 \text{ GeV}/c$.

modulate the baseline (which affects the full template) as described in equation 4.15. The uncertainties have been estimated by taking the envelope of the maximum variation among the various options. Figure 6.11 depicts the envelope estimated for pp collisions. The maximum difference is of the order of 1%. Figure 6.12 shows the envelope estimated for p-Pb collisions. Also in this case, the maximum difference is of the order of 1%. This uncertainty is $\Delta\varphi$ -dependent

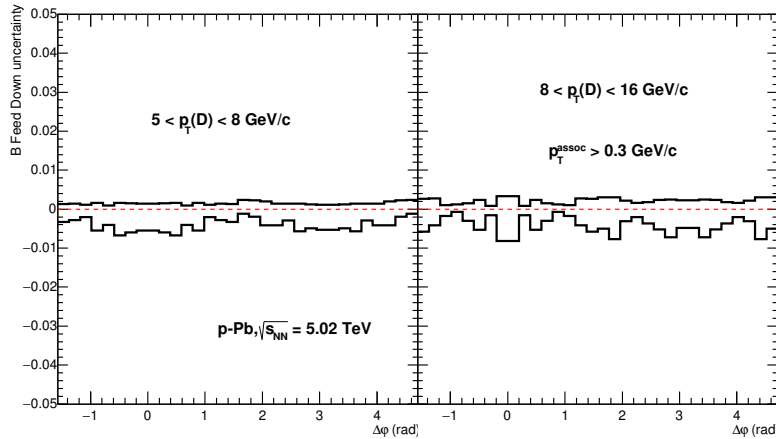


Figure 6.12: Same as figure 6.11, but for p-Pb collisions. The left panel shows the range $5 < p_T(D^{*+}) < 8 \text{ GeV}/c$ and the right panel the range $8 < p_T(D^{*+}) < 16 \text{ GeV}/c$.

6.1.7 Total systematic uncertainty

The total uncertainties for the $\Delta\varphi$ -independent uncertainty is calculated by summing in quadrature all the different sources, i.e.

$$\sigma_{corr.syst}^{tot} = \sqrt{\sum_i \sigma_{corr.syst,i}^2} \quad (6.1)$$

and will be reported in the coming sections as scale uncertainty. The $\Delta\varphi$ -dependent uncertainty is computed point-by-point as the sum in quadrature of the two contributions, i.e. the Monte Carlo closure test uncertainty and the beauty feed-down uncertainty.

7

Results

This chapter presents the results of azimuthal correlations of D^{*+} mesons and charged particles in pp and p-Pb collisions, at energies of $\sqrt{s} = 7$ TeV and $\sqrt{s_{NN}} = 5.02$ TeV, as well as the averaged results from the D^{*+} , D^0 and D^+ meson analyses [3, 4]. The measurements are performed differentially as function of the transverse momentum of the D meson and associated particle, while the other kinematical and event topology variables are integrated over the whole range (i.e. they are not studied differentially).

As already mentioned in previous chapters, in pp collisions, the results are obtained in three different intervals of p_T of the D^{*+} , namely $3 < p_T(D^{*+}) < 5$ GeV/c, $5 < p_T(D^{*+}) < 8$ GeV/c and $8 < p_T(D^{*+}) < 16$ GeV/c, while in p-Pb collisions the results are obtained for $5 < p_T(D^{*+}) < 8$ GeV/c and $8 < p_T(D^{*+}) < 16$ GeV/c.

The associated tracks have been selected in the integrated p_T interval, i.e. $p_T > 0.3$ GeV/c, as well as more differentially in two subintervals, $0.3 < p_T < 1$ GeV/c and $p_T > 1$ GeV/c. In this chapter, unless differently stated, all the results shown in the first part are related to the azimuthal correlation distribution and are shown following the following scheme: for pp collisions, the plots are distributed in a 3x3 panel, with different columns representing different p_T intervals of the D mesons (increasing from left to right), while the rows represent different p_T ranges of the associated tracks, the top row is for the integrated region ($p_T > 0.3$ GeV/c), the middle row represent the low p_T interval, while the lowers row is for the high p_T interval. In p-Pb collisions, the plotting scheme is the same but for the absence of the first column, as no measurement is available in the range $3 < p_T(D^{*+}) < 5$ GeV/c.

Exploiting the symmetry of the system, the azimuthal correlations have been reflected from the range $-\pi/2 < \Delta\varphi < 3\pi/2$ to the range $0 < \Delta\varphi < \pi$. In this way, fluctuations are reduced by construction, without any loss of information. In all the figures presented in this chapter, the $\Delta\varphi$ -independent systematic uncertainties are reported as a scale uncertainty in percentage, while the $\Delta\varphi$ -dependent uncertainties are represented as a box for each point in $\Delta\varphi$ which represents the absolute uncertainty of every single point.

The second part of the chapter discusses the fitting procedure and the results of the characterisation of the correlation distributions by studying the different correlation parameters as function of the kinematical variables.

7.1 D^{*+} -charged particle correlations

This section presents the fully-corrected azimuthal distribution of prompt- D^{*+} mesons and charged particles in pp collisions at $\sqrt{s} = 7$ TeV and in p-Pb collisions at $\sqrt{s_{NN}} = 5.02$ TeV. A qualitative description of the correlation distributions will be given, while a more quantitative description is postponed to the sections discussing the results of the average distributions for D^0 , D^+ and D^{*+} mesons.

The results for pp collisions are shown in figure 7.1.

With increasing p_T of the D meson, the near-side and away-side peaks show a stronger correlation (i.e. the peak gets narrower and higher) above the baseline. In the low p_T interval, $3 < p_T(D^{*+}) < 5$ GeV/c, the statistical fluctuations make it hard to distinguish the correlation peaks from the baseline. This is particularly evident when a D^{*+} in the range $3 < p_T(D^{*+}) < 5$ GeV/c is correlated with tracks with $p_T > 1$ GeV/c, where the statistics is reduced due to the exponentially decreasing single track p_T spectra, and the $\Delta\varphi$ distribution is dominated by fluctuations. However, the situation gets better and more stable at when the distributions are averaged with those from D^0 and D^+ mesons.

When comparing the correlations with low p_T tracks, $0.3 < p_T < 1$ GeV/c (middle column) and high p_T , $p_T > 1$ GeV/c, the correlation seems to be more “significant” at high p_T . This is mostly due to the lower value of the baseline, that decreases with increasing p_T of the associated particle.

Defining the baseline, considered as the minimum of the correlation distribution, is not trivial given the large statistical fluctuations. The strategy for its computation will be discussed in detail in section 7.3. For a qualitative discussion, looking at the average minimum of the correlation distributions from figure 7.1 it is possible to observe that in a given range of p_T of associated tracks, the baseline does not depend significantly on the p_T of the D^{*+} in the considered p_T interval.

The results of the multiplicity-integrated p-Pb analysis are shown in figure 7.2. The first evident observation is that the baseline in p-Pb collisions is higher than in pp in all the considered ranges of p_T and is due to the higher multiplicity environment in p-Pb collisions.

Similarly to the pp case the same qualitative conclusions hold: the near-side and away-side correlations get stronger with increasing p_T of the D^{*+} , the peaks are more significant when higher p_T associated tracks are considered and the baseline does not show any significant dependence on the D^{*+} p_T .

7.2 Average of D^0 , D^+ and D^{*+}

As already seen in section 7.1, the fluctuations and the large uncertainties for a single D meson analysis do not allow (especially for the lowest studied p_T range of the D^{*+}) for a clear interpretation of the results. The ALICE

7.2. AVERAGE OF D^0 , D^+ AND D^{*+}

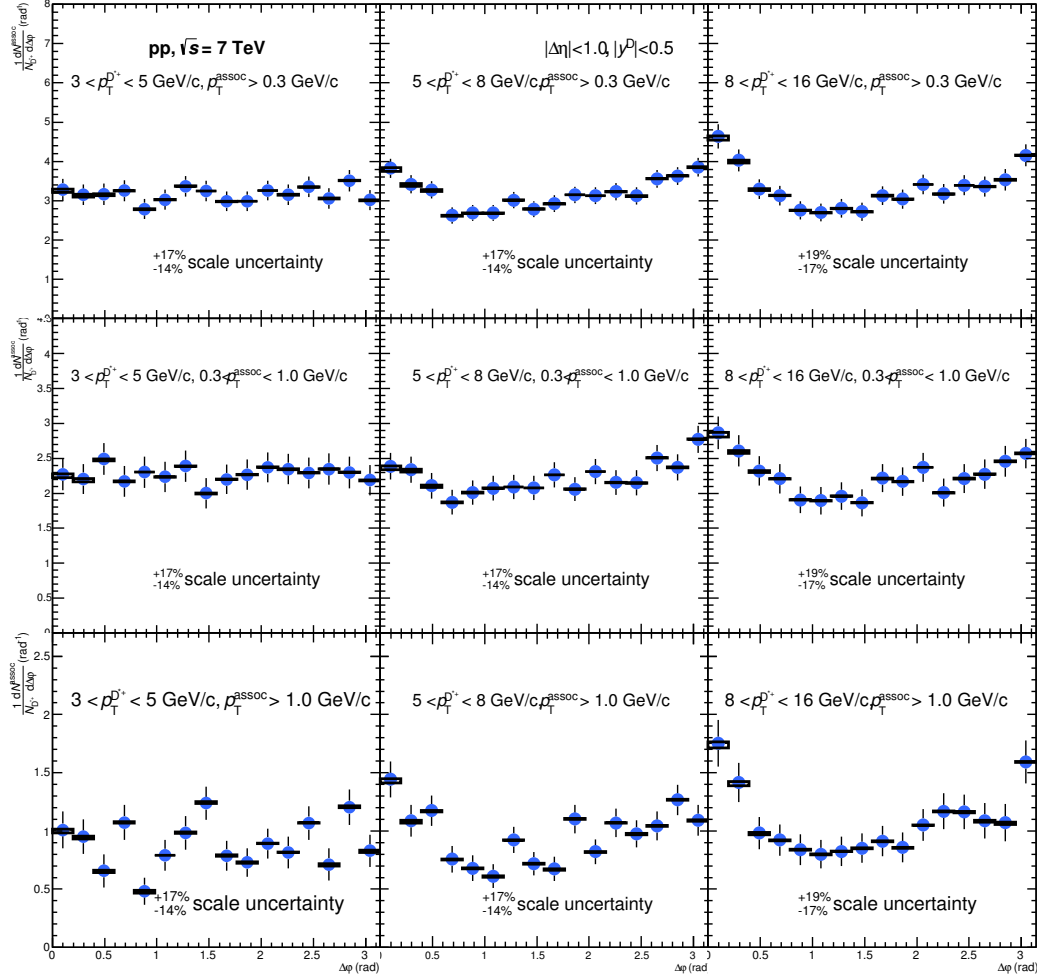


Figure 7.1: Azimuthal correlation distribution of D^{*+} mesons and charged particles in pp collisions at $\sqrt{s} = 7$ TeV. The left column corresponds to the D^{*+} mesons in the range $3 < p_T(D^{*+}) < 5$ GeV/c, the middle column to the range $5 < p_T(D^{*+}) < 8$ GeV/c, while the right column to the range $8 < p_T(D^{*+}) < 16$ GeV/c. The upper row corresponds to all the considered associated tracks ($p_T^{assoc} > 0.3$ GeV/c), the middle row corresponds to the associated tracks in the p_T range $0.3 < p_T^{assoc} < 1.0$ GeV/c while the lowest row corresponds to the associated tracks with $p_T^{assoc} > 1.0$ GeV/c.

CHAPTER 7. RESULTS

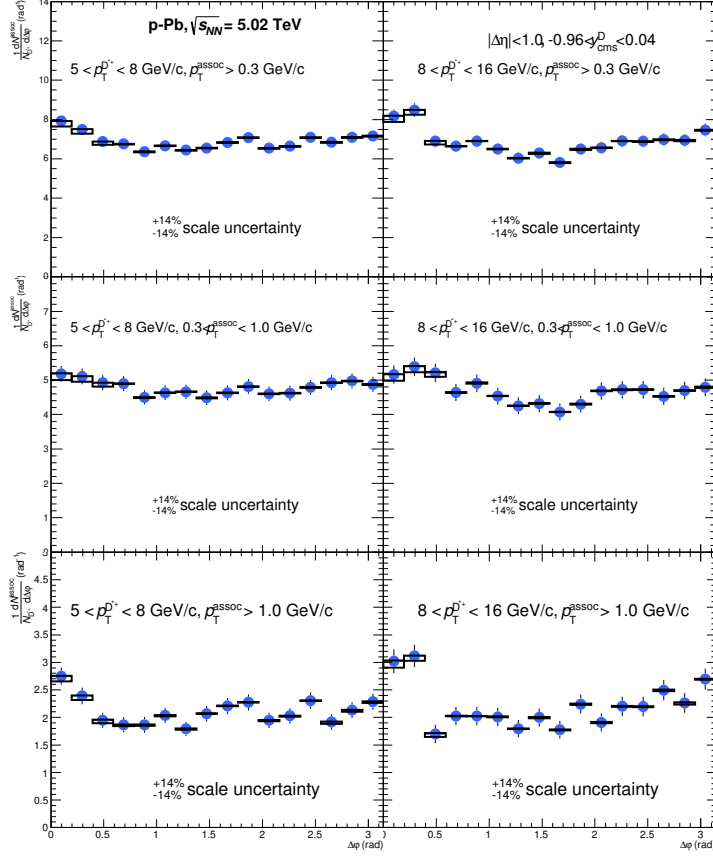


Figure 7.2: Azimuthal correlation distribution of D^{*+} mesons and charged particles in p-Pb collisions at $\sqrt{s_{NN}} = 5.02$ TeV. The left column corresponds to D^{*+} mesons in the range $5 < p_T(D^{*+}) < 8$ GeV/c, while the right column to the range $8 < p_T(D^{*+}) < 16$ GeV/c. The upper row corresponds to all the considered associated tracks ($p_T^{assoc} > 0.3$ GeV/c), the middle row corresponds to the associated tracks in the p_T range $0.3 < p_T^{assoc} < 1$ GeV/c while the lowest row corresponds to the associated tracks with $p_T^{assoc} > 1$ GeV/c.

collaboration has measured correlations of D^0 mesons and charged particles, as well as the one of D^+ mesons and charged particles [72, 73]. In order to reduce the fluctuations and to reduce the uncertainties, the weighted average of the correlation distributions of the three meson species has been computed. The D^0 and D^+ were fully reconstructed using the hadronic channels [70]:

- $D^0 \rightarrow K^-\pi^+$ (BR = 3.89 %)
- $D^+ \rightarrow K^-\pi^+\pi^+$ (BR = 9.13 %)

The analysis follows the same strategy as described in chapter 4. In the case of the D^0 , an additional source of systematic uncertainty is present: being a neutral reconstructed particle, the D^0 reconstruction is affected by reflections

(i.e. the fact that the \bar{D}^0 might be reconstructed and identified as the D^0 due to the wrong mass hypothesis on the daughters of the D meson).

Figure 7.3 shows a comparison of the correlation distributions of three D mesons in pp collisions (left panel) for the p_T ranges $5 < p_T(D) < 8$ GeV/c with the associated tracks with $p_T > 1$ GeV/c, while the right panel shows the comparison for p-Pb collisions in the p_T ranges $8 < p_T(D) < 16$ GeV/c and the associated tracks are selected with $p_T > 1$ GeV/c. Both in pp and p-Pb there is good compatibility between the three distributions within the large uncertainties, in particular the scaling uncertainty, mostly due to the D meson yield extraction and combinatorial background subtraction.

As reported in the figures, the scaling uncertainty of D^{*+} and D^0 is of the same magnitude, while the value of the scaling uncertainty for the D^+ is larger by a 5% in absolute value. This is primarily due to the background subtraction systematic uncertainty. Although the statistical significance of the D^0 peak is larger than the one of the D^{*+} , the statistical uncertainties are very similar in size. Differently from cross section measurements, the background subtraction procedure makes the statistical uncertainty depend not only on the statistical significance of the signal extraction, but also on the signal-over-background (S/B) ratio, that for the D^{*+} is one order of magnitude larger. The larger signal-over-background (S/B) compensates the lower statistical significance, resulting in similar values of the statistical uncertainties in the azimuthal correlation distribution as the D^0 meson.

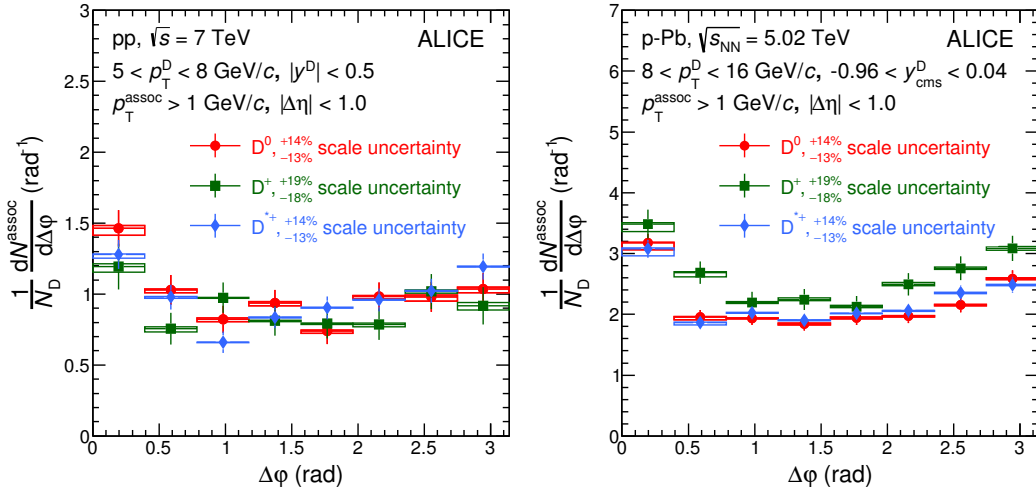


Figure 7.3: Comparison of the azimuthal correlation distribution obtained from different meson species (D^0 , D^+ and D^{*+}). Left panel: example for pp collisions at $\sqrt{s} = 7$ TeV, with $5 < p_T(D) < 8$ GeV/c and $p_T > 1$ GeV/c. Right panel: example for p-Pb collisions at $\sqrt{s_{NN}} = 5.02$ TeV, with $8 < p_T(D) < 16$ GeV/c and $p_T > 1$ GeV/c.

CHAPTER 7. RESULTS

The average has been calculated as follows

$$\left\langle \frac{1}{N_D} \frac{dN^{\text{assoc}}}{dp_T} \right\rangle_{D\text{mesons}} = \frac{\sum_{i=\text{meson}} w_i \frac{1}{N_D} \frac{dN_i^{\text{assoc}}}{d\Delta\phi}}{\sum_{i=\text{meson}} w_i}, \quad (7.1)$$

where the weight w is computed as the inverse sum in quadrature of the statistical uncertainty and the scale uncertainty, i.e.

$$w_i = \frac{1}{\sigma_{i,\text{stat}}^2 + \sigma_{i,\text{scaleuncertainty}}^2}. \quad (7.2)$$

The statistical uncertainty and the uncertainty on the yield extraction on the average were then recalculated using the formula

$$\sigma^2 = \frac{\sum_{i=\text{meson}} w_i \sigma_i^2}{\sum_{i=\text{meson}} w_i}, \quad (7.3)$$

which, for $\sigma_i^2 = 1/w_i$, coincides with the standard formula giving the uncertainty on a weighted average.

The results of the averaging of the D^0 , D^+ and D^{*+} correlations with charged particles in pp collisions is shown in figure 7.4. Compared to the D^{*+} only case, the systematic uncertainty of the scale is reduced from $^{+17\%}_{14\%}$ to $^{+13\%}_{10\%}$ for the p_T bins $3 < p_T(D) < 5$ GeV/ c and $5 < p_T(D) < 8$ GeV/ c , while in the range $8 < p_T(D) < 16$ GeV/ c it is reduced from $\pm 14\%$ to $\pm 10\%$. In addition, qualitatively speaking, the reduced fluctuations after the averaging procedure allow for a better visualisation of the near- and away-side peaks, in particular for what concerns the low p_T D-meson interval.

For the p-Pb results, the scale uncertainty is reduced from $\pm 14\%$ to 10% . Similarly to the pp case, the reduced fluctuations allow for a better visualisation of the peaks. The narrowing and strengthening of the near-side correlation peak with increasing p_T of the D meson is clear in both the pp and p-Pb cases.

Figure 7.5 shows the averaged results of D^0 , D^+ and D^{*+} correlations with charged particles in p-Pb collisions.

7.2. AVERAGE OF D^0 , D^+ AND D^{*+}

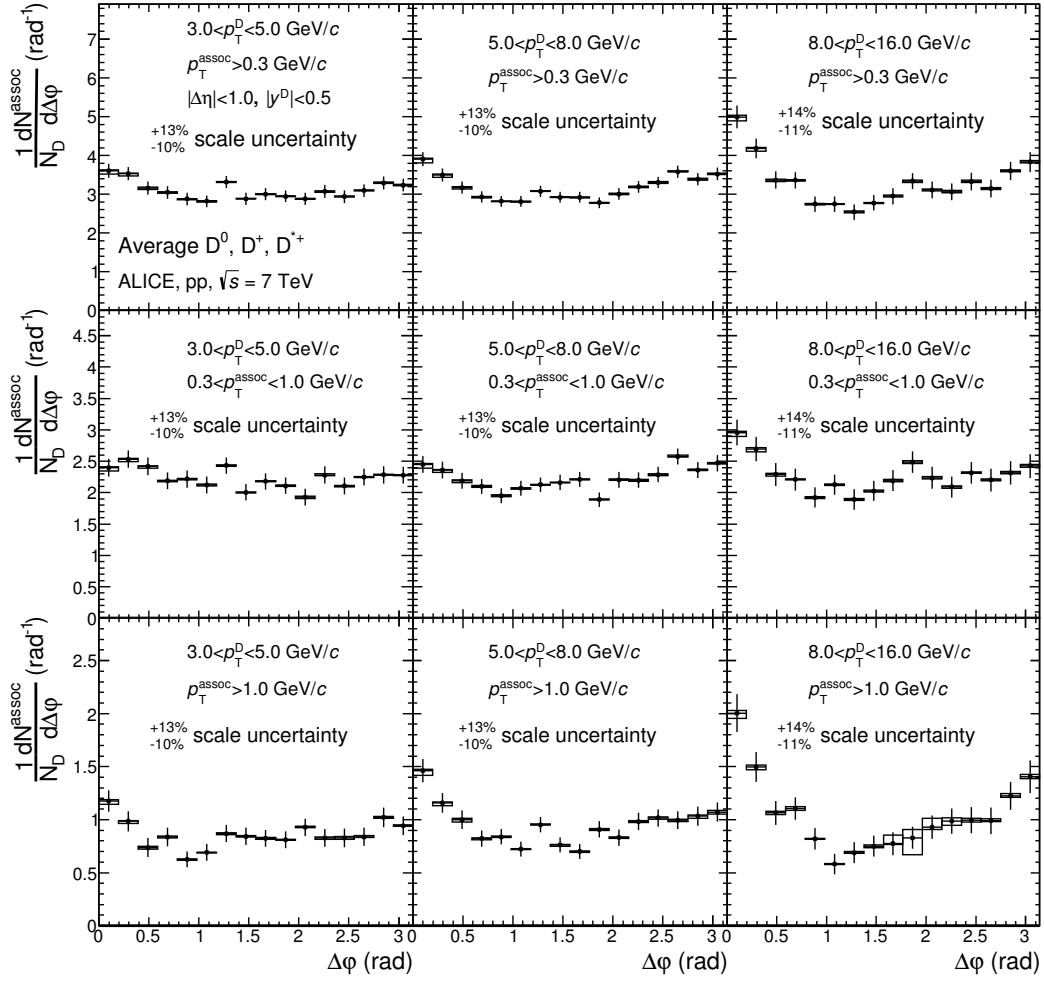


Figure 7.4: Same as figure 7.1, but showing the averaged distribution of D^0 , D^+ and D^{*+} mesons.

CHAPTER 7. RESULTS

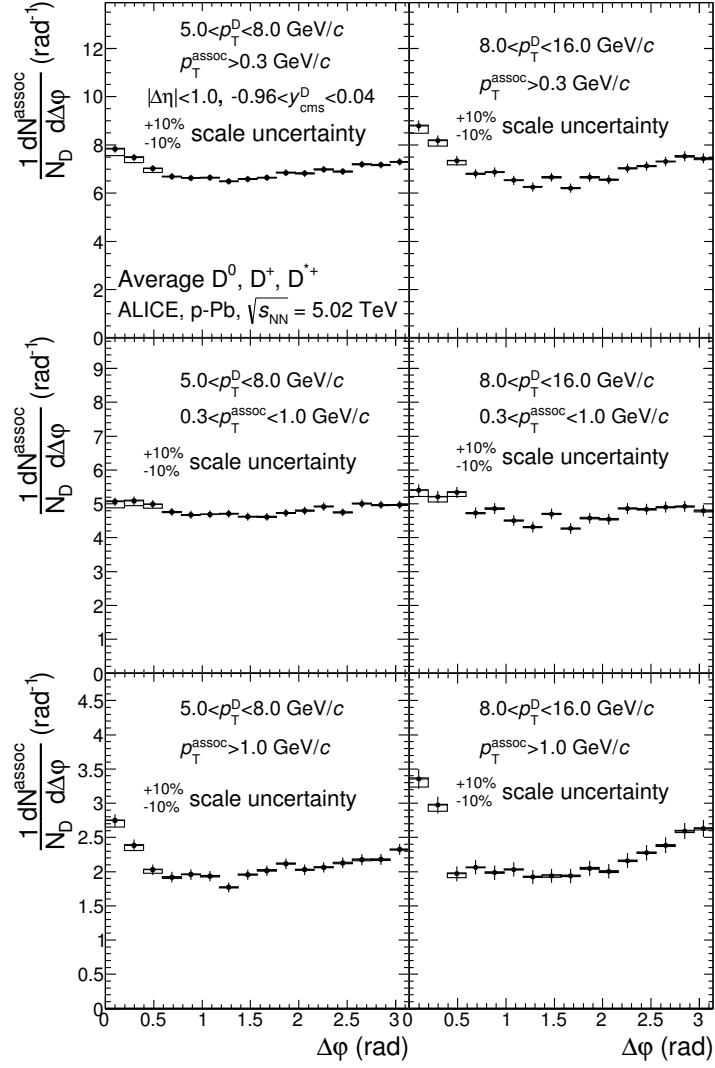


Figure 7.5: Same as figure 7.2, but for showing the averaged distribution of D^0 , D^+ and D^{*+} mesons.

7.3 Estimation of the baseline

The azimuthal correlation distribution is constructed by tracks originating from the jets created from the hard scattering processes that produce a heavy-flavour quark pair, as well as tracks originating from the so called underlying event. As in first approximation, the underlying event is not correlated with the hard-scattering process, the azimuthal distribution of those tracks is expected to be uniform with respect the D meson direction. This statement holds in a scenario where collective phenomena (flow) do not take place. For pp collisions, this hypothesis can be done safely, while in p-Pb collisions, where a modulation in the baseline was already observed for di-hadron correlations [34, 75, 76], the distribution might not be uniform anymore. This is further discussed later in this section. On the other hand, as already seen in chapter 5, the tracks that originate from the heavy-flavour hadronisation process show a correlation on the near side and away side due to the effects of different heavy-flavour pair production mechanisms.

In order to study the properties of the jets originating from heavy-flavours, the baseline has been calculated and the value has been used to:

- subtract a flat contribution from the correlation distribution, in order to be able to compare the near-side and away-side correlation structure between different collision systems and the Monte Carlo predictions;
- constrain the baseline value in the fitting procedure. More details are given in section 7.6.

In an ideal, infinite-statistics scenario, the baseline is determined using the ZYAM (Zero Yield At Minimum) approach: the minimum of the $\Delta\varphi$ distribution is the baseline value, the yield of associated pairs can be computed using this value as reference zero.

In the study presented in this thesis, the limited statistics of the datasets does not allow for the use of the ZYAM method, as a statistical fluctuation is very likely to represent the minimum of the distribution, leading to a wrong estimation of the baseline, and of the physics results. In order to limit the sensitivity to statistical fluctuations, a region in $\Delta\varphi$ has been used to estimate the baseline, rather than single points.

The cartoon in figure 7.6 illustrates the procedure to estimate the baseline. The weighted average of the points in the region $\pi/4 < |\Delta\varphi| < \pi/2$ has been used. The weight is defined as the inverse of the statistical uncertainty of the single point. As it will be shown in the later sections, the $\pi/4$ angle is larger at least twice than the gaussian width on the near-side peak, meaning that the near-side correlation yield is almost absent in that region. On the other hand, the away-side peak is broader, and $\pi/2$ represents a logical physical boundary to the away-side. The systematic uncertainty on the baseline definition has been evaluated by studying the variation of the baseline value estimated in different regions of $\Delta\varphi$, namely:

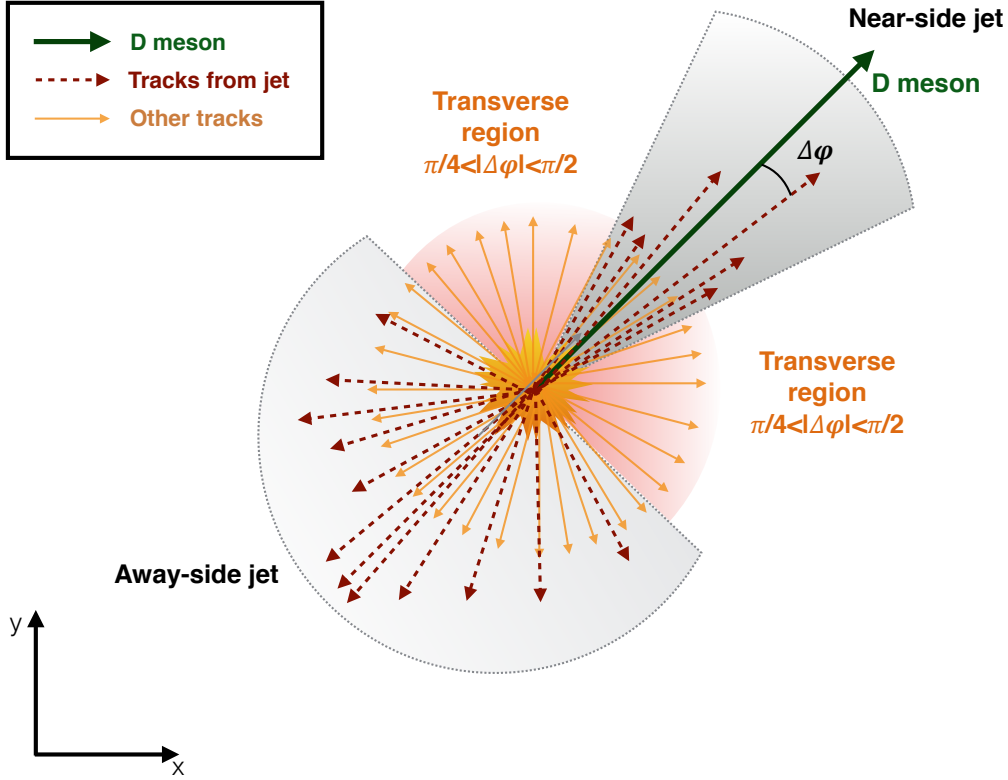


Figure 7.6: Cartoon illustrating the standard strategy to define the transverse region for this particular analysis that is then used to compute the baseline of the correlation distribution.

- $\pi/4 < |\Delta\varphi| < 3\pi/8$
- $3\pi/8 < |\Delta\varphi| < \pi/2$
- $\pi/2 < |\Delta\varphi| < 5\pi/8$
- $3\pi/8 < |\Delta\varphi| < 5\pi/8$

The total systematic uncertainty from the baseline estimation has been defined as the Root Mean Square (RMS) of the different values, and the values are reported in table 7.1.

The measured values of the baseline for pp and p-Pb collisions, are shown in figure 7.7, in the left and right panel, respectively, as function of the D meson p_T . As only the systematic uncertainty from the baseline determination is relevant for its subtraction and for the comparison of the correlation distributions between different collision systems and with Monte Carlo predictions, only this uncertainty is shown in figure 7.7. A complete study of the baseline should include also the scaling systematic uncertainty summed in quadrature. Figure 7.7 allows for some conclusions to be deduced. As already mentioned

7.3. ESTIMATION OF THE BASELINE

$p_T(D)$ (GeV/c)	pp			p-Pb	
	3-5	5-8	8-16	5-8	8-16
$p_T^{assoc} > 0.3$ GeV/c	$\pm 7\%$	$\pm 5\%$	$\pm 16\%$	$\pm 7\%$	$\pm 9\%$
$0.3 < p_T^{assoc} < 1$ GeV/c	$\pm 2\%$	$\pm 4\%$	$\pm 13\%$	$\pm 1\%$	$\pm 8\%$
$p_T^{assoc} > 1$ GeV/c	$\pm 6\%$	$\pm 2\%$	$\pm 4\%$	$\pm 6\%$	$\pm 3\%$

Table 7.1: Systematic uncertainties from the baseline calculation procedure, computed as the RMS of the variations of the results from different ranges of the baseline definition (see text for more details).

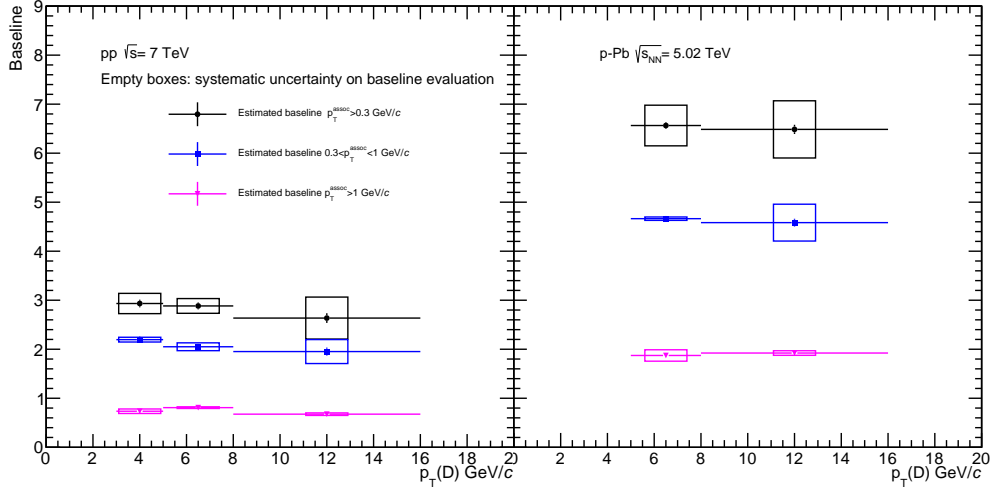


Figure 7.7: Baseline as function of the D meson p_T (x axis) and the associated track p_T (color online). The left panel shows the result for pp collisions at $\sqrt{s} = 7$ TeV while the right panel the results for p-Pb collisions at $\sqrt{s_{NN}} = 5.02$ TeV. The boxes represent only the systematic uncertainties from the baseline definition range.

in the qualitative description, within uncertainties the baseline is constant as function of the D meson p_T in the considered p_T range, and the conclusion is valid for all the considered ranges of the associated track p_T .

The baseline in p-Pb collisions is almost twice as large as the one in pp collisions, which is expected due to the larger multiplicity in p-Pb collisions.

The largest contribution to the baseline of the integrated $p_T^{assoc} > 0.3$ GeV/c originates from low p_T tracks in the range $0.3 < p_T^{assoc} < 1$ GeV/c, as it was already seen qualitatively in the previous discussions.

To estimate the baseline of the correlation distributions from the Monte Carlo generators, a slightly different approach has been used: given that the statistics in the Monte Carlo templates is large enough, the baseline has been es-

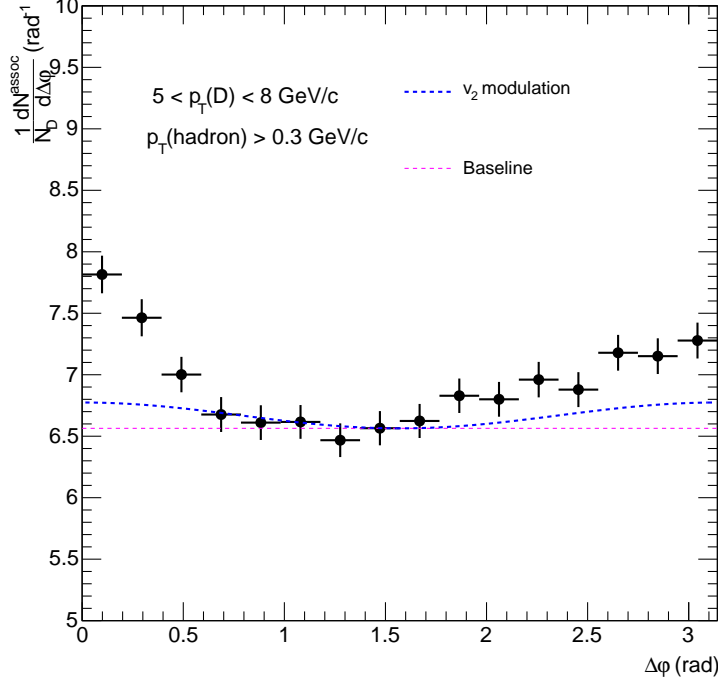


Figure 7.8: The modulation due to a non-zero v_2 of the D meson in p-Pb collisions. The v_2 of the associated tracks has been set to 0.08[34], while for the D meson a conservative hypothesis of $v_2^D = 0.1$ has been considered.

estimated using the ZYAM method, while the systematic uncertainty has been estimated by calculating the variation of the baseline computed using the two lowest point, instead of one.

As already mentioned above, in p-Pb collisions, due to collective phenomena, a modulation of the baseline of the form $1 + v_2^D v_2^{had} \cos(\Delta\varphi)$ might be necessary. However, as the measurement of the D meson v_2 coefficient in p-Pb is not available, figure 7.8 shows a modulation of the baseline in the extreme hypothesis that $v_2^D = 0.1$ (for the hadron it has been taken to be $v_2^{had} = 0.08$ [34]). The modulation is shifted in order that the minimum corresponds to the baseline computed using the transverse region (as shown in figure 7.8). A measurement of the v_2 has been tried, however the available statistics is not enough to measure the v_2 coefficient. The effect of the v_2 hypothesis is illustrated in figure 7.8 and is not further treated in the analysis of the $\Delta\varphi$ correlation distributions. It will be quantified in the section discussing the fit procedure.

7.4 Comparison to models

The structure of the near and away side correlations has been compared to predictions from PYTHIA6 using different PerugiaTunes [26], PYTHIA 8 [67] and from POWHEG [63] + PYTHIA6. These results are shown in figure 7.9 for pp collisions.

In order to focus on the structure of the correlation peaks, the baseline has been subtracted from the plots in both the distributions from data and simulations, using the strategy described in the previous section.

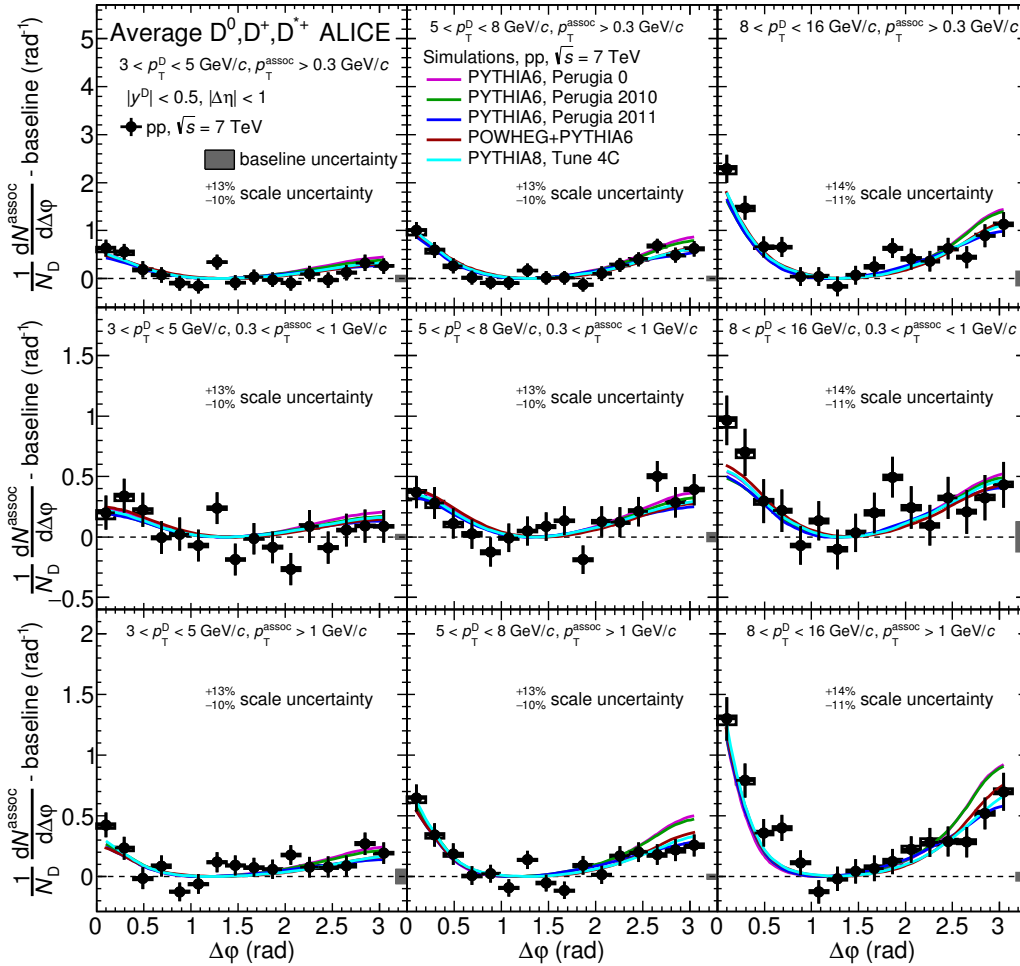


Figure 7.9: (Color online) Comparison of the azimuthal angular correlations of D mesons and charged tracks measured in pp collisions at $\sqrt{s} = 7$ TeV with simulations with PYTHIA 6 (different tunes) [26], PYTHIA 8 [67] and POWHEG [63] at the same \sqrt{s} energy. The baseline has been subtracted for both the distribution from data and from models (see text for more details).

CHAPTER 7. RESULTS

A general observation is that the different models predict a very similar behaviour on the near side, while on the away side the PYTHIA 6 Perugia 2011 Tune, PYTHIA8 and the predictions by POWHEG show a lower correlation than the PYTHIA6 Perugia2010 and Perugia0 tunes.

In the integrated region of p_T of the associated tracks a very good agreement within uncertainties is observed between the data points and the model results, for the two lowest considered p_T intervals of the D meson, while in the range $8 < p_T(D) < 16$ GeV/ c the near-side behaviour is underestimated by the models. When looking more differentially, it is observed that the discrepancy between the models and the data on the near-side occurs when combining softer tracks (i.e. in the p_T region $0.3 < p_T^{assoc} < 1$ GeV/ c with D mesons in the range $8 < p_T(D) < 16$ GeV/ c , while the models reproduce well the narrow increase of the correlation distribution when the associated track $p_T > 1$ GeV/ c is considered.

The lower away side predicted by the PYTHIA6 Perugia 2011 tune, PYTHIA8 and POWHEG, is clearly evident when looking at “hard tracks” (i.e. $p_T > 1$ GeV/ c), is in better agreement with the data points compared to the other PYTHIA tunes.

In the lowest p_T bin of the D meson ($3 < p_T(D) < 5$ GeV/ c), although the statistical fluctuations make it harder to clearly distinguish the correlation peaks, the points fluctuate around the predictions from the considered models.

7.5 Comparison of azimuthal correlations in pp and p-Pb collisions

The pp and p-Pb collisions discussed in this thesis are performed at different centre-of-mass energies ($\sqrt{s} = 7$ TeV for pp collisions and $\sqrt{s_{NN}} = 5.02$ TeV for p-Pb collisions). The different energies can produce a bias in comparing the distributions. In order to quantify this effect, figure 7.10 shows the ratio of the near-side yields for pp collisions at $\sqrt{s} = 7$ TeV and $\sqrt{s} = 5.02$ TeV, with different PYTHIA6 tunes. The near-side yield will be properly defined in the next section, and measures the average number of associated tracks per D meson on the near-side. According to PYTHIA, an average increase of 3-8 % of the near-side yields due to the different centre-of-mass \sqrt{s} , depending on the D-meson p_T and PYTHIA tune, has been observed.

Figure 7.11 shows the comparison of the correlation distributions measured in pp and p-Pb collisions, in the 6 overlapping combinations of p_T intervals of D mesons and associated tracks. The measurements are multiplicity integrated. The baseline has been subtracted as described in section 7.3. The first row of figure 7.11 shows the correlation of D mesons and charged tracks in the integrated interval of the associated track p_T , where the distributions lie on top of each other within the uncertainties. In both pp and p-Pb collisions, a

7.5. COMPARISON OF AZIMUTHAL CORRELATIONS IN PP AND P-PB COLLISIONS

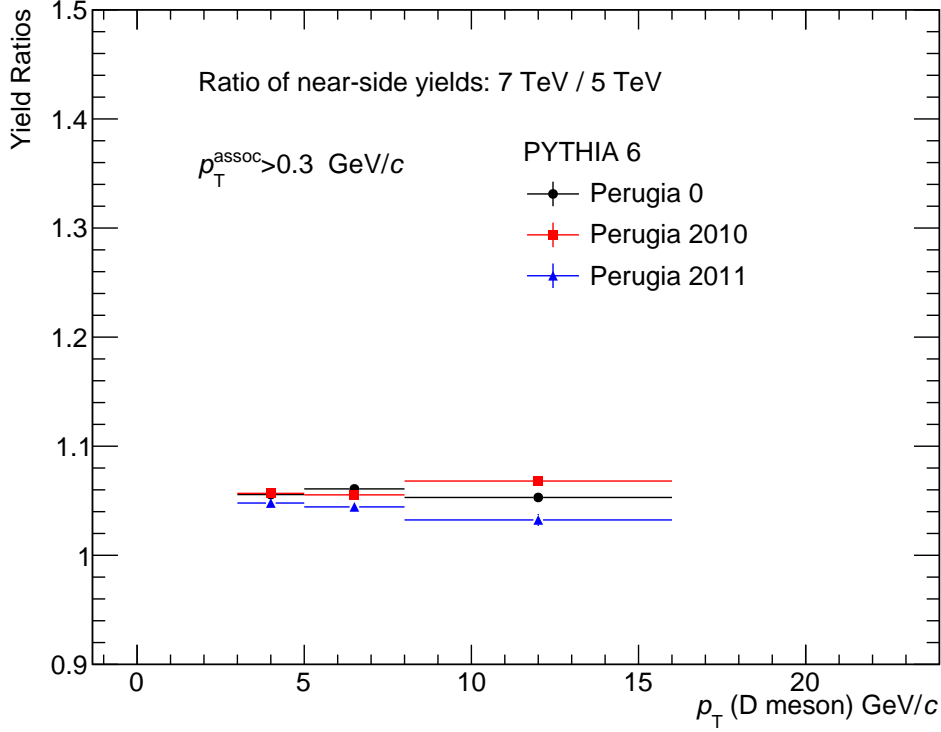


Figure 7.10: The ratio of the near-side yields extracted from fits at the $\sqrt{s} = 7 \text{ TeV}$ and $\sqrt{s} = 5.02 \text{ TeV}$ D-hadron azimuthal correlations from PYTHIA simulations, for different tunes.

narrower and higher correlation distribution is observed for increasing p_T of the D meson. Although compatible within uncertainties, a hint of a higher correlation on the near-side for D mesons in p-Pb collisions is observed in the range $5 < p_T(D) < 8 \text{ GeV}/c$.

When looking more differentially as a function of the associated track p_T , in the interval $0.3 < p_T^{\text{assoc}} < 1 \text{ GeV}/c$ the statistical fluctuations are larger, as already observed, and so are the statistical uncertainties, making the distributions compatible. When considering harder associated tracks, with $p_T > 1 \text{ GeV}/c$ in the lowest row of figure 7.11, the distributions are again compatible within uncertainties. The hint of a higher correlation observed in the integrated case seems to be mostly due to correlations of harder tracks with D mesons, however a more precise measurement is necessary to properly study the effect.

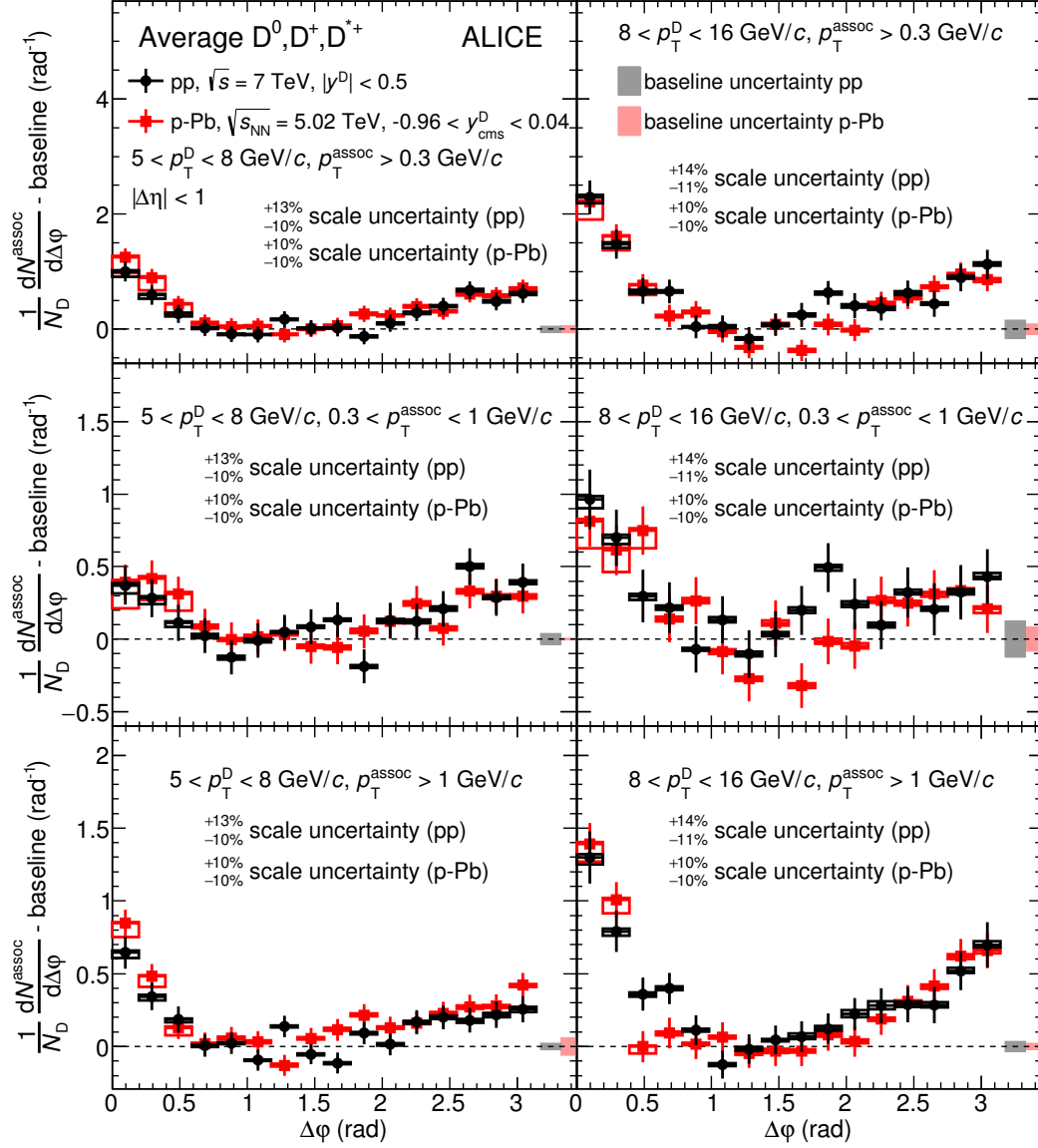


Figure 7.11: Comparison of the azimuthal correlations of D mesons and charged hadrons in pp collision at $\sqrt{s} = 7$ TeV and p-Pb collisions at $\sqrt{s_{NN}} = 5.02$ TeV, for the p_T intervals where both the measurements have been performed. For both collision systems, the baseline of the distribution has been computed and subtracted (see section 7.3 for more details).

7.6. CHARACTERISATION OF THE CORRELATION DISTRIBUTION

7.6 Characterisation of the correlation distribution

In order to characterise the measured D-hadron correlation, the last step in the analysis procedure is to fit the distributions shown in the figures of section 7.2.

The fit function used for the fit is defined as follows:

$$f(\Delta\varphi) = C + f_{NS}(\Delta\varphi) + f_{AS}(\Delta\varphi) \quad (7.4)$$

where C represents the value of the baseline and $f_{NS}(\Delta\varphi)$, defined as

$$f_{NS}(\Delta\varphi) = \frac{Y_{NS}}{\sqrt{2\pi}\sigma_{NS}} \exp\left(-\frac{(\Delta\varphi - \mu_{NS}|_0)^2}{2\sigma_{NS}^2}\right) \quad (7.5)$$

is a gaussian distribution to describe the near-side correlation peak, while $f_{AS}(\Delta\varphi)$, defined as

$$f_{AS}(\Delta\varphi) = \frac{Y_{AS}}{\sqrt{2\pi}\sigma_{AS}} \exp\left(-\frac{(\Delta\varphi - \mu_{AS}|\pi)^2}{2\sigma_{AS}^2}\right) \quad (7.6)$$

is a second gaussian distribution used to characterise the away side peak.

Y_{NS} and Y_{AS} are the associated yields on the near side and away side, respectively, that correspond to the average number of pairs of associated tracks per D meson. σ_{NS} and σ_{AS} are the widths of the near-side and away-side peaks, respectively. The means of the two gaussian functions have been fixed to the values $\mu_{NS}=0$ and $\mu_{AS}=\pi$.

Hence the free parameters of the fit are $Y_{NS}, Y_{AS}, \sigma_{NS}$ and σ_{AS} . The parameter C , representing the baseline, is computed as described in section 7.3.

An example of the fit of the data points is shown in figure 7.12, where the red curve represents the total fit obtained as the sum of the near-side gaussian (blue dashed curve) and the away-side gaussian (green dashed line) on top of the baseline computed from the transverse region (magenta line represent).

The largely fluctuating away-side peaks make the estimation of its parameters extremely unreliable. Moreover, a free fit of the distributions tends to converge to a very wide value of the away-side peak, that exceeds well the value of π , pushing down the value of the baseline and artificially increasing the near-side yield. For this purpose, the baseline has been defined as described in section 7.3, and its contribution to the systematic uncertainty will be described in section 7.6.1.

The near-side peak parameters (associated yield and width σ) as well as the baseline have been studied as function of the transverse momentum of the D meson and the associated tracks.

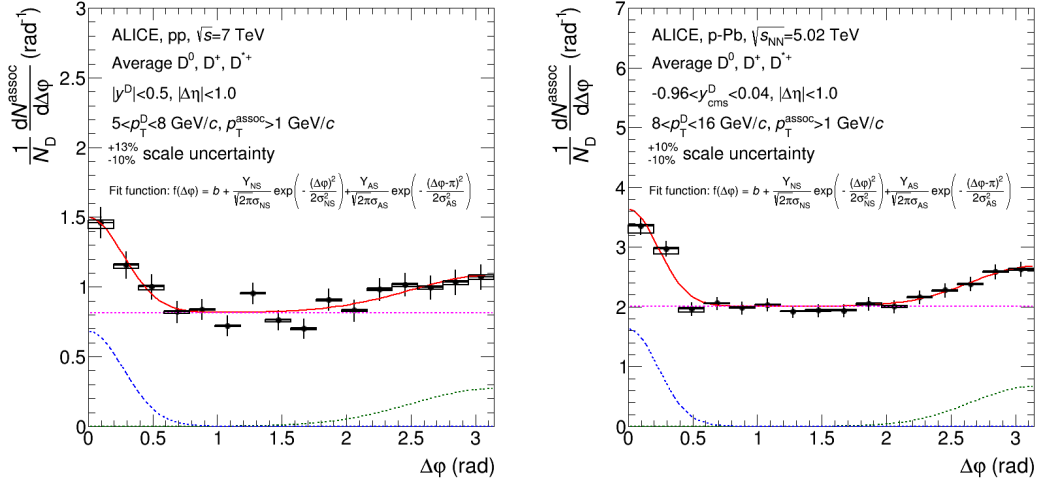


Figure 7.12: Left: Example of the fit performed on the azimuthal correlation distributions in pp collisions for D mesons in the range $5 < p_T(D) < 8$ GeV/c and associated tracks with $p_T^{assoc} > 1$ GeV/c. Right: same as left panel, but for p-Pb collisions for D mesons $8 < p_T(D) < 16$ GeV/c.

7.6.1 Systematic uncertainties from the fitting procedure

Different sources contribute to the systematic uncertainty of the parameter estimation. In first place, the baseline has been computed as already discussed in section 7.3. The different values that are obtained after varying the definition of the transverse region have been used to fix the parameter C in the equation 7.4. After that the fit has been repeated and for each variation of the transverse region, the near-side parameters have been re-extracted. The relative difference compared to the reference value computed in the region $\pi/4 < |\Delta\varphi| < \pi/2$ has been computed, and the RMS of all the variations of a given parameter (near-side yield, near-side σ) has been taken as the systematic uncertainty due to the baseline estimation.

For what concerns the near-side yield and the baseline, the value calculated as the RMS of the baseline variations is summed in quadrature with the scale uncertainty, and the square root of this sum is taken as the systematic uncertainty on the near-side yield and baseline.

The width of the distribution on the near side does not depend on the rescaling of the distribution: in this case only the uncertainty from the baseline definition has been considered as systematic uncertainty.

The systematic uncertainties the near-side yields, the near-side widths and the baseline are reported in table 7.2.

7.7. NEAR-SIDE YIELD, WIDTH AND BASELINE AS FUNCTION OF THE D MESON AND ASSOCIATED TRACK p_T

Source	pp	
Kinematic range	$5 < p_T(D) < 8 \text{ GeV}/c$, $0.3 < p_T^{assoc} < 1 \text{ GeV}/c$	$8 < p_T(D) < 16 \text{ GeV}/c$, $p_T^{assoc} > 1 \text{ GeV}/c$
NS yield	$\pm 22\%$	$\pm 15\%$
NS width	$\pm 10\%$	$\pm 5\%$
Baseline	$\pm 13\%$	$\pm 15\%$

Source	p-Pb	
Kinematic range	$5 < p_T(D) < 8 \text{ GeV}/c$, $0.3 < p_T^{assoc} < 1 \text{ GeV}/c$	$8 < p_T(D) < 16 \text{ GeV}/c$, $p_T^{assoc} > 1 \text{ GeV}/c$
NS yield	$\pm 17\%$	$\pm 12\%$
NS width	$\pm 3\%$	$\pm 12\%$
Baseline	$\pm 12\%$	$\pm 11\%$

Table 7.2: List of systematic uncertainty values for near-side yield, near-side width and baseline in pp and p-Pb collisions, for two different kinematic ranges of D mesons and associated particles. See text for details.

7.7 Near-side yield, width and baseline as function of the D meson and associated track p_T

The near-side yield, near-side width (σ) and the baseline have been extracted and studied as function of p_T of the D meson for different associated track p_T intervals, in order to quantify the observations made in section 7.4.

Figure 7.13 shows the results for pp collisions at $\sqrt{s} = 7 \text{ TeV}$, compared to results from the PYTHIA6 (different tunes) [26], PYTHIA 8 [67] and POWHEG [63] simulations at the same \sqrt{s} . The near-side yield, shown in the upper row of the figure, shows an increasing trend with increasing p_T of the D meson, confirming the strengthening of the correlation observed already at the level of the distributions. A high- p_T D meson originates from a high p_T heavy quark. Such a quark is highly energetic, meaning that it will generate more tracks in the fragmentation process than a less energetic one. This results in a larger number of associated tracks per D meson (that is the quantified by the near-side yield) with higher p_T of the latter, as observed.

This linearly increasing trend is observed when looking at integrated- p_T tracks (left column, $p_T^{assoc} > 0.3 \text{ GeV}/c$), as well as more differentially in the considered bins of associated track p_T , namely $0.3 < p_T^{assoc} < 1 \text{ GeV}/c$ in the middle column and $p_T^{assoc} > 1 \text{ GeV}/c$ in the right column.

When considering the integrated p_T case for associated tracks, it is observed that the near-side yield increase is steeper than the model prediction. In particular at $p_T(D) < 8 \text{ GeV}/c$, the model predictions and the result from data are in good agreement. For D mesons in the range $8 < p_T(D) < 16 \text{ GeV}/c$,

CHAPTER 7. RESULTS

the central value of the near-side yield is about $\sim 30\%$ larger than the one predicted by the models, although due to the large systematic uncertainty the yield and the models are still to be considered in agreement. POWHEG as well as PYTHIA8 and the PYTHIA6 Perugia 20110 tune predict a larger near-side yield than the Perugia0 and Perugia 2011 tunes, being closer to the value obtained from data. This was already observed when looking directly into the azimuthal correlation distributions. When looking more differentially

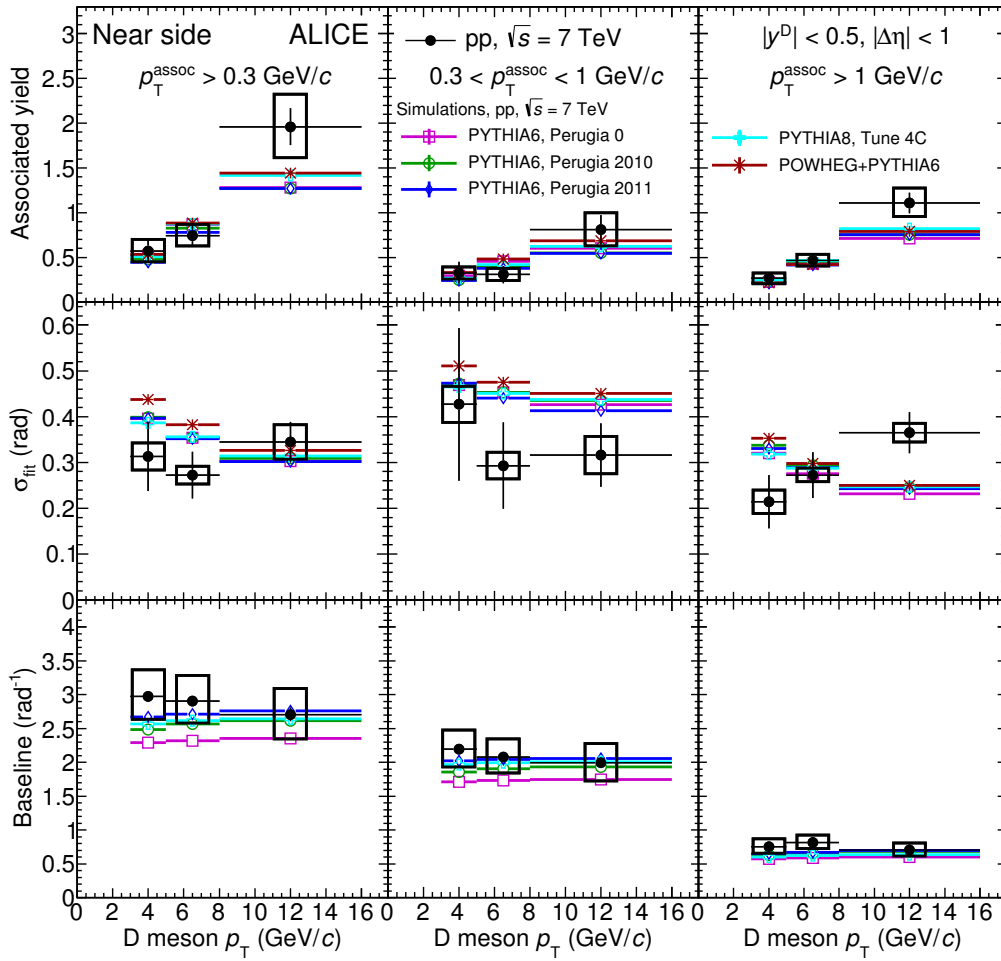


Figure 7.13: Upper row: Near side yield from D-hadron correlations in pp collisions at $\sqrt{s} = 7$ TeV as a function of the p_T of D meson for associated tracks with $p_T^{assoc} > 0.3$ GeV/c (left panel), $0.3 < p_T^{assoc} < 1$ GeV/c (middle panel) and $p_T^{assoc} > 1$ GeV/c compared to predictions from PYTHIA6 (different tunes)[26], PYTHIA 8 [67] and POWHEG [63]. Middle row: near-side peak width following the same scheme as the upper row. Lower row: same as middle row, but for showing the baseline instead of the near-side peak width.

7.7. NEAR-SIDE YIELD, WIDTH AND BASELINE AS FUNCTION OF THE D MESON AND ASSOCIATED TRACK p_T

as a function of the associated track p_T , for both the considered intervals, the near-side yield for D mesons in $8 < p_T(D) < 16$ GeV/c is larger than the model predictions, however the correlations of D mesons with harder tracks (i.e. $p_T^{assoc} > 1$ GeV/c) show a more pronounced discrepancy than the one with softer tracks.

The width of the near-side peak is another parameter that can be extracted from the azimuthal correlation distributions. All the models predict a decreasing trend of the distribution with increasing p_T of the D meson. This is expected due to the larger relativistic boost. The different PYTHIA tunes predict a very similar trend, while POWHEG predicts larger values of the near-side peak width. In the integrated p_T case of the associated tracks, the model prediction are compatible with the measured values within the very large uncertainty, that does not allow to discriminate between them. The widths of the correlations with associated tracks in the ranges $0.3 < p_T^{assoc} < 1$ GeV/c and $p_T^{assoc} > 1$ GeV/c are still in agreement with the models within the very large uncertainties. A general observation in both the p_T ranges of associated tracks, that is then reflected also in the integrated range, is that in the case of low- p_T D mesons, the fit functions results in narrower distributions compared to the predictions of all the considered models, although the large uncertainties make them compatible.

The azimuthal correlations of D mesons in the p_T range $8 < p_T(D) < 16$ GeV/c and $p_T^{assoc} > 1$ GeV/c present a very wide correlation peak, that is about $\sim 2 \sigma$ away from the Monte Carlo predictions. Looking back at figure 7.4, it can be observed that the fluctuations of the points at $\Delta\varphi \sim \pi/8$ leads the enlargement of the distribution in this particular p_T bin.

The fact that in the lowest D-meson p_T interval the widths seems to be overestimated by the models, and that at large D-meson p_T the fluctuating point enlarges artificially the distribution, creates the visual impression that the widths follow a different trend in data and models for the $p_T^{assoc} > 1$ GeV/c case.

The bottom row of figure 7.13 represents the baseline as a function of the p_T of the D meson for different associated tracks p_T intervals. Differently from figure 7.7, where the empty box represented only the systematic uncertainty due to the calculation of the baseline, in figure 7.13 the later is summed in quadrature with the scale uncertainty. All the models tend to underestimate the value of the baseline, although to considering the systematic uncertainty, all of them are compatible with the measured values. The PYTHIA tunes Perugia 2010 and 2011 predict a larger value of the baseline, closer to the data points, which is expected given that the parameters describing multi parton interactions in the underlying event have been tuned using early LHC data from ATLAS [26].

Figure 7.14 shows the comparison of the near-side yields and widths measured in p-Pb collisions at $\sqrt{s_{NN}} = 5.02$ TeV with the same models shown in the pp case (fig. 7.13), but calculated at the centre of mass energy $\sqrt{s} = 5.02$ TeV. In addition, the centre-of-mass frame of the simulated sample is boosted in

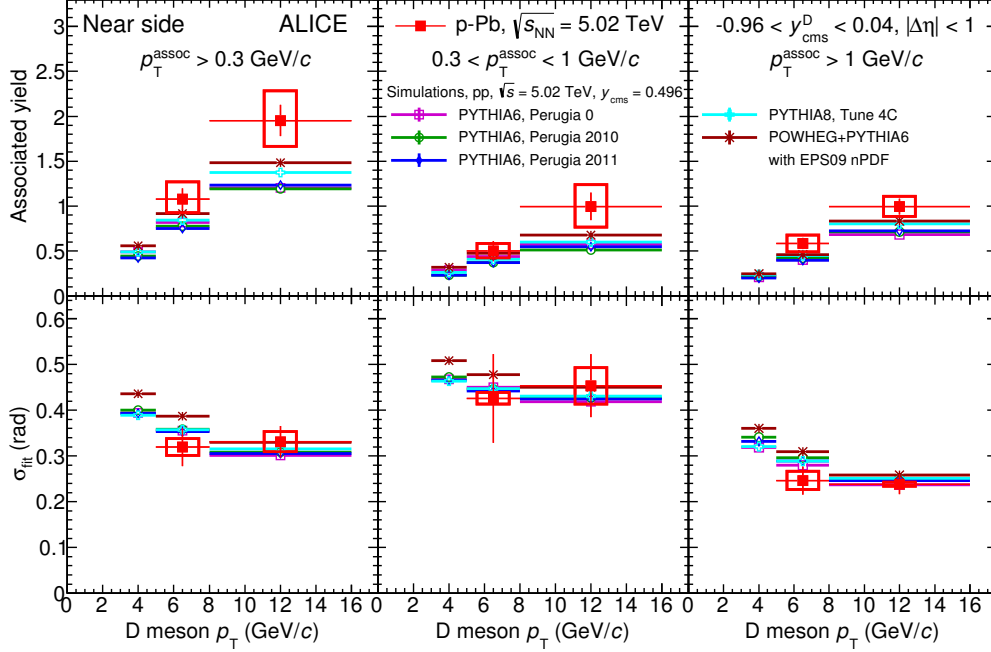


Figure 7.14: Upper row: Near-side yield from D-hadron correlations in p-Pb collisions at $\sqrt{s_{NN}} = 5.02$ TeV as function of the p_T of D meson for associated tracks with $p_T^{assoc} > 0.3$ GeV/c (left panel), $0.3 < p_T^{assoc} < 1$ GeV/c (middle panel) and $p_T^{assoc} > 1$ GeV/c (right panel) compared to predictions from PYTHIA [26], PYTHIA 8 [67] and POWHEG [63] + PYTHIA6 (the last model is computed with corrected PDFs of the protons, using the CT10nlo [77] + EPS09[78] parametrisation). Lower row: near-side peak width following the same scheme as the upper row.

rapidity by $\Delta y_{NN} = 0.465$, to account for the asymmetric collisional system present in the data. In the case of the POWHEG + PYTHIA Monte Carlo sample, the proton PDFs are corrected for nuclear effects (CT10nlo [77] with EPS09[78]).

For D mesons in both the measured p_T ranges ($5 < p_T(D) < 8$ GeV/c and $8 < p_T(D) < 16$ GeV/c) and associated tracks in the integrated p_T region, $p_T^{assoc} > 0.3$ GeV/c, the measured central value is $\sim 40\%$ larger than the predictions from models.

The discrepancies can also be observed more differentially for the associated tracks in the ranges $0.3 < p_T^{assoc} < 1$ GeV/c and $p_T^{assoc} > 1$ GeV/c, although in this particular case the larger uncertainties make the models and the results from data more compatible.

The near-side widths, differently from what was the case in pp collisions, are very well reproduced by the pp-like simulations: as already discussed, differently from pp collisions, the results are less fluctuating, making the determi-

7.7. NEAR-SIDE YIELD, WIDTH AND BASELINE AS FUNCTION OF THE D MESON AND ASSOCIATED TRACK P_T

nation of the baseline more stable, and therefore also the estimation of the other parameters. As a consequence of the good agreement of the widths, the hint of the increased near-side yield can be interpreted to be due to a larger associated production of particles than what predicted by the models, rather than artificial increases due to a strong correlation between the two parameters of the fit, namely the near-side yield and width.

A direct study of cold-nuclear matter effects on the azimuthal correlations can be obtained by comparing the parameters obtained in pp collisions and p-Pb collisions. This comparison is shown in figure 7.15. As already discussed in the model comparison, in both pp and p-Pb collisions, the near-side yields show a similar increasing trend with increasing p_T of the D meson, for all the considered p_T ranges of associated tracks. The measured values are in agreement within the large systematical uncertainties. As it was shown in figure 7.10, the different collision energy results, according to PYTHIA, in a $\sim 10\%$ larger yield when comparing the yields at $\sqrt{s} = 7$ TeV to those at $\sqrt{s} = 5$ TeV. To have a one-to-one comparison, the near-side yields in pp collisions at $\sqrt{s} = 7$ TeV should be rescaled using the values shown in figure 7.10: however,

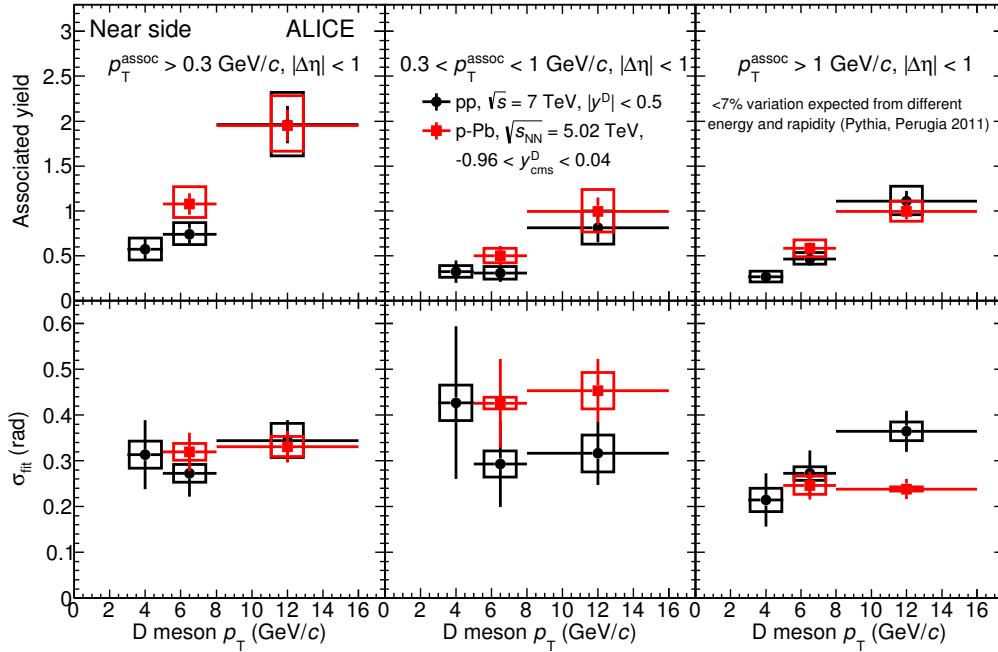


Figure 7.15: Upper row: Near side yield in p-Pb collisions at $\sqrt{s_{NN}} = 5.02$ TeV compared to the near-side yield in pp collisions at $\sqrt{s} = 7$ TeV as function of the p_T of D meson for associated tracks with $p_T^{assoc} > 0.3$ GeV/c (left panel) $p_T^{assoc} > 1$ GeV/c (middle panel) and $0.3 < p_T^{assoc} < 1$ GeV/c (right panel). Lower row: near-side width in the two collision systems following the same scheme as the upper row.

CHAPTER 7. RESULTS

given that the current uncertainties are way larger than the observed effect, the measurement is not sensitive to this difference, which would lead to the same conclusion of compatibility within the large uncertainties. The widths of the near-side peak in the correlation distributions (lower row of figure 7.15) for associated tracks with $p_{\text{T}}^{\text{assoc}} > 0.3 \text{ GeV}/c$ are well in agreement. The correlations with associated tracks in the p_{T} sub-ranges are also compatible within the uncertainties. This quantitative agreement of the correlation parameters within uncertainties follows as a direct consequence of the already discussed compatibility of the $\Delta\varphi$ -distributions shown in figure 7.11.

8

Outlook

Besides the results in pp collisions at $\sqrt{s} = 7$ TeV and p-Pb collisions at $\sqrt{s_{NN}} = 5.02$ TeV discussed in the previous chapter, different studies have been conducted to understand the feasibility of measuring the D-hadron correlations in different collision systems (namely Pb-Pb collisions), as well as extracting more differential information using triggered data. Before concluding this manuscript, a brief description of those results is provided.

8.1 D^{*+} -charged particle correlations in Pb-Pb collisions at $\sqrt{s_{NN}} = 2.76$ TeV

The main purpose of the ALICE experiment is to study the properties of the Quark Gluon Plasma using the data from collisions of heavy-ions.

ALICE collected $1.6 \cdot 10^7$ central Pb-Pb collisions, at a centre-of-mass energy of $\sqrt{s_{NN}} = 2.76$ TeV in 2011. The sample allows for the measurements of the nuclear modification factor of fully reconstructed D mesons [1] and of their elliptic flow coefficient [2, 47], providing new insights in the physics of heavy-quarks in the QGP.

As described in section 1.4.2, azimuthal correlations provide an excellent tool for better understanding the energy loss mechanisms, as well as providing an indirect measurement of the fragmentation process. In the extremely high multiplicity environment of heavy-ion collisions, the reconstruction of D mesons is more challenging than in smaller systems, like pp and p-Pb collisions. The strategy for the reconstruction is the same as the one discussed in section 4.2, with tighter topological selections to cope with the overwhelming combinatorial background due to the high multiplicity. In this PhD project, the correlation analysis has been performed on the Pb-Pb data sample collected on 2011, using centrality-based triggers and selecting the 0-10 % most central collisions.

The results for the D^{*+} -charged particle analysis are shown in figure 8.1, for D mesons in the p_T ranges $8 < p_T(D^{*+}) < 16$ GeV/ c in the left panel, and $16 < p_T(D^{*+}) < 36$ GeV/ c , with charged particles selected with $p_T > 2$ GeV/ c . Only the high- p_T intervals are shown: charm quarks with high transverse momentum (that give origin to high p_T D mesons) leave the medium faster and are

CHAPTER 8. OUTLOOK

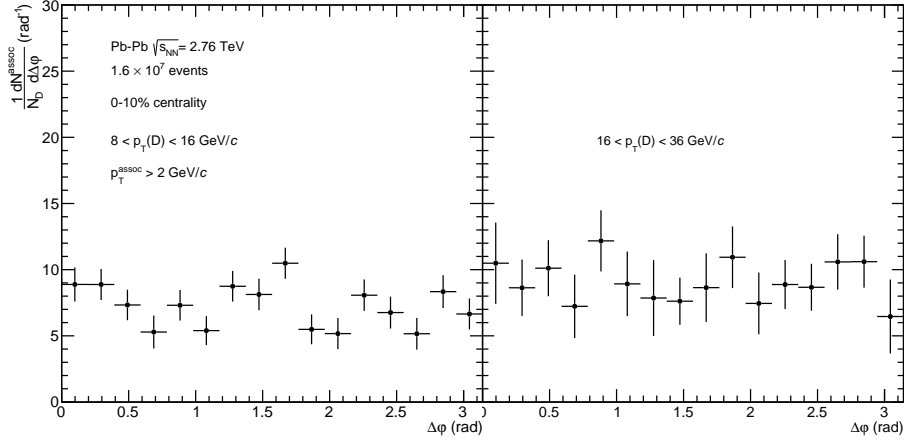


Figure 8.1: Azimuthal correlations of D^{*+} mesons and charged particles in Pb-Pb collisions at $\sqrt{s_{NN}} = 2.76$ TeV, for $8 < p_T(D^{*+}) < 16$ GeV/ c in the left panel, and $16 < p_T(D^{*+}) < 36$ GeV/ c in the right panel.

less affected by the plasma itself. Moreover, as already observed in the smaller systems, a higher transverse momentum of the D mesons means a higher absolute value of the correlation above the baseline, as well as a narrower peak. In addition, at higher p_T , the S/B ratio increases, reducing the uncertainty due to the background subtraction. Therefore, if any correlation is to be observed with the limited statistics available it would be for this p_T region. The choice of high p_T associated tracks has been done to reduce the level of the baseline (dominated by lower p_T tracks) that makes the observation of the peak extremely challenging.

The effect of the limited statistics is clearly visible in figure 8.1. The large error bars and the fluctuating points make it difficult to define the baseline of uncorrelated tracks, as well as to observe the near-side correlation peak on top of that. A larger data sample (about one order of magnitude) is expected from LHC-RUN 2 (i.e. in the years 2015-2018), however it is expected that the measurement will be possible after the long shut-down and the detector upgrades. More details about the upgrades given in the next section

8.2 ALICE upgrades

After the end of LHC-RUN 2 (year 2018), a two-year shutdown period at LHC is planned, where all the four major experiments will undergo relevant upgrades of the detector systems.

The two main detectors of ALICE will also be upgraded: the current read-out system of the TPC based on the MWPC technology will be replaced by a GEM read-out [79], increasing the read-out frequency from the order of tens of kHz to the order of the MHz, allowing to take data with a much higher

instantaneous luminosity.

A major upgrade for the ITS is also planned [80]: the current layout of six silicon detectors layers will be modified by adding one extra layer, closer to the interaction point. Figure 8.2 shows the new layout. All the seven layers will use Monolithic Active Pixel Sensors (MAPS), that incorporate a matrix of diodes with a pitch of the order of $30\text{ }\mu\text{m}$. This will improve the resolution on the track impact parameter by a factor 2-5 depending on the p_T of the track. This results in an improved reconstruction of the secondary vertices, and therefore in a better reconstruction of D mesons. Figure 8.3 shows the expected statistical uncertainty on the raw D^{*+} meson yield with the upgraded ITS. In the p_T range covered in this thesis, the uncertainty is below 1%. This reflects itself in the azimuthal correlations, where a better precision for the D meson reconstruction, apart from the fact that increases the number of triggers, provides a better signal over background ratio, that results in a more precise estimation of the correlation distribution. The expected correlation distribution for D mesons in the p_T region $8 < p_T(D) < 16\text{ GeV}/c$, with the upgraded ITS are shown in figure 8.4, in the left panel showing the integrated p_T range of associated tracks, while the right panel the $p_T > 2\text{ GeV}/c$. The statistical uncertainties are very small and the stability of the baseline grants a clear observation of the correlation peaks, allowing to clearly identify the away-side structure as well.

This has a direct impact on the extracted associated yields. The relative uncertainty for the near-side yield is shown in the left panel of figure 8.5 as a function of the minimum p_T used to select the associated tracks. The expected uncertainty varies from 8-10 % for the lowest p_T -bin of the D meson

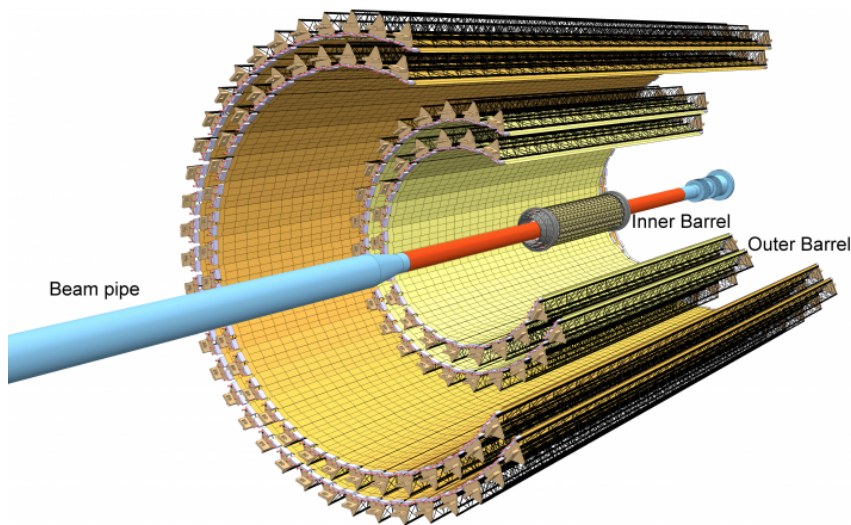


Figure 8.2: Layout of the new ITS with seven layers of silicon-pixel-based detectors, to be installed during the long shutdown starting at the end of 2018 and to be operational in 2020.

CHAPTER 8. OUTLOOK

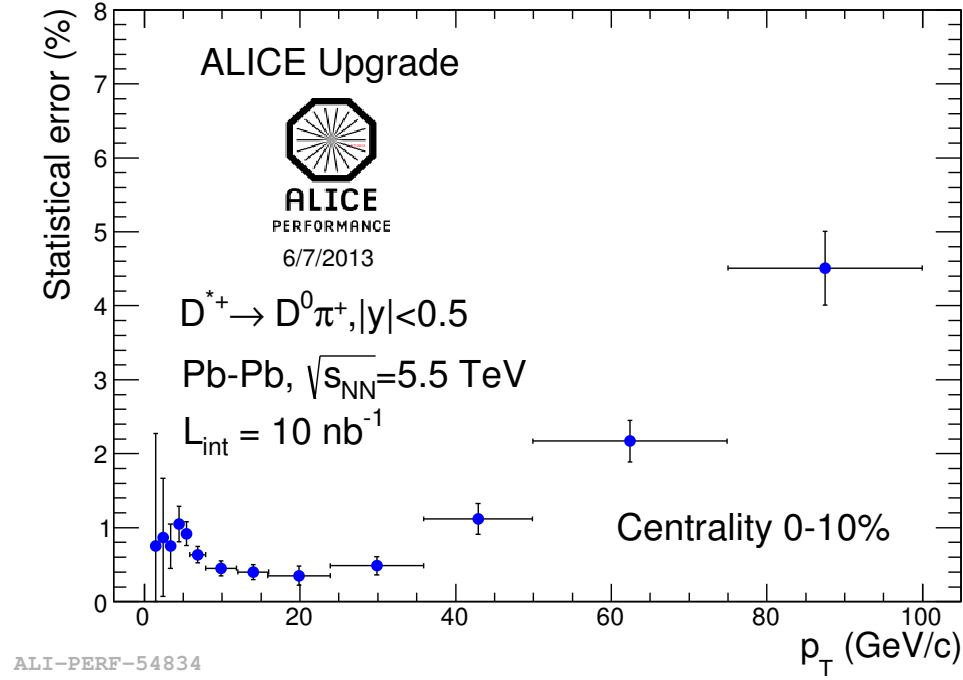


Figure 8.3: Relative statistical uncertainty on the D^{*+} meson yield extraction in Pb-Pb collisions with the upgraded ITS

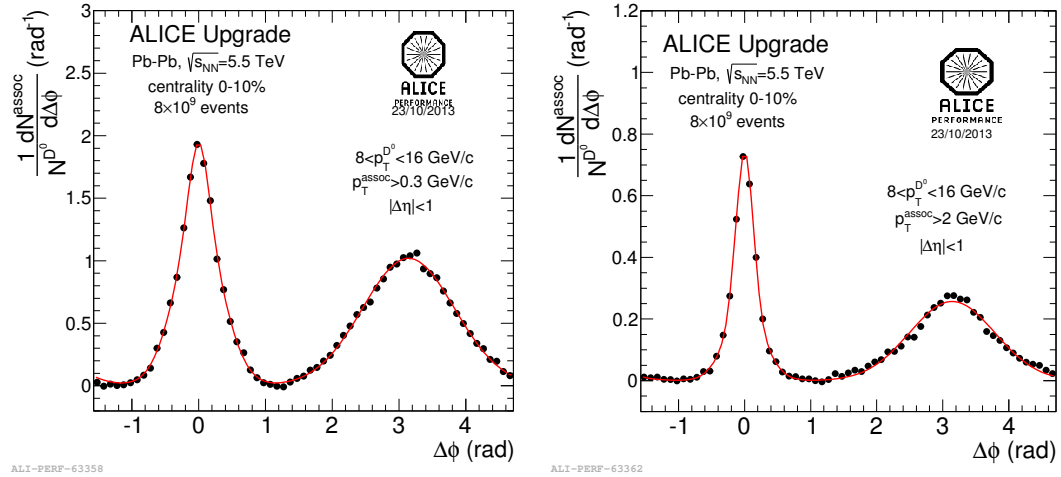


Figure 8.4: Simulated azimuthal correlations of D mesons and charged particles in Pb-Pb collisions at $\sqrt{s_{NN}} = 5.5$ TeV with the upgraded ITS, for $8 < p_T(D^{*+}) < 16 \text{ GeV}/c$, with $p_T^{assoc} > 0.3 \text{ GeV}/c$ in the left panel and $p_T^{assoc} > 2 \text{ GeV}/c$ in the right panel.

8.3. AZIMUTHAL CORRELATIONS WITH EMCAL TRIGGER

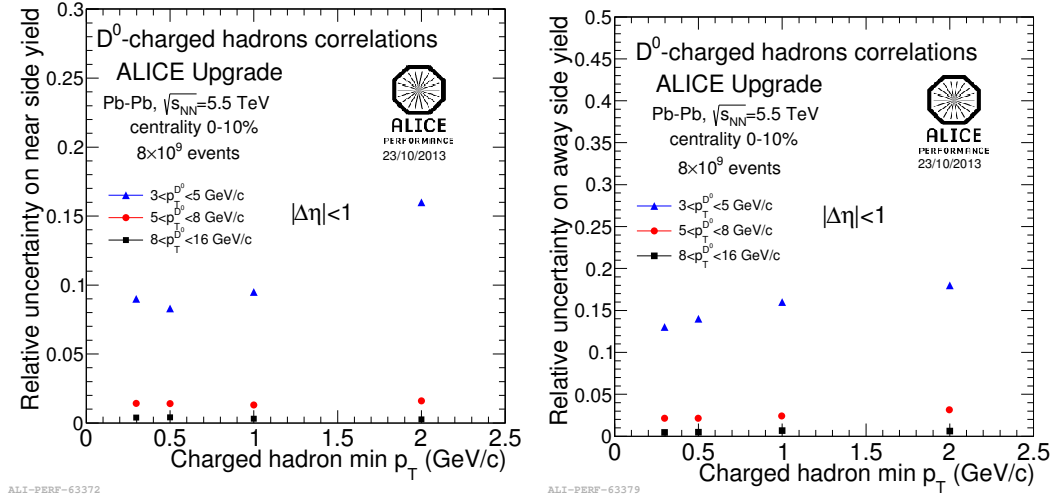


Figure 8.5: Left panel: relative uncertainty on the near-side associated yield of azimuthal correlations of D mesons and associated tracks with the upgraded ITS. Right panel: same as left, but for the away side instead of the near side.

($3 < p_T(D) < 5$ GeV/c) and to less than 2 % for higher p_T -bins.

The precision on the away-side yield is of the same order for $p_T(D) > 5$ GeV/c, and while for lower values of D meson p_T the expected precision is of the order of 12 % for the integrated p_T of the associated tracks and increases to 20% when increasing the lower threshold.

In this scenario, the measurement of the away-side peak properties will become feasible, which is of big interest as it will provide a deeper insight in the nature of the energy loss of the heavy-quarks produced in the hard scattering process.

8.3 Azimuthal correlations with EMCAL trigger

During the 2012 data taking, a sample of $3.3 \cdot 10^7$ pp collisions at $\sqrt{s} = 8$ TeV events have been collected using a trigger based on the energy deposit in the electromagnetic calorimeter.

EMCAL is triggered by either a photon, or a high- p_T electron. The latter case is of particular interest for the correlation analyses involving D mesons: namely, a high- p_T electron is likely to originate from a heavy-flavour decay, hence enhancing the fraction of events including a heavy-flavour quark. On the other hand, the trigger can enhance events that present a jet in the final state that, if originating from a heavy-flavour production process can be used for near- and away-side correlation studies.

The reconstruction strategy for D^{*+} mesons is the same as described in the previous sections. The first gain of the used trigger is that the (raw) number of reconstructed D mesons per event is, on average, an order on magnitude

CHAPTER 8. OUTLOOK

larger. In addition, the p_T -range of the D^{*+} can be extended up to 24 GeV/c, allowing to add an additional p_T -bin for the correlation study.

Figure 8.6 shows the raw correlation distribution of D^{*+} mesons and charged particles in the p_T ranges $3 < p_T(D^{*+}) < 5$ GeV/c, $5 < p_T(D^{*+}) < 8$ GeV/c, $8 < p_T(D^{*+}) < 16$ GeV/c, already available in minimum bias data, and the additional bin $16 < p_T(D^{*+}) < 24$ GeV/c. As this is part of an outlook estimation, the presented distributions include the event-mixing correction but not the other corrections, such as D meson and single track efficiency, beauty feed-down subtraction and purity, as well as trigger bias corrections.

An additional bias due to the trigger is present in the event mixing distribution. This is due to the limited acceptance of the EMCAL detector. Indeed, as already discussed in section 3.2, the EMCAL covers about 1/4 of the azimuthal range ($80^\circ < \varphi < 180^\circ$) and a pseudo-rapidity range of $|\eta| < 0.7$. This means that events triggered by the EMCAL will present a topology with electrons or jets pointing to one particular direction. As the D mesons are very likely to point in the same direction, a mixed-event distribution presents a peak structure in the direction $(\Delta\varphi, \Delta\eta) = (0,0)$, as it can be seen from figure 8.7.

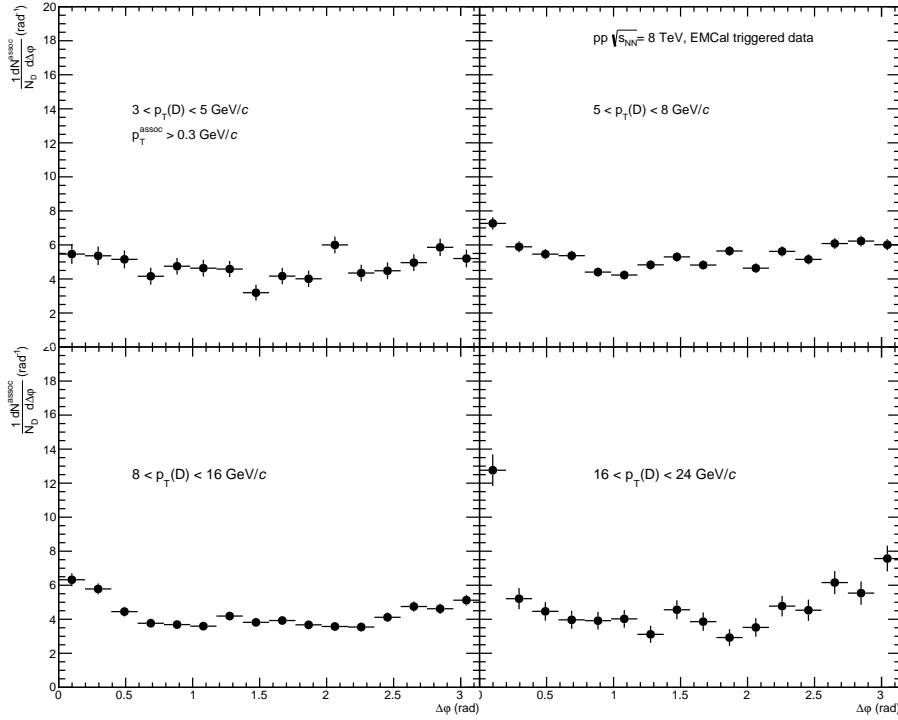


Figure 8.6: Raw azimuthal correlations of D^{*+} mesons and charged particles in pp collisions at $\sqrt{s} = 8$ TeV with the EMCAL trigger, for $3 < p_T(D^{*+}) < 5$ GeV/c in the upper left panel, $5 < p_T(D^{*+}) < 8$ GeV/c in the upper right panel, $8 < p_T(D^{*+}) < 16$ GeV/c in the lower left panel and $16 < p_T(D^{*+}) < 36$ GeV/c in the lower right panel. All the four panels are for $p_T^{assoc} > 0.3$ GeV/c.

8.3. AZIMUTHAL CORRELATIONS WITH EMCAL TRIGGER

A similar structure is indeed expected by construction when considering both the “trigger” particle and the associated particle azimuthal distribution not being constant, but showing a structure in the same region. In the latter case, the event-mixing distribution is expected to account for it by presenting a near-side structure.

However, the structure observed in figure 8.7 is a convolution of two effects: first the above-mentioned non-uniform φ distribution of “trigger” and associated particles, and second the fact that the mixed-event distribution is biased by the presence of mostly jet-like events with a preferred direction.

Using a triggered sample for this particular study would for sure be beneficial in terms of statistics and p_T -reach, but would first need a profound understanding of the underlying biases and a strategy for implementing the necessary corrections.

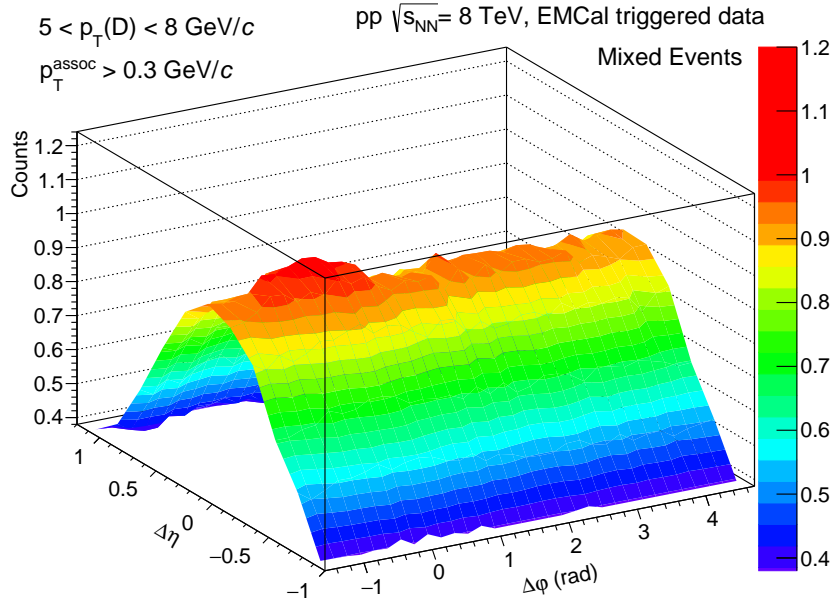


Figure 8.7: Azimuthal correlations of D^{*+} mesons and charged particles in mixed events in pp collisions at $\sqrt{s} = 8$ TeV using the EMCAL trigger, for $5 < p_T(D^{*+}) < 8$ GeV/c and $p_T^{assoc} > 0.3$ GeV/c.

9

Conclusions

This thesis presented the first analysis of the angular correlations of D^{*+} mesons and charged particles in pp collision at $\sqrt{s} = 7$ TeV and p-Pb collisions at $\sqrt{s_{NN}} = 5.02$ TeV, measured with the ALICE detector at the LHC. The measurement has been performed differentially as a function of the D meson p_T in the intervals $3 < p_T(D^{*+}) < 5$ GeV/ c , $5 < p_T(D^{*+}) < 8$ GeV/ c , $8 < p_T(D^{*+}) < 16$ GeV/ c , and as a function of the associated track p_T , the integrated range with only a lower threshold of $p_T^{assoc} > 0.3$ GeV/ c , as well as a more differential study by separating “soft” (low p_T) tracks, i.e. with $0.3 < p_T^{assoc} < 1$ GeV/ c and “hard” (high p_T) tracks, with $p_T^{assoc} > 1$ GeV/ c .

The main focus of this manuscript is on the D^{*+} meson. A similar effort has been done within the ALICE collaboration for the analysis of correlations of D^0 and D^+ mesons with charged tracks.

The compatibility of the results between the different analyses allows for the averaging of their results: this procedure grants for a reduction of the uncertainties as well as for a greater stability of the obtained distributions. Therefore, those distributions were used for extracting the physics information.

In both the collision systems, the correlation distributions show a similar behaviour. The near-side peaks get narrower and higher with increasing p_T of the D meson. A similar qualitative behaviour is observed also with increasing p_T of the associated tracks.

Apart from the baseline, defined as the minimum of the correlation distribution (obtained as the average of the measured points around $\Delta\varphi=\pi/2$), the near-side and away-side structures in pp and p-Pb are compatible within errors. The difference in the baseline level is due to the higher multiplicity environment in p-Pb collisions compared to pp collisions. The same conclusion on compatibility of the pp and p-Pb distributions can be obtained when comparing the parameters describing the near-side peak in the correlation distributions, namely the (near-side) associated yield and width. Those parameters are extracted by fitting the measured distributions.

Moreover, the distributions in pp and p-Pb collisions have been compared to distributions obtained from Monte Carlo event generators, namely PYTHIA and POWHEG for pp, and only PYTHIA in the case of p-Pb collisions, at the respective collision energy $\sqrt{s} = 7$ and 5.02 TeV. The models describe the correlation distributions qualitatively well, although the large uncertainty does

CHAPTER 9. CONCLUSIONS

not allow for a distinction between them. The same conclusion can be drawn by comparing the associated yields and widths from data and simulations. Summarising, within the precision available with the current measurements, cold-nuclear matter effects do not seem to influence the correlation distribution. This statement can be strengthened or disproved by more precise measurements expected with the larger samples from LHC RUN-2 (2015-2018) as well as by more differential measurement, for example as function of the event multiplicity.

A first measurement in heavy-ion collisions with the first LHC data was not possible due to the limited available statistics. The expected detector upgrades from the long shutdown at LHC (2018) are expected to improve the reconstruction efficiency as well as provide a larger statistical sample: this will provide a precise measurement and complete the picture of the physics behind azimuthal correlations involving heavy-flavour particles.

Bibliography

- [1] **ALICE** Collaboration, J. Adam *et al.*, “Transverse momentum dependence of D-meson production in Pb-Pb collisions at $\sqrt{s_{NN}} = 2.76$ TeV,” [arXiv:1509.06888 \[nucl-ex\]](#).
- [2] **ALICE** Collaboration, B. B. Abelev *et al.*, “Azimuthal anisotropy of D meson production in Pb-Pb collisions at $\sqrt{s_{NN}} = 2.76$ TeV,” *Phys. Rev. C* **90** no. 3, (2014) 034904, [arXiv:1405.2001 \[nucl-ex\]](#).
- [3] **ALICE** Collaboration, S. Bjelogrić, “Heavy-flavour correlations in pp, p-Pb and Pb-Pb collisions,” *Nucl. Phys. A* **931** (2014) 563–568.
- [4] **ALICE** Collaboration, J. Adam *et al.*, “Measurement of azimuthal correlations of D mesons and charged particles in pp collisions at $\sqrt{s} = 7$ TeV and p-Pb collisions at $\sqrt{s_{NN}} = 5.02$ TeV.” In preparation.
- [5] P. W. Higgs, “Broken Symmetries and the Masses of Gauge Bosons,” *Phys. Rev. Lett.* **13** (1964) 508–509.
- [6] **ATLAS** Collaboration, G. Aad *et al.*, “Observation of a new particle in the search for the Standard Model Higgs boson with the ATLAS detector at the LHC,” *Phys. Lett. B* **716** (2012) 1–29, [arXiv:1207.7214 \[hep-ex\]](#).
- [7] **CMS** Collaboration, S. Chatrchyan *et al.*, “Observation of a new boson at a mass of 125 GeV with the CMS experiment at the LHC,” *Phys. Lett. B* **716** (2012) 30–61, [arXiv:1207.7235 \[hep-ex\]](#).
- [8] S. Bethke, “Experimental tests of asymptotic freedom,” *Prog. Part. Nucl. Phys.* **58** (2013) 351–386, [arXiv:hep-ex/0606035 \[hep-ex\]](#).
- [9] **LHCb** Collaboration, R. Aaij *et al.*, “Observation of J/ψ Resonances Consistent with Pentaquark States in $\Lambda_b^0 \rightarrow J/\psi K^- p$ Decays,” *Phys. Rev. Lett.* **115** (2015) 072001, [arXiv:1507.03414 \[hep-ex\]](#).
- [10] **HotQCD** Collaboration, M. Cheng, “The QCD equation of state and transition at finite temperature,” *PoS LAT2009* (2009) 175, [arXiv:0912.0044 \[hep-lat\]](#).
- [11] **Wuppertal-Budapest** Collaboration, S. Borsanyi, Z. Fodor, C. Hoelbling, S. D. Katz, S. Krieg, C. Ratti, and K. K. Szabo, “Is there still any T_c mystery in lattice QCD? Results with physical masses in the continuum limit III,” *JHEP* **09** (2010) 073, [arXiv:1005.3508 \[hep-lat\]](#).
- [12] **HotQCD** Collaboration, A. Bazavov *et al.*, “Equation of state in (2+1)-flavor QCD,” *Phys. Rev. D* **90** (2014) 094503, [arXiv:1407.6387 \[hep-lat\]](#).

BIBLIOGRAPHY

- [13] “USQCD, strongly interacting matter under extreme conditions.”
[Http://www.usqcd.org/extreme.html](http://www.usqcd.org/extreme.html).
- [14] “The Ohio State University, evolution of heavy ion collisions.”
[Https://u.osu.edu/vishnu/physics](https://u.osu.edu/vishnu/physics).
- [15] **ALICE** Collaboration, B. Abelev *et al.*, “Centrality determination of Pb-Pb collisions at $\sqrt{s_{NN}} = 2.76$ TeV with ALICE,” *Phys. Rev.* **C88** no. 4, (2013) 044909, [arXiv:1301.4361](#) [nucl-ex].
- [16] **ALICE** Collaboration, K. Aamodt *et al.*, “Elliptic flow of charged particles in Pb-Pb collisions at 2.76 TeV,” *Phys. Rev. Lett.* **105** (2010) 252302, [arXiv:1011.3914](#) [nucl-ex].
- [17] A. Bilandzic, R. Snellings, and S. Voloshin, “Flow analysis with cumulants: Direct calculations,” *Phys. Rev.* **C83** (2011) 044913, [arXiv:1010.0233](#) [nucl-ex].
- [18] **STAR** Collaboration, J. Adams *et al.*, “Experimental and theoretical challenges in the search for the quark gluon plasma: The STAR Collaboration’s critical assessment of the evidence from RHIC collisions,” *Nucl. Phys.* **A757** (2005) 102–183, [arXiv:nucl-ex/0501009](#) [nucl-ex].
- [19] **PHENIX** Collaboration, K. Adcox *et al.*, “Formation of dense partonic matter in relativistic nucleus-nucleus collisions at RHIC: Experimental evaluation by the PHENIX collaboration,” *Nucl. Phys.* **A757** (2005) 184–283, [arXiv:nucl-ex/0410003](#) [nucl-ex].
- [20] **ALICE** Collaboration, J. Adam *et al.*, “Anisotropic flow of charged particles in Pb-Pb collisions at $\sqrt{s_{NN}} = 5.02$ TeV,” [arXiv:1602.01119](#) [nucl-ex].
- [21] R. Thomas, B. Kampfer, and G. Soff, “Gluon emission of heavy quarks: Dead cone effect,” *Acta Phys. Hung.* **A22** (2005) 83–91, [arXiv:hep-ph/0405189](#) [hep-ph].
- [22] R. J. Glauber and G. Matthiae, “High-energy scattering of protons by nuclei,” *Nucl. Phys.* **B21** (1970) 135–157.
- [23] **ALICE** Collaboration, K. Aamodt *et al.*, “Suppression of Charged Particle Production at Large Transverse Momentum in Central Pb-Pb Collisions at $\sqrt{s_{NN}} = 2.76$ TeV,” *Phys. Lett.* **B696** (2011) 30–39, [arXiv:1012.1004](#) [nucl-ex].
- [24] **CMS** Collaboration, S. Chatrchyan *et al.*, “Observation and studies of jet quenching in PbPb collisions at nucleon-nucleon center-of-mass energy = 2.76 TeV,” *Phys. Rev.* **C84** (2011) 024906, [arXiv:1102.1957](#) [nucl-ex].

-
- [25] **ATLAS** Collaboration, G. Aad *et al.*, “Observation of a Centrality-Dependent Dijet Asymmetry in Lead-Lead Collisions at $\sqrt{s_{NN}} = 2.77$ TeV with the ATLAS Detector at the LHC,” *Phys. Rev. Lett.* **105** (2010) 252303, [arXiv:1011.6182 \[hep-ex\]](#).
 - [26] P. Z. Skands, “Tuning Monte Carlo Generators: The Perugia Tunes,” *Phys. Rev. D* **82** (2010) 074018, [arXiv:1005.3457 \[hep-ph\]](#).
 - [27] M. Gyulassy and X.-N. Wang, “HIJING 1.0: A Monte Carlo program for parton and particle production in high-energy hadronic and nuclear collisions,” *Comput. Phys. Commun.* **83** (1994) 307, [arXiv:nucl-th/9502021 \[nucl-th\]](#).
 - [28] **STAR** Collaboration, J. Adams *et al.*, “Evidence from d + Au measurements for final state suppression of high p(T) hadrons in Au+Au collisions at RHIC,” *Phys. Rev. Lett.* **91** (2003) 072304, [arXiv:nucl-ex/0306024 \[nucl-ex\]](#).
 - [29] **ALICE** Collaboration, K. Aamodt *et al.*, “Particle-yield modification in jet-like azimuthal di-hadron correlations in Pb-Pb collisions at $\sqrt{s_{NN}} = 2.76$ TeV,” *Phys. Rev. Lett.* **108** (2012) 092301, [arXiv:1110.0121 \[nucl-ex\]](#).
 - [30] A. Accardi, “Cronin effect in proton nucleus collisions: A Survey of theoretical models,” [arXiv:hep-ph/0212148 \[hep-ph\]](#).
 - [31] N. Armesto, “Nuclear shadowing,” *J. Phys.* **G32** (2006) R367–R394, [arXiv:hep-ph/0604108 \[hep-ph\]](#).
 - [32] F. Gelis, E. Iancu, J. Jalilian-Marian, and R. Venugopalan, “The Color Glass Condensate,” *Ann. Rev. Nucl. Part. Sci.* **60** (2010) 463–489, [arXiv:1002.0333 \[hep-ph\]](#).
 - [33] N. Armesto, L. McLerran, and C. Pajares, “Long Range Forward-Backward Correlations and the Color Glass Condensate,” *Nucl. Phys. A* **781** (2007) 201–208, [arXiv:hep-ph/0607345 \[hep-ph\]](#).
 - [34] **ALICE** Collaboration, B. Abelev *et al.*, “Long-range angular correlations on the near and away side in p-Pb collisions at $\sqrt{s_{NN}} = 5.02$ TeV,” *Phys. Lett. B* **719** (2013) 29–41, [arXiv:1212.2001 \[nucl-ex\]](#).
 - [35] **CMS** Collaboration, S. Chatrchyan *et al.*, “Observation of long-range near-side angular correlations in proton-lead collisions at the LHC,” *Phys. Lett. B* **718** (2013) 795–814, [arXiv:1210.5482 \[nucl-ex\]](#).
 - [36] **ATLAS** Collaboration, G. Aad *et al.*, “Measurement with the ATLAS detector of multi-particle azimuthal correlations in p+Pb collisions at $\sqrt{s_{NN}}=5.02$ TeV,” *Phys. Lett. B* **725** (2013) 60–78, [arXiv:1303.2084 \[hep-ex\]](#).
-

BIBLIOGRAPHY

- [37] E. Norrbin and T. Sjostrand, “Production and hadronization of heavy quarks,” *Eur. Phys. J.* **C17** (2000) 137–161, [arXiv:hep-ph/0005110 \[hep-ph\]](#).
- [38] M. Cacciari, S. Frixione, N. Houdeau, M. L. Mangano, P. Nason, and G. Ridolfi, “Theoretical predictions for charm and bottom production at the LHC,” *JHEP* **10** (2012) 137, [arXiv:1205.6344 \[hep-ph\]](#).
- [39] M. Cacciari and E. Gardi, “Heavy quark fragmentation,” *Nucl. Phys.* **B664** (2003) 299–340, [arXiv:hep-ph/0301047 \[hep-ph\]](#).
- [40] M. Cacciari and P. Nason, “Is there a significant excess in bottom hadroproduction at the tevatron?,” *Phys. Rev. Lett.* **89** (Aug, 2002) 122003. <http://link.aps.org/doi/10.1103/PhysRevLett.89.122003>.
- [41] M. Cacciari, S. Frixione, M. L. Mangano, P. Nason, and G. Ridolfi, “QCD analysis of first b cross-section data at 1.96-TeV,” *JHEP* **07** (2004) 033, [arXiv:hep-ph/0312132 \[hep-ph\]](#).
- [42] B. A. Kniehl, G. Kramer, I. Schienbein, and H. Spiesberger, “Inclusive $D^{*+/-}$ production in p anti- p collisions with massive charm quarks,” *Phys. Rev.* **D71** (2005) 014018, [arXiv:hep-ph/0410289 \[hep-ph\]](#).
- [43] **OPAL** Collaboration, G. Alexander *et al.*, “A Study of charm hadron production in $Z^0 \rightarrow c$ anti- c and $Z^0 \rightarrow b$ anti- b decays at LEP,” *Z. Phys.* **C72** (1996) 1–16.
- [44] J. Pumplin, D. R. Stump, J. Huston, H. L. Lai, P. M. Nadolsky, and W. K. Tung, “New generation of parton distributions with uncertainties from global QCD analysis,” *JHEP* **07** (2002) 012, [arXiv:hep-ph/0201195 \[hep-ph\]](#).
- [45] **ALICE** Collaboration, B. Abelev *et al.*, “Measurement of charm production at central rapidity in proton-proton collisions at $\sqrt{s} = 7$ TeV,” *JHEP* **01** (2012) 128, [arXiv:1111.1553 \[hep-ex\]](#).
- [46] **ALICE** Collaboration, B. B. Abelev *et al.*, “Measurement of prompt D -meson production in $p - Pb$ collisions at $\sqrt{s_{NN}} = 5.02$ TeV,” *Phys. Rev. Lett.* **113** no. 23, (2014) 232301, [arXiv:1405.3452 \[nucl-ex\]](#).
- [47] **ALICE** Collaboration, B. Abelev *et al.*, “ D meson elliptic flow in non-central Pb-Pb collisions at $\sqrt{s_{NN}} = 2.76$ TeV,” *Phys. Rev. Lett.* **111** (2013) 102301, [arXiv:1305.2707 \[nucl-ex\]](#).
- [48] S. Wicks, W. Horowitz, M. Djordjevic, and M. Gyulassy, “Elastic, inelastic, and path length fluctuations in jet tomography,” *Nucl. Phys.* **A784** (2007) 426–442, [arXiv:nucl-th/0512076 \[nucl-th\]](#).

-
- [49] M. He, R. J. Fries, and R. Rapp, “Heavy Flavor at the Large Hadron Collider in a Strong Coupling Approach,” *Phys. Lett.* **B735** (2014) 445–450, [arXiv:1401.3817 \[nucl-th\]](#).
 - [50] M. Monteno, W. M. Alberico, A. Beraudo, A. De Pace, A. Molinari, M. Nardi, and F. Prino, “Heavy-flavor dynamics in nucleus-nucleus collisions: from RHIC to LHC,” *J. Phys.* **G38** (2011) 124144, [arXiv:1107.0256 \[hep-ph\]](#).
 - [51] R. Auerbeck, N. Bastid, Z. C. del Valle, P. Crochet, A. Dainese, and X. Zhang, “Reference Heavy Flavour Cross Sections in pp Collisions at $\sqrt{s} = 2.76$ TeV, using a pQCD-Driven s-Scaling of ALICE Measurements at $\sqrt{s} = 7$ TeV,” [arXiv:1107.3243 \[hep-ph\]](#).
 - [52] M. Djordjevic and M. Gyulassy, “Heavy quark radiative energy loss in QCD matter,” *Nucl. Phys.* **A733** (2004) 265–298, [arXiv:nucl-th/0310076 \[nucl-th\]](#).
 - [53] M. Nahrgang, J. Aichelin, P. B. Gossiaux, and K. Werner, “Influence of hadronic bound states above T_c on heavy-quark observables in Pb + Pb collisions at the CERN Large Hadron Collider,” *Phys. Rev.* **C89** no. 1, (2014) 014905, [arXiv:1305.6544 \[hep-ph\]](#).
 - [54] J. Uphoff, O. Fochler, Z. Xu, and C. Greiner, “Open Heavy Flavor in Pb+Pb Collisions at $\sqrt{s} = 2.76$ TeV within a Transport Model,” *Phys. Lett.* **B717** (2012) 430–435, [arXiv:1205.4945 \[hep-ph\]](#).
 - [55] T. Lang, H. van Hees, J. Steinheimer, and M. Bleicher, “Heavy quark transport in heavy ion collisions at RHIC and LHC within the UrQMD transport model,” [arXiv:1211.6912 \[hep-ph\]](#).
 - [56] S. Cao, G.-Y. Qin, and S. A. Bass, “Heavy-quark dynamics and hadronization in ultrarelativistic heavy-ion collisions: Collisional versus radiative energy loss,” *Phys. Rev.* **C88** (2013) 044907, [arXiv:1308.0617 \[nucl-th\]](#).
 - [57] M. Djordjevic, “Heavy flavor puzzle at LHC: a serendipitous interplay of jet suppression and fragmentation,” *Phys. Rev. Lett.* **112** no. 4, (2014) 042302, [arXiv:1307.4702 \[nucl-th\]](#).
 - [58] **ALICE** Collaboration, J. Adam *et al.*, “Centrality dependence of high- p_T D meson suppression in Pb-Pb collisions at $\sqrt{s_{NN}} = 2.76$ TeV,” *JHEP* **11** (2015) 205, [arXiv:1506.06604 \[nucl-ex\]](#).
 - [59] **CMS** Collaboration, S. Chatrchyan *et al.*, “Suppression of non-prompt J/ψ , prompt J/ψ , and $Y(1S)$ in PbPb collisions at $\sqrt{s_{NN}} = 2.76$ TeV,” *JHEP* **05** (2012) 063, [arXiv:1201.5069 \[nucl-ex\]](#).
-

BIBLIOGRAPHY

- [60] M. Nahrgang, J. Aichelin, P. B. Gossiaux, and K. Werner, “Influence of hadronic bound states above T_c on heavy-quark observables in pb + pb collisions at the cern large hadron collider,” *Phys. Rev. C* **89** (Jan, 2014) 014905. <http://link.aps.org/doi/10.1103/PhysRevC.89.014905>.
- [61] M. Djordjevic, M. Djordjevic, and B. Blagojevic, “RHIC and LHC jet suppression in non-central collisions,” *Phys. Lett. B* **737** (2014) 298–302, [arXiv:1405.4250 \[nucl-th\]](#).
- [62] A. Beraudo, A. De Pace, M. Monteno, M. Nardi, and F. Prino, “Heavy flavors in heavy-ion collisions: quenching, flow and correlations,” *Eur. Phys. J. C* **75** no. 3, (2015) 121, [arXiv:1410.6082 \[hep-ph\]](#).
- [63] S. Frixione, P. Nason, and G. Ridolfi, “A Positive-weight next-to-leading-order Monte Carlo for heavy flavour hadroproduction,” *JHEP* **09** (2007) 126, [arXiv:0707.3088 \[hep-ph\]](#).
- [64] M. Nahrgang, J. Aichelin, P. B. Gossiaux, and K. Werner, “Azimuthal correlations of heavy quarks in Pb + Pb collisions at $\sqrt{s} = 2.76$ TeV at the CERN Large Hadron Collider,” *Phys. Rev. C* **90** no. 2, (2014) 024907, [arXiv:1305.3823 \[hep-ph\]](#).
- [65] X. Zhu, N. Xu, and P. Zhuang, “Effect of partonic “wind” on charm quark correlations in high-energy nuclear collisions,” *Phys. Rev. Lett.* **100** (Apr, 2008) 152301. <http://link.aps.org/doi/10.1103/PhysRevLett.100.152301>.
- [66] S. Cao, G.-Y. Qin, and S. A. Bass, “Correlations of heavy flavor pairs in Au-Au collisions at 200 AGeV at RHIC,” *Phys. Rev. C* **92** (2015) 054909, [arXiv:1505.01869 \[nucl-th\]](#).
- [67] T. Sjostrand, S. Mrenna, and P. Z. Skands, “A Brief Introduction to PYTHIA 8.1,” *Comput. Phys. Commun.* **178** (2008) 852–867, [arXiv:0710.3820 \[hep-ph\]](#).
- [68] **STAR** Collaboration, L. Adamczyk *et al.*, “Measurements of D^0 and D^* Production in $p + p$ Collisions at $\sqrt{s} = 200$ GeV,” *Phys. Rev. D* **86** (2012) 072013, [arXiv:1204.4244 \[nucl-ex\]](#).
- [69] **ALICE** Collaboration, Belikov and oters, “Kalman Filtering Application for Track Recognition and Reconstruction in ALICE Tracking System,”.
- [70] **Particle Data Group** Collaboration, J. Beringer *et al.*, “Review of Particle Physics (RPP),” *Phys. Rev. D* **86** (2012) 010001.
- [71] A. Dainese, *Charm production and in-medium QCD energy loss in nucleus nucleus collisions with ALICE: A Performance study*. PhD thesis, Padua U., 2003. [arXiv:nucl-ex/0311004 \[nucl-ex\]](#).

- [72] **ALICE** Collaboration, B. Abelev *et al.*, “D-hadron correlations in p-p collisions at $\sqrt{s} = 7$ TeV.” Analysis note - ALICE internal use only.
- [73] **ALICE** Collaboration, B. Abelev *et al.*, “D-hadron correlations in p-Pb collisions at $\sqrt{s_{NN}} = 5.02$ TeV.” Analysis note - ALICE internal use only.
- [74] R. Brun, F. Bruyant, M. Maire, A. C. McPherson, and P. Zancarini, “GEANT3,”.
- [75] **CMS** Collaboration, S. Chatrchyan *et al.*, “Observation of long-range near-side angular correlations in proton-lead collisions at the LHC,” *Phys. Lett. B* **718** (2013) 795–814, [arXiv:1210.5482 \[nucl-ex\]](#).
- [76] **ATLAS** Collaboration, G. Aad *et al.*, “Observation of Associated Near-Side and Away-Side Long-Range Correlations in $\sqrt{s_{NN}}=5.02$ TeV Proton-Lead Collisions with the ATLAS Detector,” *Phys. Rev. Lett.* **110** no. 18, (2013) 182302, [arXiv:1212.5198 \[hep-ex\]](#).
- [77] H.-L. Lai, M. Guzzi, J. Huston, Z. Li, P. M. Nadolsky, J. Pumplin, and C. P. Yuan, “New parton distributions for collider physics,” *Phys. Rev. D* **82** (2010) 074024, [arXiv:1007.2241 \[hep-ph\]](#).
- [78] K. J. Eskola, H. Paukkunen, and C. A. Salgado, “EPS09: A New Generation of NLO and LO Nuclear Parton Distribution Functions,” *JHEP* **04** (2009) 065, [arXiv:0902.4154 \[hep-ph\]](#).
- [79] **ALICE** Collaboration, T. Gunji, “Future Upgrade and Physics Perspectives of the ALICE TPC,” *Nucl. Phys. A* **931** (2014) 1152–1157, [arXiv:1408.3484 \[physics.ins-det\]](#).
- [80] **ALICE ITS** Collaboration, S. Senyukov, “The upgrade of the ALICE Inner Tracking System,” *Nucl. Instrum. Meth. A* **732** (2013) 164–167, [arXiv:1304.1306 \[physics.ins-det\]](#).

Samenvatting

Het Quark Gluon Plasma (QGP) is een ongeboden staat van materie die enige miljoenen van een seconde na de Big Bang heeft bestaan. Om het QGP te creëren zijn er hoge temperatuur en druk nodig. Deze extreme omstandigheden kunnen bereikt worden in ultra-relativistische botsingen van lood ionen bij de “Large Hadron Collider” (LHC) bij CERN.

De eigenschappen van het QGP kunnen worden onderzocht met behulp van zware quarks. Zware quarks (charm and beauty) worden geproduceerd voordat het QGP gevormd wordt. Ze interageren met het botsingsmedium en ze ondergaan de volledige evolutie van het systeem.

Metingen aan proton-proton botsingen (pp) zijn nodig om de productie van zware quark zonder medium te kunnen bestuderen. Daarnaast is het in botsingen van protonen en lood ionen (p-Pb) mogelijk om de effecten van de koude nucleaire materie te bestuderen.

Met behulp van de ALICE detector worden D mesonen via hadronische vervalkanalen reconstrueerd.

Dit proefschrift gaat over de analyse van hoekcorrelaties ($\Delta\varphi$ correlaties) tussen D^{*+} mesonen en geladen deeltjes in proton-proton botsingen met een botsingsenergie van $\sqrt{s} = 7$ TeV en proton-lood ion botsingen met $\sqrt{s_{NN}} = 5.02$ TeV die met het ALICE detector worden gemeten.

De analyse is uitgevoerd voor D^{*+} mesonen met transversale impuls (p_T) in de intervallen $3 < p_T(D^{*+}) < 5$ GeV/c, $5 < p_T(D^{*+}) < 8$ GeV/c, $8 < p_T(D^{*+}) < 16$ GeV/c en geassocieerde deeltjes met $p_T p_T^{assoc} > 0.3$ GeV/c, en meer differentieel door het scheiden van zachte deeltjes (met $0.3 < p_T^{assoc} < 1$ GeV/c) en harde deeltjes (met $p_T^{assoc} > 1$ GeV/c).

Dit proefschrift is gericht op het D^{*+} hadron. Gelijksortige analyses worden uitgevoerd voor de D^0 en D^+ hadronen binnen de “ALICE collaboration”.

Omdat de resultaten van de verschillende analyses overeenstemmen, is het mogelijk deze te middelen. Deze methode vermindert de onzekerheden van de distributies en verbetert hun stabiliteit. De gemiddelde distributies worden gebruikt om de gegevens te interpreteren.

De correlatie distributies gedragen zich op een gelijke manier. De “near-side peak” wordt smaller en hoger voor toenemende D meson p_T . Kwalitatief vergelijkbaar gedrag wordt waargenomen voor toenemende p_T van de geassocieerde deeltjes.

De grondlijn van de correlatie distributie, die gedefinieerd is als het minimum van de distributie, wordt berekend als het gemiddelde van de meting rond $\Delta\varphi = \pi/2$. Met uitzondering van deze grondlijn zijn de “near-side” en “away-side” structuren compatibel binnen de onzekerheden. Het verschil in grondlijn kan verklaard worden vanuit de grotere deeltjesproductie in p-Pb botsingen.

Dezelfde conclusie over compatibiliteit kan getrokken worden over de parameters van de “near-side peak” van hoekcorrelatie-distributies. Deze parameters, de “near-side yield” en “near-side width”, worden verkregen door de distributies te fitten.

De distributies van pp en p-Pb botsingen worden ook vergeleken met de distributies van “Monte Carlo” simulaties, namelijk PYTHIA en POWHEG voor pp botsingen en alleen PYTHIA voor p-Pb botsingen, met botsingsenergie van respectievelijk $\sqrt{s} = 7$ en 5.02 TeV. De modellen beschrijven de correlatiedistributies kwalitatief goed, maar vanwege de grote onzekerheden is het niet mogelijk een onderscheid te maken. Dezelfde conclusie volgt na de vergelijking van de “near-side yield” en “near-side width” tussen data en simulaties.

Kort samengevat lijkt dat, binnen de nauwkeurigheid van de huidige metingen, koude nucleaire effecten de correlatiedistributie niet beïnvloeden. Deze uitspraak kan bevestigd of weerlegd worden met de grote hoeveelheid data die met de LHC RUN-2 (2015-2018) wordt verzameld en met de mogelijkheden om meer differentiële studie te doen (bijvoorbeeld als functie van de hoeveelheid geproduceerde deeltjes).

Metingen aan lood-lood botsingen konden niet uitgevoerd worden vanwege de beperkte hoeveelheid beschikbare data.

De verwachte upgrades van de ALICE detector na de lange afsluiten van de LHC (2018) zal de efficiëntie van D^{*+} -reconstructie verbeteren, en de hoeveelheid data vergroten. Dit zal nauwkeurigere metingen mogelijk maken, die het begrip van hoekcorrelaties met zware quarks compleet zullen maken.

Acknowledgements

Since I moved to the Netherlands, I have met many wonderful persons that made my journey to the achievement of this academic milestone incredible, and who I would like to thank.

First I would like to thank my supervisor, André Mischke, who offered me the opportunity to conduct my PhD research in his group, and with useful suggestions, long conversation and a lot of support in difficult moments made the reaching of this goal possible.

Thanks to Raimond Snellings, for accepting the role and responsibility of being my PhD promotor. It was a pleasure working with you.

I would like to express my gratitude to Alessandro Grelli: thanks for always being available with many good suggestions, providing solutions to many problems and spicing up the working days with lots of fun moments full of laughs. Special thanks to my two paranimphs, Gwen and Jacopo.

Gwen, although even today I still do not remember how we met, the years we spent together in Utrecht have been incredible, with lots of unforgettable moments. Thanks for being such a great friend.

Jacopo, thanks for sharing a lot of positive energy and mood. As soon as I met you back in 2014, I recognised in you the amazing and supportive friend you became.

The Utrecht group, where I spent most of my PhD career, has been a great intellectual, challenging and fun place to work.

First I would like to thank my beloved officemates: starting with Deepa, for all the fun and great moments we shared in the office together. And Andrea, in whom I found a wonderful person and a true friend, who often I perceived as part of my family and with whom I shared a long summer writing our theses. Davide and Alberto, my beloved Sicilian friends, thanks for all your kindness, fun moments and great friendship.

Redmer and Lydia, thanks for being my dutch teachers in the moments when I needed it most.

Marco, Thomas, Panos, Paul, Ton, Grazia, Naghmeh, Alis, Ante, Raoul, Marek, Marta, Carlos, Ermes, Sarah, Chiara, Darius, Annelies, Jasper, You, Misha, Sonia, Fatiha and all the other great colleagues I met at the Utrecht University... thanks for the many interesting and constructive discussions and for your support.

The journey leading to this day passed through CERN, where I spent an amazing year in one of the greatest scientific environments worldwide. There I met some really brilliant persons, who made me grow intellectually to the level where I am today. Particular thanks to Andrea, Fabio, Elena, Jitendra, Somnath and all the other members from the HFCJ group: collaborating with you has been a great pleasure.

Many thanks to Francesco, Zaida, Alexander and all the other colleagues that challenged me intellectually and from whom I have learned a lot.

Antonio, life at CERN would not have been the same without the many fun

moments we had together.

And Emilia, who now belongs to the Utrecht group, but I had the pleasure to meet in Geneva. You have been a great and true friend, not to mention a “great” wing(wo)man.

Life in Utrecht would have not been the same without the many great people that I encountered here.

I would like to thank my two original flatmates, beginning with the youngest one: Marko, you have been a person that I have known since the tender age. Thank you for being a very important person and a true friend throughout my whole life!

And Dražen, after meeting you in front of a cup of tea, my life has been enlightened with your charming style, your unique personality and your sincere friendship. Guys, thanks for all the great moments we shared at the “*Croatian Embassy*”, for all the “one for the road”s and the many, many great “Fridays”. Melissa, with your little bit of pink craziness, you took over the role of “*the new Marko*”, and you have been a great housemate and most importantly, a great friend.

I would like to thank Aleksandra, Spinuso (for teaching me the different meanings of the word “lekker”), Lisa, Sara, Alexis, Dewi, Anna, Anna, Tania, Laura, Claudia, Diana, Dorota, Joana, Benedetta, Guillame, Monica, Morena, little Gaia, Ivano, Pierfrancesco, Valentin, Panos, Andrei, Daniel, Matteo, Federica and all the other great people, that turned every moment in Utrecht in a unique, unforgettable experience.

Special thanks to all the members of the volleyball club Boni, for all the fun and great moments during and after the games.

I would like to express my gratitude to my family that, despite being far away, has always been very supportive and helpful in any moment.

In the period when the first words were typed in what will later become this thesis, my path crossed that of a wonderful person who completely changed my life. I would like to spend the last words of this manuscript to thank you, Sophie, for being such a great and lovely person, for all your support and encouragement, for all our marvellous moments together and for all your deep and true love.

Curriculum vitae

BSc. Physics

2005-2008

University of Trieste, Trieste, Italy

Thesis: Massless particles in perturbation theory: analogies and differences between photons and gravitons

MSc. Physics (Nuclear and Subnuclear Physics)

2008-2010

University of Trieste, Trieste, Italy

Thesis: Effects of the muon $g-2$ discrepancy on the Higgs boson searches at LHC

PhD candidate, Subatomic Physics

2011-2015

Utrecht University, Utrecht, the Netherlands

Thesis: Azimuthal angular correlations of D mesons and charged particles with the ALICE detector at the LHC

IT Specialist

2015-present

ING Bank, Amsterdam, the Netherlands
